

# **Development of M-type hexaferrite films for microwave device application**

**A**

**Thesis**

**Submitted for the award of degree of**

**Doctor of Philosophy**

**By**

**Santhoshkumar M**

**(Registration No. 901512006)**

**Under the supervision of**

**Dr. Puneet Sharma**

**Professor**



**THAPAR INSTITUTE**  
OF ENGINEERING & TECHNOLOGY  
(Deemed to be University)

**School of Physics & Materials Science**  
**Thapar Institute of Engineering & Technology, Patiala**  
**Punjab-147004**  
**September-2021**

அகர முதல எழுத்தெல்லாம் ஆதி  
பகவன் முதற்றே உலகு.

- Thiruvalluvar

A, as its first of letters, every speech maintains;  
The "Primal Deity" is first through all the world's domains.






## CERTIFICATE

This is to certify that the thesis entitled “**Development of M-type hexaferrite films for microwave device application**” which is being submitted by Santhoshkumar M in the fulfilment of the requirement for the award of the degree Doctor of Philosophy in the School of Physics & Materials Science, Thapar Institute of Engineering & Technology (TIET), is an authentic record of candidate’s own work carried out by him under my supervision and guidance. The matter presented in this thesis has not been submitted in part or full for the award of any degree in any other University or Institute.

Date: 10-09-2021

Place: Patiala



**Dr. Puneet Sharma**

(Professor)

School of Physics & Materials Science

Thapar Institute of Engineering & Technology

(TIET), Patiala (147004) Punjab.

## Acknowledgement

Foremost, I would like to express my sincere gratitude to my advisor **Dr. Puneet Sharma**, Professor, Thapar Institute of engineering & Technology (TIET) Patiala, Punjab for the continuous support of my research, for his patience, motivation, enthusiasm, and immense knowledge. His guidance helped me in all the time of research and writing of this thesis. Without his able guidance, this thesis would not be possible and I shall be eternally grateful to him for his assistance.

I offer my special thanks to **Dr. O. P. Pandey**, Professor & former head and **Dr. Kulvir Singh**, Professor & head, School of Physics & Materials Science, Thapar Institute of Engineering & Technology (TIET), Patiala, for providing all the necessary facilities in the department. I extend my gratitude to my doctoral committee members **Dr. Bhupendrakumar Chudasama**, **Dr. Bhasker Chandra Mohanty** and **Dr. Rajesh Khanna** and all faculty members of the SPMS who supported and encouraged me throughout my doctorate program.

I am thankful to my seniors **Dr. Mintu Tyagi**, **Dr. Samiksha Verma**, **Dr. Shiwani Sharma Malhotra**, and fellow labmates **Mr. Anoop Pratap Singh**, **Dr. Chhavi Pahwa**, **Mrs. Shivani Jindal**, **Mr. Parminder Singh**, **Ms. Sonal Singh** and **Ms. Anupriya Choudhary**. I must mention my gratitude to all our charming M.Sc scholars (completed/ongoing) for the extraordinary contribution towards my research work.

I would like to thank SAI Lab, Thapar Institute of Engineering & Technology for SEM and XRD facility. My special thanks to **Mr. Pardeep Bhatia** HI-instrument operator SAI lab for his extensive contribution for characterisation. I like to extend my gratitude to **Dr. Vasant Sathe**, **Dr. V. Raghavendra Reddy** and all scientist of UGC-DAE Consortium for Scientific Research, Khandwa Road, Indore, India for the characterisation. My special thanks to **Dr. Sukhleen Bindra Narang**, Professor, Department of Electronics Technology, Guru Nanak Dev University, Amritsar, India for her valuable support towards my research. I like to convey my regards to **Dr. Manoj Kumar** and **Mr. Munish Verma**, Department of Physics and Materials Science Engineering at Jaypee Institute of Information Technology (Noida) for characterizations.

I am grateful to all non-teaching staff of School of Physics and Materials Science who never turn me down whenever I approached for any help.

I gratefully acknowledge Department of Science and Technology (DST) Science and Engineering Research Board (SERB) (SERB – No.SB/S2/CMP-081/2013) and the Council of Scientific and Industrial Research (CSIR) (grant no. 03(1449)/18/EMR-II for the financial support in the form of Junior Research Fellowship and Research Associateship.

I gratefully acknowledge DST-FIST for providing magnetic measurement facility.

I would like to convey my sincere gratitude to my friends **Mr. Kaushlendra Pandey, Dr. Aayush Gupta, Mrs. Raveena Choudhary, Dr. Amandeep Kaur, Dr. Piyush Sharma, Dr. Nethu Bansal, Mr. Savidh Khan, Ms. Kaveri Ajravat** and **Mrs. Amanpreet Kaur** for creating cheerful atmosphere during my stay. Special thanks to my friends, **Ms. Amanpreet Kaur** School of Chemistry and Biochemistry and **Ms. Manju Rawat** Department of Chemical Engineering for kind and moral support during my stay in TIET.

My parent's **Mr. R. Mahadevan** and **Mrs. J. Rathi Bai** deserve special mention for their unflinching support and encouragement in my all odds and evens. I like to mention my special thanks to my sister's **Mrs. Ananthi Gagan Nambi** and her family, and **Dr. Shiwani Sharma Malhotra** and her Family for a moral support throughout my PhD. Last but not least, I am greatly indebted to my wife **Mrs. Ratchakambal Santhoshkumar** for her close companionship, sacrifices, constant inspiration and encouragement. Finally, I express my apologies, if I miss to mention any name.



**Santhoshkumar M**

### List of Publications

1. **Santhoshkumar Mahadevan**, Vasant Sathe, V Raghavendra Reddy, Puneet Sharma, Site occupation and magnetic studies in La-Co substituted barium hexaferrite, *IEEE Trans. Magn.* 56 (2020) 1–6.
2. **Santhoshkumar Mahadevan**, Sukhleen Bindra Narang, Puneet Sharma, Effect of three-step calcination on structural, magnetic and microwave properties of BaFe<sub>11.5</sub>Ti<sub>0.5</sub>O<sub>19</sub> hexaferrite, *Ceram. Int.* 45 (2019) 9000–9006.
3. **Santhoshkumar Mahadevan**, Chhavi Pahwa, Sukhleen Bindra Narang, Puneet Sharma, Structural, dielectric and magnetic properties of BaFe<sub>12-x</sub>Al<sub>x</sub>O<sub>19</sub> hexaferrite thick films, *J. Magn. Magn. Mater.* 441 (2017) 465-474.
4. **Santhoshkumar Mahadevan**, Puneet Sharma, Charge transport mechanism in BaFe<sub>12</sub>O<sub>19</sub> and BaFe<sub>11</sub>CoO<sub>19</sub>, *J. Magn. Magn. Mater.* 514 (2020) 167174.
5. **Santhoshkumar Mahadevan**, Chhavi Pahwa, Puneet Sharma, Microwave sintered textured barium hexaferrite thick films for microwave device application (Manuscript submitted)

### Other publication

1. Denis Vinnik, **Santhoshkumar Mahadevan**, and Puneet Sharma. "Magnetic Study on Divalent Ion Substituted Barium Hexaferrites." *Defect Diffus. Forum.* 410 (2021) 714-719.
2. Chhavi Pahwa, **Santhoshkumar Mahadevan**, Sukhleen Bindra Narang, Puneet Sharma, "Studies on exchange-coupled magnetodielectric ceramics for microwave application in Ku-band" *IEEE Trans. Magn.* 57 (2021) 1–7
3. Samiksha Verma, **Santhoshkumar Mahadevan**, Chhavi Pahwa, Anoop Pratap Singh, Sukhleen Bindra Narang, Neha Aggarwal, Puneet Sharma, Improved Magnetic and Microwave Properties of La-Substituted Barium Hexaferrite Screen-Printed Thick Films, *J. Supercond. Nov. Magn.* 33 (2020) 2507–2512.
4. Chhavi Pahwa, **Santhoshkumar Mahadevan**, Sukhleen Bindra Narang, Puneet Sharma Structural, magnetic and microwave properties of exchange coupled and non-exchange coupled BaFe<sub>12</sub>O<sub>19</sub>/NiFe<sub>2</sub>O<sub>4</sub> nanocomposites, *J. Alloys Compd.* 725 (2017) 1175–1181.

### **List of Conferences (National/International)**

1. **Santhoshkumar Mahadevan**, Vasant Sathe, V Raghavendra Reddy, Sukhleen Bindra Narang, Puneet Sharma, “Role of anisotropy variation on magnetic and microwave performance of La-Co substituted barium hexaferrite”, 12th International Conference on Ferrites (ICF-12, 2019), October 29- November 01, 2019, Boston ,MA, USA. (*Oral presentation*)
2. **Santhoshkumar Mahadevan**, Puneet Sharma “High coercive Al-substituted M-type hexaferrite thick films for microwave device application.” International Conference on Magnetism and Magnetic Materials (ICMAGMA- 2018) December 09-13, 2018, NISER, Bhubaneswar (*Poster presentation*)
3. **Santhoshkumar Mahadevan**, Puneet Sharma “Effect of structural and magnetic properties of  $\text{BaFe}_{12-x}\text{Al}_x\text{O}_{19}$  hexaferrite thick films processed via two different methodology”. Young Materials Researchers’ Meet 2017 (YMRM-2017) December 10-11, 2017, BARC, Mumbai (*Poster presentation – Best poster award*)
4. **Santhoshkumar Mahadevan**, Chhavi Pahwa, Anoop Pratap Singh and Puneet Sharma “Structural and magnetic properties of  $\text{BaFe}_{12-x}\text{Al}_x\text{O}_{19}$  hexaferrite thick films” National symposium on materials for advanced technology (MAT-2017), February 20-21, 2017, DIT university, Dehradun (*Poster presentation – Best poster award*)
5. **Santhoshkumar Mahadevan**, Puneet Sharma, “Structural, magnetic and vibrational properties of  $\text{BaFe}_{11.5}\text{Ti}_{0.5}\text{O}_{19}$  prepared by three step calcination method” International Conference on Magnetism and Magnetic Materials (ICMAGMA- 2017) February 01-03, 2017, DMRL, Hyderabad (*Oral presentation*)

## List of Figures

|                   |  |    |
|-------------------|--|----|
| <b>Fig. 1.1.</b>  | Ternary compositional diagram of hexagonal ferrite.  | 4  |
| <b>Fig. 1.2.</b>  | (a) Perspective view of M-type Barium ferrite and (b) An illustration of magnetic super exchange interaction between various sites in M-type.    | 5  |
| <b>Fig. 3.1.</b>  | General methodology of solid state ceramic method.   | 22 |
| <b>Fig. 3.2.</b>  | Flowchart & pictorial representation for the preparation of BaM thick film   | 23 |
| <b>Fig. 4.1.</b>  | XRD pattern for BaM powder   | 27 |
| <b>Fig. 4.2.</b>  | (a & b) SEM microstructure and particle size distribution of BaM powder.   | 28 |
| <b>Fig. 4.3.</b>  | M-H plot of BaM powder.  | 28 |
| <b>Fig. 4.4.</b>  | SEM micrograph of sintered BaM thick film (a) 1150 °C (b) 1250 °C (c) 1350 °C and (d) cross sectional.   | 29 |
| <b>Fig. 4.5.</b>  | Representative M-H plots for BaM thick film sintered at (a) 1150°C, (b) 1250 °C and (c) 1350 °C  | 30 |
| <b>Fig. 4.6.</b>  | Variation in (a) $4\pi M$ , (b) SQ and (c) $H_c$ with sintering temperature.   | 31 |
| <b>Fig. 4.7.</b>  | (a) Surface morphology and (b) Grain size distribution.  | 32 |
| <b>Fig. 4.8.</b>  | M-H plot of thick film with BaM buffer layer.  | 32 |
| <b>Fig. 4.9.</b>  | X-ray diffraction pattern of Al- substituted BaM.  | 33 |
| <b>Fig. 4.10.</b> | Refined XRD pattern of BaM and BaAl <sub>2</sub> M. Inset depicts peak shift towards higher $2\theta$ .  | 34 |
| <b>Fig. 4.11.</b> | Variation in lattice parameters and crystallite size with Al-substitution.   | 35 |
| <b>Fig. 4.12.</b> | FTIR spectrum of BaFe <sub>12-x</sub> Al <sub>x</sub> O <sub>19</sub> .  | 36 |
| <b>Fig. 4.13.</b> | SEM micrograph and respective EDS images of BaFe <sub>12-x</sub> Al <sub>x</sub> O <sub>19</sub> (a) $x = 0.0$ and (b) $x = 2.0$ .               | 37 |
| <b>Fig. 4.14.</b> | M-H loop of BaFe <sub>12-x</sub> Al <sub>x</sub> O <sub>19</sub> powders.  | 39 |
| <b>Fig. 4.15.</b> | Representative linear fit for law of saturation.   | 39 |
| <b>Fig. 4.16.</b> | (a) M-T plot and (b) $dM/dT$ vs T for BaFe <sub>12-x</sub> Al <sub>x</sub> O <sub>19</sub> . Inset (b) shows M-H behaviour at Curie temperature. | 40 |
| <b>Fig. 4.17.</b> | SEM micrographs of substituted BaM thick films (a) cross section (b) BaM and (c) BaAl <sub>2</sub> M.  | 41 |

|                   |   |    |
|-------------------|---|----|
| <b>Fig. 4.18.</b> | Grain size distribution of (a) BaM and (b) BaAl <sub>2</sub> M.   | 42 |
| <b>Fig. 4.19.</b> | M-H loops of BaFe <sub>12-x</sub> Al <sub>x</sub> O <sub>19</sub> thick films   | 43 |
| <b>Fig. 4.20.</b> | Frequency dependent (a) real and (b) imaginary permeability of BaFe <sub>12-x</sub> Al <sub>x</sub> O <sub>19</sub> in X-band.  | 44 |
| <b>Fig. 4.21.</b> | Frequency dependent reflection loss of BaFe <sub>12-x</sub> Al <sub>x</sub> O <sub>19</sub> in X-band   | 45 |
| <b>Fig. 4.22.</b> | Representative XRD plot for BaM and BaTiM. The enlarged plot depicts peak shift in Ti-substituted powder  | 46 |
| <b>Fig. 4.23.</b> | FTIR spectrum of BaM and BaTiM powders.   | 47 |
| <b>Fig. 4.24.</b> | Micro-Raman spectrum of BaM 3 and BaTiM 3 powders.  | 48 |
| <b>Fig. 4.25.</b> | M-H plots of BaM and BaTiM powders.   | 49 |
| <b>Fig. 4.26.</b> | SEM micrograph of (a) BaM, (b) BaTiM and (c & d) respective EDS spectrum  | 50 |
| <b>Fig. 4.27.</b> | Grain size distribution of (a) BaM and (b) BaTiM.   | 50 |
| <b>Fig. 4.28.</b> | M-H plots of (a) pure and (b) Ti-substituted BaM films.   | 51 |
| <b>Fig. 4.29.</b> | Real and imaginary part of (a & b) complex permittivity and (c & d) complex permeability for substituted BaM in K <sub>u</sub> - band.  | 52 |
| <b>Fig. 4.30.</b> | Microwave absorbance vs frequency plot of BaM and BaTiM.  | 53 |
| <b>Fig. 4.31.</b> | XRD plot for pure and substituted barium hexaferrite.   | 54 |
| <b>Fig. 4.32.</b> | Variation in lattice parameter for substituted BaM.   | 55 |
| <b>Fig. 4.33.</b> | FTIR spectrum of substituted BaM.   | 56 |
| <b>Fig. 4.34.</b> | Raman spectra for substituted BaM   | 58 |
| <b>Fig. 4.35.</b> | Representative deconvoluted Raman spectra for substituted barium hexaferrite.   | 58 |
| <b>Fig. 4.36.</b> | Representative deconvoluted Mössbauer spectra of pure and substituted BaM.  | 60 |
| <b>Fig. 4.37.</b> | Variation in (a) site occupation number (N <sub>Fe</sub> ) and (b) vacancy fraction of Fe ions at different sites.  | 61 |
| <b>Fig. 4.38.</b> | SEM micrograph of (a) BaM and (b) BaLa <sub>0.15</sub> Co <sub>0.15</sub> M   | 62 |
| <b>Fig. 4.39.</b> | (a) M-H plot and (b) $\delta M/\delta T$ Vs temperature plot for substituted barium hexaferrite. Inset (a) shows M-H plot for BaLa <sub>0.15</sub> Co <sub>0.15</sub> M at T <sub>c</sub> = 437 °C. | 64 |
| <b>Fig. 4.40.</b> | M-H plots of pure and La-Co substituted BaM films.  | 64 |
| <b>Fig. 4.41.</b> | Microwave absorbance vs frequency plots of substituted BaM.   | 65 |

|                   |   |    |
|-------------------|---|----|
| <b>Fig. 5.1.</b>  | X-ray diffraction patterns for BaM powder milled for different time.  | 68 |
| <b>Fig. 5.2.</b>  | Variation in FWHM and crystallite size with milling time.   | 68 |
| <b>Fig. 5.3.</b>  | SEM micrograph of (a) 0h (b) 12h, (c) 72h ball-milled powder and (d) EDS of 72h milled powder. Inset (b & c) shows the agglomerated particles.                            | 69 |
| <b>Fig. 5.4.</b>  | M-H plots for BaM powder with different milling time  | 70 |
| <b>Fig. 5.5.</b>  | X-ray diffraction pattern of screen printed BaM thick film.   | 71 |
| <b>Fig. 5.6.</b>  | M-H plots of BaM thick film fabricated from various milled powder.  | 72 |
| <b>Fig. 5.7.</b>  | (a) Angular variation in $4\pi M$ and (b) Polar SQ plot for screen printed BaM thick films fabricated with different milled powders.                                      | 73 |
| <b>Fig. 5.8.</b>  | Magnetic properties (a) $4\pi M$ , (b) SQ and (c) $H_c$ of screen printed BaM thick films with milling time.  | 73 |
| <b>Fig. 5.9.</b>  | SEM micrographs of sintered BaM thick film fabricated from (a) 0h, (b) 12h, (c) 72h milled powders and (d-f) respective grain size distribution.                          | 75 |
| <b>Fig. 5.10.</b> | Cross sectional micrographs of sintered BaM thick film fabricated from (a) 0h, (b) 12h and (c) 72h milled powders. Inset shows the typical alignment of fabricated films. | 76 |

## List of Tables

|                    |   |    |
|--------------------|---|----|
| <b>Table 1.1.</b>  | Classification and magnetic parameters of microwave ferrites  | 2  |
| <b>Table 1.2.</b>  | The typical magnetic moment of BaM Hexaferrites   | 4  |
| <b>Table 2.1.</b>  | Summarized BaM screen printed thick film and its properties   | 17 |
| <b>Table 4.1.</b>  | Wavenumber, force constant ( $K$ ) and atomic radius ( $r$ ) for octahedral and tetrahedral sites of substituted BaM. | 36 |
| <b>Table 4.2.</b>  | Magnetic properties of BaFe <sub>12-x</sub> Al <sub>x</sub> O <sub>19</sub> powders                                   | 40 |
| <b>Table 4.3.</b>  | Magnetic properties of BaFe <sub>12-x</sub> Al <sub>x</sub> O <sub>19</sub> thick films.                              | 42 |
| <b>Table 4.4.</b>  | FTIR modes of BaM and BaTiM.  | 48 |
| <b>Table 4.5.</b>  | Raman modes of BaM and BaTiM.   | 49 |
| <b>Table 4.6.</b>  | Magnetic properties of BaM and BaTiM powders.   | 49 |
| <b>Table 4.7.</b>  | Magnetic properties of BaM and BaTiM sintered thick films.  | 51 |
| <b>Table 4.8.</b>  | FTIR modes and bond length of substituted BaM.  | 56 |
| <b>Table 4.9.</b>  | Raman data for substituted BaM.   | 59 |
| <b>Table 4.10.</b> | Hyperfine parameters of substituted BaM powders.  | 62 |
| <b>Table 4.11.</b> | Magnetic parameter of substituted BaM.  | 64 |
| <b>Table 5.1.</b>  | Magnetic properties of ball-milled powders.   | 70 |
| <b>Table 6.1.</b>  | Summarized magnetic and microwave properties of substituted BaM.  | 80 |
| <b>Table 6.2.</b>  | Summarized magnetic properties of textured BaM thick film.  | 80 |

## Symbols used

|                 |                               |
|-----------------|-------------------------------|
| $M_s$           | Saturation magnetization      |
| $H_c$           | Coercivity                    |
| $M_r$           | Remanent magnetization        |
| $H_a$           | Magnetocrystalline anisotropy |
| $\Delta H$      | FMR linewidth                 |
| $T_c$           | Curie Temperature             |
| $f_r$           | FMR frequency                 |
| $\tau$          | Crystallite size              |
| $\varepsilon'$  | Real permittivity             |
| $\varepsilon''$ | Imaginary permittivity        |
| $\mu'$          | Real permeability             |
| $\mu''$         | Imaginary permeability        |
| $Z$             | Impedance                     |
| $R_L$           | Reflection loss               |
| $T$             | Tesla                         |
| $Oe$            | Oersted                       |
| $G$             | Gauss                         |
| $A(\omega)$     | Absorbance                    |

## Abbreviations used

|                      |  |
|----------------------|--|
| BaM                  | Barium Hexaferrite (BaFe <sub>12</sub> O <sub>19</sub> ) |
| FMR                  | Ferromagnetic resonance                                  |
| EM                   | Electromagnetic  |
| <i>M-H</i>           | Magnetic hysteresis loop                                 |
| <i>M-T</i>           | Magnetization vs. Temperature                            |
| <i>RT</i>            | Room temperature   |
| XRD                  | X-ray diffraction  |
| FTIR                 | Fourier transformer infrared                             |
| SEM                  | Scanning Electron Microscopy                             |
| VSM                  | Vibrating Sample Magnetometer                            |
| VNA                  | Vector Network Analyzer                                  |
| X-band               | 8.2 – 12.4 GHz   |
| K <sub>u</sub> -band | 12.4 – 18 GHz  |
| nm                   | Nanometre  |
| μm                   | Micrometre   |
| GHz                  | Gigahertz  |
| dB                   | Decibel  |

## Preface

M-type hexaferrite has been extensively used in microwave devices due to its large magnetocrystalline anisotropy, high magnetization and ferromagnetic resonance frequency over 50 GHz. Its high versatility in magnetic and dielectric properties with low losses in off-resonance frequency provides a significant important in non-reciprocal devices such as circulator, isolators, phase shifter and band filters. Substantial effort has been drawn to miniaturize these devices with self- biased ferrite materials. In the present dissertation, barium hexaferrite (BaM) powders with various substitution (Al, Ti, La, Co) were prepared. To understand the insight of the substitution, the powder were characterized by Raman spectroscopy, FTIR, and Mössbauer spectroscopy. As substituted powder were used to fabricate the screen printed thick films. The microstructural and magnetic properties of the films were measured in perpendicular and in-plane direction. Microwave properties of substituted sample were compared with pure BaM in X-band and Ku band. Apart from isotropic thick films, anisotropic microwave sintered thick films were also prepared under the presence of external magnetic field of 0.8 T. The effect of milling time on structural and magnetic properties of thick films were investigated.

The above mentioned studies are organized in the following sections:

**Chapter 1 (Introduction):** This chapter gives a brief introduction and classification of magnetic ferrites useful in various microwave applications. The important magnetic parameters of different ferrite are tabulated. The compositional diagram and crystal structure of M-type barium hexaferrite (BaM) are detailed. Further, the advantages of screen printed BaM thick films over other film deposition techniques has been briefed.

**Chapter 2 (Literature Review):** In this chapter, the important work carried out on hexaferrite in particular for M-type (BaM) ferrite are reviewed for its structural, magnetic and microwave properties. To start with, the initial research on BaM single crystals are briefed followed by a detailed description of pure and substituted polycrystalline BaM powders. Further, studies on polycrystalline thin and thick BaM films made by PLD, sputtering, LPE and screen printing are discussed. In the last, the selective work on screen printed thick films are compared and tabulated. Finally, the chapter is concluded with gaps in the study, motivation and objectives of the dissertation.

**Chapter 3 (Experimental & Characterization Techniques):** In this chapter, the adopted processing methodology for the synthesis of M-type hexagonal ferrite ( $\text{BaFe}_{12}\text{O}_{19}$ ) is explained. A brief description of thick film fabrication technique by screen printed method is depicted with pictorial representation. Various characterization techniques used to study structural, morphological, magnetic and microwave properties are briefed.

**Chapter 4 (Results and Discussions - I):** This chapter reports the structural, magnetic and microwave properties of barium hexaferrite (BaM) processed in a conventional muffle furnace. The results are divided into two major sections. In the first section, preparation of pure BaM powders are discussed. And in the second section, processing of BaM thick films and its effect of different processing parameters, i.e. sintering temperature, buffer layer and substitution (Al, Ti & La-Co).

**Chapter 5 (Results and Discussions - II):** In this chapter, screen printed anisotropic thick films are prepared from the BaM powders milled for different duration of time. The effect of ball mill time on structural and magnetic properties of powder and microwave sintered BaM thick films are discussed.

**Chapter 6 (Conclusions):** In this chapter, important outcomes from this research are summarized. The impact of various substitution (Al, Ti & La-Co) on magnetic and microwave properties of powders and thick films are concluded. The microwave sintering and novel result obtained from textured BaM thick films are showcased. All the important parameters obtained in the result and discussion are summarized in the table. Finally, the future scope of the work is presented at the end of this chapter.

|   |            |
|---|------------|
| <i>Certificate</i>                      | <i>i</i>   |
| <i>Acknowledgement</i>                  | <i>ii</i>  |
| <i>List of Publications</i>             | <i>iv</i>  |
| <i>List of Conferences and Workshop</i> | <i>v</i>   |
| <i>List of Figures</i>                  | <i>vi</i>  |
| <i>List of Tables</i>                   | <i>ix</i>  |
| <i>Symbol used</i>                      | <i>x</i>   |
| <i>Abbreviations used</i>               | <i>xi</i>  |
| <i>Preface</i>                          | <i>xii</i> |

## **Contents**

|   |    |
|---|----|
| Chapter 1 .....   | 1  |
| Introduction.....   | 1  |
| 1.1 Preamble.....   | 2  |
| 1.2 M-type Barium hexaferrite.....                        | 3  |
| 1.3 BaM thick films.....                                  | 5  |
| Chapter 2.....  | 7  |
| Literature Review.....                                    | 7  |
| 2.1 Single crystal BaM.....                               | 8  |
| 2.2 Polycrystalline BaM.....                              | 10 |
| 2.2.1 BaM thin films.....                                 | 13 |
| 2.2.2 BaM thick films.....                                | 15 |
| 2.3 Gaps in the Study.....                                | 18 |
| 2.4 Motivation and objectives.....                        | 18 |
| Chapter 3.....  | 20 |
| Experimental & Characterization Techniques.....           | 20 |
| 3.1 Sample preparation.....                               | 21 |
| 3.1.1 Powder preparation.....                             | 21 |
| 3.1.2 Preparation of thick films.....                     | 22 |
| 3.2 Characterization Techniques.....                      | 24 |
| 3.2.1 X-ray diffraction (XRD).....                        | 24 |
| 3.2.2 Fourier Transform Infrared (FTIR) Spectroscopy..... | 24 |

|                                 |  |    |
|---------------------------------|--|----|
| 3.2.3                           | Raman Spectroscopy.....  | 24 |
| 3.2.4                           | Mössbauer spectroscopy .....   | 24 |
| 3.2.5                           | Scanning Electron Microscope (SEM) .....                                   | 25 |
| 3.2.6                           | Vibrating sample magnetometer (VSM).....                                   | 25 |
| 3.2.7                           | Vector network analyzer .....  | 25 |
| Chapter 4.....                  |  | 26 |
| Results and Discussion - I..... |  | 26 |
| 4.1                             | Characterization of BaM powder .....                                       | 27 |
| 4.2                             | Screen printed BaM thick films .....                                       | 29 |
| 4.2.1                           | Effect of sintering temperature .....                                      | 29 |
| i.                              | Microstructural study.....   | 29 |
| ii.                             | Magnetic studies .....   | 30 |
| 4.2.2                           | Effect of BaM buffer layer.....  | 31 |
| 4.2.3                           | Effect of substitution.....  | 33 |
| 4.2.3.1                         | Effect of Al-substitution .....  | 33 |
| i.                              | X-ray diffraction studies .....  | 33 |
| ii.                             | Fourier Transformer Infrared (FTIR) spectroscopy .....                     | 35 |
| iii.                            | Microstructural study.....   | 36 |
| iv.                             | Magnetic studies .....   | 37 |
| v.                              | Microstructural and morphological study of Al-substituted BaM thick film.. | 41 |
| vi.                             | Magnetic studies of Al-substituted BaM thick film .....                    | 42 |
| vii.                            | High frequency complex permeability.....                                   | 43 |
| viii.                           | Microwave reflection losses .....  | 44 |
| 4.2.3.2                         | Effect of Ti- substitution.....  | 46 |
| i.                              | X-ray diffraction studies .....  | 46 |
| ii.                             | Fourier Transformer Infrared (FTIR) spectroscopy .....                     | 46 |
| iii.                            | Raman Spectroscopy .....   | 48 |
| iv.                             | Magnetic studies .....   | 49 |
| v.                              | Microstructural study.....   | 50 |
| vi.                             | Magnetic studies Ti-substituted BaM thick film .....                       | 51 |
| vii.                            | High frequency complex permittivity and permeability .....                 | 51 |
| viii.                           | Microwave absorbance .....   | 52 |
| 4.2.3.3                         | Effect of La-Co substitution.....  | 54 |
| i.                              | X-ray diffraction studies .....  | 54 |
| ii.                             | Fourier Transformer Infrared (FTIR) spectroscopy .....                     | 55 |

|  |     |
|--|-----|
| iii. Raman Spectroscopy .....                                  | 57  |
| iv. Mössbauer Studies .....                                    | 60  |
| v. Microstructural Study .....                                 | 62  |
| vi. Magnetic Studies .....                                     | 63  |
| vii. Magnetic studies of La-Co substituted BaM thick film..... | 64  |
| viii. Microwave absorbance .....                               | 65  |
| Chapter 5.....   | 66  |
| Results and Discussion - II .....                              | 66  |
| 5.1 Development of anisotropic thick films .....               | 67  |
| 5.2 Studies on high energy milled powders .....                | 67  |
| i. X-ray diffraction studies .....                             | 67  |
| ii. Microstructural Study .....                                | 68  |
| iii. Magnetic Studies .....                                    | 69  |
| 5.3 Studies on BaM thick film .....                            | 71  |
| i. X-ray diffraction studies .....                             | 71  |
| ii. Magnetic studies .....                                     | 72  |
| iii. Microstructural study.....                                | 74  |
| Chapter 6.....   | 77  |
| Conclusions.....   | 77  |
| Future Scope.....  | 81  |
| References .....   | 82  |
| Supplementary studies .....                                    | S-1 |

# *Chapter 1*

## *Introduction*

---

---

### **Overview**

This chapter gives a brief introduction and classification of magnetic ferrites useful in various microwave applications. The important magnetic parameters of different ferrite are tabulated. The compositional diagram and crystal structure of M-type barium hexaferrite (BaM) are detailed. Further, the advantages of screen printed BaM thick films over other film deposition techniques has been briefed.

---

---

## 1.1 Preamble

Magnetic ferrites possess significant importance in microwave devices due to their intriguing magnetic and microwave properties. Over the years, a wide range of ferrite materials were developed to perform multiple operations in the modern electronic devices such as low loss substrate, self-biasing magnets and high insulator etc. [1–4]. On the basis of their natural ferromagnetic resonance (FMR) frequency, permeability and permittivity, these ferrites can operate over a wide frequency range, i.e. 1 GHz to 100 GHz. The operational frequency of microwave ferrites are generally defined by its anisotropic field ( $H_a$ ) and FMR ( $f_r$ ) as per the following equation:

$$f_r \cong \gamma(H_0 + H_a - 4\pi M_s) \quad (1.1)$$

where,  $f_r$ ,  $H_0$  and  $M_s$  are the FMR, applied magnetic field and magnetisation respectively.  $\gamma$  represents the gyromagnetic ratio.

Magnetic ferrites either operates at near natural resonance frequency such as microwave absorbers or off-resonance non-reciprocal microwave devices such as isolators, phase shifter and circulators. Table 1.1 depicts the important classes of magnetic ferrites along with their magnetic characteristics.

**Table 1.1.** Classification and magnetic parameters of microwave ferrites.

| Type        | Formula  | Abbreviation | $4\pi M_s$<br>kG | $H_a$<br>kOe | $H_c$<br>kOe | $f_r^*$<br>GHz |         |
|-------------|--|--------------|------------------|--------------|--------------|----------------|---------|
| Spinel      | FeFe <sub>2</sub> O <sub>4</sub>                                 | -            | 6.0[5]           | -            | -            | 750 MHz-1GHz   |         |
|             | MgFe <sub>2</sub> O <sub>4</sub>                                 | MgFO         | 2.2              | 0.17 [6]     | 0.002        |                |         |
|             | MnFe <sub>2</sub> O <sub>4</sub>                                 | MnFO         | 4.8 [7]          | 5.4 [7]      | 0.20 [8]     |                |         |
|             | CoFe <sub>2</sub> O <sub>4</sub>                                 | CFO          | 5.2 [9]          | 6.8 [10]     | 1.25 [9]     |                |         |
|             | NiFe <sub>2</sub> O <sub>4</sub>                                 | NFO          | 3.3 [11]         | 0.43         | 0.006        |                |         |
| Garnet      | Y <sub>3</sub> Fe <sub>5</sub> O <sub>12</sub>                   | YIG          | 1.7 [12]         | 0.08 [12]    | -            |                |         |
| Hexaferrite | BaFe <sub>12</sub> O <sub>19</sub>                               | BaM          | 4.7 [13]         | 17.5 [14]    | 6.0 [15]     |                | 36      |
|             | SrFe <sub>12</sub> O <sub>19</sub>                               | SrM          | 4.5 [13]         | 19.0 [16]    | 6.6 [17]     |                | 50      |
|             | Ba <sub>2</sub> MnZnFe <sub>12</sub> O <sub>22</sub>             | MnZnY        | 2.0 [18]         | 9.5 [18]     | 0.06 [18]    |                | Upto 14 |
|             | BaCo <sub>2</sub> Fe <sub>16</sub> O <sub>27</sub>               | Co2W         | 4.8 [19]         | 21.0 [19]    | 0.08 [19]    |                | 3.0     |
|             | Ba <sub>3</sub> Co <sub>2</sub> Fe <sub>24</sub> O <sub>41</sub> | Co2Z         | 3.3 [20]         | 12.0 [20]    | 0.02 [20]    | 1.3            |         |
|             | Ba <sub>2</sub> Co <sub>2</sub> Fe <sub>28</sub> O <sub>46</sub> | Co2X         | 3.4 [21]         | 9.5 [22]     | 0.05 [22]    | 3.0            |         |
|             | Ba <sub>4</sub> Zn <sub>2</sub> Fe <sub>36</sub> O <sub>60</sub> | Zn2U         | 4.2 [23]         | 10.0 [23]    | 2.6 [24]     | 30             |         |

Spinel ferrites and garnets are soft magnetic in nature and have cubic structure, whereas hexaferrites possess complex hexagonal structure. The planar and perpendicular magnetic

anisotropy make hexaferrites magnetically soft (Y and Z- type) and hard (M and W-type), respectively.

As suggested from table 1.1, the low  $H_a$  of cubic ferrites restricts their operational frequency below 5 GHz [25], whereas, high  $H_a$  and non-reciprocal behaviour in some hexaferrites (M and W-type) allow these materials operable up to 50 GHz [19]. Among the hexagonal ferrites; M-type is a most commercially used hexaferrite due to its ease and cost of processing [13,26]. These have dominant position in permanent magnets market due to their moderate remanent magnetization ( $M_r$ ), large coercivity ( $H_c$ ), high  $H_a$  and Curie temperature ( $T_c$ ) [27]. Apart from permanent magnet, BaFe<sub>12</sub>O<sub>19</sub> (BaM) hexaferrite is extensively used in microwave devices due to its low microwave losses, zero-field *FMR* frequency near 50 GHz [4] and self-biasing nature [28]. The non-reciprocal self-biasing properties of BaM make it suitable for miniaturization of circulators, isolators and phase shifters. It is also used as microwave absorbing materials due to its high dielectric and magnetic losses at resonance condition [29]. Other than preceded applications; BaM found multitude of interest in magnetic sensors, magnetoelectric, data storage and recording devices [13,30,31]. Therefore, in this dissertation, BaM hexaferrites has been chosen for the investigation. The composition and crystal structure of BaM are explained below.

## 1.2 M-type Barium hexaferrite

BaM hexaferrite with the formula of BaO.6Fe<sub>2</sub>O<sub>3</sub>, is isostructural with magnetoplumbite and have the simplest chemical structure among various hexaferrites [13]. Fig 1.1 shows the ternary compositional diagram of various hexaferrites. It is found that BaM shows ease of phase formation in a wide molar ratio (5.5-6.0) of Fe<sub>2</sub>O<sub>3</sub> without any secondary phase formation.

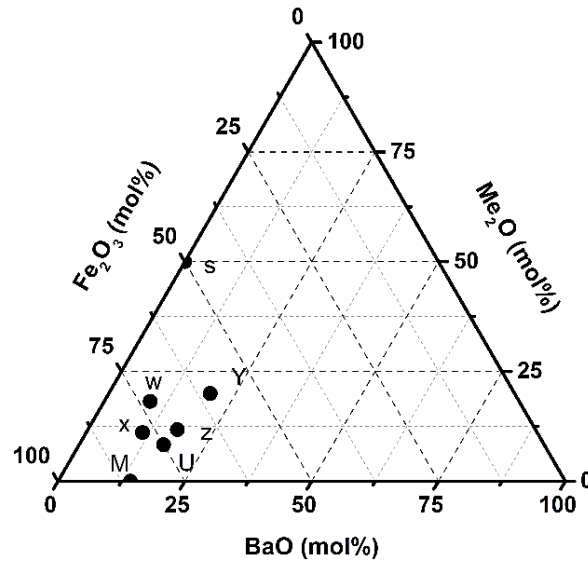


**Fig. 1.1.** Ternary compositional diagram of hexagonal ferrite[32].

A typical unit cell of BaM consists of two formula units with 64 di/trivalent ions stacked in building blocks of S and R. The S block is simply a spinel block with two formula unit iron oxide ( $2(\text{Fe}_3\text{O}_4)$ ). The R block with the basic formula of  $\text{AFe}_6\text{O}_{11}$  (A: Pb, Ba, Sr or rare-earth ions) consisted of three hexagonally packed oxygen layers where one oxygen ion in the middle layer was replaced with similar sized  $\text{Ba}^{2+}$  metal ions. The presence of divalent metal ions at dodeca coordination produce a slight perturbation in this layer and form a unique fivefold trigonal bipyramidal site with five oxygen atoms.

Among various ions,  $24\text{Fe}^{3+}$  ions remain in five crystallographic coordinates, namely three octahedral ( $12k$ ,  $2a$  and  $4f_2$ ), one tetrahedral ( $4f_1$ ) and one trigonal bipyramidal ( $2b$ ) sites.  $12k$ ,  $2a$  and  $2b$  sites are spin up, whereas  $4f_1$  and  $4f_2$  sites are spin down; this compiles eight unparallel spins with an effective magnetic moment of  $40 \mu_B$  per unit cell (detailed in Table 1.2) [33]. A typical alignment and superexchange interaction between various crystallographic sites are shown in fig. 1.2.

**Table 1.2.** Spin alignment of different crystallographic sites of BaM.

| Sites  | Coordination         | Spin position  | Net Moment ( $\mu_B$ ) |
|--------|----------------------|----------------|------------------------|
| $12k$  | Octahedral           | $12 \uparrow$  | 40                     |
| $4f_1$ | Octahedral           | $4 \downarrow$ |                        |
| $4f_2$ | Tetragonal           | $4 \downarrow$ |                        |
| $2a$   | Octahedral           | $2 \uparrow$   |                        |
| $2b$   | Trigonal bipyramidal | $2 \uparrow$   |                        |

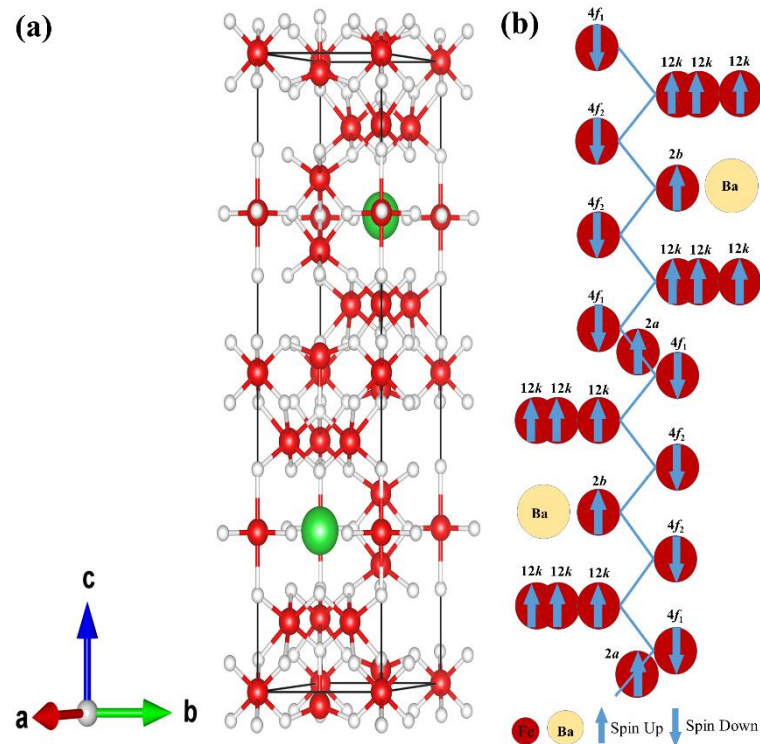


**Fig. 1.2.** (a) Perspective view of M-type Barium ferrite and (b) An illustration of magnetic superexchange interaction between various site in M-type.

A small variation in the form of substitution in any of the site will drastically affect the net magnetic moment and its characteristic properties. It is demonstrated with various cationic substitution and its preferential site occupation in BaM make this material operational up to 100 GHz [34–38].

### 1.3 BaM thick films

The magnetic properties of BaM hexaferrite are largely investigated for its application as bulk permanent magnets. Also, numerous attempts have been made to investigate the magnetic properties of BaM thin films; however, they have not gained commercial importance. The most commonly used methods for film depositions are sputtering [39], pulsed laser deposition [40], liquid phase epitaxy [41], thermal evaporation [42], and spin coating [43]. For non-reciprocal microwave devices operable up to 100 GHz, the thick BaM films  $>50 \mu\text{m}$  are prerequisite [44]. The as-mentioned deposition techniques are not suitable to obtain such thickness as they require a large number of iteration. Also, small deposition area along with high DC and RF losses in high frequency region are another disadvantages. To overcome said limitations, screen printing [45] is an alternative and effective method to deposit thick films with large surface area and low processing cost [46].

In recent years, considerable attention has been laid to develop BaM screen printed thick films for self-bias microwave devices operable in the mm-wave frequency range [4,47,48]. These self-biased thick films are capable to produce miniaturized structures with better properties over to conventional dielectric materials where external bias field ( $H$ ) is required to tune operational frequency [3,49]. Considering the importance of BaM and its thick films, the present work focus on the development of substituted BaM and realization it into the thick films.

## *Chapter 2*

### *Literature Review*

---

---

#### **Overview**

In this chapter, the important work carried out on hexaferrite in particular for M-type (BaM) ferrite are reviewed for its structural, magnetic and microwave properties. To start with, the initial research on BaM single crystals are briefed followed by a detailed description of pure and substituted polycrystalline BaM powders. Further, studies on polycrystalline thin and thick BaM films made by PLD, sputtering, LPE and screen printing are discussed. In the last, the selective work on screen printed thick films are compared and tabulated. Finally, the chapter is concluded with gaps in the study, motivation and objectives of the dissertation.

---

---

After the discovery of M-type ferrites in 1949 by Philips Laboratories and its magnetic studies by *Went et al.* [50] made this material commercially important for permanent magnet and high density recording media. Further, its high anisotropy ( $H_a$ ), ferromagnetic resonance (*FMR*) and self-biasing nature makes significantly important for non-reciprocal microwave devices such as circulator, isolator and phase shifter etc. Statistically, BaM alone accounting 50% of the total magnetic materials manufactured globally, at over 300 kilo tons per year [13,51].

To understand the structural processing property relationship of hexaferrite, various synthesis techniques have been adopted over the year. These materials were largely synthesized as single crystal and polycrystalline. For the single crystal, molten salt method was used to produce good quality crystals [52]. Initially, BaM single crystal was widely used for microwave device due to its low loss at high frequencies; however, its cost of production was a major drawback which leads to utilize polycrystalline materials in the form of bulk, thick and thin films. To understand the structural dependent properties various synthesis techniques such as co-precipitation [53], salt- melt [54,55], ion exchange [56,57], sol-gel [58,59], citrate synthesis [60,61], hydrothermal synthesis [62,63], glass crystallization [64], combustion method [65], self-propagation high temperature synthesis [66], spray drying [67], water in oil microemulsion [68] and standard solid state ceramic technique [69] were used. Among various techniques solid state ceramic method is commercially adopted technique.

On the other hand, physical vapour deposition (Sputtering, PLD, Molecular beam epitaxy, etc.), chemical vapour deposition (thermal evaporation, liquid phase's epitaxy and electron beam evaporation) and chemical solution methods (Spin coating, dip coating, tape casting/ screen printing) were commonly used film (thin and thick) deposition method [42,70–75]. These ferrites were usually used in the form of thick films (>50 microns) for various non-reciprocal self-biased devices.

In the following section, important work carried out for BaM single crystal, polycrystalline powder, thin and thick films are reviewed with a focus on magnetic and microwave properties.

## 2.1 Single crystal BaM

Single crystal M-type hexaferrite is the primary choice for permanent magnets and microwave material due to its low microwave loss and high power handling capacity [26,76]. Initial effort to grow single crystal hexaferrite was made by *Wijin et al.*[77].

However, the first single crystal was successfully synthesized and reported by *Stuiji et al.* in 1959 [78]. Its magnetic and microwave properties such as *FMR* ( $f_r$ ) frequency and loss were investigated by *Wang et al.* [52] and shift in a resonance frequency above 50 GHz with a small external biasing field was reported.

*Lemke M et al.* [79,80] proposed high  $H_a$  single crystal BaM for tunable mm-wave bandpass filter and Gunn-Oscillator. The single crystal grown by top seeding method yield high  $H_a$  (16.3) kG and relative permittivity ( $\epsilon_r$ ) of 12.5 in a perpendicular direction at 78 GHz. Further, *Labeyrie M et al.* [81] showed microwave loss varies with different shape and size of the single crystal and shift in the resonance frequency with applied field was observed. *Nicholson D et al.* [82] developed two sphere resonator bandpass filter with single crystal hexagonal ferrite and demonstrated better performance in U-band with low insertion losses and maximum tuning current of 350 mA at 60 GHz. With this advancement, a tunable ferrite filter has been developed by *Silber LM et al.* [83], and reported single crystal BaM of 0.33 mm diameter ferrite shows low microwave loss (3.0 dB) and narrow  $\Delta H$  at 58 GHz. Similarly, *Lau YS et al.* [84] proposed Gunn mm-wave oscillator with polished BaM single crystal and reported low microwave loss of 2dB bandwidth up to 55 GHz. *Labeyrie et al.* [85] demonstrated that 0.64 mm diameter single crystal SrM showed extremely low  $\Delta H$  at 94 GHz. Further, *Truedson J R et al.* [86] investigated conductivity losses in BaM at 10 GHz and suggested material with thickness  $> 0.3$ mm will be affected by eddy current losses. *Wittenauer MA et al.* [87] fabricated high purity BaM single crystal and room temperature  $\Delta H_{eff}$  shows a linear increase with frequency due to the Landau-Lifshitz damping mechanism at a 0.04 mm thick sample.

Apart from pure single crystals, some substituted hexaferrites were also widely investigated for its magnetic and microwave properties. *Wilber WD et al.* [88] first reported Mn-In co-substituted single crystal BaM shows low  $H_a$  and marginally high  $\Delta H_{eff}$  at 36 GHz. *Menashi WP et al.* [89] demonstrated the production of single crystal Zn-Ti-Mn substituted BaM with Czochralski growth method for possible usage in 20-50 GHz frequency. Later, *Sole et al.* [90] reported similar result with Sn-Co substituted BaM and suggested that magnetization and anisotropy field depended on substitution. *Dixon et al.* [91] reported that 15-20mm diameter single crystal  $BaFe_9Zn_{1.5}Ti_{1.5}O_{19}$  produced by modified pulling technique showed relatively low  $\Delta H$  of 36 Oe compared to 42 Oe obtained for a free nucleated crystal. *Ustinov A B. et al.* [92] investigated magnetic and microwave properties of Al-substituted 100  $\mu$ m thick BaM single crystal. A single crystal  $BaFe_{10}Al_2O_{19}$  showed high  $H_a$  of the order of 33.68 kOe.

As described above, most of this single crystal were optimized for  $H_a$  and  $f_r \Delta H$ . However, for the devices fabrication, the material also needs to be self-biased with high magnetic retentivity ( $M_r$ ) and coercivity ( $H_{ci}$  or  $H_c$ ) which are the signature properties of polycrystalline materials [47]. Moreover, synthesis of single crystal was challenging with low production yield compare to polycrystalline hexaferrite. The following session elaborate important work carried out on polycrystalline hexaferrite.

## 2.2 Polycrystalline BaM

Polycrystalline hexaferrite has been considered as a crucial material for microwave device fabrication ever since *Chait et al.* in early 1953 [93] proposed low loss in the microwave region. Numerous patent has been published in the late 1950s, which potentially implemented ferrites in the microwave devices [94–96].  $f_r$  in BaM (ferroxdure commercial name) was first investigated by *Weiss MT et al.* [97] in 1955 and reported that the textured materials with high  $H_a$  possess zero-field resonance at 50 GHz. Further, to understand the relation between anisotropy and crystal structure *Rensen J G et al.*[98] investigated Mössbauer spectroscopy and reported  $2b$  trigonal bi-pyramidal site with complex fivefold coordination showed high distortion and found contributed for higher anisotropy in BaM. Structure and magnetic properties of pure BaM hexaferrite were lately studied by various researchers [99–103].

*Mondin L Ya* [104] studied the degree of ferritization of BaM powder and showed isotropic magnetic behaviour in randomly oriented BaM particle. Anisotropy nature and preferential orientation of BaM was achieved by a strong external field. The effect of rapid cooling on BaM polycrystalline powder showed significant improvement in the magnetic properties. Formation of BaM from barium carbonate and iron oxide precursors were investigated and showed highest initial magnetisation of 66.5 emu/g at 1000 °C whereas, powders reheated at 1250°C showed  $M_s$  of 67.3 emu/g [105].

*Hodge MH et al.* [106] proposed a synthesis methodology for textured polycrystalline BaM and showed 90% similar magnetic properties of single crystal. The magnetic retentivity ( $B_r$ ) and energy product ( $BH_{max}$ ) are 2.6 kG and 1.07 MGOe for textured BaM whereas, isotropic materials showed 1.8 kG and 0.61 MGOe respectively.

Degree of orientation and magnetic properties of textured BaM was investigated by *Gershov I Y* [107] and showed grain growth in sintered samples were right angle to the preferential orientation of hexagonal axes and improved with sintering above 1220 °C. On

the basis of study, BaM with  $H_c > 2.9$  kOe are single-domain grains, whereas,  $< 2$  kOe are predominantly a multi-domain characteristic.

Apart from permanent magnets, textured BaM was also used in microwave devices. *Akaiwa Y et al.* [108] proposed a concept of self-biasing mm-wave device from textured BaM and SrM. The study showed  $B_r$  and  $H_c$  of  $\sim 3.5$  kG and  $\sim 2.0$  kOe with  $\Delta H$  of  $\sim 2.0$  kOe.  $\epsilon_r$  and losses found to be 13 and 0.003, respectively. Further, it reported that no external bias was required for device fabrication. The isolation loss of 20 dB was found at 2.4 GHz with an insertional loss of 1.1 dB

Role of pure BaM in microwave devices was studied and reviewed by various researchers [109,110]. However, significant efforts were also made to tailor the magnetic and microwave properties by partial cationic substitution for Fe and Ba ions to operate this material in a wide frequency range. For instance,  $\text{Sc}^{3+}$  and  $\text{In}^{3+}$  ion substitution for  $\text{Fe}^{3+}$  reportedly reduces the  $H_a$  and allow these materials to operate in X- to K<sub>a</sub>-band, whereas, the substitution of  $\text{Al}^{3+}$  and  $\text{Ga}^{3+}$  increases  $H_a$  and make suitable to operate up to W-band [34–36,111]. A short description of various substitution carried out in the past few years is as follows:

Al- substituted ( $\text{BaFe}_{12-x}\text{Al}_x\text{O}_{19}$ ) were widely investigated by many researchers over a large substitution amount. The presence of  $\text{Al}^{3+}$  in BaM sublattices reduces  $M_s$  and  $M_r$ , whereas,  $H_c$  improves drastically [112],[113]. Site preferential occupation of Al- substituted BaM was investigated by *Choi D H et al.* [114] and showed  $\text{Al}^{3+}$  ions preferentially occupy octahedral ( $2a$  &  $12k$ ) spin up and tetrahedral ( $4f_2$ ) spin down sites. Further, the distribution of ions among five crystal sublattice controls the variation of magnetic properties. Microwave absorption properties of Al-substituted BaM was investigated by *Qiu J et al.* [115,116].  $\text{Al}^{3+}$  ion substitution gradually increases  $\epsilon_r$  and shift  $\mu_r$  to a higher frequency. Microwave properties of Al-substituted BaM in the frequency range of 32-50 GHz was studied and explained on the basis of various polarisation such as dipole, resonant and electronic etc. [117]. Further, this substituent also showed multiple electrical phase transition similar to those of ferroelectric BNT ( $\text{Bi}_{0.5}\text{Na}_{0.5}\text{TiO}_3$ ) [118].

Bi-substituted BaM hexaferrite and its cationic distribution was investigated by *Winotai P et al.* [119] showed a reduction in  $M$  due to presence of  $\text{Bi}^{3+}$  ions in the pseudo-tetrahedral site and then octahedral site in R block.

*Malassis et al.* [120] investigated the effect of  $\text{Co}^{2+}$  ion in BaM crystal structure and reported the formation secondary W-type phase. A few more studies on Co-substituted BaM showed high reflection losses of -45 dB in K<sub>u</sub>- band [121,122]. Apart from single

substitution **Kreisel J et al.** [123] investigated Ir-Co co-substitution on magnetic anisotropy by neutron diffraction and showed spin canting from 0 to 90° through magnetic structure. Further, Co substitution in Ni-Zr- substituted BaM was investigated by **Gruskova A et al.** [124] and showed Zr<sup>4+</sup> ions preferential occupied 2*b*, 2*a* and 4*f<sub>l</sub>* sites and restricts Co<sup>2+</sup> ions in 4*f<sub>2</sub>* and 12*k* sites. Further such substitution was showed a positive temperature coefficient of  $H_c$  [125]. Co-Si co-substitution in BaM with polymer matrix composite showed the best reflection losses of -29 dB in X-band with  $\epsilon'$  and  $\epsilon''$  of ~11.5 and 2.3, respectively for a sample thickness of 2 mm [126]. Later, an investigation in Co = 0.9 and Si = 0.95 showed increase in electromagnetic properties with a reflection loss of -24.5dB (>99% absorption ) for absorber thickness of 1.6 mm [127]. Co-Ti substitution in BaM showed an increase in  $M$  initially up to Co=Ti=0.5 due to the presence of low sip Co<sup>2+</sup>ion (3  $\mu_B$ ) in spin down. The presence of Co-Ti hampers the  $T_c$  to 491 K for  $x = 2.5$ [128]. The existence of planer anisotropic in this material provide significant importance in microwave devices and perpendicular recording media [129,130].

**Thompson G K et al.**[131] investigated order and disordered magnetic exchange interaction in In and Ga substituted SrM and found a change in  $H_{eff}$  at 12*k* sites. Substitution of Mn-ions in BaM crystal system preferred to occupy 12*k*, 4*f<sub>2</sub>* and 2*a* sites and showed decreases in magnetic properties [132]. Later, such substitution is widely used for catalytic properties for methane combustion [133].

The first Ti-substituted BaM was investigated by **Brabers et al.**[134] and reported an increase of  $H_a$  for low substitution amount; however, magnetic properties were found to decrease with higher concentration. Further, Ti<sup>4+</sup> ion substitution showed significant changes in textured growth along (00*l*) direction as estimated from torque curve [135,136]. Recent studies on ac conductivity showed a decrease in activation energy with Ti concentration and exhibited moderate magnetic properties. Such materials are of greater interest in magnetoelectric devices [137]. Substitution of Ru-Ti in BaM system showed preferential occupation at 2*b* sites and caused a decrease in  $H_c$ . [68]. Zn-Ti co-substituted BaM has been adopted for low temperature co-fired ceramics (LTCC) for modern communication devices [138].

Apart from substitution for Fe<sup>3+</sup> ion, substitution of Ba<sup>2+</sup> ions with rare earth substituents such as La, Gd, Pr, Sm and Nd were investigated by various researchers in the past [139–143]. La-substituted BaM has been widely studied for its optical and microwave properties [140,144]. The existence of La<sup>3+</sup> ion increases  $M_s$  and  $H_c$  and reduces for higher concentration. **Lotgering et al.** [145] and **kupferling et al.** [146] found high  $H_a$  with La<sup>3+</sup>

ion concentration. Simultaneously substituted La-Co hexaferrite were widely investigated due to its enhanced magnetic properties and well exploited for the production of commercial permanent magnets [147]. The effect of La/Co substitution on its crystallographic properties and exchange interaction are well explained by various theoretical studies. The superexchange interaction in La-substituted BaM was explained by molecular field approximation (MFA) and random phase approximation (RPA). Studies suggested that antiferromagnetic superexchange interactions between various Fe-Fe ion were more prominent between  $2a-4f_1$ ,  $2a-12k$ ,  $2b-4f_1$  and  $2b-12k$  [148,149]. **J. Park et al.** derived the electronic structure of La-Co substituted SrM by first principle calculation and predicted a reduction in lattice constant and net magnetic moment. The study also suggested its half-metallic behaviour with cobalt substitution [150]. Beside theoretical studies, the effect of site occupation on intrinsic properties and crystal collinearity were also experimentally investigated [151,152]. Polycrystalline bulk BaM has significant importance in permanent magnets.

Polycrystalline thin and thick films are having a scope for miniaturization in microwave devices due to comparable magnetic and microwave properties of bulk counterpart. In the following section, important studies on BaM thin and thick films are discussed.

### 2.2.1 BaM thin films

BaM thin films have been deposited by various growth technique such as PLD, sputtering, spin coating and metalorganic chemical vapour deposition (MOCVD). Magnetic and structural properties of BaM film deposited by PLD on  $c$ - and  $m$ -plane sapphire first studied by **P.Dorsey et al.** [153] in 1992. The study reported  $\Delta H$  of 200 Oe and 450 Oe at 85 GHz for 15  $\mu\text{m}$  thick film on  $c$ -plane and  $m$ -plane respectively. The high  $H_a$  of 16 KOe was found for sample fabricated on  $c$ -plane. Later, **Huang F et al.** [154] successfully deposited well crystallize  $c$ -axis oriented BaM thin film of 230 nm on a LLC garnet ferrite (111). Further, **Y.song et al.** [40] fabricated single phase BaM thin films with the narrowest possible  $\Delta H$  of 27 Oe at 60.3 GHz and  $H_a$  of 16.4 kOe by PLD technique. **Yoon S D et al.** [155] investigate magnetic and microwave properties of  $c$ -axis oriented BaM films on  $a$ -plane sapphire. Torque measurement confirms easy magnetization direction lies in the plane of the film with  $\Delta H$  of 1-1.4 kOe. Films with 14  $\mu\text{m}$  thickness showed large stress due to crystallographic and thermal mismatches. **Chen Z et al.**[156] studied epitaxially grown BaM thin films on 6H SiC substrate with 10 nm MgO (111) under layer. The study

reported bilayer films resolves lattice mismatch and inter-diffusion between film and substrate. The films showed low  $\Delta H$  of 96 Oe at 53 GHz with high  $H_a$ , and  $M$  of 16.9 kOe, 4.4 kG respectively.

BaM films were also deposited by sputtering and investigated. **Takahashi *et al.*** [157] made a successful attempt to deposit BaM thin films of 1-2  $\mu\text{m}$  by RF sputtering and investigate its crystallization kinetics with annealing temperature. Later, **Adam J D *et al.*** [1] in 1990 proposed ferrite thin films for Micro and mm-wave application. For the study, oriented BaM thin films are deposited with RF diode sputtering on  $\text{SiO}_2/\text{Si}$  (100) and found higher crystallization in the range 700 – 800 °C. Further, **Lacroix E *et al.*** [158] studied the effect of different substrate  $\text{SiO}_2$  (amorphous), ZnO (001),  $\text{Gd}_3\text{Ga}_5\text{O}_{12}$  also called GGG (111), and  $\text{Al}_2\text{O}_3$  (012). It was found that GGG and  $\text{Al}_2\text{O}_3$  substrate were suitable for achieving single phase BaM film. In 1996 **Acharya BR *et al.*** [159] fabricated SrM thin film by RF sputtering technique. Effect of annealing, different substrates and target to substrate distance were investigated. It was found that substrate and rapid annealing promotes orientation in the films. **Capraro *et al.*** [160] developed an integrated microwave devices combining BaM films of 5  $\mu\text{m}$  by RF sputtering deposition technique. The post annealed BaM thick films showed 14 dB isolation loss at 50 GHz with insertion losses up to 9 dB. **Dehlinger A S *et al.*** [161] developed integrated circulator based on 10  $\mu\text{m}$  BaM films showed a circulation effect up to 50 GHz. **Li Y *et al.*** [162] investigated highly oriented BaM thin films on Pt coated Si substrates. The films showed good out of plane magnetic properties annealed at 600 °C.  $M_r$ , squareness and  $H_c$  found to be 3.80 kG, 0.96 and 1.76 kOe, respectively. In 2014 **Anderson *et al.*** [163] proposed a multilayer magnetic waveguide with 20  $\mu\text{m}$  BaM films. The non-reciprocal microwave propagation at 50-70 GHz range showed attenuation differences more than 75 dB/cm at 56.18 GHz. **Peng B. *et al.*** [164] investigated BaM thin films with different thickness 100nm, 1  $\mu\text{m}$  and 8  $\mu\text{m}$ , 20  $\mu\text{m}$  on sapphire substrate with amorphous BaM seeding layer. The study found up to 8  $\mu\text{m}$  thick BaM films deposited on BaM buffer layer showed random orientation with better adhesion. A good  $c$ -axis orientation was observed in 100 nm thick films. Later, **Bodeux R. *et al.*** [165] developed tetragonal tungsten bronze (TTB)/BaM bilayers by RF magnetron sputtering on  $\text{Pt}/\text{TiO}_2/\text{SiO}_2/\text{Si}$  substrates. The films showed bulk like magnetic properties with dielectric constant  $\epsilon$  of 150 at lower sub-gigahertz frequencies. **Dong X *et al.*** [166] investigated textured BaM thin film of 500 nm by magnetron sputtering on a  $\text{Pt}/\text{TiO}_2/\text{SiO}_2/\text{Si}$  substrate. Lotgering factor of 96% was observed with  $M_s$ , squareness and  $H_a$  of 3.9 kG, 0.95 and 16.37 kOe, respectively with  $\Delta H$  of 162 Oe at 55 GHz.

**Donahue E J et al.** [167] developed BaM films by metalorganic chemical vapour deposition (MOCVD) on MgO (polycrystalline) and ZnGa<sub>2</sub>O<sub>4</sub> (oriented film) substrates. The  $H_a$  of 13.4 kOe and 22.3 kOe were observed for MgO and oriented substrates, respectively. **Ryder DF et al.** [168] investigated thin film of BaM deposited by Spin coating on a resistor grade alumina showed  $M_s$ ,  $H_c$  and squareness of 375 emu/cm<sup>3</sup>, 2.2 kOe and 0.58, respectively. **Ghasemi A. et al.** [43] performed spin coating of BaM and reported isotropic crack-free films of 15  $\mu$ m with  $H_c$  of 5 kOe. Later **Salemizadeh S. et al.** [169] successfully deposited BaM thin films on Si (110) substrate via spin-coating technique. The films calcined at 700 °C showed good magnetic properties  $H_c = 5.2$  kOe,  $M_r = 141.3$  emu/cm<sup>3</sup> and  $M_s = 185.2$  emu/cm<sup>3</sup>. **Masoudpanah S. et al.** [170] SrM thin films synthesized on (100) silicon substrate by spin coating. The 900 nm thick films showed relatively high  $M_s$  of 267.5 emu/cm<sup>3</sup> and  $H_c$  of 4.29 KOe. **Harward I et al.** [171] developed Al substituted BaM thin film by metal-organic decomposition method followed by rapid thermal annealing. The squareness and  $H_a$  found to increase up to 0.92 and 27.5 kOe with Al substitution, whereas,  $M_s$  decreased to 2.2 kG.  $\Delta H$  of fabricated films 370 Oe and found increase linearly within 45 – 60 GHz frequency range.

### 2.2.2 BaM thick films

BaM thick films greater than 50  $\mu$ m gained significant importance in microwave devices due to bulk-like properties, ease of production and self-bias nature. Methods such as liquid phase epitaxy (LPE), screen printing and tape casting were predominantly used for thick film fabrication.

In 1978 **Glass HL et al.** [172] developed first hexaferrite thick films by LPE technique on a non-magnetic spinel substrate and reported low  $\Delta H$  of 26 Oe at 36 GHz. Initially, LPE was used to develop BaM films less than 50  $\mu$ m [173] [174]. Later, LPE was also used to develop thick film above 50  $\mu$ m. **Y.Kranov et al.** [41] reported growth of thick BaM films of 300-550  $\mu$ m on sapphire Al<sub>2</sub>O<sub>3</sub> (0001) substrate by LPE with  $H_c$  of 100 Oe. **Jalli J et al.** [175] developed 144  $\mu$ m BaM thick film on Gd<sub>3</sub>Ga<sub>5</sub>O<sub>19</sub> substrate by LPE technique. Textured magnetic behaviour has been observed and magnetic properties  $M$  and  $H_a$  found to be 4.2 kG and 16 kOe, respectively. The  $\Delta H$  of 100 Oe at 35 GHz was observed.

Screen printing technique has been initially introduced for microwave devices such as circulator and isolator. **Zivanov Lj D et al.** [176,177] developed the first screen printed BaM thick films for potential use in fin line isolator. **Chen Y et al.** [178] fabricated 200-500  $\mu$ m thick films on alumina substrate and showed large  $M_r$  (3.8kG) and SQ (0.96) with

narrow  $\Delta H$  of 310 Oe at 55.6 GHz. Further, studies found BaM films on silicon substrate and sintered at 1300 °C showed secondary phases [179]. Later, Al<sub>2</sub>O<sub>3</sub> seeding layer for screen printing deposition was explored and found enhanced properties in isotropic BaM films [180]. *Kulkarni D C. et al.* [181] investigated 15-60 μm thick BaM films on a polycrystalline alumina substrate. The result showed high  $\epsilon'$  (35) and  $\mu'$  (6.41) with microwave absorbance of 87% in K<sub>u</sub>-band. *S.Verma et al.* [44] investigated Co-Ti substituted screen printed thick film on Al<sub>2</sub>O<sub>3</sub> substrate showed maximum  $M$  and  $H_a$  of 57 emu/g and 10.02 kOe, respectively.

**Table 2.1.** Summarized BaM screen printed thick films and its structural, magnetic and microwave properties from literature.

| Sr. No | Year and Author                             | Synthesis procedure  | Magnetic and microwave properties   |
|--------|---|--|---|
| 1.     | 1988/<br><b>Zivanov Lj D et al.</b> [176]   | 15 $\mu\text{m}$ screen printed BaM thick film fabricated on alumina substrate sintered at 850 $^{\circ}\text{C}$ for 10 min   | Bandwidth isolation loss greater than 30 dB at 48.5 GHz   |
| 2.     | 2006 <b>Chen Y et al.</b> [178]             | 200-500 $\mu\text{m}$ oriented screen printed thick film fabricated on 0.25mm thick alumina substrate by hot pressing method and sintered at 900-1300 $^{\circ}\text{C}$                                   | Polycrystalline films showed large remanence 3.8 kG, higher squareness of 0.96, low microwave loss with $\Delta H$ of 310 Oe at 55.6 GHz.                                   |
| 3.     | 2006 <b>Chen Y et al.</b> [179]             | 100-400 $\mu\text{m}$ oriented screen printed thick film fabricated on silicon and alumina substrate by hot pressing method and sintered up to 1300 $^{\circ}\text{C}$                                     | Squareness of 0.93 and $f_r$ $\Delta H$ of 1.2 KOe at 40 GHz  |
| 4.     | 2006 <b>Chen Y et al.</b> [179]             | 100-500 $\mu\text{m}$ oriented screen printed thick film fabricated on alumina substrate by hot pressing method and sintered up to 1300 $^{\circ}\text{C}$ and compared with conventional sintering method | Squareness of $>0.95$ , coercivity $\sim 1.9\text{kOe}$ , peak to peak $f_r$ $\Delta H$ 320 Oe at U band  |
| 5.     | 2008 <b>Chen Y et al.</b> [180]             | 50-200 $\mu\text{m}$ screen printed thick film fabricated on Silicon substrate with $\text{Al}_2\text{O}_3$ buffer layer sintered at 1150 $^{\circ}\text{C}$ up to 40 mins                                 | BaM film with $\text{Al}_2\text{O}_3$ buffer layer showed no secondary phase. $M \sim 1.5$ kG and $H_c \sim 4.4$ kG.  |
| 6.     | 2010<br><b>Kulkarni DC et al.</b> [181,182] | 15-60 $\mu\text{m}$ screen printed thick film fabricated on polycrystalline $\text{Al}_2\text{O}_3$ sintered at 900 $^{\circ}\text{C}$ for 2h  | Real $\epsilon'$ up to 35, $\mu'$ maximum of 6.41 microwave absorbance of 87 % in Ku-band. Reflection loss of -37 dB at X-band  |
| 7.     | 2012 <b>Da-Ming C et al.</b> [183]          | 50-400 $\mu\text{m}$ tape cast film sintered up to 1200 $^{\circ}\text{C}$ for 4h  | Textured film with lotgering factor of 0.73 for 50 $\mu\text{m}$ with high $M_r \sim 3.3$ kG and $H_c \sim 4.0$ kG.   |
| 8.     | 2015 <b>Verma S et al.</b> [28]             | 60 $\mu\text{m}$ screen printed BaM thick film on polycrystalline $\text{Al}_2\text{O}_3$ substrate pressed at $1\text{kg}/\text{cm}^2$ and sintered at 1300 $^{\circ}\text{C}$ for 2h                     | $M$ 53.9 emu/g and $H_a \sim 10$ kOe for a 5.5-mole ratio of $\text{Fe}_2\text{O}_3$ . reflection loss -29.26 dB at 16.12 GHz for 6.0-mole ratio of $\text{Fe}_2\text{O}_3$ |
| 9.     | 2015 <b>Verma S et al.</b> [44]             | 72 $\mu\text{m}$ Co-Ti substituted BaM screen printed thick films on polycrystalline $\text{Al}_2\text{O}_3$ substrate pressed at $1\text{kg}/\text{cm}^2$ and sintered at 1250 $^{\circ}\text{C}$ for 2h  | $M \sim 57$ emu/g and $H_a$ of 10.02 kOe  |

### 2.3 Gaps in the Study

BaM has been potentially employed in microwave devices as single crystal, polycrystalline bulk and films form. For non-reciprocal microwave devices, the film thickness of 50-400  $\mu\text{m}$  is prerequisite. The development of such thick films with traditional physical and chemical vapour deposition technique is always complicated, time consuming and cannot be realized commercially. Screen printing technique overcomes the thickness limitation and provide ease of production at industrial scale. However, to obtain a required magnetic properties, thick films with fine microstructure, dense morphology with minimal porosity is essential to low FMR line width. The required microstructure features primarily depend upon powder size and sintering parameters. Effect of these process parameter on structural and magnetic properties is lagging and not been investigated so far.

Also the magnetic properties of the films depend upon the substitution for Ba and Fe sites. Till now, substituted BaM thick films were limited to Sc and In ion substituent only. Hence, it is important to investigate the effect of other substitutions. In the presents study we extended our research to  $\text{Al}^{3+}$ ,  $\text{Co}^{2+}$  and  $\text{Ti}^{4+}$  substituent for  $\text{Fe}^{3+}$  ions, and  $\text{La}^{2+}$  for  $\text{Ba}^{3+}$  ions. Further, it is reported that Al and La substitution in BaM enhances  $H_a$ , whereas  $\text{Co}^{2+}$  and  $\text{Ti}^{4+}$  reduces the  $H_c$  without affecting the intrinsic magnetisation of BaM powders. No work with these substitution has been carried out for successful deposition of thick film.

Also, the preparation of such thick films with conventional furnaces has been predominately reported. In this thesis, task has been taken to investigate the effect of microwave sintering on microstructural and magnetic properties of screen printed thick films.

### 2.4 Motivation and objectives

As stated above that screen printing technique is able to produce the film thickness over 50  $\mu\text{m}$ , which is not possible by any other physical/chemical deposition techniques. Apart from advantage of thickness, it is also important to produce these films with desired magnetic properties. The intrinsic magnetic properties, i.e.  $H_a$ ,  $M_s$ , can be suitably modified by the various cationic substitution for Ba/Fe ions. Whereas, FMR linewidth and absorption losses strongly depend upon microstructural characteristics such as grain size, shape and porosity. Hence, the development of screen printed thick films with dense microstructure, and minimal porosity are extremely challenging.

To develop high dense screen printed thick films with various cationic substitution, the following objective were carried out:

- Preparation of conventional / microwave sintered thick films by screen printing.
- To investigate the effect of various structural parameters, e.g. grain size, film thickness, porosity etc. on magnetic and microwave properties.
- To investigate the effect of various cationic substitutions (Al, Ti & Co) on the structural magnetic and microwave properties of the screen printed films.

## *Chapter 3*

# *Experimental & Characterization Techniques*

---

---

### **Overview**

In this chapter, the adopted processing methodology for the synthesis of M-type hexagonal ferrite ( $\text{BaFe}_{12}\text{O}_{19}$ ) is explained. A brief description of thick film fabrication technique by screen printed method is depicted with pictorial representation. Various characterization techniques used to study structural, morphological, magnetic and microwave properties are briefed.

---

---

### 3.1 Sample preparation

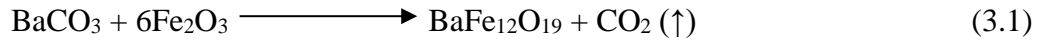
The preparation of the samples has been divided into two sub-sections. At first, substituted  $\text{BaFe}_{12}\text{O}_{19}$  (BaM) powders were prepared by solid state ceramic method. And, in second section preparation of screen printed thick films using as-prepared powder are explained.

The following series of substituted  $\text{BaFe}_{12}\text{O}_{19}$  (BaM) were prepared:

- a.  $\text{BaFe}_{12}\text{O}_{19}$
- b.  $\text{BaFe}_{12-x}\text{Al}_x\text{O}_{19}$  ( $x = 0.0 - 2.0$ )
- c.  $\text{BaFe}_{12-x}\text{Ti}_x\text{O}_{19}$  ( $x = 0.0 - 0.5$ )
- d.  $\text{Ba}_{1-y}\text{La}_y\text{Fe}_{12-x}\text{Co}_x\text{O}_{19}$  ( $x = 0.0 - 1.0$ ,  $y = 0.0 - 0.20$ )

#### 3.1.1 Powder preparation

Analytical grade barium carbonate ( $\text{BaCO}_3$ ), iron (III) oxide ( $\text{Fe}_2\text{O}_3$ ), cobalt oxide ( $\text{CoO}$ ), titanium dioxide ( $\text{TiO}_2$ ) and lanthanum oxides ( $\text{La}_2\text{O}_3$ ) were used as precursors. For the synthesis, precursors were weighed in stoichiometric composition given below:



The powders were wet mixed in zircon jar for 3h using a planetary ball mill. Rotation per minute (RPM) and ball-to-charge ratio were fixed to 200 and 5:1 respectively. As-mixed powders were dried and pelletized using 10 mm die at a pressure of 150 MPa by a hydraulic press. The pellets were calcined at 1200 °C for 3h under ambient conditions in a resistance furnace. Heating and cooling rate were fixed to 5 °C/minute. The calcined pellets were subsequently pulverized using vibratory mill model FRITSCH analysette 3 and sieved through 25  $\mu\text{m}$  mesh. For Ti- substituted BaM, calcination followed by pulverization were carried out three times to achieve single phase. The flow chart of powder preparation is shown in fig. 3.1. The powder prepared by the said method has been further used for screen printing of thick films. To understand the role of particle size distribution, as prepared powders were further milled in a high energy ball mill for different duration (2, 6, 12, 24, 48 and 72h) in a tungsten carbide jar. The ball-to-charge ratio and RPM were fixed to 20:1 and 300, respectively.

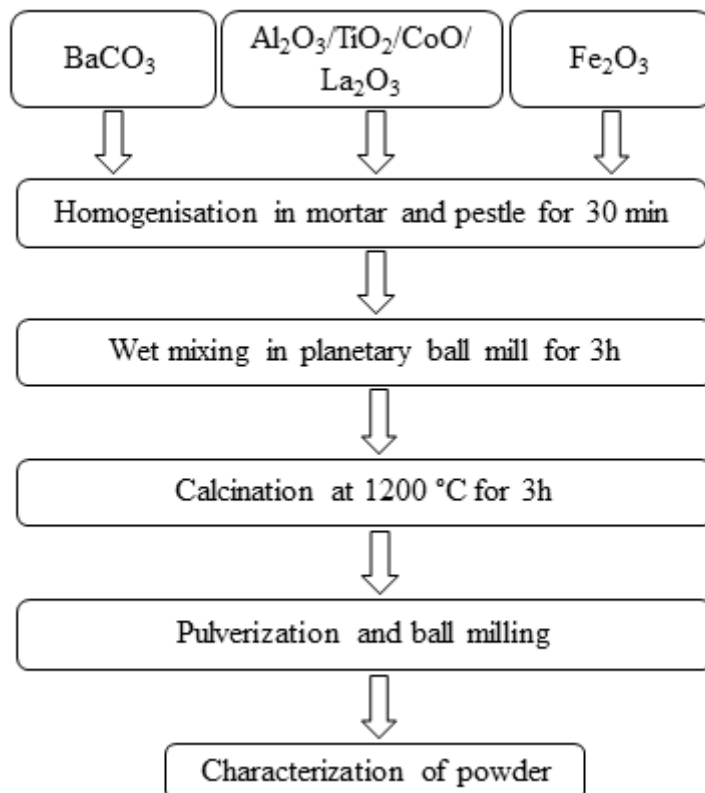


**Fig. 3.1.** General methodology of solid state ceramic method.

### 3.1.2 Preparation of thick films

For the preparation of thick films, 10% of polyvinyl butyral (PVB) has been mixed with the as-prepared BaM powders and screen printed on commercial grade alumina ( $\text{Al}_2\text{O}_3$ ) substrate of dimensions  $9 \times 9 \times 0.65 \text{ mm}^3$ . The thickness of the films was controlled using 100 and 175  $\mu\text{m}$  stencils. Three different methodologies have been adopted for better adhesion between film and substrate. In the first method; 3%  $\text{Bi}_2\text{O}_3$  (analytical grade) has been mixed in the BaM powders. In the second and third method, sputtered BaM and melt quenched  $\text{Bi}_2\text{O}_3$  buffer layer were deposited on  $\text{Al}_2\text{O}_3$  substrate respectively. The as-deposited films were dried overnight at room temperature with and without a magnetic field, followed by heating at 120  $^\circ\text{C}$  for 5 minutes to remove any residual moisture. Permanent magnets with the constant magnetic field of 8 KG were used for orientation.

After drying, the films were sintered from 1150 to 1350  $^\circ\text{C}$  for different duration (20min & 1h) using conventional and microwave furnace. The heating rate was fixed to 10  $^\circ\text{C}/\text{min}$  and 20  $^\circ\text{C}/\text{min}$  for conventional and microwave sintering, respectively. Microwave sintering of the films were carried in a custom made microwave furnace (VB ceramic, India) with 4 magnetrons operable up to 5 KW of power at 2.4 GHz RF frequency. After

sintering the thick films were cooled down naturally to room temperature. The flow chart and pictorial representation of screen printing are given in fig. 3.2.

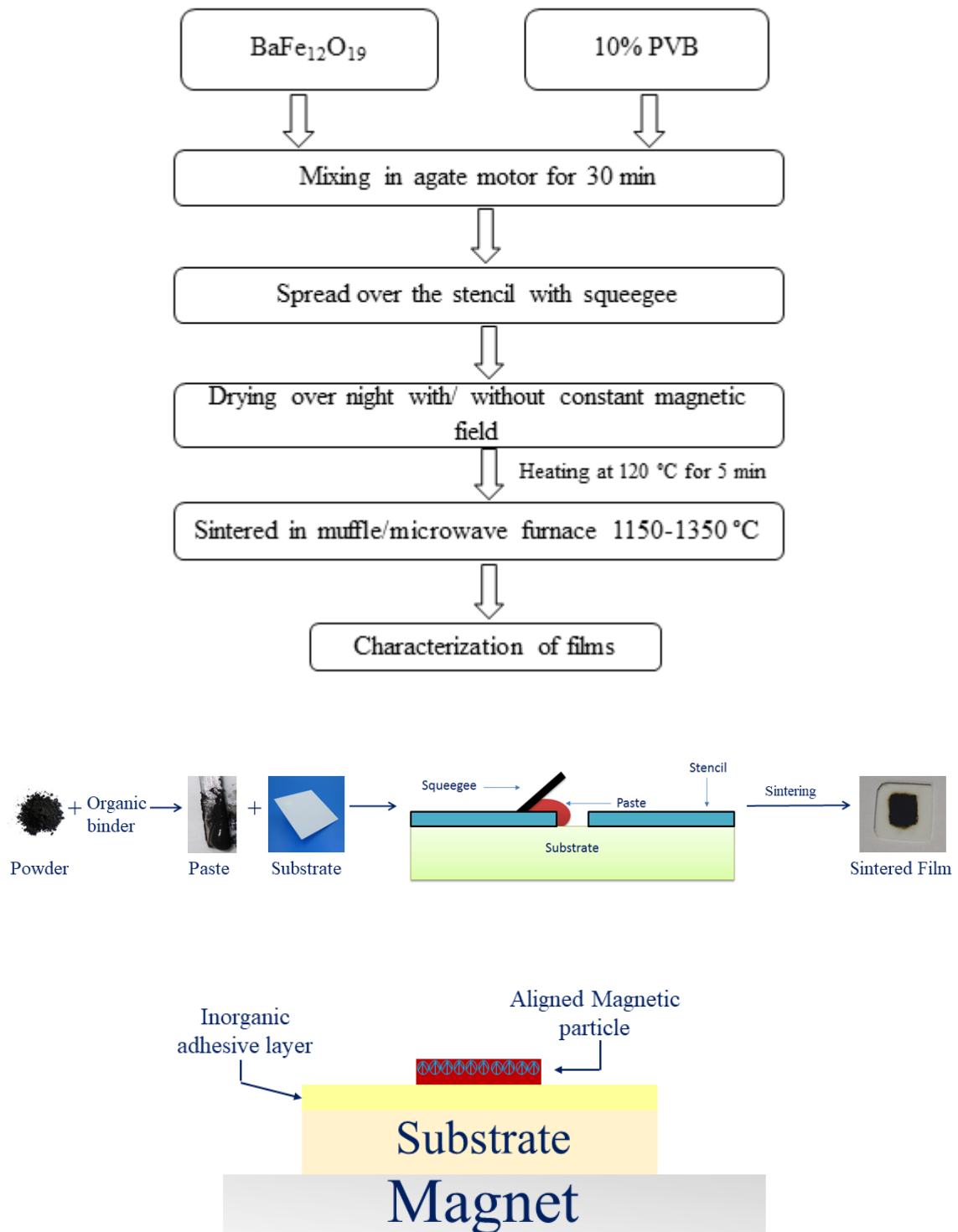


**Fig. 3.2** Flowchart & pictorial representation for the preparation of BaM thick film

## 3.2 Characterization Techniques

The structural, morphological, magnetic and microwave properties of BaM powders and thick films are carried out by following techniques.

### 3.2.1 X-ray diffraction (XRD)

Synthesized BaM powders and films were examined by X-ray diffraction (XRD) XRD-6000 SHIMADZU, Japan and X'PERT Pro-Panalytical (PANalytical), using Cu-K $\alpha$ 1 (1.54 Å) radiation. The diffraction data were recorded at room temperature within 2 $\theta$  range from 20° -70°. The scan rate was fixed to 0.02 °/second. The diffraction data were matched with BaM standard data card no. 84-0757, 78-0133, 39-1433 and 72-0738 with a space group of P6 $_3$ /mmc. The Rietveld refinement of XRD patterns were carried out using Fullprof and Match 3 software. The goodness of fit ( $\chi^2$ ) and characteristic reliability factors ( $R_p$ ,  $R_{wp}$  &  $R_{exp}$ ) were kept below 2 and 5, respectively.

### 3.2.2 Fourier Transform Infrared (FTIR) Spectroscopy

FTIR spectroscopy was carried out by Perkin Elmer spectrum 400 and IRAffinity-1S spectrometer. The powder samples have been grounded thoroughly and mixed with KBr. The ratio between kBr and powder were fixed to 25:1. All the experiment were done in an ambient atmosphere.

### 3.2.3 Raman Spectroscopy

Raman spectroscopy was carried by Renishaw RA 802 series equipped with a 514.5 nm Ar<sup>+</sup> laser at 20 mW and JOBIN YVON HORIBA HR800 spectra analyzer (instrumental resolution  $\pm 1$  cm<sup>-1</sup>) equipped with a 632.8 nm helium-neon laser at 9mW power. The spectral signature obtained from Raman spectroscopy were deconvoluted by Lorentzian fit to verify different Raman active modes [184].

### 3.2.4 Mössbauer spectroscopy

Zero field room temperature (RT) Mössbauer measurements of La-Co powders were performed using <sup>57</sup>Co (Rh)  $\gamma$ -ray source in transmission geometry by WissEl make Mössbauer spectrometer. The velocity calibration was performed with the standard natural iron absorber. For the measurement, a thin layer of finely ground powder was coated on a diamagnetic polymer film and placed near the source. The obtained spectral signature was analyzed with a non-linear least-square fitting method.

### 3.2.5 Scanning Electron Microscope (SEM)

The morphology of the prepared samples has been observed by SEM JEOL model 6510, coupled with energy dispersive X-ray Spectroscopy (EDS). All images were taken in secondary electron mode. The cross sectional SEM was carried out to measure the thickness of screen printed films. To avoid electron charging during measurement, the sample surface was coated by thin Au film.

### 3.2.6 Vibrating sample magnetometer (VSM)

The *RT* and *HT* magnetic measurements were carried out by Lake Shore model 7404 magnetometer coupled with Lake Shore 74035 single-stage variable temperature assembly. Mass and/or dimension of samples were precisely noted prior to the experiment. To determine  $T_c$ , *M-T* measurements were also carried out. For *HT* magnetic measurement, the BaM powder was kept in the alumina sample holder.

### 3.2.7 Vector network analyzer

Microwave properties in X- (8.2 - 12.4 GHz) and  $K_u$ - (12.4 - 18 GHz) band were measured using Agilent 5225A PNA series network analyzer. For the measurement, powders were compacted in a rectangular shape at a pressure of 150 MPa and sintered. The final dimensions of the samples were  $22.86 \times 10.16 \times 2.1 \text{ mm}^3$  and  $15.74 \times 7.96 \times 2.1 \text{ mm}^3$  X-band and  $K_u$  -band respectively. Prior to measurement two-port calibrations was done on the test setup to eliminate error due to source/load mismatch and isolation [171].

## *Chapter 4*

### *Results and Discussion - I*

---

---

#### **Overview**

This chapter reports the structural, magnetic and microwave properties of barium hexaferrite (BaM) processed in a conventional muffle furnace. The results are divided into two major sections. In the first section, preparation of pure BaM powders are discussed. And in the second section, processing of BaM thick films and its effect of different processing parameters, i.e. sintering temperature, buffer layer and substitution (Al, Ti & La-Co).

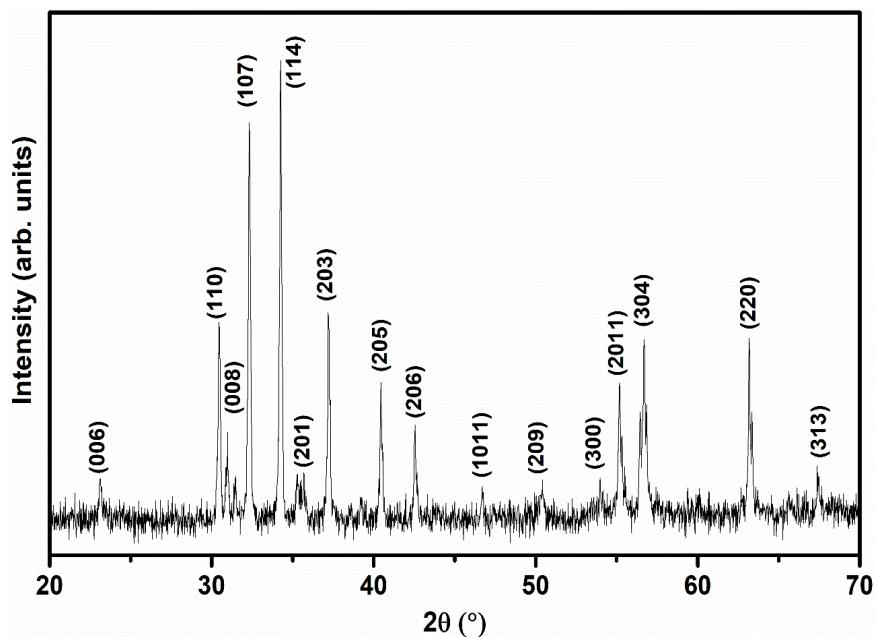
---

---

Pure and substituted BaM powders were prepared by solid state ceramic method and their thick films were screen printed on  $\text{Al}_2\text{O}_3$  substrate. A small amount of ( $\sim 3\%$ )  $\text{Bi}_2\text{O}_3$  is also added for better adhesion with the substrate. The films are conventionally sintered at different temperature for 1h. Further, an attempt has been made to develop BaM thin film under layered thick film at  $1250\text{ }^\circ\text{C}$ . Finally, the effect of various substitutions on magnetic properties of powder and isotropic films are studied. The microwave properties (X-band and  $\text{K}_u$ -band) of substituted BaM are also investigated, which may also reflect the microwave behaviour of thick films.

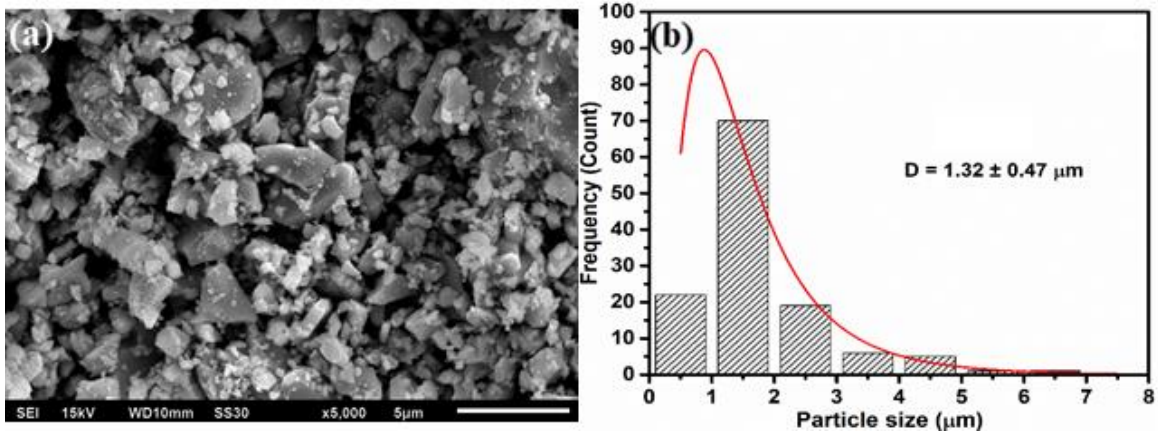
#### 4.1 Characterization of BaM powder

Fig. 4.1 shows X-ray diffraction pattern of BaM powder calcined at  $1200\text{ }^\circ\text{C}$  for 3h. After calcination, the powder is pulverized and ball milled for 2h for further fabrication of the thick films. All peaks were matched with standard data card #00-039-1433 with  $\text{P6}_3/\text{mmc}$  space group. The calculated crystallite size was nearly 55 nm.



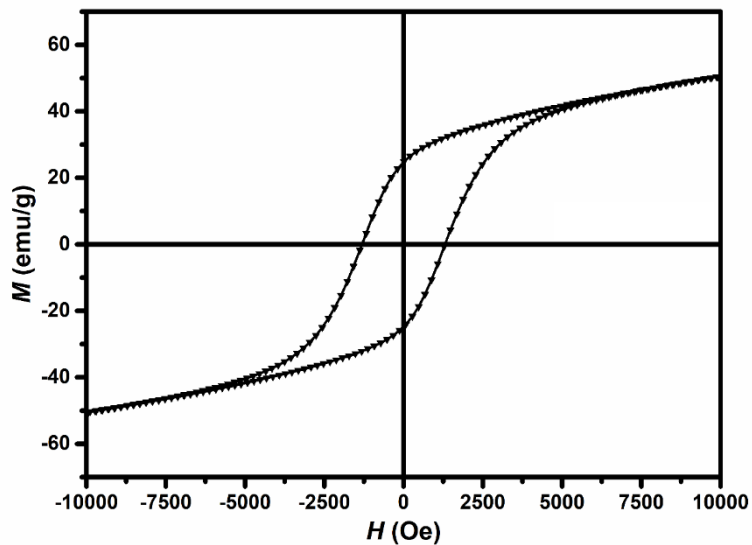
**Fig. 4.1.** XRD pattern for BaM powder

Fig 4.2 (a) shows the SEM micrograph of BaM powder calcined at  $1200\text{ }^\circ\text{C}$ . The obtained microstructures reveal equiaxed particles with a maximum particle size of  $7\text{ }\mu\text{m}$ . The particle size distribution obtained from microstructure is shown in fig 4.2 (b). The average particle size of  $1.32\text{ }\mu\text{m}$  was obtained from log-normal fit.



**Fig. 4.2.** (a & b) SEM microstructure and particle size distribution of BaM powder.

Fig. 4.3 shows the  $M$ - $H$  plot for BaM powders measured up to a maximum field of 1 T. The magnetic loop for powder confirms hard magnetic behaviour of BaM. The measured coercivity ( $H_c$ ), magnetization ( $M$ ) and remanent magnetization ( $M_r$ ) are 1.31 kOe, 51.04 emu/g and 24.96 emu/g, respectively.



**Fig. 4.3.**  $M$ - $H$  plot of BaM powder.

## 4.2 Screen printed BaM thick films

After the successful preparation of BaM powder, it was mixed with a binder and thick films of 100  $\mu\text{m}$  thickness were screen printed on  $\text{Al}_2\text{O}_3$  substrate. The films were dried overnight in the absence of magnetic field. Finally, films were sintered in a conventional furnace for different temperature (1150 - 1350  $^\circ\text{C}$ ) for 1h. In the following section, effect of sintering temperature on structural and magnetic properties of thick films are discussed.

### 4.2.1 Effect of sintering temperature

#### i. Microstructural study

Fig. 4.4 (a-c) shows representative micrographs of screen printed BaM thick film sintered at 1150  $^\circ\text{C}$ , 1250  $^\circ\text{C}$  and 1350  $^\circ\text{C}$  for 1h. With the increase in temperature, porosity found decreased, and grain was increased. Whereas, films sintered at 1350  $^\circ\text{C}$  shows liquid phase sintering with inter- diffused grain structure. A poor porous surface and irregular grain with an average grain size of 2.3  $\mu\text{m}$  were observed. An average grain size of 2.3  $\mu\text{m}$  and 4.5  $\mu\text{m}$  are observed for 1150 and 1250  $^\circ\text{C}$ , respectively. Fig. 4.4 (d) shows the cross sectional microstructure of BaM thick film sintered at 1250  $^\circ\text{C}$ . An average of 96  $\mu\text{m}$  thickness is observed.

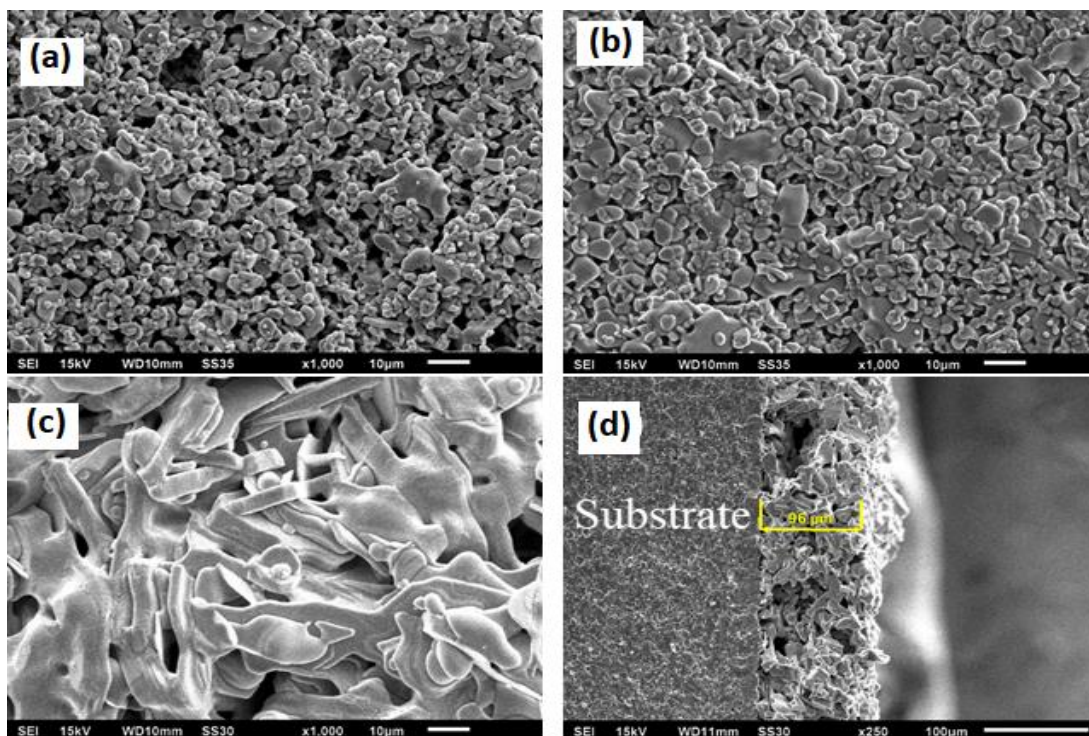


**Fig. 4.4.** SEM micrographs of sintered BaM thick film (a) 1150  $^\circ\text{C}$  (b) 1250  $^\circ\text{C}$  (c) 1350  $^\circ\text{C}$  and (d) cross sectional.

ii. *Magnetic studies*

Fig. 4.5 (a-c) shows representative  $M$ - $H$  plots for BaM thick film sintered at 1150 °C, 1250 °C, 1350 °C for 1h. The obtained plots show isotropic nature with slightly enhanced magnetic properties in  $\parallel$  directions. The variation in magnetization ( $4\pi M$ ), squareness (SQ) and coercivity ( $H_c$ ) are shown in fig 4.6 (a-c).  $4\pi M$  found decreased monotonically with sintering temperature. The lowest of 2.2 kG was found for 1350 °C sintered films which may be due to interdiffusion of films and substrate. Fig. 4.6 (b) shows SQ is slightly higher in  $\parallel$  direction and remain constant (0.5) up to 1250 °C and reduces drastically after that.  $H_c$  found to decrease with sintering temperature due to grain coarsening. The reduction in SQ and  $H_c$  confirms the existence of multi-domain grain.

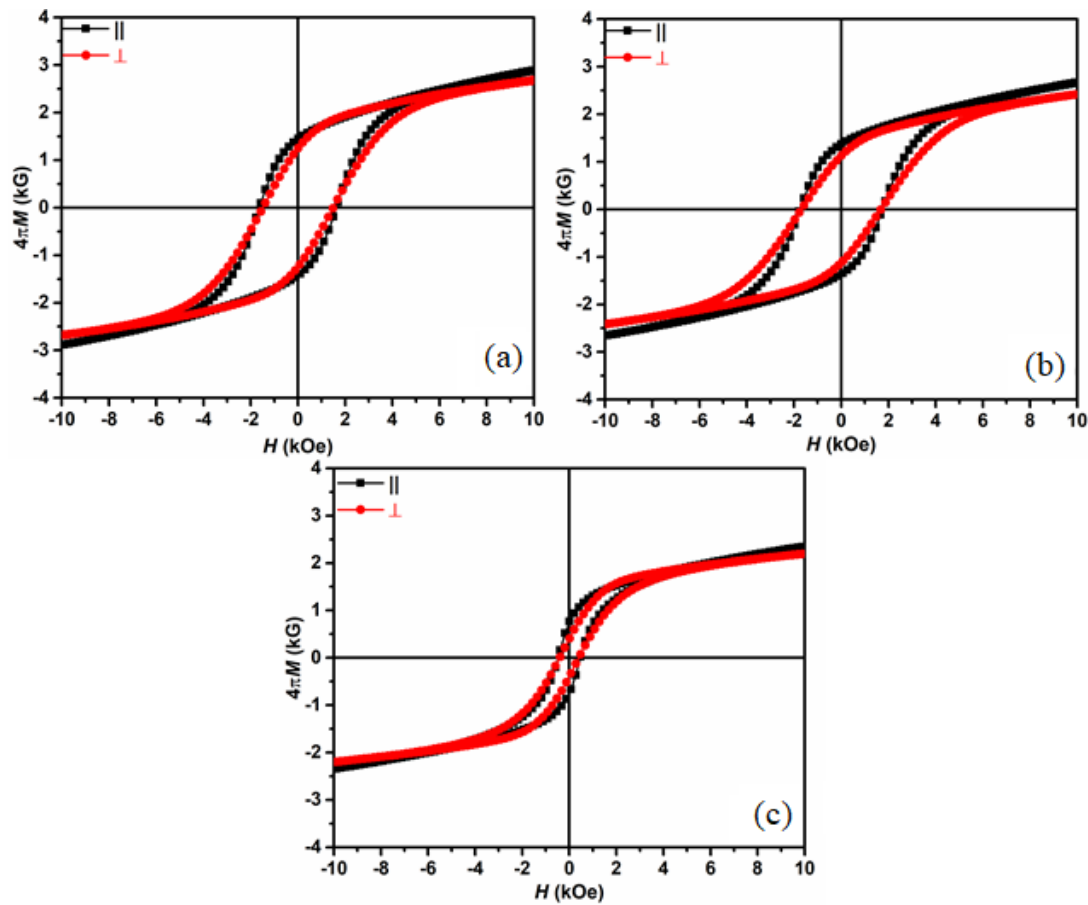


**Fig. 4.5.** Representative  $M$ - $H$  plots for BaM thick film sintered at (a) 1150°C, (b) 1250 °C and (c) 1350 °C

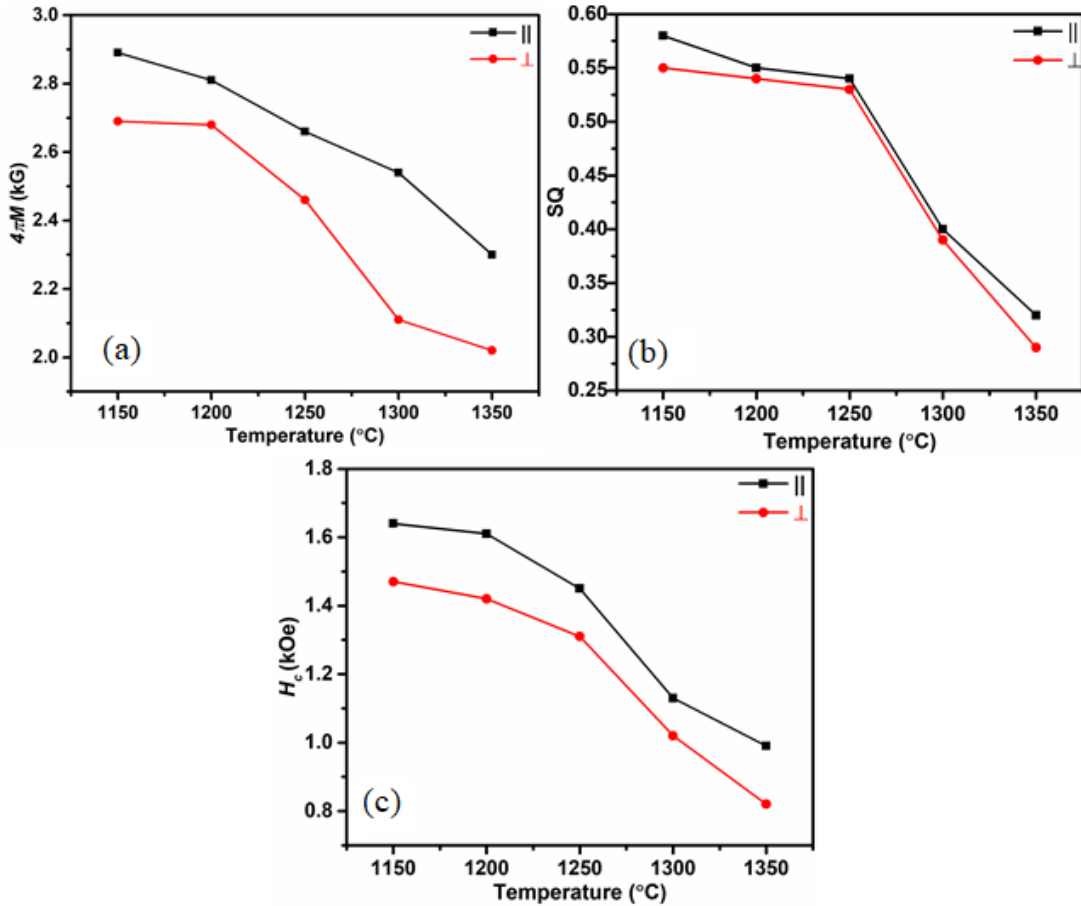
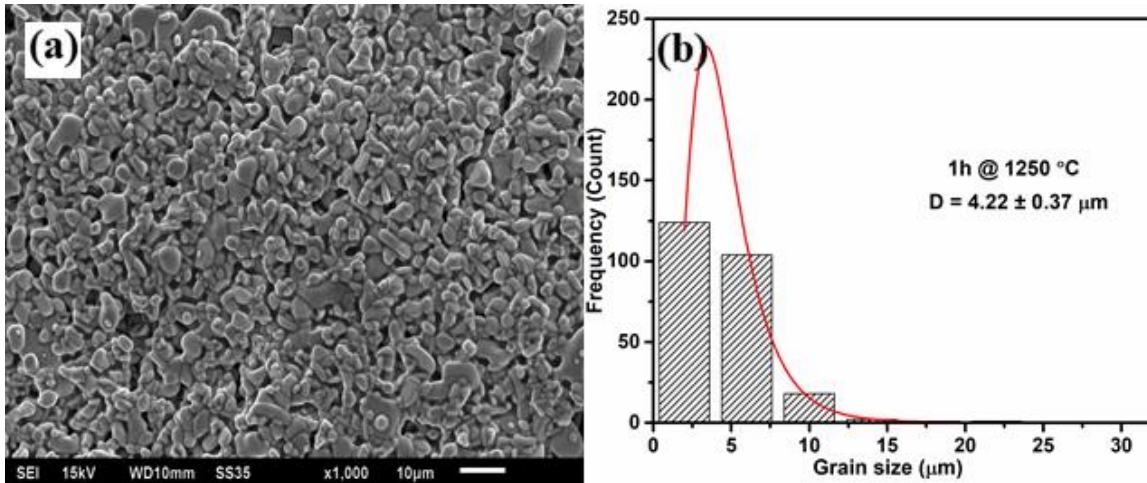


**Fig. 4.6.** Variation in (a)  $4\pi M$ , (b) SQ and (c)  $H_c$  with sintering temperature.

#### 4.2.2 Effect of BaM buffer layer

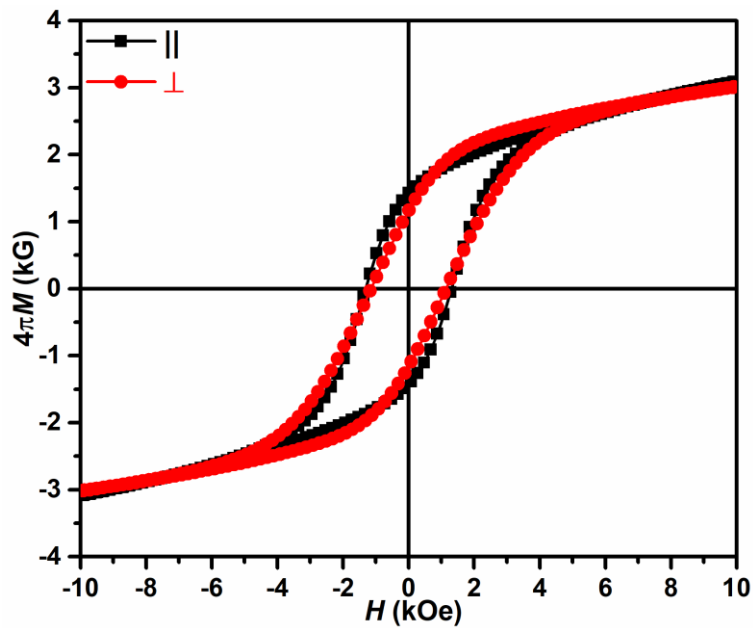
Addition of  $\text{Bi}_2\text{O}_3$  in the BaM powders for better film substrate adhesion has an adverse effect in terms of deterioration of magnetic properties. Due to its non-magnetic nature which lower down the magnetization. To avoid this, an attempt has been made to prepare screen printed film on BaM buffer layer deposited by magnetron RF sputtering. Such films may possess higher magnetization along with substrate adhesion. The details of BaM buffer layer deposition is given in the supplementary section of this dissertation.

Fig. 4.7 (a) shows the microstructure of BaM thick film deposited on BaM buffer layer and sintered at 1250 °C. The grain size found to be 4.22  $\mu\text{m}$  (Fig. 4.7 (b)) which is comparably lesser than  $\text{Bi}_2\text{O}_3$  added films (fig 4.4 (b)). No topoaxial growth was observed with the buffer layer.



**Fig. 4.7.** (a) Surface morphology and (b) Grain size distribution.

Fig. 4.8 shows the  $M$ - $H$  plot of BaM thick film. The  $M$  of 3.2 kG is observed with BaM buffer layered film, which is marginally higher than  $\text{Bi}_2\text{O}_3$  additives films (2.7 kG). The SQ of 0.44 and 0.39 obtained in  $\parallel$  and  $\perp$  direction which less than  $\text{Bi}_2\text{O}_3$  added films. No notable change has been found in  $H_c$ .



**Fig. 4.8.**  $M$ - $H$  plot of thick film with BaM buffer layer.

### 4.2.3 Effect of substitution

In the present section, screen printed thick films were prepared from Al, Ti, & La-Co substituted BaM powders. Following series of powders were processed solid state ceramic method.

1.  $\text{BaFe}_{12-x}\text{Al}_x\text{O}_{19}$  ( $x = 0.0, 0.5, 1.0, 1.5, 2.0$  &  $2.5$ )
2.  $\text{BaFe}_{12-x}\text{Ti}_x\text{O}_{19}$  ( $x = 0.0$  and  $0.5$ )
3.  $\text{Ba}_{1-y}\text{La}_y\text{Fe}_{12-x}\text{Co}_x\text{O}_{19}$  ( $x = 0.0, 0.10, 0.15, 0.20, 0.50$  &  $1.0$ )

The effect of substitution on structural and magnetic properties of samples (powders and films) are discussed. To measure the microwave properties, powders were compacted in the desired rectangular dimension and sintered. The sintering temperature of films and the pellets were kept constant.

#### 4.2.3.1 Effect of Al-substitution

##### i. X-ray diffraction studies

X-ray diffraction patterns of all substituted BaM powder were shown in fig. 4.9. Reitveld refinement for obtained XRD pattern has been carried by full prof software. Fig. 4.10 (a & b) shows the representative refined XRD pattern of pure and Al-substituted BaM powders. All the diffraction peaks correspond to single phase BaM without any impurity. It is clear from inset that the peak at  $32.2^\circ$  for pure BaM has been shifted to  $32.4^\circ$  with  $\text{Al}^{3+}$  substitution. The shift towards higher angle suggests tensile stress within the system due to smaller ionic radii of  $\text{Al}^{3+}$  ( $0.52\text{\AA}$ ) compare to  $\text{Fe}^{3+}$  ( $0.67\text{\AA}$ ) ion [185,186].

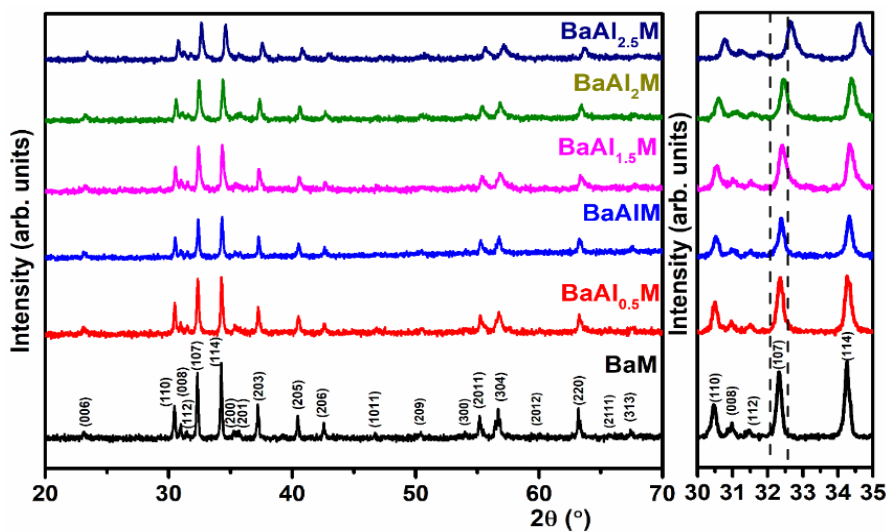


Fig 4.9. X-ray diffraction pattern of Al-substituted BaM

The crystallite size is calculated by Scherrer relation [187].  $\beta$  related in the equation is the full width at half maxima calculated by Caglioti equation [188].

$$H = [u \tan^2\theta + v \tan\theta + w]^{1/2} \quad (4.1)$$

where,  $u$ ,  $v$  and  $w$  are the shape parameters obtained from Reitveld refinement.

It is clear from Fig. 4.11, lattice parameter and crystallite size is decreasing with  $\text{Al}^{3+}$  substitution due to lower ionic radii of the  $\text{Al}^{3+}$  ion, which causes lattice shrinkage.

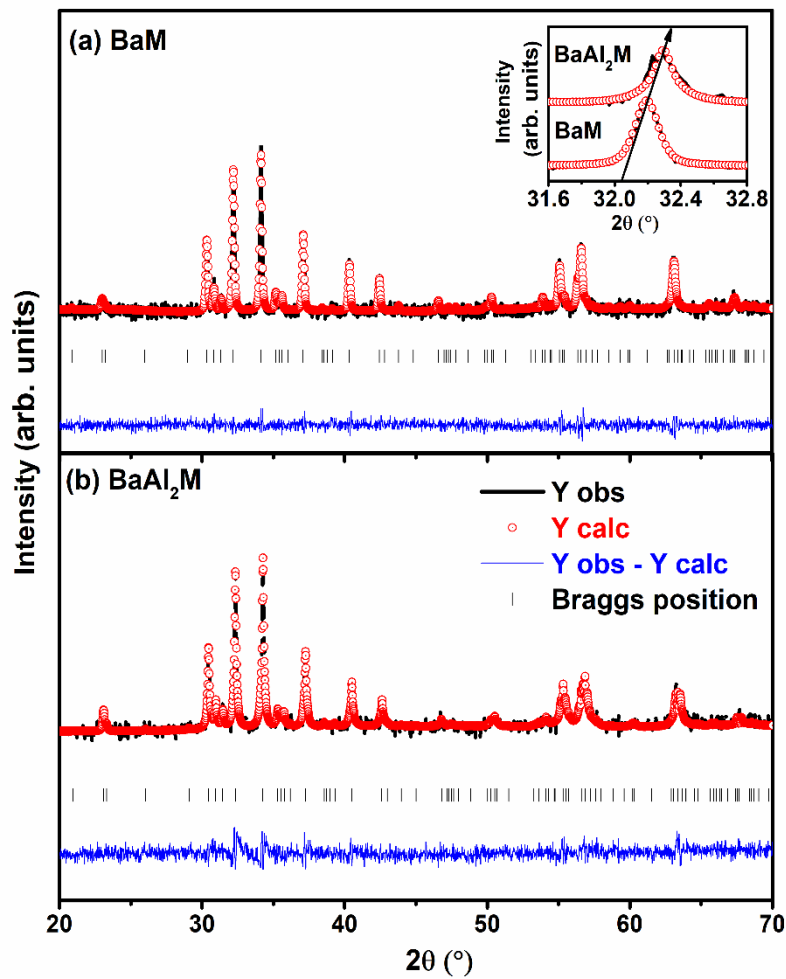


**Fig. 4.10.** Representative refined XRD pattern of BaM and BaAl<sub>2</sub>M. Inset depicts peak shift towards higher 2θ.

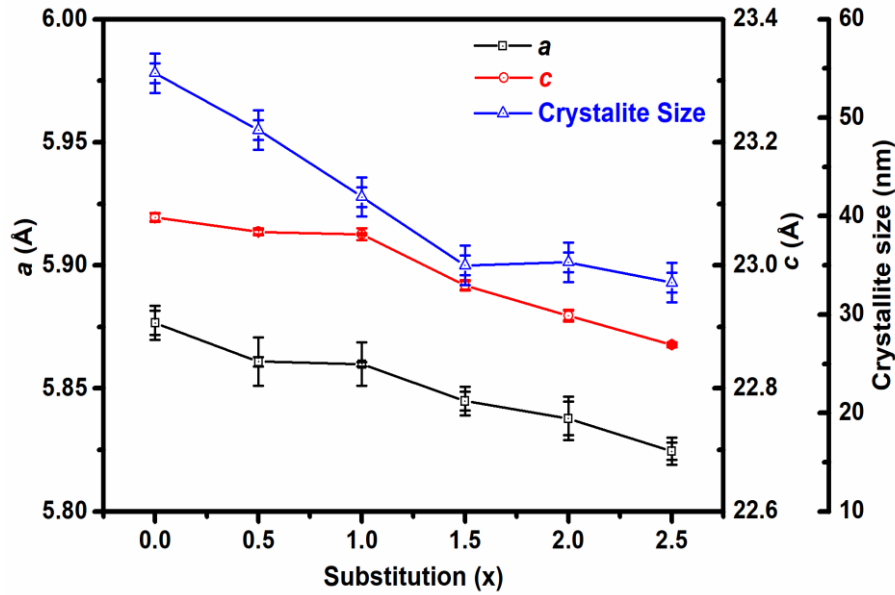


**Fig. 4.11.** Variation in lattice parameters and crystallite size with Al-substitution.

ii. *Fourier Transformer Infrared (FTIR) spectroscopy*

Fig. 4.12 depicts FTIR plots of  $\text{BaFe}_{12-x}\text{Al}_x\text{O}_{19}$  ( $x = 0.0, 1.0$  &  $2.0$ ) from  $3000\text{--}400\text{ cm}^{-1}$ . As a result of group theory, BaM compound may give rise to 189 optical modes [189], whereas, only 31 modes ( $13 A_{2u} + 18 E_{1u}$ ) are IR active. In the present case, only two active modes at  $447$  and  $613\text{ cm}^{-1}$  of Fe-O bond in octahedral ( $4f_2$ ) and tetrahedral ( $4f_1$ ) sites are visible due to vibrational modes of  $E_{1u}$  [190]. With the  $\text{Al}^{3+}$  substitution, a slight blue shift from  $447$  to  $462\text{ cm}^{-1}$  and  $613$  to  $621\text{ cm}^{-1}$  is observed, which is due to lesser atomic weight of  $\text{Al}^{3+}$  ions compared to  $\text{Fe}^{3+}$  ions as wavenumber is inversely proportional to atomic weight [186]. The bond length of Fe-O is determined by using the frequency of vibrational modes and force constant  $K$ . The  $K$  is correlated to the average bond length ( $r$ ) by following relation [191]:

$$K = \frac{17}{r^3} \quad (4.2)$$

where  $K$  is calculated by following relation:

$$\nu = \frac{1}{2\pi c} \sqrt{\frac{K}{\mu}} \quad (4.3)$$

where  $\nu$  is the frequency of vibration,  $c$  is the velocity of light, and  $\mu$  is effective mass. Effective mass is defined as follows:

$$\mu = \frac{M_O \times M_{Fe}}{M_O + M_{Fe}} \quad (4.4)$$

where  $M_O$  &  $M_{Fe}$  are the atomic weight of O and Fe.

The calculated bond length values are tabulated in table 4.1, which suggests that the bond length is reducing with  $\text{Al}^{3+}$  substitution and supports the unit cell shrinkage as observed from XRD. The increase in  $K$  and decrease in  $r$  is due to smaller ionic radii of  $\text{Al}^{3+}$  ion. Further, the reduction in bond length confirms that  $\text{Al}^{3+}$  ions has a preferential occupation in the spin-down sites ( $4f_1$  and  $4f_2$ ) as reported [192]. Previous studies on site occupation also confirmed that  $\text{Al}^{3+}$  preferably occupies  $4f_1$  and  $12k$  sites [114,193].

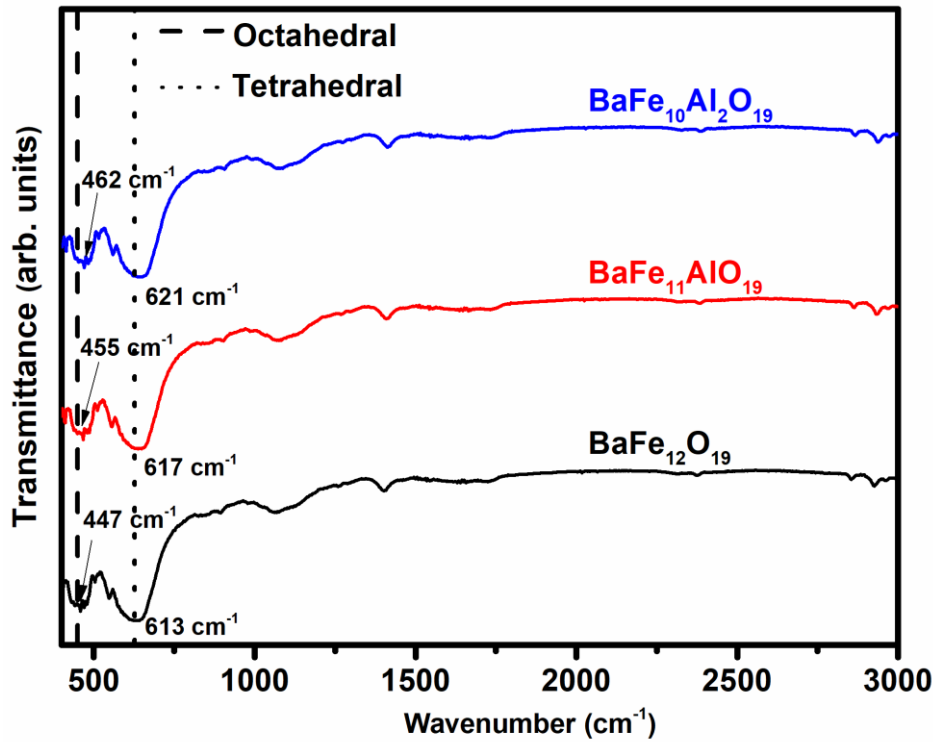


Fig. 4.12. FTIR spectrum of  $\text{BaFe}_{12-x}\text{Al}_x\text{O}_{19}$ .

Table 4.1. Wavenumber, force constant ( $K$ ) and atomic radius ( $r$ ) for octahedral and tetrahedral sites of substituted BaM.

| Site        | Sample              | Wavenumber<br>$\text{cm}^{-1}$ | $K$<br>$\text{N/m}$ | $r$<br>$\text{\AA}$ |
|-------------|---------------------|--------------------------------|---------------------|---------------------|
| Octahedral  | BaM                 | 447                            | 138.27              | 2.30                |
|             | BaAlM               | 455                            | 143.26              | 2.28                |
|             | BaAl <sub>2</sub> M | 462                            | 147.70              | 2.26                |
| Tetrahedral | BaM                 | 613                            | 260.03              | 1.87                |
|             | BaAlM               | 617                            | 263.44              | 1.86                |
|             | BaAl <sub>2</sub> M | 621                            | 266.86              | 1.85                |

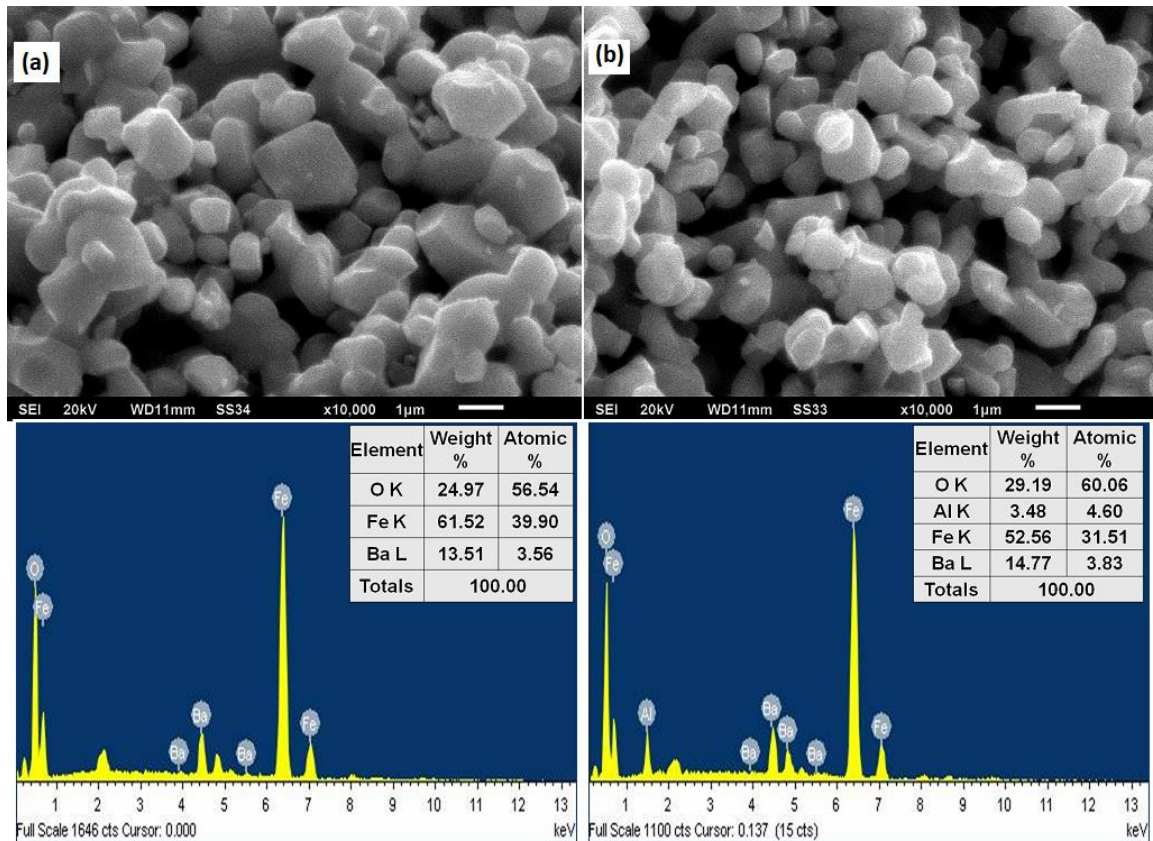
### iii. Microstructural study

Fig. 4.13 shows the SEM micrographs of pure and Al-substituted BaM powders. The powders show similar morphology; however, particle size slightly decreased (1.5 to 1  $\mu\text{m}$ ) with  $\text{Al}^{3+}$  substitution. The decrease in particle size could be ascribed to two reasons, firstly, due to pinning effect by residual  $\text{Al}_2\text{O}_3$  particles, which may remain unsubstituted and

secondly, due to decrease in crystallite size (Fig.4.10). However, the residual  $\text{Al}_2\text{O}_3$  is not evidenced in XRD patterns due to its small fraction. The XRD peak shift towards higher angle side confirms that  $\text{Al}^{3+}$  ions are also occupying the vacant  $\text{Fe}^{3+}$  sites. Further, particle size reduction is confirmed by measuring the crystallinity index ( $I_{\text{cry}}$ ) [191].

$$I_{\text{cry}} = \frac{D_p(\text{SEM,TEM})}{\tau(\text{XRD})} \quad (4.5)$$

where,  $D_p$  and  $\tau$  are the average particle and crystallite size obtained from SEM and Scherrer relation, respectively. The calculated values of  $I_{\text{cry}}$  for pure and Al-substituted BaM are found to be same, i.e.  $\sim 25$ , which suggest the lattice shrinkage is due to  $\text{Al}^{3+}$  substitution. The corresponding EDS spectrum shows the elemental composition of as-synthesized powders which confirms the presence of Ba, O and Fe. In the substituted sample, a peak of Al is also present.



**Fig. 4.13.** SEM micrographs and respective EDS images of  $\text{BaFe}_{12-x}\text{Al}_x\text{O}_{19}$  (a)  $x = 0.0$  and (b)  $x = 2.0$ .

#### iv. Magnetic studies

Fig. 4.14 shows the  $M-H$  behaviour of pure and Al-substituted BaM powders. It is clear that  $M$  at 1T is decreasing while  $H_c$  is increasing with  $\text{Al}^{3+}$  substitution. The decrease in  $M$  is attributed to the substitution of nonmagnetic  $\text{Al}^{3+}$  ions at spin up magnetic  $\text{Fe}^{3+}$  ( $12k$ ,  $2a$ ,

2b) sites [185]. Previous Mössbauer studies reported that  $\text{Al}^{3+}$  ions also occupy spin down  $4f_1$  and  $4f_2$  sites at lower substitution amount ( $\text{BaAl}_{1.5}\text{M}$ ) [192]. However, the larger fraction of  $\text{Al}^{3+}$  substitution at spin up sites suppresses the contribution to net magnetization [114]. The  $H_c$  is increasing with the increase in  $\text{Al}^{3+}$  substitution. The  $H_c$  is primarily governed by intrinsic ( $H_a$ ) and extrinsic (particle size and shape) factors.

The law of approach to saturation is used to obtain  $H_a$  and first anisotropy constant ( $k_1$ ) for the powder [194].

$$M(H) = M_s \left( 1 + \frac{A}{H} + \frac{B}{H^2} \right) + X_p H \quad (4.6)$$

where,  $H$  is applied field,  $\chi_p$  is the field consociated with the magnetization of domains. ‘A’ defined as inhomogeneity parameter in which  $A/H$  is related to the state of inhomogeneities in the microcrystal. Magnetocrystalline anisotropy contribution is defined by the term  $B/H^2$ . To specify the linear nature of anisotropy contribution the linear nature of  $M$  vs  $1/H^2$  plotted (fig. 4.15) in the field 6 – 10 kOe. The terms  $A/H$  considered inhomogeneity parameter and field associated with magnetization of domains are merely negligible. The term B was obtained from the slope of the straight line. The term  $B$  and  $H_a$  can be related as [28]:

$$B = -\frac{1}{15} H_a^2 \quad (4.7)$$

The first anisotropy constant ( $K_1$ ) is calculated by a simple relation as follows:

$$H_a = \frac{2k_1}{M_s}, \quad (4.8)$$

where,  $k_1$  is the first anisotropy constant,  $H_a$  denoted the associated field to obtain the first anisotropy constant and  $M_s$  is the saturation magnetization obtained from VSM.

The calculated values of  $H_a$  and  $k_1$  (Table 4.2) found to decrease with  $\text{Al}^{3+}$  substitution. In the present study,  $H_c$  is increasing despite the decrease in anisotropic constant ( $k_1$ ); hence, the increase in  $H_c$  is dominated by decrease in crystallite size with  $\text{Al}^{3+}$  substitution and the pinning by residual  $\text{Al}_2\text{O}_3$ .

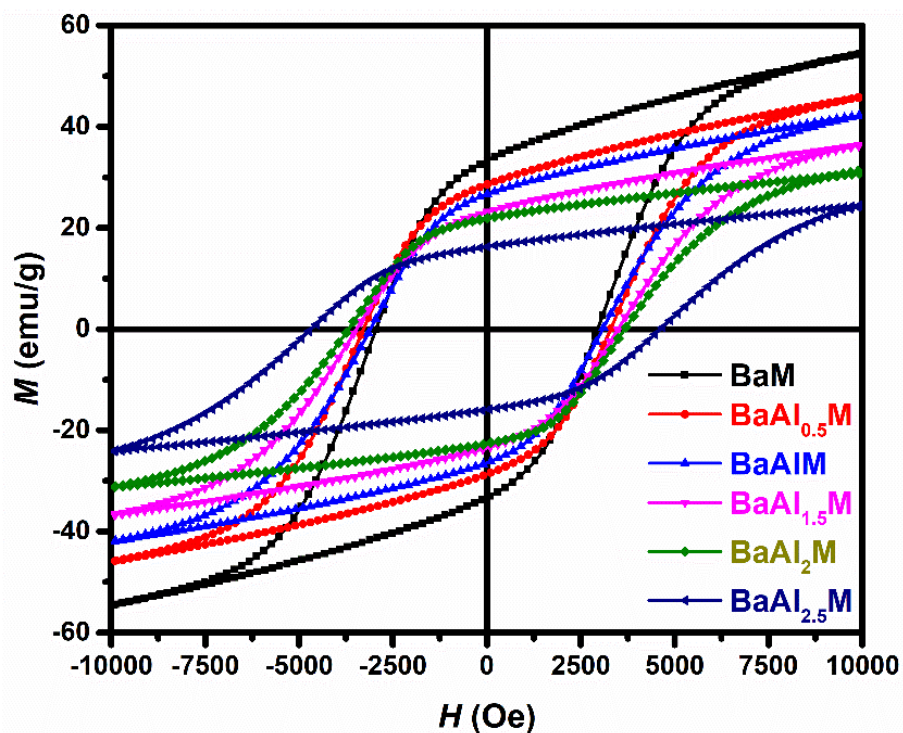


Fig. 4.14.  $M$ - $H$  loop of  $\text{BaFe}_{12-x}\text{Al}_x\text{O}_{19}$  powders.

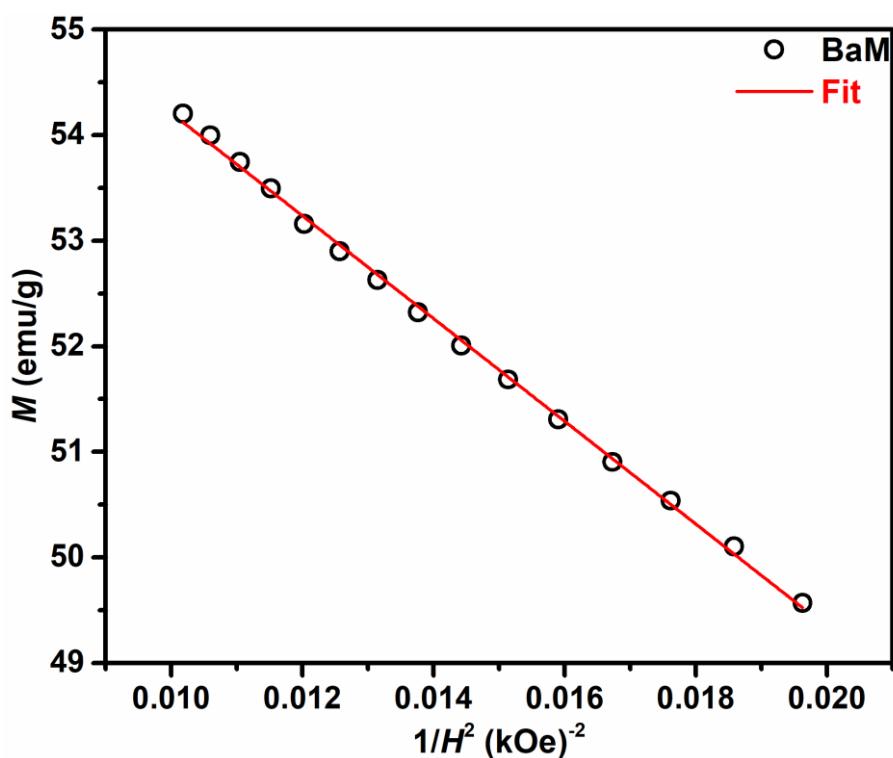


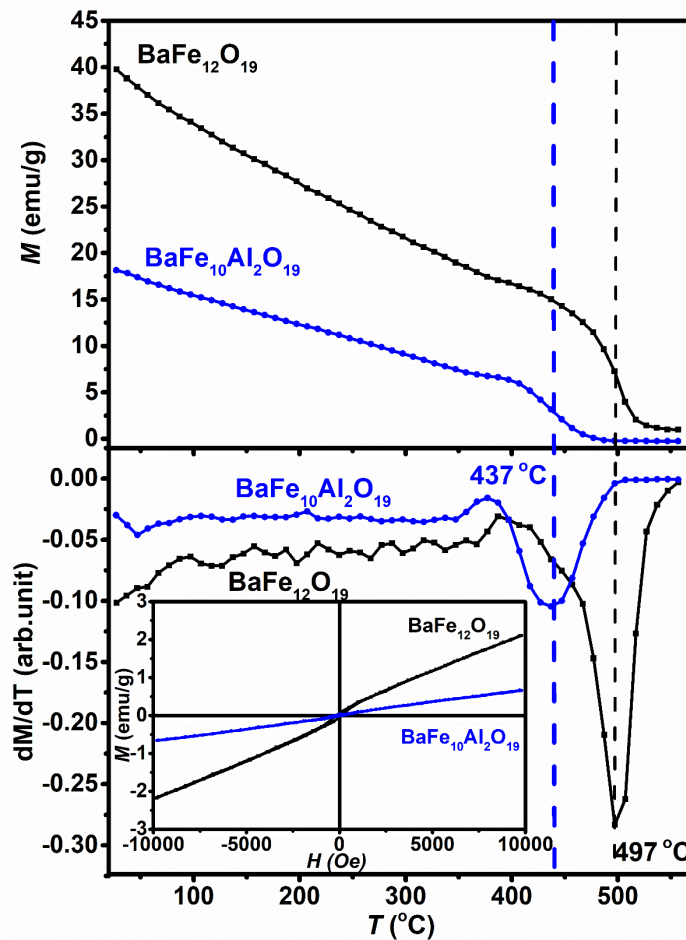
Fig. 4.15. Representative linear fit for law of saturation.

Fig. 4.16 (a) shows the magnetization vs temperature ( $M$ - $T$ ) behaviour for pure and substituted BaM. The decrease in  $M$  with temperature is due to thermal effect. Curie

temperature ( $T_c$ ) is measured by plotting derivative of  $M$  ( $dM/dT$ ) with respect to  $T$  (Fig. 4.16 (b)). The  $T_c$  found to decrease from 497 °C (BaM) to 437 °C (BaAl<sub>2</sub>M).  $T_c$  can be expressed in terms of number of exchange interactions between Fe<sup>3+</sup> - O<sup>2-</sup> - Fe<sup>3+</sup> ions [195]. The reduction in  $T_c$  is due to weakening of superexchange coupling between various subsites [196]. The inset fig. 4.16 (b) shows the  $M$ - $H$  behaviour at  $T_c$ , which clearly shows the paramagnetic nature of the samples.

**Table 4.2.** Magnetic properties of BaFe<sub>12-x</sub>Al<sub>x</sub>O<sub>19</sub> powders

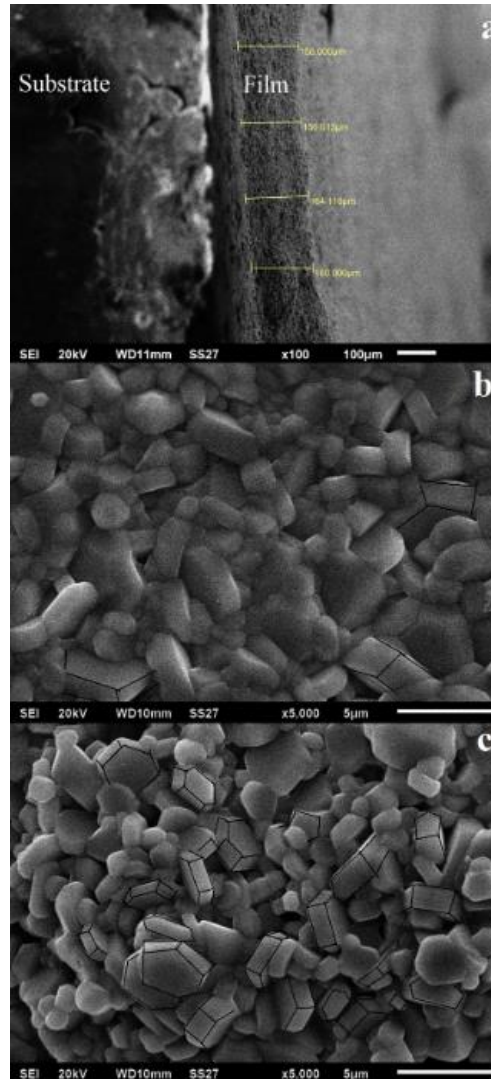
| Sample                | $M$<br>emu/g | $M_r$<br>emu/g | $H_c$<br>kOe | $H_a$<br>kOe | $k_1 \times 10^6$<br>erg/cm <sup>3</sup> |
|-----------------------|--------------|----------------|--------------|--------------|--|
| BaM                   | 54.4         | 33.3           | 2.95         | 8.54         | 1.57                                     |
| BaAl <sub>0.5</sub> M | 45.8         | 28.6           | 3.29         | 7.82         | 1.19                                     |
| BaAlM                 | 42.2         | 26.6           | 3.09         | 7.45         | 1.04                                     |
| BaAl <sub>1.5</sub> M | 36.4         | 23.3           | 3.48         | 6.89         | 0.81                                     |
| BaAl <sub>2.0</sub> M | 31.3         | 22.3           | 3.68         | 5.75         | 0.56                                     |
| BaAl <sub>2.5</sub> M | 24.4         | 16.1           | 4.65         | 5.67         | 0.45                                     |



**Fig. 4.16.** (a)  $M$ - $T$  plot and (b)  $dM/dT$  vs  $T$  for BaFe<sub>12-x</sub>Al<sub>x</sub>O<sub>19</sub>. Inset (b) shows  $M$ - $H$  behaviour at Curie temperature.

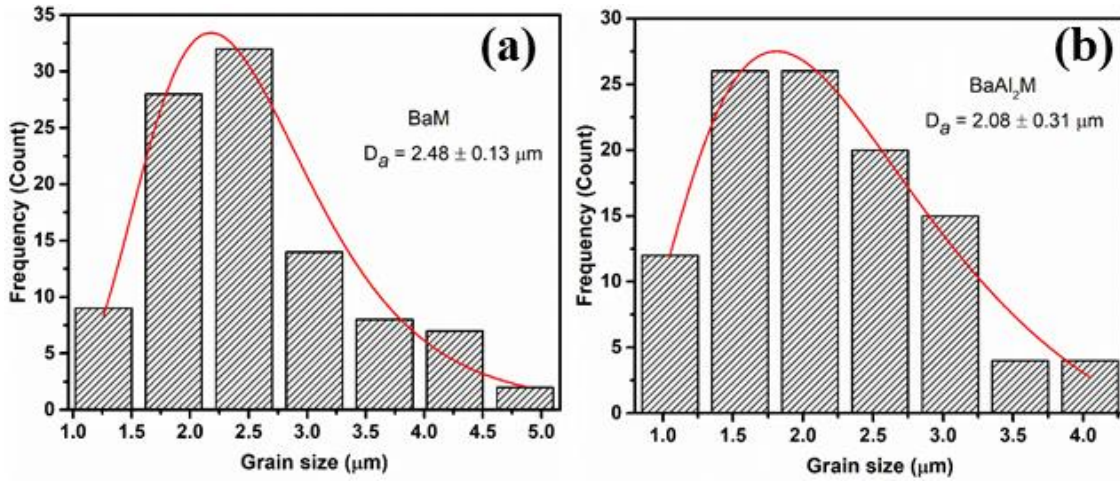
v. *Microstructural and morphological study of Al-substituted BaM thick film*

Fig. 4.17 (a-c) shows the cross sectional and surface micrographs of the pure and Al-substituted screen printed films, sintered at 1250 °C. A uniform thickness of ~160 μm is evident from fig. 4.17 and confirms that the films are well sintered; however, film surface is rough with limited porosity.



**Fig. 4.17.** SEM micrographs of BaM thick films (a) cross section (b) BaM and (c) BaAl<sub>2</sub>M.

The grain size distribution shown in fig. 4.18 reveals that the average grain size of pure BaM films is ~ 2.5 μm, which found to be smaller (~2 μm) for the substituted film BaAl<sub>2</sub>M. It is also clear from micrographs that Al<sup>3+</sup> substitution is promoting hexagonal shaped grains. The average diameter to thickness ratio of hexagonal plates is decreasing from 0.65 for BaM to 0.36 for BaAl<sub>2</sub>M.



**Fig. 4.18.** Grain size distribution of (a) BaM and (b) BaAl<sub>2</sub>M.

vi. *Magnetic studies of Al-substituted BaM thick film*

$M$ - $H$  plots of pure and Al-substituted BaM thick films were recorded at 2 T, as shown in fig. 4.19. The magnetic properties of Al-substituted BaM films are shown in table 4.3.  $M$  and  $M_r$  are found to be higher for  $\parallel$  direction; however,  $H_c$  is nearly same for both  $\parallel$  and  $\perp$  direction.  $H_c$  of BaM film (1.7 kOe) is found to be less than the powder (3.0 kOe) due to the apparent increase in grain size after sintering. However, on contrary, the  $H_c$  of the substituted films is very high despite its larger grain size. The highest  $H_c$  of 7.47 kOe is observed for BaAl<sub>2</sub>M is due to dominant Al<sub>2</sub>O<sub>3</sub> pinning effect in sintered films [111,197].

**Table 4.3.** Magnetic properties of BaFe<sub>12-x</sub>Al<sub>x</sub>O<sub>19</sub> thick films.

| Sample                | $4\pi M$<br>@2T<br>kG |         | $4\pi M_r$<br>kG |         | $H_c$<br>kOe |         | $H_a$<br>kOe |         | $k_l \times 10^6$<br>erg/cm <sup>3</sup> |         |
|-----------------------|-----------------------|---------|------------------|---------|--------------|---------|--------------|---------|--|---------|
|                       | $\parallel$           | $\perp$ | $\parallel$      | $\perp$ | $\parallel$  | $\perp$ | $\parallel$  | $\perp$ | $\parallel$                              | $\perp$ |
| BaM                   | 4.14                  | 3.53    | 2.01             | 2.01    | 1.73         | 1.74    | 12.63        | 12.55   | 2.10                                     | 1.77    |
| BaAlM                 | 3.12                  | 2.55    | 1.70             | 1.36    | 4.77         | 4.79    | 11.17        | 10.63   | 1.39                                     | 1.06    |
| BaAl <sub>2.0</sub> M | 1.20                  | 1.08    | 0.71             | 0.63    | 7.47         | 7.45    | 7.03         | 6.72    | 0.34                                     | 0.29    |

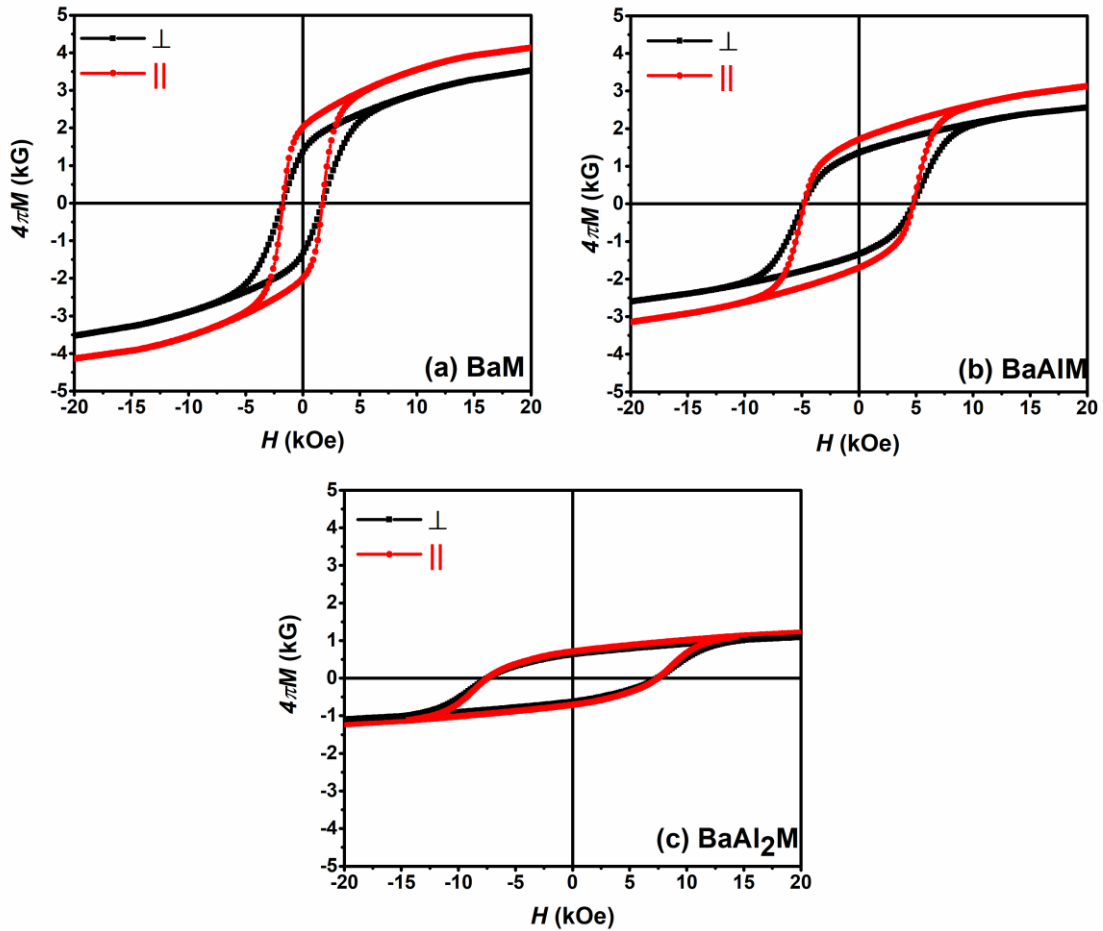


**Fig. 4.19.**  $M$ - $H$  loops of  $\text{BaFe}_{12-x}\text{Al}_x\text{O}_{19}$  thick films

vii. *High frequency complex permeability*

Fig. 4.20 (a & b) shows the variation of real ( $\mu'$ ) and imaginary ( $\mu''$ ) part of complex permeability ( $\mu_r = \mu' - j\mu''$ ) for pure and Al- substituted BaM as a function of frequency. Parameters  $\mu'$  and  $\mu''$  represents the storage and losses of magnetic energy, respectively. It is observed that  $\mu'$  of the Al-substituted BaM is lesser than the pure BaM. However, within the substitution,  $\mu'$  increases with Al content. The variation may be attributed to the non-magnetic nature of  $\text{Al}^{3+}$  ions. It is clear from the fig. 4.20 (b) that  $\mu''$  for Al-substituted BaM is more significant and maximum were observed for  $x = 1$ . These losses may due to change in grain size, sintered density, or lag between magnetization and applied field [198].

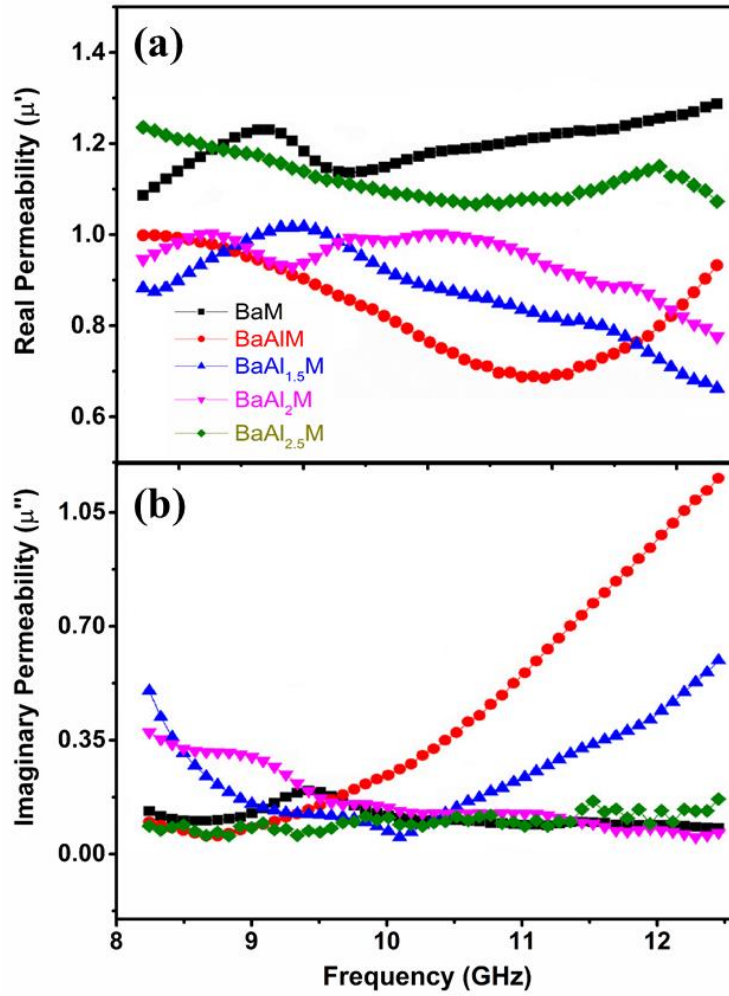


**Fig. 4.20.** Frequency dependent (a) real and (b) imaginary permeability of  $\text{BaFe}_{12-x}\text{Al}_x\text{O}_{19}$  in X-band.

viii. *Microwave reflection losses*

The following relations were used to calculate reflection loss;

$$R_L = 20 \log \left| \frac{(Z_{in} - Z_0)}{(Z_{in} + Z_0)} \right| \quad (4.9)$$

where  $Z_{in}$  is given by:

$$Z_{in} = Z_0 \sqrt{\frac{\mu_r}{\epsilon_r}} \tanh \left\{ j \left( \frac{2\pi f t}{c} \right) \sqrt{\mu_r \epsilon_r} \right\} \quad (4.10)$$

where  $f$  is the frequency,  $t$  is the thickness of sample,  $\mu_r$  and  $\epsilon_r$  are the complex relative permeability and permittivity of the sample,  $c$  is the velocity of the light,  $Z_0$  is the impedance of the air and  $Z_{in}$  is the input impedance at the absorber surface.

The reflection loss dips are observed at the frequency where absorption is maximum. It can be seen (Fig. 4.21) that all compositions have reflection dip in the studied frequency range except for the composition  $x = 1$ . The observed reflection loss RL is

varying from -14.05 dB (BaM) to -47.06 dB (BaAl<sub>1.5</sub>M) at 9.3 GHz frequency. Thus, these reflection losses dip shows that Al-substitution improves the absorption property of BaM.

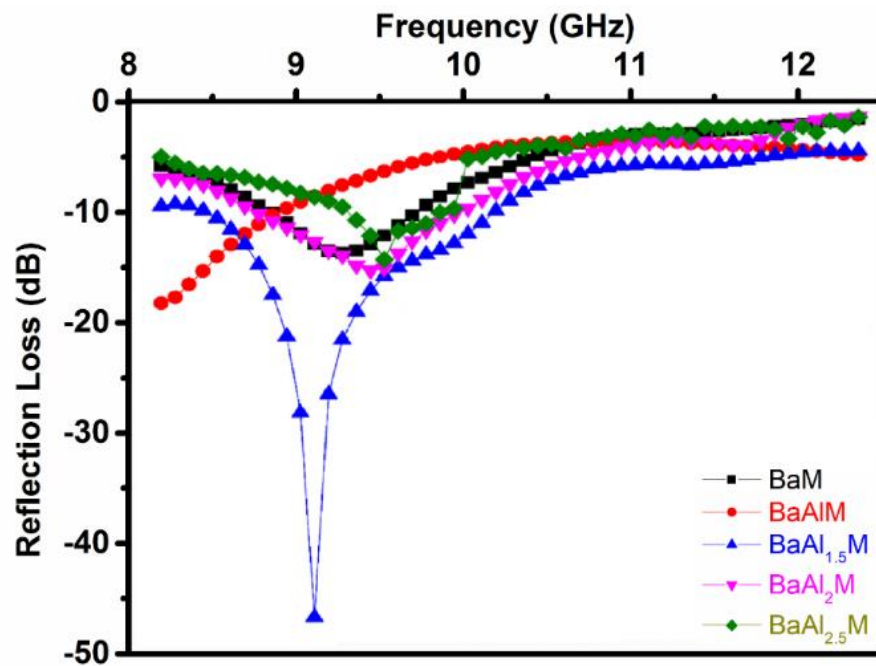


**Fig. 4.21.** Frequency dependent reflection loss of BaFe<sub>12-x</sub>Al<sub>x</sub>O<sub>19</sub> in X-band

#### 4.2.3.2 Effect of Ti- substitution

BaFe<sub>11.5</sub>Ti<sub>0.5</sub>O<sub>19</sub> powder was prepared by solid state ceramic method. Single calcination was not sufficient to obtain the phase purity in Ti substituted BaM, a small traces of residual Fe<sub>2</sub>O<sub>3</sub> was observed. Therefore, a three-step calcination method is adopted for adequate substitution and single phase formation. Calcination temperature and time was 1200 °C and 3h, respectively, for every step.

##### i. X-ray diffraction studies

Fig. 4.22 shows representative XRD patterns of first and third step calcined BaM and BaTiM powders. In BaM, single phase was formed in first step calcination. No further changes were observed after subsequent calcinations. Whereas, BaTiM shows residual Fe<sub>2</sub>O<sub>3</sub> (~2%) up to second step calcination and diminished in third step calcination. After third step calcination, a marginal peak shift from 34.08° to 34.14° suggested the effective substitution. Due to comparable ionic radii of Ti<sup>4+</sup> and Fe<sup>3+</sup> ions, no noticeable change in lattice parameters were observed [199]. A marginal increase in calculated crystallite size [187] from 30 nm to 37 nm was observed with the calcination step.

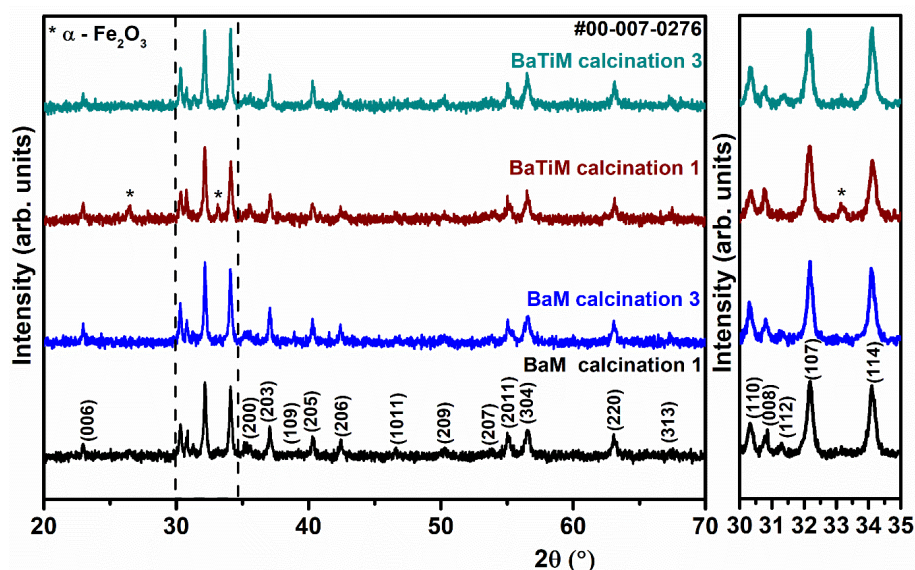


**Fig. 4.22.** Representative XRD plot for BaM and BaTiM. The enlarged plot depicts peak shift in Ti-substituted powder

##### ii. Fourier Transformer Infrared (FTIR) spectroscopy

Fig. 4.23 shows the FTIR spectrum (2500 – 100 cm<sup>-1</sup>) of pure and substituted BaM. Among 30 IR active modes (13A<sub>2u</sub> + 17E<sub>1u</sub>), only six active modes were observed due to partial superimposition of “spinel block” region [184]. FTIR spectrum for BaM shows the negligible effect on calcination steps, whereas, BaTiM shows a slight variation in the spectra over successive calcination. The observed frequency modes and the calculated bond

length are tabulated in table 4.4. The band at  $100\text{-}150\text{ cm}^{-1}$  ( $A_{2u}$ ) primarily associated with dodecacordinated alkali heavy metals, the redshift ( $152 - 140\text{ cm}^{-1}$ ) obtained in this region shows a stronger correlation between  $2b$  bipyramidal site and  $Ba^{2+}$  ions [200]. The splitted IR band around  $220$  and  $240\text{ cm}^{-1}$  depicts iron-oxygen bond for  $2b$  ( $FeO_5$ ) and  $12k_1$  ( $FeO_6$ ) sites, respectively. This  $2b$  band was not observed for BaTiM calcination 1, however, in BaTiM calcination 2 and 3 band at  $223$  and  $226\text{ cm}^{-1}$  respectively were observed. The  $12k_1$  band shows an increment in wavenumber over calcination process due to the increase in site occupation by  $Ti^{4+}$  ions. The band at  $309\text{ cm}^{-1}$  is due to residual  $Fe_2O_3$  as supported by XRD. The band at  $360\text{ cm}^{-1}$  belongs to  $A_{2u}$  &  $E_{1u}$  modes of  $2a$  ( $FeO_6$ ) site. The  $A_{2u}$  mode of  $4f_1$  and  $4f_2$  site are visible at  $620\text{ cm}^{-1}$  and  $450\text{ cm}^{-1}$ , respectively [201]. The gradual shift of  $4f_1$  and  $4f_2$  band towards higher wavenumber suggested the substitution of smaller  $Ti^{4+}$  ions. An overall blue shift in BaTiM calcination 3 as compared to BaM calcination 3 was due to  $Ti^{4+}$  occupation. The bond length for  $4f_1$  and  $4f_2$  band was calculated by force constant method as suggested previously [202]. The continuous reduction in bond length from  $2.27\text{ \AA}$  to  $2.25\text{ \AA}$  and  $1.86\text{ \AA}$  to  $1.83\text{ \AA}$  were observed with calcination steps. Additionally, this result supports that  $Ti^{4+}$  ion prefers to occupy the spin down  $4f_2$  and  $4f_1$  sites. A broad frequency band at  $830\text{ cm}^{-1}$  depicts the existence of heavier  $Ba^{2+}$  ions [203]. To verify the substitution of  $Ti^{4+}$  ions with calcination step; Raman studies were carried out.

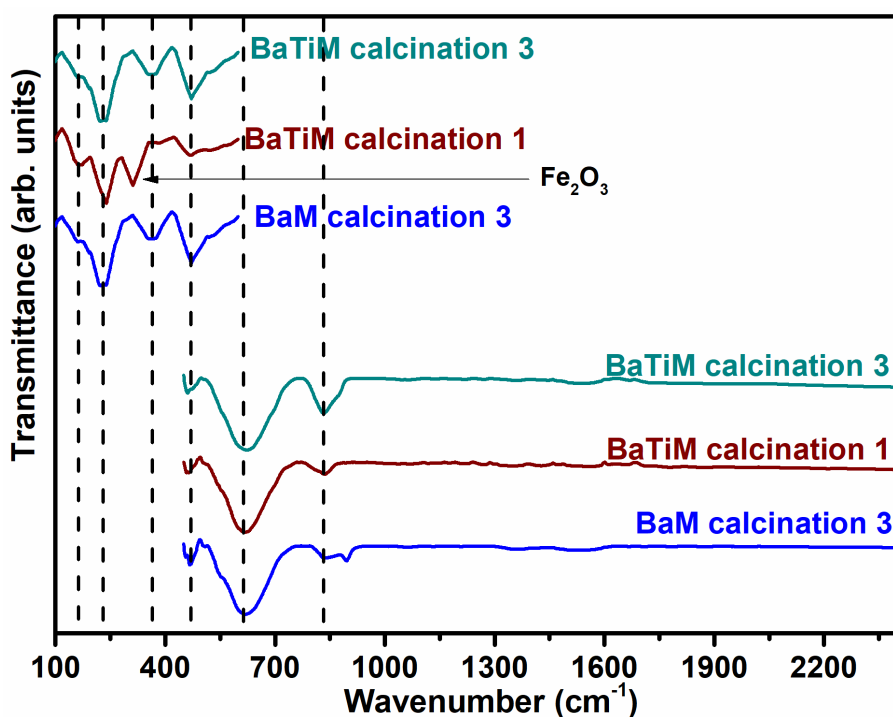


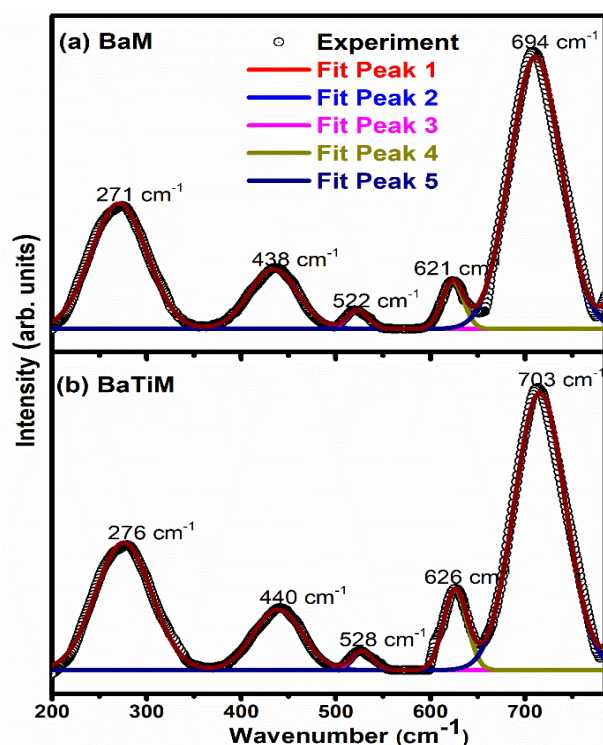
Fig. 4.23. FTIR spectrum of BaM and BaTiM powders.

**Table 4.4.** FTIR modes of BaM and BaTiM.

| Bond                     | Mode                              | Site             | BaM<br>cm <sup>-1</sup> | BaTiM<br>cm <sup>-1</sup> |
|--------------------------|-----------------------------------|------------------|-------------------------|---------------------------|
| Ba-O                     | A <sub>2u</sub>                   |                  | 135                     | 140                       |
| Fe – O                   | A <sub>2u</sub>                   | 2b               | 222                     | 226                       |
|                          | A <sub>2u</sub>                   | 12k <sub>1</sub> | 238                     | 242                       |
| Fe – O                   | A <sub>2u</sub> + E <sub>1u</sub> | 2a               | 362                     | 366                       |
| Fe – O                   | A <sub>2u</sub>                   | 4f <sub>2</sub>  | 458                     | 464                       |
| Fe – O                   | A <sub>2u</sub>                   | 4f <sub>1</sub>  | 620                     | 625                       |
| Mass of Ba <sup>2+</sup> | -                                 | -                | 837                     | 833                       |

iii. Raman Spectroscopy

Fig. 4.24 shows the fitted Raman spectra recorded in the range of 200 – 800 cm<sup>-1</sup>. Among 42 Raman active modes (11A<sub>1g</sub> + 14E<sub>1g</sub> + 17E<sub>2g</sub>) [189] only five distinct signature peaks were observed at 271, 438, 522, 621 and 694 cm<sup>-1</sup> for substituted BaM. The obtained Raman modes of calcined powders are given in table 4.5. The peak at 271 cm<sup>-1</sup> signifies vibration mode of E<sub>1g</sub> for O – Fe – O bridge. The broad frequency band at 438 cm<sup>-1</sup> corresponds to A<sub>1g</sub> metal oxide mode of 12k (↑) site [204]. The minor peak at 522 cm<sup>-1</sup> denotes E<sub>1g</sub> mode of metal oxide bonds for the mixed site 12k (↑) and 2a (↑). The modes at 694 cm<sup>-1</sup> seem to be superimposed band of weak 2b (690 cm<sup>-1</sup>) and strong 4f<sub>1</sub> (710 cm<sup>-1</sup>) sites. This band shows the characteristic behaviour of A<sub>1g</sub> tetrahedral oxygen coordinates. The slight blue shift observed in the Raman spectroscopy confirm the substitution of Ti<sup>4+</sup> ions.

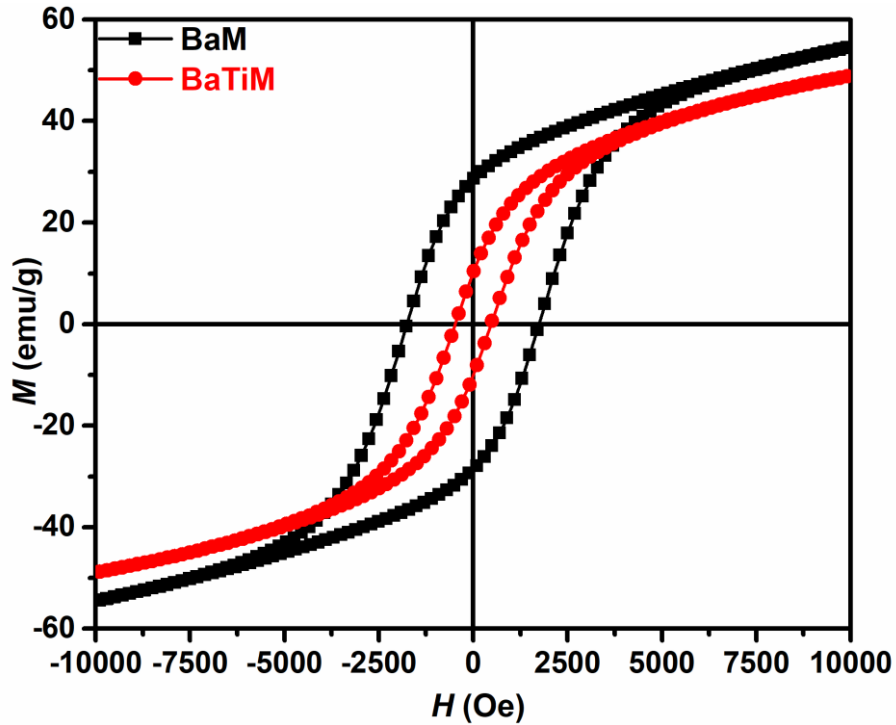
**Fig. 4.24.** Micro-Raman spectrum of BaM 3 and BaTiM 3 powders.

**Table 4.5.** Raman modes of BaM and BaTiM.

| Bond        | Mode            | Site            | BaM<br>cm <sup>-1</sup> | BaTiM<br>cm <sup>-1</sup> |
|-------------|-----------------|-----------------|-------------------------|---------------------------|
| Fe-O bridge | E <sub>1g</sub> | -               | 271                     | 276                       |
| Fe-O        | E <sub>2g</sub> | 12k             | 438                     | 440                       |
| Fe-O        | E <sub>1g</sub> | 12k + 2a mixed  | 522                     | 528                       |
| Fe-O        | A <sub>1g</sub> | 4f <sub>2</sub> | 621                     | 626                       |
| Fe-O        | A <sub>1g</sub> | 4f <sub>1</sub> | 694                     | 703                       |

iv. *Magnetic studies*

Fig. 4.25 shows the  $M$ - $H$  behaviour of BaM and BaTiM samples. The measured magnetic properties are tabulated in table 4.6. The reduction in  $M$ ,  $M_r$  and  $H_c$  suggest Ti<sup>4+</sup> ions effectively substituted in BaM crystal structure. Further,  $H_a$  was found to reduce from 8.89 – 8.45 kOe with Ti substitution due to the substitution of nonmagnetic Ti<sup>4+</sup> ions.

**Fig. 4.25.**  $M$ - $H$  plots of BaM and BaTiM powders.**Table 4.6.** Magnetic properties of BaM and BaTiM powders.

| Samples | $M$<br>(at 1 T)<br>emu/g | $M_r$<br>emu/g | $H_c$<br>kOe | $H_a$<br>kOe |
|---------|--------------------------|----------------|--------------|--------------|
| BaM     | 54.45                    | 29.60          | 1.75         | 8.89         |
| BaTiM   | 48.82                    | 13.45          | 0.47         | 8.45         |

v. *Microstructural study*

Ti-substituted BaM thick films of 100  $\mu\text{m}$  were screen printed on  $\text{Al}_2\text{O}_3$  substrate and sintered at 1250  $^\circ\text{C}$ . Fig. 4.26 (a & b) shows the surface topography of BaM and BaTiM films. Films exhibit equiaxed grain with occasional porosity irrespective of Ti substitution. EDS spectrum shown in fig. 4.26 (c & d) confirms the presence of Ba, O, Fe and Ti in the substituted system. The average grain size (Fig. 4.27) of the BaM films were found to be 3.66  $\mu\text{m}$ , whereas,  $\text{Ti}^{4+}$  substitution shows 3.32  $\mu\text{m}$ .

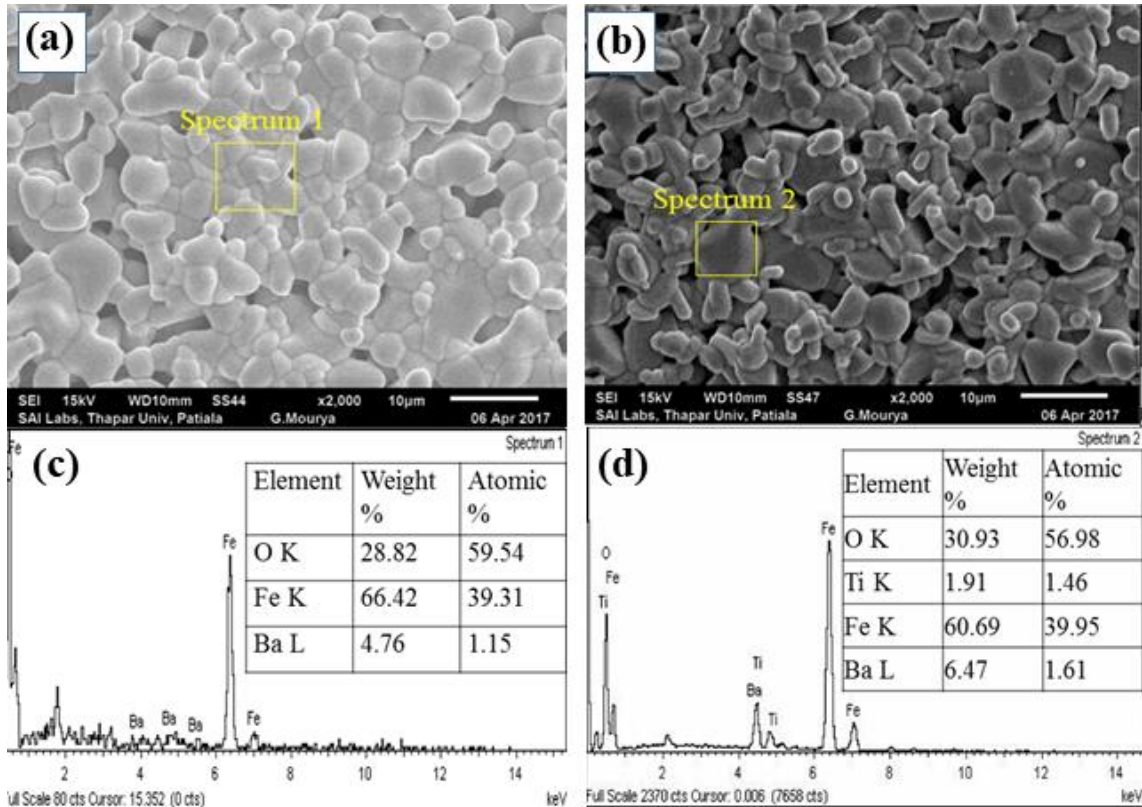


**Fig. 4.26.** SEM micrographs of (a) BaM, (b) BaTiM and (c & d) respective EDS spectrum

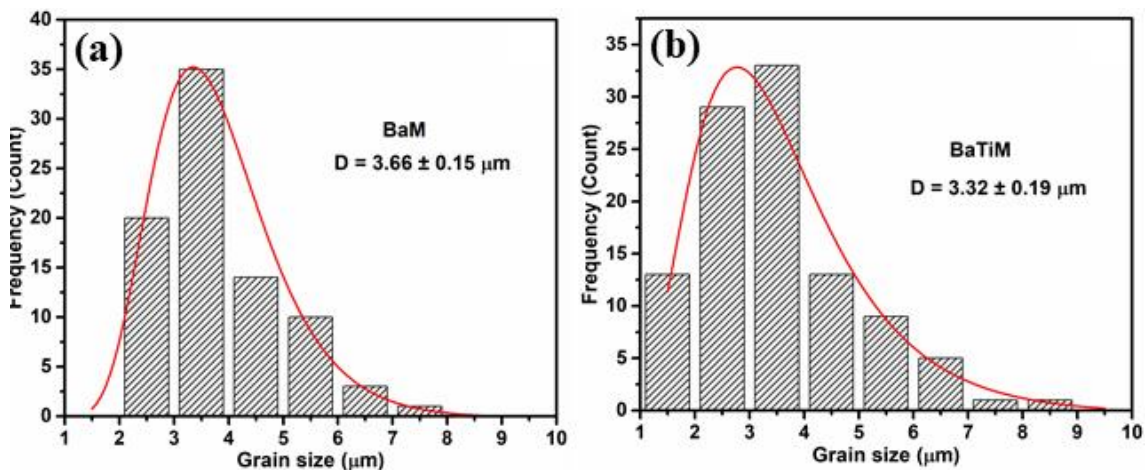


**Fig. 4.27.** Grain size distribution of (a) BaM and (b) BaTiM.

vi. *Magnetic studies Ti-substituted BaM thick film*

Fig. 4.28 (a & b) shows the direction depended magnetic plots for pure and Ti substituted BaM thick film. Low  $M$  and  $H_c$  were found in Ti-substituted samples. The films exhibit isotropic magnetic behaviour with comparable  $M_r$ ,  $H_c$  and  $SQ$  in  $\parallel$  and  $\perp$  direction. The reduction in magnetic properties (Table 4.7) are due to Ti ions substitution.

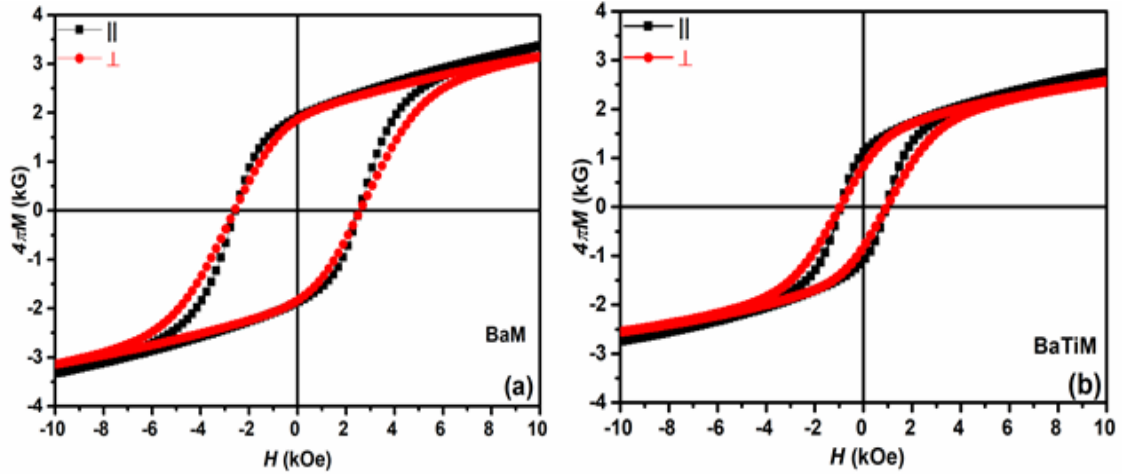


**Fig. 4.28.**  $M$ - $H$  plots of (a) pure and (b) Ti-substituted BaM films.

**Table 4.7.** Magnetic properties of the BaM and BaTiM sintered thick films.

| Sample | $4\pi M$<br>kG |         | $4\pi M_r$<br>kG |         | $SQ$        |         | $H_c$<br>kOe |         | $H_a$<br>kOe |         |
|--------|----------------|---------|------------------|---------|-------------|---------|--------------|---------|--------------|---------|
|        | $\parallel$    | $\perp$ | $\parallel$      | $\perp$ | $\parallel$ | $\perp$ | $\parallel$  | $\perp$ | $\parallel$  | $\perp$ |
| BaM    | 3.32           | 3.15    | 1.91             | 1.85    | 0.57        | 0.59    | 2.54         | 2.58    | 8.65         | 7.90    |
| BaTiM  | 2.74           | 2.56    | 1.11             | 0.81    | 0.40        | 0.33    | 0.94         | 0.95    | 8.06         | 7.30    |

vii. *High frequency complex permittivity and permeability*

The variations in the dielectric constant ( $\epsilon'$ ) and loss ( $\epsilon''$ ) in  $K_u$ - band are shown in fig. 4.29 (a & b). In BaM, the decrease in  $\epsilon'$  is due to suppression of interfacial and dipole polarization at higher frequencies [205]. The presence of  $Ba^{2+}$ ,  $Fe^{3+}$  and  $O^{2-}$  ions in BaM contributes oscillatory behaviour of  $\epsilon'$  and  $\epsilon''$  as an effect of dipole polarization and relaxation [127]. The  $\epsilon'$  for BaM was found maximum (19) at 13.97 GHz and comparable to previous studies [206]. The minimum in  $\epsilon'$  at maximum  $\epsilon''$  gives good agreement for damping of dipole polarization [198]. On the other hand, substituted BaM shows a suppressed oscillatory behaviour in  $\epsilon'$  throughout the frequency range. This suppressed behaviour is associated with multiple dipoles and relaxation, persuaded by  $Ti^{4+}$  ions [127]. Minimal  $\epsilon''$  was observed (0.4-0.5) for substituted BaM, which, suggest  $Ti^{4+}$  substitution lower the lossy behaviour in the  $K_u$ - band, which is prerequisite for microwave absorbing materials [29].

Fig. 4.29 (c & d) shows  $\mu'$  and  $\mu''$  of complex permeability spectra in K<sub>u</sub>- band. The  $\mu'$  and  $\mu''$  for pure BaM show oscillatory behaviour and increase with frequency. The variation in  $\mu'$  and  $\mu''$  were attributed to domain wall resonance with relaxation type dispersion [198]. The peak maxima of  $\mu'$  (1.53) and  $\mu''$  (0.62) for BaM was obtained at 14.98 and 14.45 GHz, respectively. The observed oscillatory behaviour in  $\mu'$  and  $\mu''$  are in comparison with previously reported studies [206]. However, suppression in such oscillations was observed for substituted BaM (Fig. 4.29 (d)). Highest  $\mu'$  for substituted samples were found to be  $\sim 1.52$  at 15.31 GHz for BaTiM. The peaks in  $\mu''$  and  $\epsilon''$  at same frequency may contribute to reduces the impedance mismatch [206].

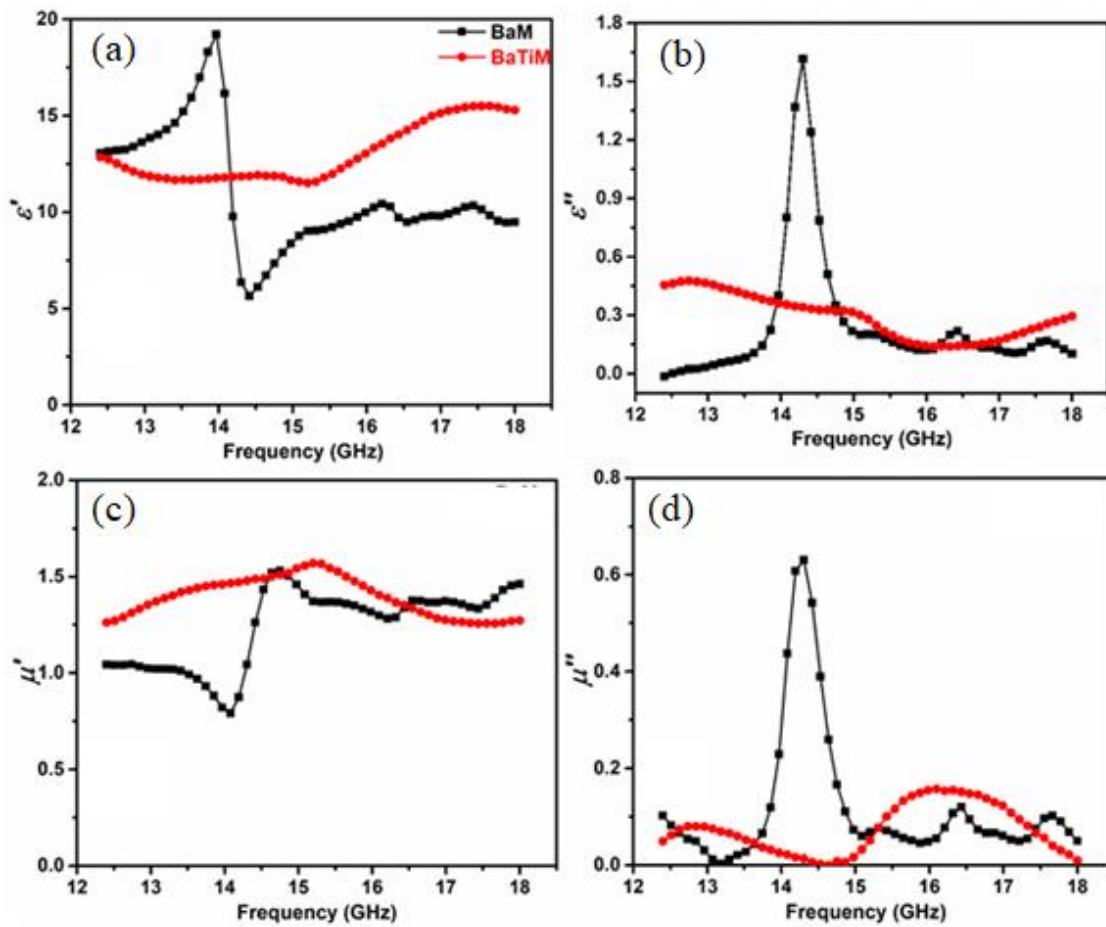


**Fig. 4.29.** Real and imaginary part of (a & b) complex permittivity, and (c & d) complex permeability for substituted BaM in K<sub>u</sub>- band.

#### viii. Microwave absorbance

Absorbance  $A(\omega)$  in a microwave region is related to reflection coefficient and transmission coefficient by the relation:

$$A(\omega) = 1 - \text{Reflectance (R}(\omega)) - \text{Transmittance (T}(\omega)) = 1 - |S_{11}|^2 - |S_{12}|^2 \quad (4.11)$$

where  $S_{11}$  is reflection and  $S_{12}$  is transmission coefficient.

Fig. 4.30 shows  $A(\omega)$  plots for substituted BaM sintered pellets. BaM showed  $A(\omega)$  peaks at 14.53 GHz and 16.43 GHz with the coefficients of 0.93 and 0.70 respectively. Since the full FMR values cannot be obtained from these data as natural FMR of BaM occurs at much higher frequencies (above 40 GHz); therefore, the observed absorbance peaks in  $K_u$ -band were primarily due to domain wall motion as evident from our permittivity and permeability studies [205].  $Ti^{4+}$  substitution suppressed oscillatory behaviour in the  $A(\omega)$  obtain  $K_u$ -band. The maximum absorbance for BaTiM was found to be 0.90 at 15.93 GHz. It is to mention that the absorption in the X and Ku bands is still of great interest for radar absorbing RAM applications [13,207]

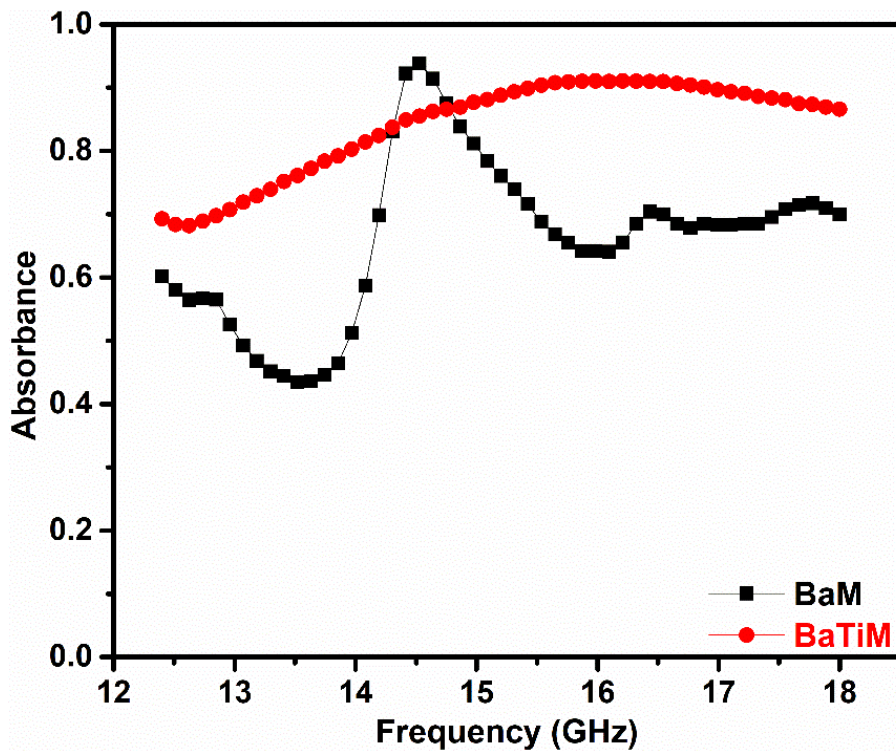


Fig. 4.30. Microwave absorbance vs frequency plot of BaM and BaTiM.

#### 4.2.3.3 Effect of La-Co substitution

La-Co substituted BaM samples were prepared by solid state ceramic method. To provide more insight, to their preferential site occupation, simultaneously substituted La-Co hexaferrites were studied and compared with individually substituted La and Co ions. Furthermore, screen printed thick films has been made with the best suitable materials.

##### i. X-ray diffraction studies

Fig. 4.31 (a & b) shows the X-ray diffraction patterns of pure and substituted BaM. All peaks correspond to  $P6_3/mmc$  space group (#00-007-0276 & #00-039-1433) without any impurity or residual  $Fe_2O_3$  phase except for samples BaCoM and BaLa<sub>0.15</sub>CoM.

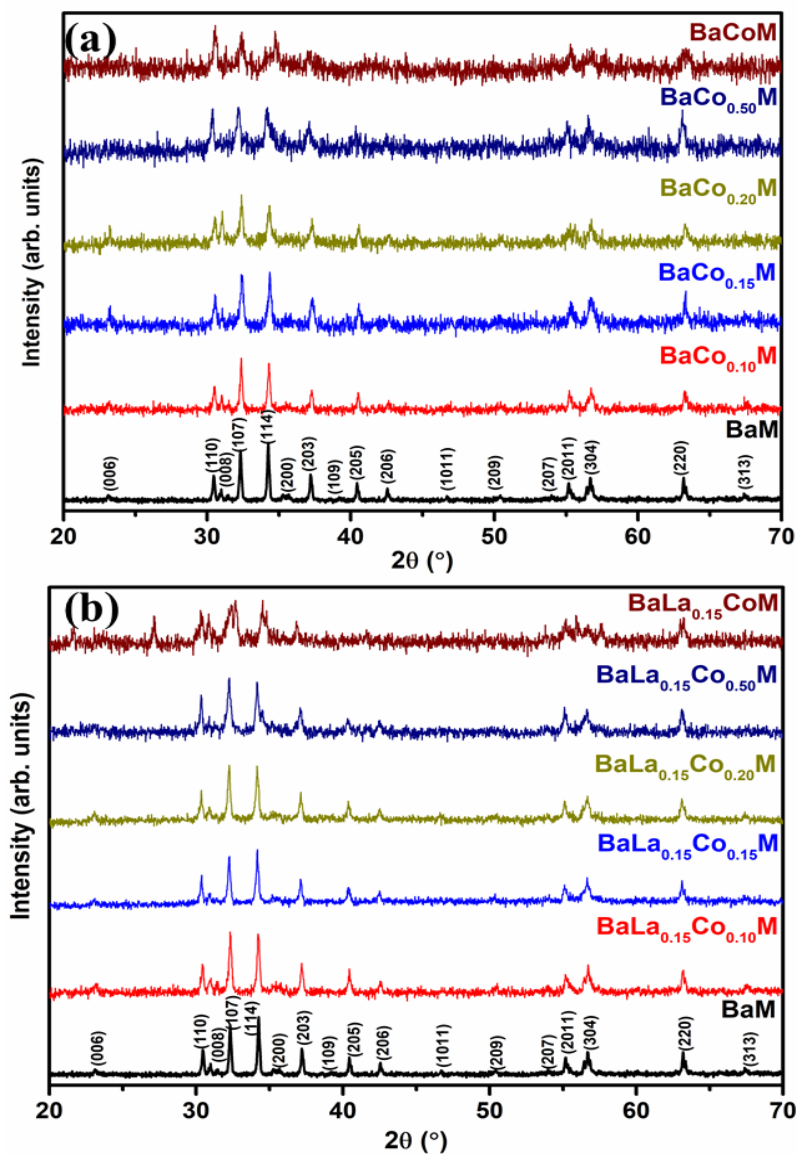
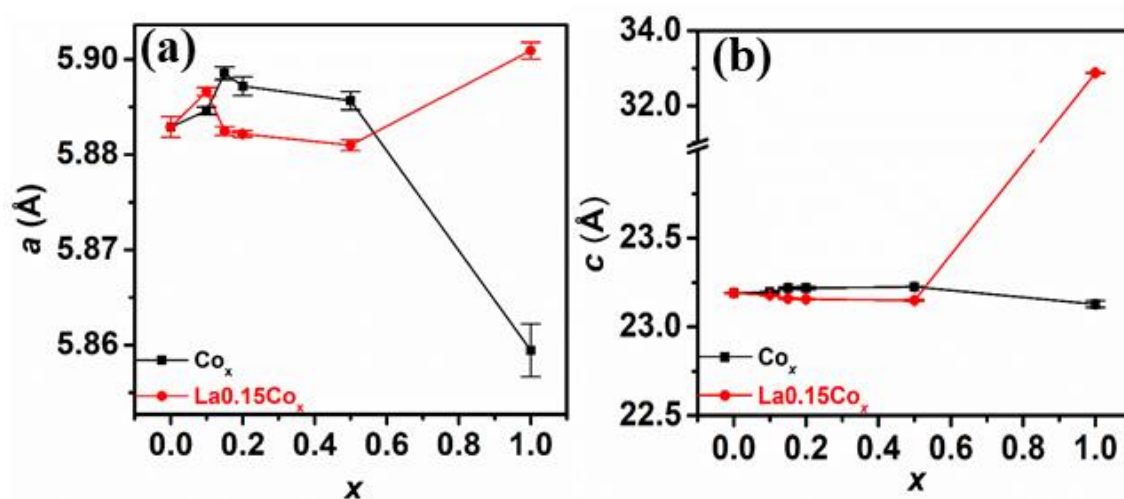


Fig. 4.31. XRD plot for pure and substituted barium hexaferrite.

Lattice parameters obtained from refinement are shown in fig. 4.32 (a & b). No noticeable variation has been observed in lattice constant 'a' except slight shrinkage in BaLa<sub>0.15</sub>M (5.88 Å) due to smaller ionic radii of La<sup>3+</sup> (1.16 Å) at dodecaoordination [208,209]. On other hand with Co<sup>2+</sup> ion substitution, c- axis was increased from 23.19 Å to 23.24 Å for BaCo<sub>0.5</sub>M due to its bigger ionic radii (0.72 Å) and/or oxygen deficiencies. Further increase in Co content (BaCoM), a slight reduction in lattice parameters are observed and traces of minor W-type phase are found. For La-Co co-substitution, the slight shrinkage in c- axis is observed, which suggests La<sup>3+</sup> ion is dominant over Co<sup>2+</sup> ion substitution. However, it is found that substitution of Co = 1.0 with La = 0.15, the M-type phase largely converted into W-type ferrite. The crystallite size for all samples lies in between 39 nm and 65 nm.



**Fig. 4.32.** Variation in lattice parameter for substituted BaM.

ii. *Fourier Transformer Infrared (FTIR) spectroscopy*

Fig. 4.33 shows the FTIR plots for pure and substituted BaM. Four well resolved band has been obtained among 30 IR active mode, as suggested in group theory [184]. The bands at 613 cm<sup>-1</sup> and 447 cm<sup>-1</sup> of A<sub>2u</sub> mode represent 4f<sub>1</sub> and 4f<sub>2</sub> sites.

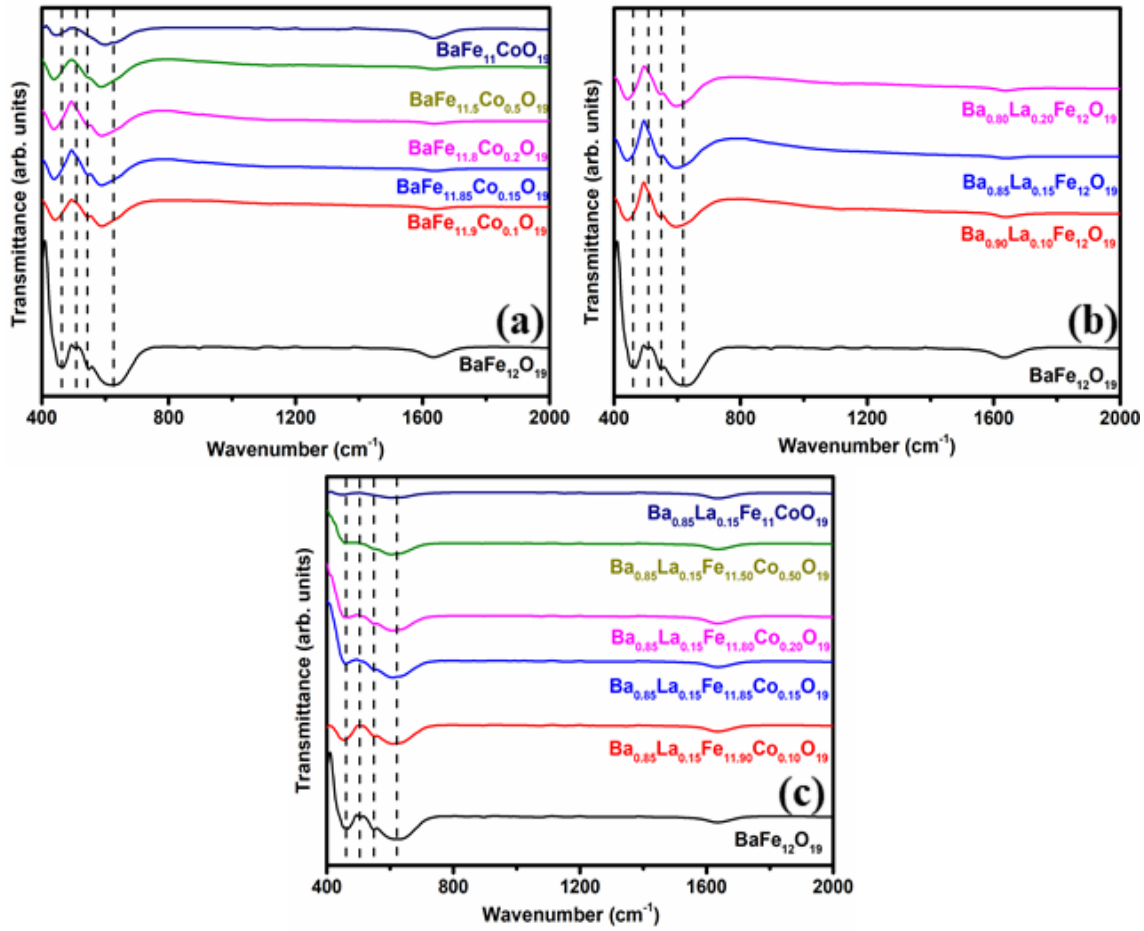


**Fig. 4.33.** FTIR spectrum of substituted BaM.

**Table 4.8.** FTIR modes and bond length of substituted BaM.

| Composition                               | Band 1<br>$cm^{-1}$ | K<br>$N/m$ | R<br>$\text{Å}$ | Band 2<br>$cm^{-1}$ | Band 3<br>$cm^{-1}$ | Band 4<br>$cm^{-1}$ | K<br>$N/m$ | R<br>$\text{Å}$ |
|---|---------------------|------------|-----------------|---------------------|---------------------|---------------------|------------|-----------------|
| BaM                                       | 447                 | 146.61     | 2.26            | 506                 | 544                 | 613                 | 275.72     | 1.83            |
| BaLa <sub>0.1</sub> M                     | 442                 | 143.35     | 2.28            | -                   | 545                 | 595                 | 259.77     | 1.87            |
| BaLa <sub>0.15</sub> M                    | 441                 | 142.70     | 2.28            | -                   | 546                 | 596                 | 260.64     | 1.87            |
| BaLa <sub>0.2</sub> M                     | 443                 | 144.00     | 2.28            | -                   | 547                 | 596                 | 260.64     | 1.87            |
| BaCo <sub>0.1</sub> M                     | 442                 | 143.35     | 2.28            | -                   | 546                 | 591                 | 256.28     | 1.88            |
| BaCo <sub>0.15</sub> M                    | 439                 | 141.41     | 2.29            | -                   | 541                 | 588                 | 253.69     | 1.89            |
| BaCo <sub>0.2</sub> M                     | 439                 | 141.41     | 2.29            | -                   | 547                 | 588                 | 253.69     | 1.89            |
| BaCo <sub>0.5</sub> M                     | 439                 | 141.41     | 2.29            | -                   | -                   | 587                 | 252.83     | 1.89            |
| BaCoM                                     | 446                 | 145.95     | 2.27            | 497                 | -                   | 600                 | 264.15     | 1.86            |
| BaLa <sub>0.15</sub> Co <sub>0.1</sub> M  | 453                 | 150.57     | 2.24            | 507                 | 551                 | 609                 | 272.13     | 1.84            |
| BaLa <sub>0.15</sub> Co <sub>0.15</sub> M | 459                 | 154.59     | 2.22            | 508                 | 551                 | 610                 | 273.03     | 1.84            |
| BaLa <sub>0.15</sub> Co <sub>0.2</sub> M  | 467                 | 160.02     | 2.20            | 508                 | 551                 | 608                 | 271.24     | 1.84            |
| BaLa <sub>0.15</sub> Co <sub>0.5</sub> M  | 471,<br>486         | 162.78     | 2.19            | -                   | -                   | 604,<br>626         | 267.68     | 1.85            |
| BaLa <sub>0.15</sub> CoM                  | 444,<br>455         | 167.42     | 2.27            | -                   | -                   | 602,<br>633         | 265.91     | 1.86            |

La and Co substitution found to decrease the force constant (K) and increase the bond length (R) (Table. 4.8). The decrease in the force constant may be ascribed to oxygen deficiency and/or presence of Fe<sup>2+</sup> and Co<sup>2+</sup> ions. On contrary, La-Co co-substitution shows an increase in force constant and decrease in bond length. The result suggests that La and Co are substituted in BaM and effect of La<sup>3+</sup> ions dominated in the crystal structure over Co<sup>2+</sup> ion substitution as supported from X-ray studies. Further to confirm FTIR results, Raman modes were analyzed.

iii. *Raman Spectroscopy*

Fig. 4.34 shows micro Raman spectra of substituted BaM, where peak represents the various bands suggested in group theory [184]. Peak parameters obtained by 12 Lorentzian fit (Representative spectra shown in fig. 4.35) are given in table 4.9. A doublet at 171 cm<sup>-1</sup> and 183 cm<sup>-1</sup> of E<sub>1g</sub> band are associated with whole spinel block. The peak 171 cm<sup>-1</sup> is unaltered with substitution, which shows that the overall effective mass of spinel co-ordinate is comparable due to nearly similar atomic weight of Fe (55.8 g/mol) and Co (58.9 g/mol) ions in Co and La-Co substituted samples. In BaLaM, La<sup>3+</sup> ion substitute Ba<sup>2+</sup> ion in R block, hence its effect in spinel block was negligible. The peak at 183 cm<sup>-1</sup> is more sensitive to localized molecular vibration in spinel block. The presence of Co<sup>2+</sup> ions at 2a site distorts local vibration and causes a slight red shift in BaCo<sub>0.15</sub>M substitution [204]. It is noted, the shifted peak is almost constant with increasing the Co concentration, which suggests no further substitution has occurred beyond BaCo<sub>0.15</sub>M. However, no such shift was noticed in La, and La-Co substituted BaM. Peaks at 315, 615, 683 and 719 cm<sup>-1</sup> represent A<sub>1g</sub> bands of 2a, 4f<sub>2</sub>, 2b and 4f<sub>1</sub> sites, respectively. The peak position at 337 cm<sup>-1</sup> denotes E<sub>2g</sub> band of 12k site, whereas peak 411 cm<sup>-1</sup> represents A<sub>1g</sub> band of mixed 12k and 2a sites. Further, peaks at 212, 285, 468 and 522 cm<sup>-1</sup> represent spinel co-ordinates of different crystallographic sites.

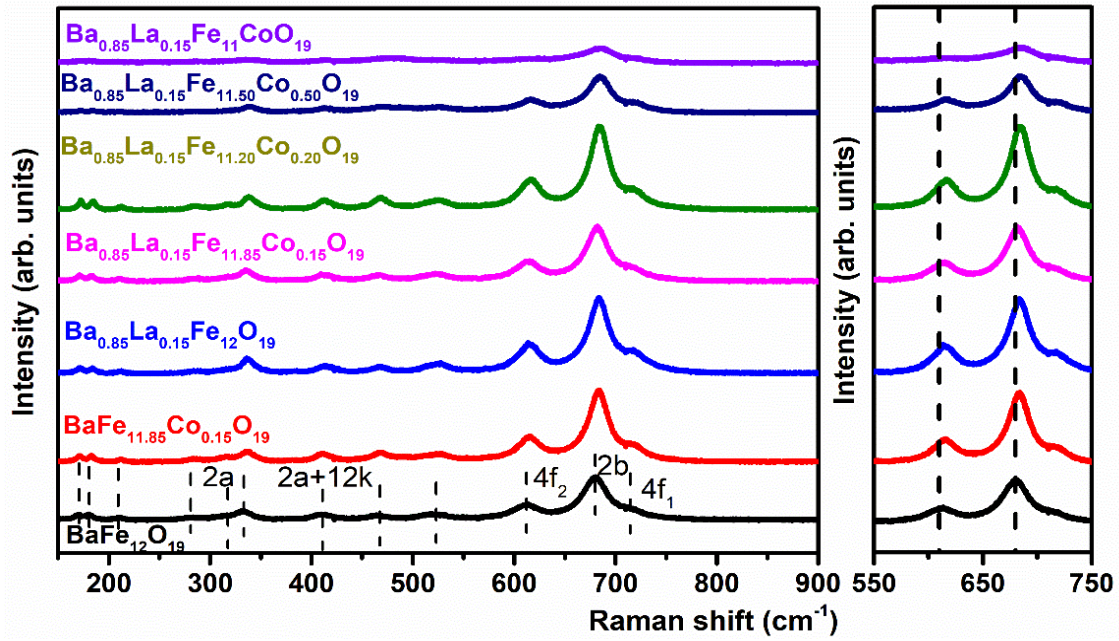


Fig. 4.34. Raman spectra for substituted BaM

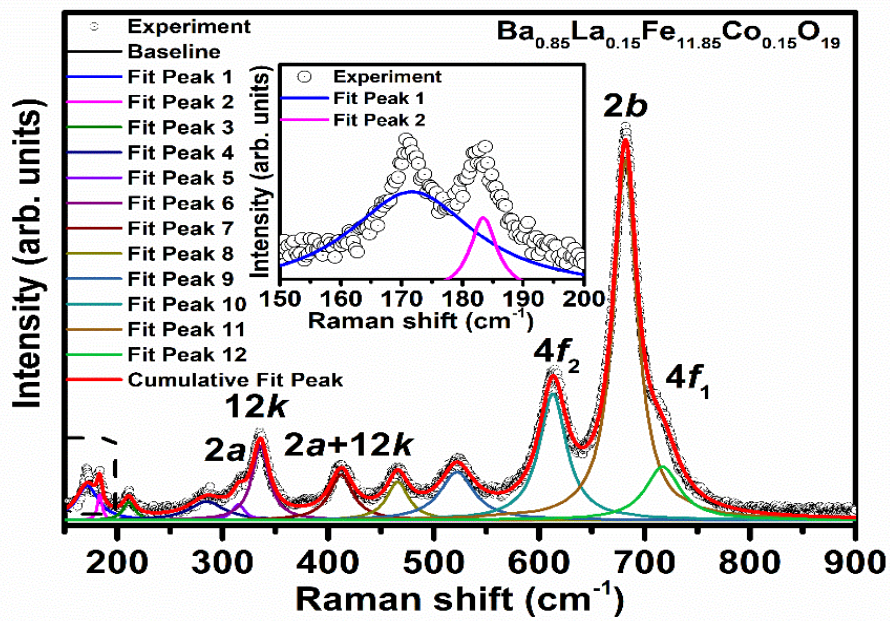


Fig. 4.35. Representative deconvoluted Raman spectra for substituted barium hexaferrite.

**Table 4.9.** Raman data for substituted BaM.

| Site<br>Sample                            | spinel blocks   | spinel blocks   | --              | --              | 2a              | 12k             | 12k+2a          | --              | --              | 4f <sub>2</sub> | 2b              | 4f <sub>1</sub> |
|---|-----------------|-----------------|-----------------|-----------------|-----------------|-----------------|-----------------|-----------------|-----------------|-----------------|-----------------|-----------------|
|   | E <sub>1g</sub> | E <sub>1g</sub> | E <sub>1g</sub> | E <sub>1g</sub> | A <sub>1g</sub> | E <sub>2g</sub> | A <sub>1g</sub> | A <sub>1g</sub> | E <sub>2g</sub> | A <sub>1g</sub> | A <sub>1g</sub> | A <sub>1g</sub> |
| Wavenumber (cm <sup>-1</sup> )            |                 |                 |                 |                 |                 |                 |                 |                 |                 |                 |                 |                 |
| BaM                                       | 171.11          | 183.09          | 211.74          | 284.57          | 314.83          | 336.84          | 411.39          | 468.13          | 521.69          | 614.94          | 683.27          | 719.35          |
| BaLa <sub>0.15</sub> M                    | 171.24          | 184.25          | 211.53          | 285.38          | 312.97          | 337.39          | 414             | 467.15          | 523.81          | 614.65          | 683.54          | 719.66          |
| BaCo <sub>0.15</sub> M                    | 170.02          | 181.08          | 209.82          | 281.73          | 313.01          | 333.02          | 410.2           | 464.6           | 519.9           | 611.29          | 679.89          | 716.09          |
| BaCo <sub>0.5</sub> M                     | 170.21          | 181.13          | 209.84          | 283.85          | 314.79          | 335.58          | 411.34          | 468             | 520.96          | 614.14          | 682.34          | 718.75          |
| BaCoM                                     | 169.42          | 181.63          | 204.83          | 286.09          | -               | 333.23          | -               | -               | -               | 580.83          | 680.38          | 718.39          |
| BaLa <sub>0.15</sub> Co <sub>0.1</sub> M  | 172.25          | 183.8           | 212.82          | 286.14          | 316.74          | 340             | 417.27          | 469.35          | 524.96          | 616.84          | 685.42          | 719.16          |
| BaLa <sub>0.15</sub> Co <sub>0.15</sub> M | 171.07          | 183.25          | 210.67          | 283.91          | 315.38          | 335.93          | 412.58          | 466.04          | 522.02          | 613.12          | 681.87          | 717.19          |
| BaLa <sub>0.15</sub> Co <sub>0.20</sub> M | 172.2           | 184.47          | 212.11          | 285.86          | 315.97          | 338.88          | 413.28          | 468.09          | 523.51          | 615.6           | 684.16          | 719.78          |
| BaLa <sub>0.15</sub> Co <sub>0.50</sub> M | 171.73          | 184.41          | 210.27          | 286.61          | 317.13          | 339.25          | 414.2           | 469.52          | 525.18          | 616.13          | 684.43          | 719.76          |
| BaLa <sub>0.15</sub> CoM                  | 172.43          | 182.12          | 207.4           | 284.39          | -               | 339.52          | 414.42          | 447.67          | 526.25          | 617.86          | 685.25          | 721.03          |

iv. *Mössbauer Studies*

RT Mössbauer spectra were obtained for substituted BaM samples and fitted with five discrete sextets corresponded to different crystallographic sites. For BaM and BaLa<sub>0.15</sub>M sub-spectral area ratio were constrained to 6:2:2:1:1, and kept free for remaining samples. Representative fitted Mössbauer spectra for BaM and BaLa<sub>0.15</sub>Co<sub>0.15</sub>M are shown in fig. 4.36. The fitted parameter, *i.e.*, line width ( $\Gamma$ ), isomer shift ( $\delta$ ), quadrupolar shift ( $QS$ ), hyperfine field ( $B_{hf}$ ) and relative sub-spectral area ( $S$ ) are given in table 4.10.

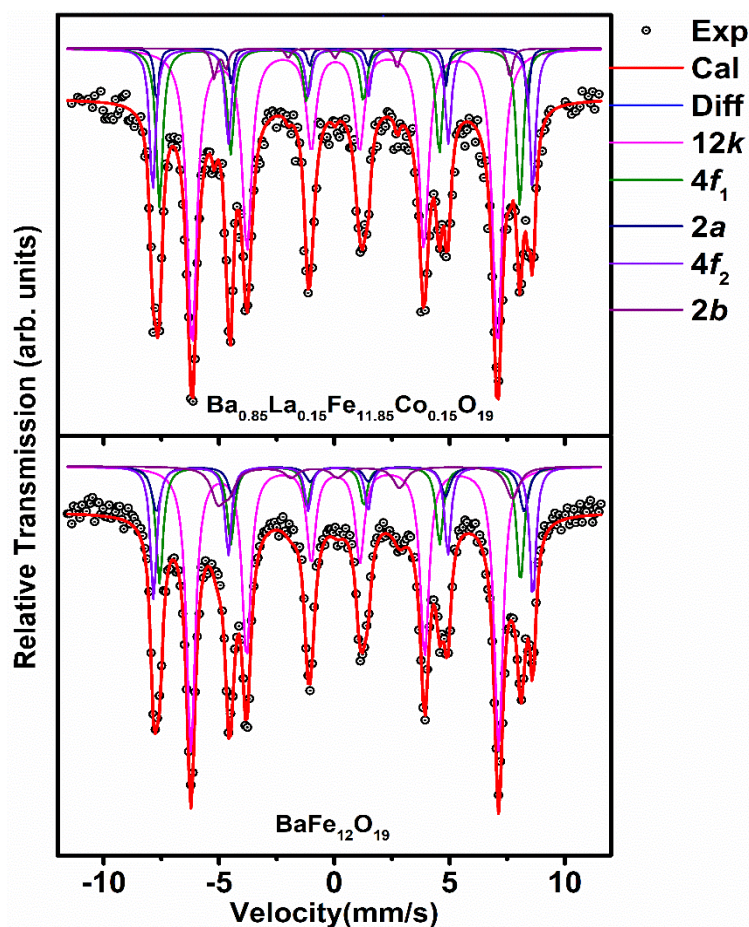


**Fig. 4.36.** Representative deconvoluted Mössbauer spectra of pure and substituted BaM.

The  $\delta$  at  $2b$  site was mostly affected irrespective of substitution with the lowest value of 0.13 mm/s for BaLa<sub>0.15</sub>Co<sub>0.15</sub>M. The change in  $\delta$  with a corresponding decrease in the sub-spectral area suggest that Co<sup>2+</sup> ion is occupying  $2b$  site. In general, this site is highly distorted and have close interaction with Ba<sup>2+</sup> ions, hence, the substitution of La<sup>3+</sup> ion will reduce  $\delta$  and  $QS$  significantly due to change in chemical environment [210,211]. It is noted in BaCo<sub>0.15</sub>M and BaLa<sub>0.15</sub>Co<sub>0.15</sub>M,  $2a$  site shows a negligible variation in  $\delta$  irrespective of cobalt presence [212]. Fig. 4.37 shows the calculated occupation number ( $N_{Fe}(i)$ ) and

vacancy fraction ( $F(i)$ ) of Fe ions for all five crystallographic sites. The  $N_{Fe}(i)$  and  $F(i)$  were determined by following relation:

$$N_{Fe}(i) = C_{Fe} \left[ \frac{S(i)}{\sum_{i=1}^5 S(i)} \right] \quad (4.12)$$

$$F(i) = \frac{N(i) - N_{Fe}(i)}{N(i)} \times 100 \% \quad (4.13)$$

where,  $C_{Fe}$  denotes the Fe content,  $S(i)$  and  $N(i)$  are the sub-spectral area and occupation number, respectively, for the  $i^{th}$  site [44]. For BaCoM,  $F(i)$  at  $2a$  and  $2b$  sites increases to 85% and 60% respectively, which confirms Co substitution. The La-Co substitution shows a marginal increase in  $F(i)$  at  $4f_2$  site. This change may ascribe to conversion of  $Fe^{3+}$  to  $Fe^{2+}$  or  $Co^{2+}$  ions occupation [213]. Since La-Co substitution itself can compensate the charge variation, hence an observed  $F(i)$  may ascribed to  $Co^{2+}$  ion occupation, as supported by decrease in  $B_{hf}$  (51.68 to 50.09 T) and previous reported studies [147,151,214]. No measurable changes in hyperfine parameters for  $12k$  and  $4f_1$  sites with substitution are observed.

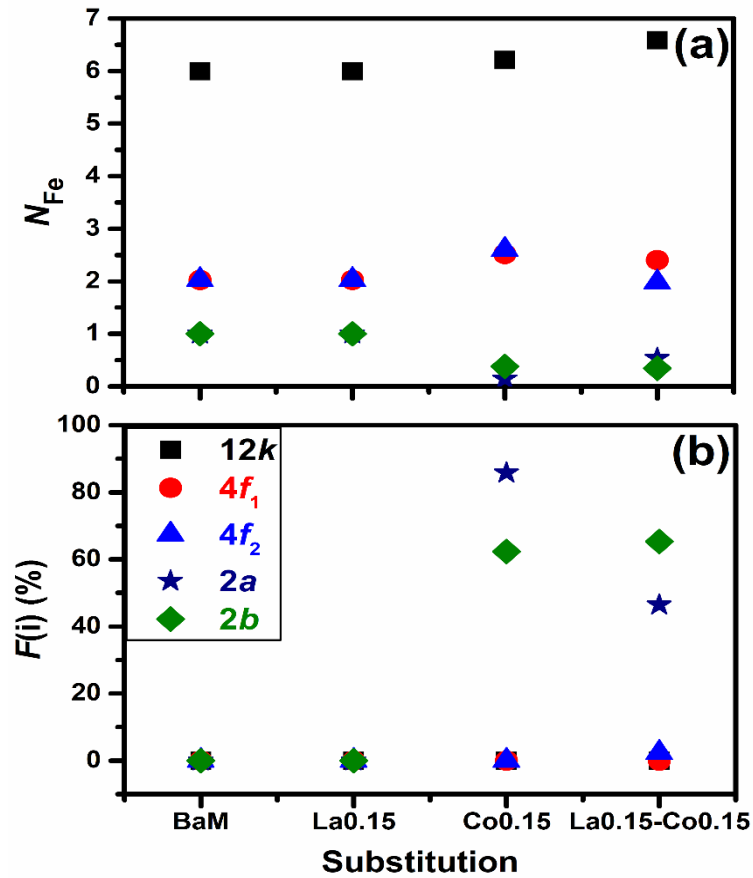


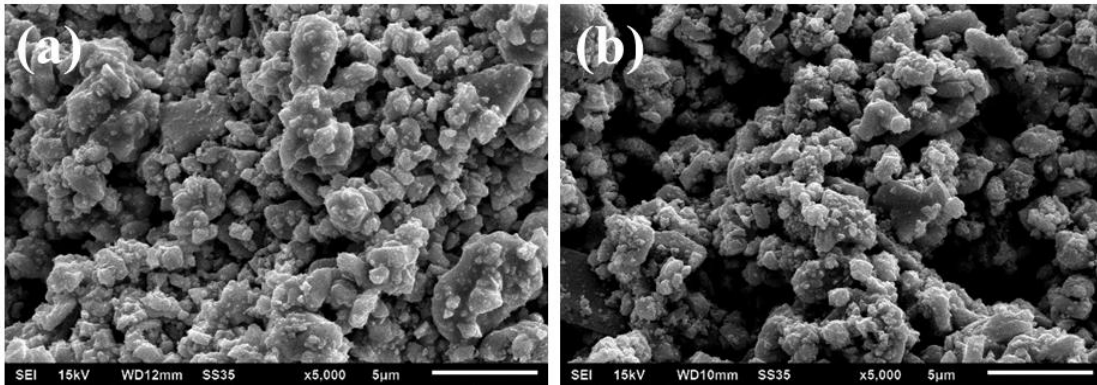
**Fig. 4.37.** Variation in (a) site occupation number ( $N_{Fe}$ ) and (b) vacancy fraction of Fe (i) (%) ions at different sites.

**Table 4.10.** Hyperfine parameters of substituted BaM powders.

| Sites           | Substitution                              | $WID$<br>(mm/s) | $IS$<br>(mm/s) | $QS$<br>(mm/s) | $B_{hf}$<br>(T) | $S$<br>(%) |
|-----------------|---|-----------------|----------------|----------------|-----------------|------------|
| 12k             | BaM                                       | 0.36            | 0.25           | 0.40           | 41.35           | 50.0       |
|                 | BaCo <sub>0.15</sub> M                    | 0.48            | 0.26           | 0.41           | 41.10           | 52.41      |
|                 | BaLa <sub>0.15</sub> M                    | 0.46            | 0.26           | 0.40           | 41.37           | 50.0       |
|                 | BaLa <sub>0.15</sub> Co <sub>0.15</sub> M | 0.51            | 0.25           | 0.41           | 41.10           | 55.56      |
| 4f <sub>1</sub> | BaM                                       | 0.27            | 0.17           | 0.22           | 49.05           | 16.66      |
|                 | BaCo <sub>0.15</sub> M                    | 0.45            | 0.17           | 0.21           | 48.56           | 21.25      |
|                 | BaLa <sub>0.15</sub> M                    | 0.37            | 0.15           | 0.21           | 48.53           | 16.66      |
|                 | BaLa <sub>0.15</sub> Co <sub>0.15</sub> M | 0.35            | 0.13           | 0.20           | 48.47           | 20.28      |
| 2a              | BaM                                       | 0.20            | 0.26           | 0.08           | 50.42           | 8.33       |
|                 | BaCo <sub>0.15</sub> M                    | 0.11            | 0.26           | 0.06           | 49.70           | 1.20       |
|                 | BaLa <sub>0.15</sub> M                    | 0.48            | 0.24           | 0.05           | 49.46           | 8.33       |
|                 | BaLa <sub>0.15</sub> Co <sub>0.15</sub> M | 0.22            | 0.27           | 0.14           | 49.87           | 4.52       |
| 4f <sub>2</sub> | BaM                                       | 0.23            | 0.27           | 0.15           | 51.68           | 16.66      |
|                 | BaCo <sub>0.15</sub> M                    | 0.37            | 0.28           | 0.17           | 50.96           | 21.96      |
|                 | BaLa <sub>0.15</sub> M                    | 0.33            | 0.28           | 0.23           | 51.01           | 16.66      |
|                 | BaLa <sub>0.15</sub> Co <sub>0.15</sub> M | 0.32            | 0.27           | 0.19           | 50.09           | 16.71      |
| 2b              | BaM                                       | 0.54            | 0.30           | 2.35           | 39.97           | 8.33       |
|                 | BaCo <sub>0.15</sub> M                    | 0.26            | 0.23           | 2.33           | 40.09           | 3.18       |
|                 | BaLa <sub>0.15</sub> M                    | 0.68            | 0.26           | 2.21           | 39.62           | 8.33       |
|                 | BaLa <sub>0.15</sub> Co <sub>0.15</sub> M | 0.27            | 0.12           | 2.19           | 39.77           | 2.93       |

v. *Microstructural Study*

Fig. 4.38 shows SEM micrograph of BaM and BaLa<sub>0.15</sub>Co<sub>0.15</sub>M calcined powders. Identical morphology is observed with average particle size of ~2.5  $\mu$ m and ~2  $\mu$ m for BaM and BaLa<sub>0.15</sub>Co<sub>0.15</sub>M respectively

**Fig. 4.38.** SEM micrographs of (a) BaM and (b) BaLa<sub>0.15</sub>Co<sub>0.15</sub>M

vi. *Magnetic Studies*

Fig. 4.39 (a) shows the  $M$ - $H$  behaviour of substituted BaM powders. The obtained magnetic parameters are given in table 4.11. The magnetic properties are an interplay of Fe ion at different crystallographic sites and their exchange interaction. In complex oxide, superexchange interaction occurs through oxygen ions; hence its vacancy significantly affects exchange interactions. It is noted that  $\text{Co}^{2+}$  substitution decreases  $M$  from 53 to 51 emu/g, which is due to presence of lower magnetic moment  $\text{Co}^{2+}$  ( $3.6 \mu_B$ ) ions in spin up sites and/or  $\text{O}^{2-}$  deficiencies. Whereas,  $\text{BaLa}_{0.15}\text{M}$  and  $\text{BaLa}_{0.15}\text{Co}_{0.15}\text{M}$  showed a considerable increase in  $M$  up to 55 emu/g due to existence of  $\text{Fe}^{2+}/\text{Co}^{2+}$  in antiparallel  $4f_2$  site as evident by Mössbauer studies.  $H_c$  decreases from 1.38 to 1.12 kOe for  $\text{BaLa}_{0.15}\text{M}$  and further 1.02 kOe for  $\text{BaCo}_{0.15}\text{M}$ . It was reported that  $H_c$  primarily depended upon magnetocrystalline anisotropy and structural parameters, *i.e.*, crystallite size, particle size and its shape [215]. The  $H_a$  of polycrystalline powders is significantly less than single crystal due to their random orientation. Nevertheless, its variation provides a suggestive to  $H_a$ . It is clear from table 4.11 that  $H_a$  is lower for all substituted powders. For  $\text{BaCoM}$ , the reduction in  $H_a$  is due to Co occupation, which reduces the collinearity along  $c$ -axis [216]. It is to be noted that a decrease in  $H_{ci}$  with La substitution is less compared to Co substitution, despite a higher reduction in  $H_a$ . The effect may be ascribed to smaller crystallite size of  $\text{BaLa}_{0.15}\text{M}$ .  $H_a$  for  $\text{BaLa}_{0.15}\text{Co}_{0.15}\text{M}$  is decreased due to a perturbation in  $2a$  site as evident from increase in  $QS$ . The  $QS$  for  $2b$  site decreased to 2.19 mm/s from 2.35 mm/s (Table. 4.10). Fe located at the  $2b$  site contributes to quadrupole splitting most, therefore, to  $H_a$ . However, in the present study  $H_a$  of polycrystalline powder found to be low; hence a marginal increase in  $H_{ci}$  dominate by particle size as evident from fig. 4.38 [32,217].

Further, to understand the exchange interaction quantitatively,  $T_c$  of all substituted powders were determined, as shown in fig. 4.39 (b). For  $\text{BaLa}_{0.15}\text{M}$ ,  $T_c$  increase from 497 to 507 °C due to overall lattice reduction, which enhances the superexchange coupling in a hexagonal crystal. However, the substitution of cobalt in BaM and  $\text{BaLa}_{0.15}\text{M}$  decreases  $T_c$  to 437 °C. The result suggests that  $\text{Co}^{2+}$  ion plays a significant role in deciding  $T_c$ . The decrease in  $T_c$  may ascribe to two reasons. First, valance state of  $\text{Fe}^{3+}$  and  $\text{Co}^{2+}$  weakens superexchange interaction due to different electronegativity [218]. Second,  $\text{Co}^{2+}$  substitution creates oxygen vacancies, which also changes the oxidation degree of 3d- metal cations. The changing of charge state as a consequence of oxygen vacancy will significantly

affect the magnetic properties such as  $T_c$  [219,220].  $M$ - $H$  behaviour of  $\text{BaLa}_{0.15}\text{Co}_{0.15}\text{M}$  at  $T_c$  (inset Fig. 4.39 (a)) confirms the paramagnetic nature.

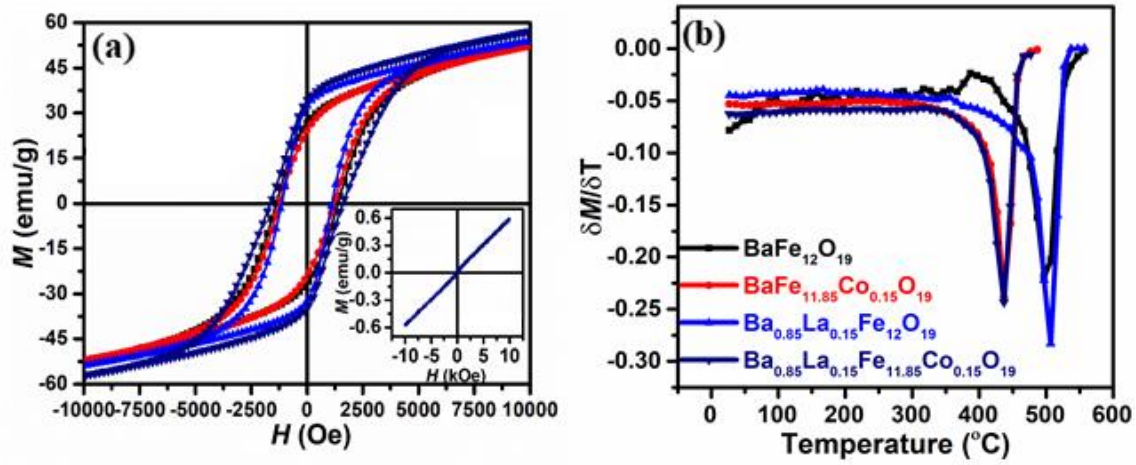


**Fig. 4.39.** (a)  $M$ - $H$  plots and (b)  $\delta M/\delta T$  vs temperature plot for substituted barium hexaferrite. Inset (a) shows  $M$ - $H$  plot for  $\text{BaLa}_{0.15}\text{Co}_{0.15}\text{M}$  at  $T_c = 437^\circ\text{C}$ .

**Table 4.11.** Magnetic parameter of substituted BaM.

| Sample                                       | $M_s$<br>emu/g | $H_c$<br>kOe | $M_r$<br>emu/g | $H_a$<br>kOe | SQ   | $T_c$<br>$^\circ\text{C}$ |
|--|----------------|--------------|----------------|--------------|------|---------------------------|
| BaM  | 52.61          | 1.38         | 26.56          | 9.46         | 0.50 | 497                       |
| $\text{BaCo}_{0.15}\text{M}$                 | 51.94          | 1.02         | 23.91          | 8.96         | 0.46 | 437                       |
| $\text{BaLa}_{0.15}\text{M}$                 | 53.60          | 1.12         | 32.19          | 8.51         | 0.60 | 507                       |
| $\text{BaLa}_{0.15}\text{Co}_{0.15}\text{M}$ | 54.28          | 1.49         | 34.22          | 8.59         | 0.63 | 437                       |

vii. *Magnetic studies of La-Co substituted BaM thick film*

Fig. 4.40 shows La-Co substituted BaM thick films. Isotropic magnetic properties were found irrespective of substitution. A marginal reduction in magnetic properties was due to  $\text{Bi}_2\text{O}_3$  additive.

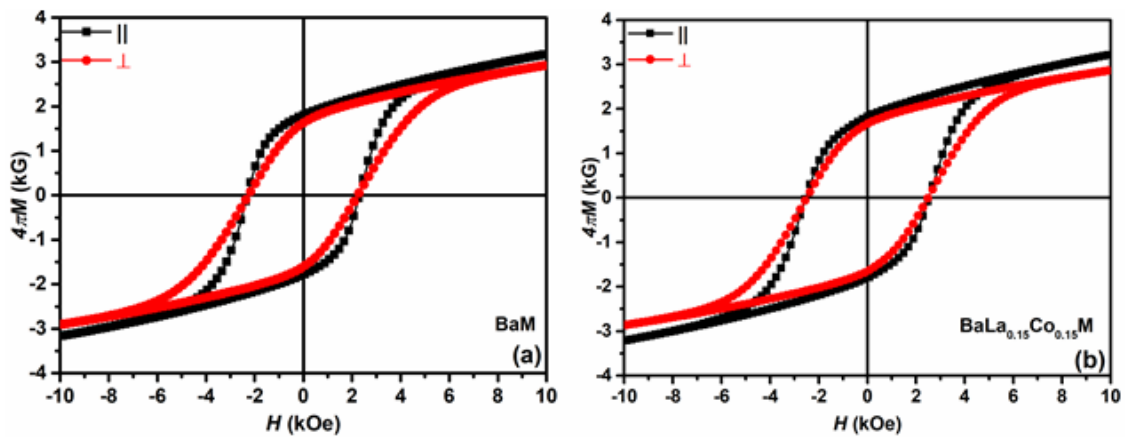


**Fig.4.40.**  $M$ - $H$  plots of pure and La-Co substituted BaM films.

## viii. Microwave absorbance

Fig. 4.41 shows  $A(\omega)$  plot for pure and substituted BaM sintered magnets. Multiple absorbance peaks were obtained for pure BaM at 13.86, 15.2 and 16.21 GHz. Fig 4.41 (a) illustrates the effect of Co substitution on  $A(\omega)$ , which shows wave-like nature as of pure BaM. However, the oscillation was compressed, and overall  $A(\omega)$  was improved for BaCo<sub>0.15</sub>M sample. BaCoM shows three visible peaks at 12.96, 15.53 and 16.66 GHz. The marginal shift from BaM ascribed to the presence of small secondary phase. Fig. 4.41 (b) shows  $A(\omega)$  plots La and La-Co co-substituted BaM magnets. The oscillatory behaviour was suppressed, and overall  $A(\omega)$  was improved for all samples. BaLa<sub>0.15</sub>Co<sub>0.20</sub>M shows 90 % absorbance at 16.4 GHz.

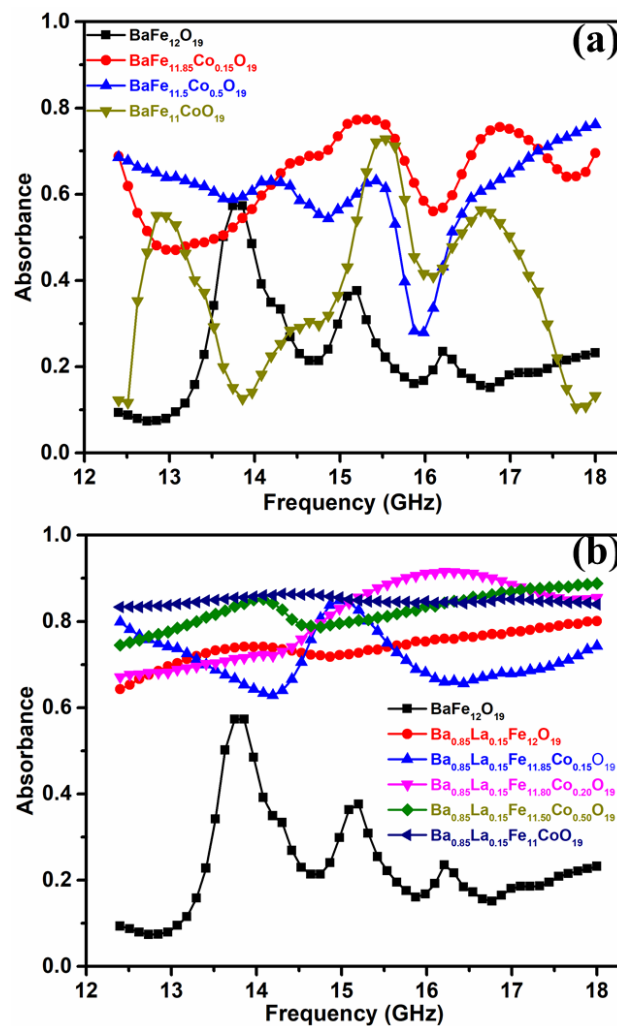


**Fig. 4.41.** Microwave absorbance vs frequency plots of substituted BaM.

## *Chapter 5*

### *Results and Discussion - II*

---

---

#### **Overview**

In this chapter, screen printed anisotropic thick films are prepared from the BaM powders milled for different duration of time. The effect of ball mill time on structural and magnetic properties of powder and microwave sintered BaM thick films are discussed.

---

---

## 5.1 Development of anisotropic thick films

From the preceding studies on BaM thick films shows that all films were isotropic and in-plane  $4\pi M$  was higher than the out of plane. The similar kind of effect has been observed in substituted thick films. Therefore, in the present chapter, an attempt has been made to develop thick films with perpendicular anisotropy. To accomplish this, BaM powders with different particle size distribution were made by high energy ball milling (HEBM), for different duration of time. HEBM is one of the effective way to induce size variation in ceramic powders. As-milled powders were screen printed on  $\text{Al}_2\text{O}_3$  substrates coated with thin melt quenched  $\text{Bi}_2\text{O}_3$  layer for better adhesion. The perpendicular orientation in the films was induced by an external magnetic field of 0.8 T. Compared to deposition of BaM buffer layer, the melt quenched  $\text{Bi}_2\text{O}_3$  layer provides ease of processing. Moreover, oriented films sintered with BaM buffer layer have given poor scrambled morphology.

## 5.2 Studies on high energy milled powders

### *i. X-ray diffraction studies*

Fig 5.1 shows the X-ray diffraction pattern of 0h, 6h, 12h, 24h, 48h and 72h milled BaM powders. It is clear from the figure that peak intensity is reducing with ball mill time which suggests that excessive milling cause amorphous and disorder state of the powders. No significant shift in characteristic peaks position are observed. Fig 5.2 shows FWHM of (107) peak and average crystallite size variation for milled samples. An obvious decrease in crystallite size is observed with milling time. The minimum crystallite size of 14 nm was obtained for 48h milled powder, which remained constant up to 72h milling. The interpretation suggests that the extended hours of milling may fragment the BaM particles and reduce crystallite size which are responsible for broadening in the diffraction peaks.

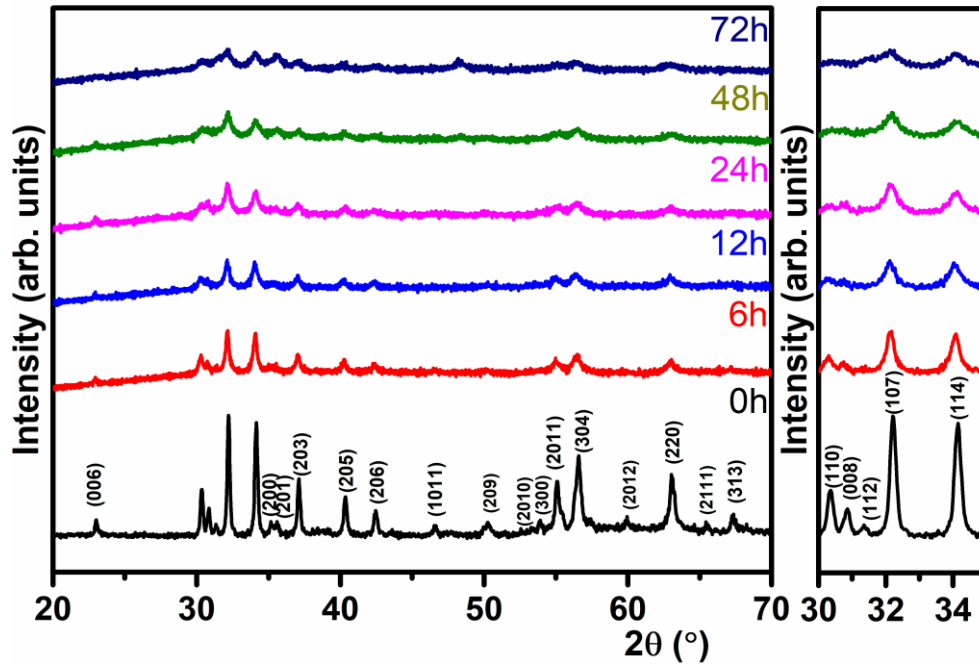


Fig. 5.1. X-ray diffraction patterns for BaM powder milled for different time.

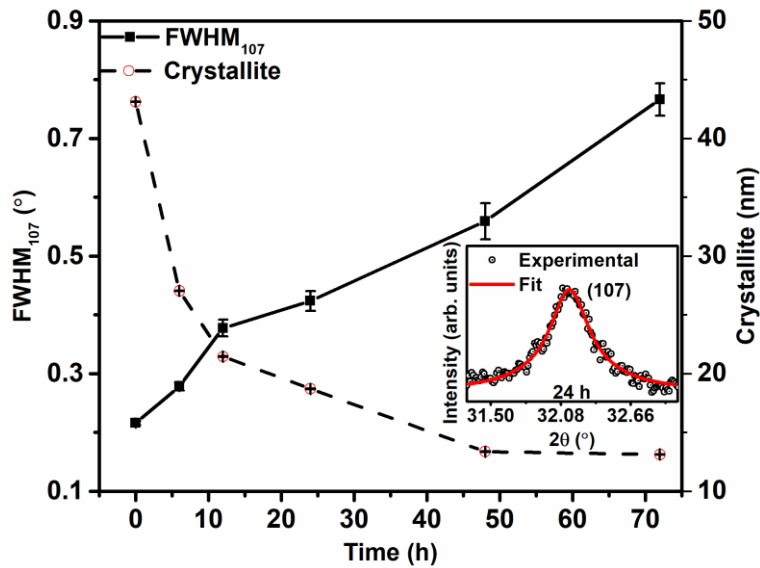
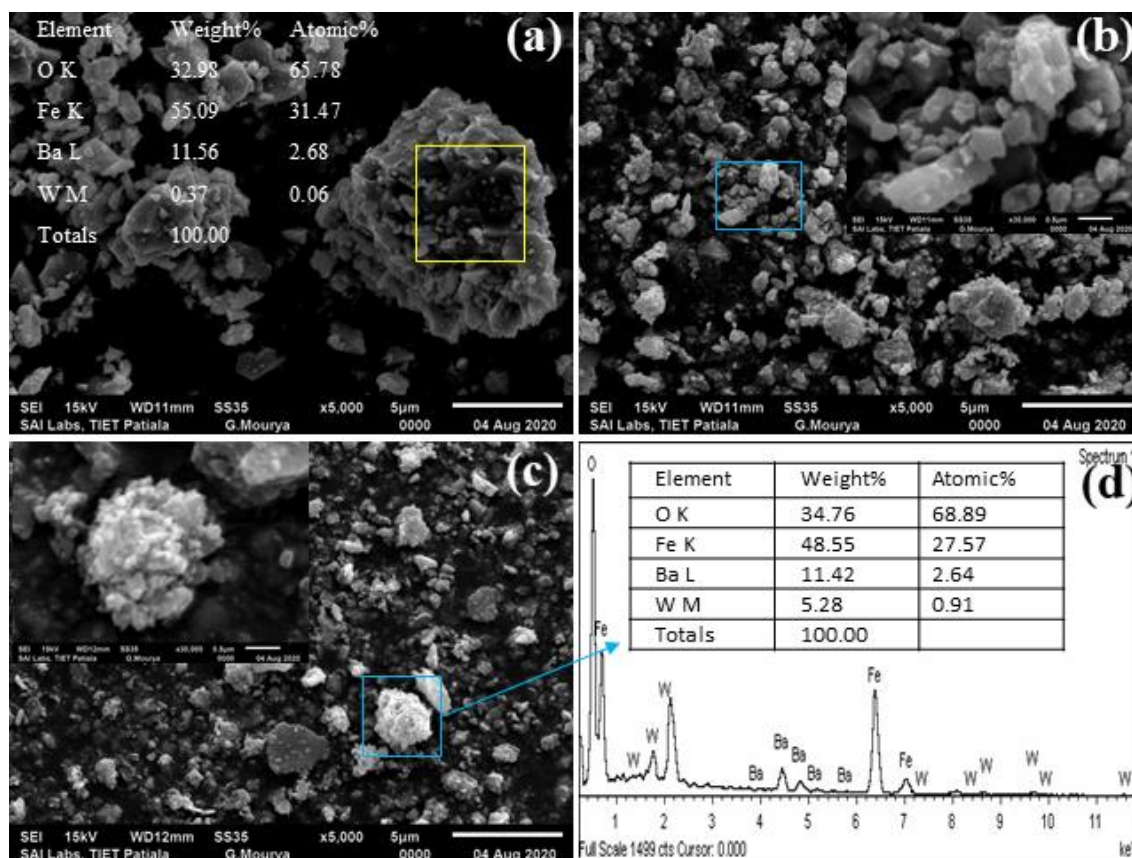


Fig. 5.2. Variation in FWHM and crystallite size with milling time.

ii. *Microstructural Study*

Fig. 5.3 shows the representative SEM micrographs for BaM powders and its corresponding energy dispersive spectroscopy (EDS). Clusters up to 10  $\mu\text{m}$  are seen for unmilled powder whereas, agglomerated sub-micron ranged particle are observed in 12h and 72h milled powders. Inset fig. 5.10 (b & c) shows enlarged view of agglomerated particles. The EDS spectrum shows that tungsten carbide contamination is increasing with

milling time. Prolonged hour of ball milling causes abrasion of milling media and contaminate the powder.



**Fig. 5.3.** SEM micrographs of (a) 0h (b) 12h, (c) 72h ball-milled powder (d) EDS of 72h milled powder. Inset (b & c) shows the agglomerated particles.

### iii. Magnetic Studies

Fig 5.4 shows room temperature  $M-H$  plots for milled BaM powder. It is clear from the figure that magnetization ( $M$ ) and retentivity ( $M_r$ ) decreases with milling times. The decrease in  $M$  is due to amorphization of the crystallite surface and the contamination by milling media [221].  $H_c$  of the powders initially increase up to 12h milling and then decreases.  $H_c$  is primarily dominated by intrinsic ( $H_a$  and substitution) and extrinsic (crystallite size and shape) factors. The initial increase is due to particle size reduction above which crystallinity of the powder decrease and hence the  $H_c$ [222]. It is found that  $H_a$  decreases irrespective of  $H_c$ . The magnetic properties are given in table 5.1.

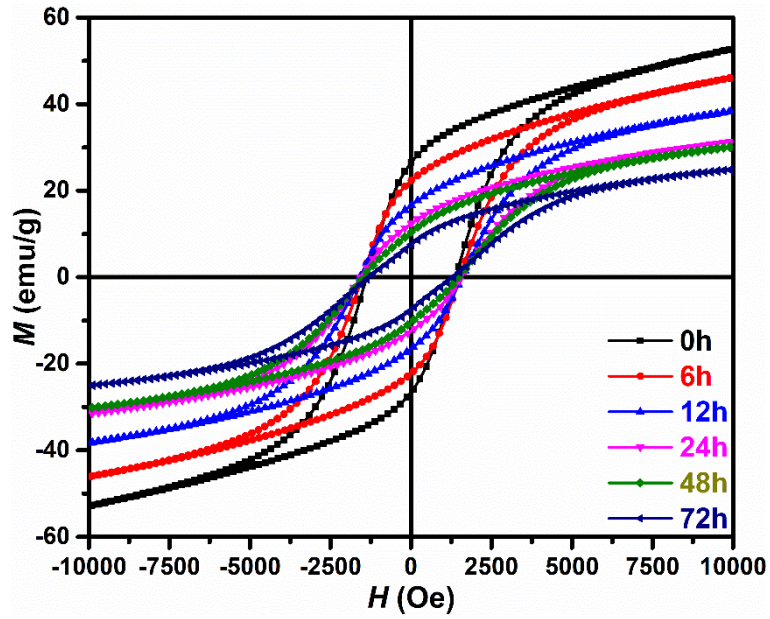


Fig. 5.4.  $M$ - $H$  plots for BaM powder with different milling time

Table 5.1. Magnetic properties of ball-milled powders.

| Sample | $M$<br>$emu/g$ | $M_r$<br>$emu/g$ | $SQ$ | $H_c$<br>$kOe$ | $H_a$<br>$kOe$ | $K_1 \times 10^6$<br>$erg/cm^3$ |
|--------|----------------|------------------|------|----------------|----------------|---------------------------------|
| 0h     | 52.61          | 26.72            | 0.51 | 1.38           | 8.94           | 1.24                            |
| 6h     | 45.99          | 22.25            | 0.48 | 1.52           | 8.45           | 1.03                            |
| 12h    | 38.26          | 16.58            | 0.43 | 1.58           | 7.75           | 0.78                            |
| 24h    | 31.38          | 12.37            | 0.39 | 1.57           | 7.05           | 0.58                            |
| 48h    | 30.16          | 10.39            | 0.34 | 1.49           | 6.99           | 0.56                            |
| 72h    | 24.94          | 7.47             | 0.30 | 1.30           | 6.38           | 0.42                            |

### 5.3 Studies on BaM thick film

As mentioned, screen printed films were made by milled powders and dried under the field of 0.8 T. The dried films were microwave sintered at 1200 °C for 20 minutes. After studies the sintering time and temperature (not shown), the sintering conditions for the films are chosen.

#### i. X-ray diffraction studies

Fig. 5.5 shows XRD patterns for sintered screen printed BaM thick films prepared from milled powders. Single phase BaM has been observed in the films, however, a small secondary  $\text{Fe}_2\text{O}_3$  peak was observed in film fabricated from 48h and 72h milled powders. Extended millings in powder reduce into  $\text{Fe}_2\text{O}_3$  due to some recrystallization kinetics [221,223,224]. It is clear from the enlarged XRD image that the intensity of (008) peak is high in the films prepared by milled powder. This suggests films are perpendicularly oriented and confirms textured growth. Film from 12h milled powder shows high (008) peak compared to its inevitable (107). The variation in relative intensity of (008) and (107) peaks with milling time, confirms that the particles plays an important role to induce perpendicular anisotropy.

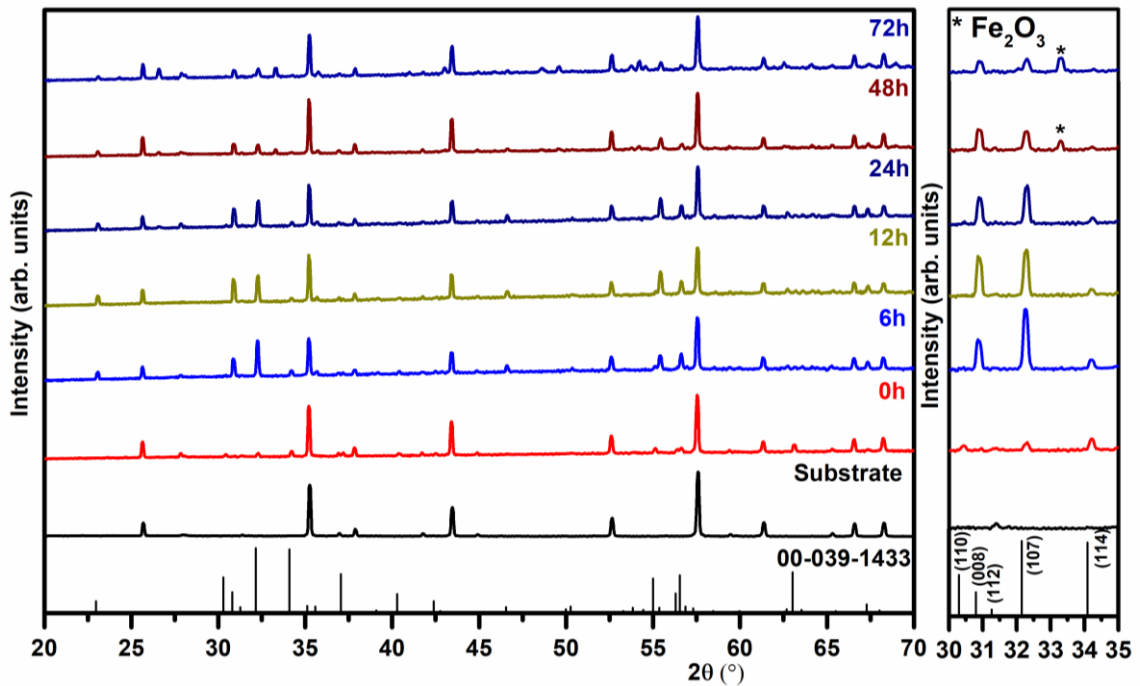


**Fig. 5.5.** X-ray diffraction patterns of screen printed BaM thick film.

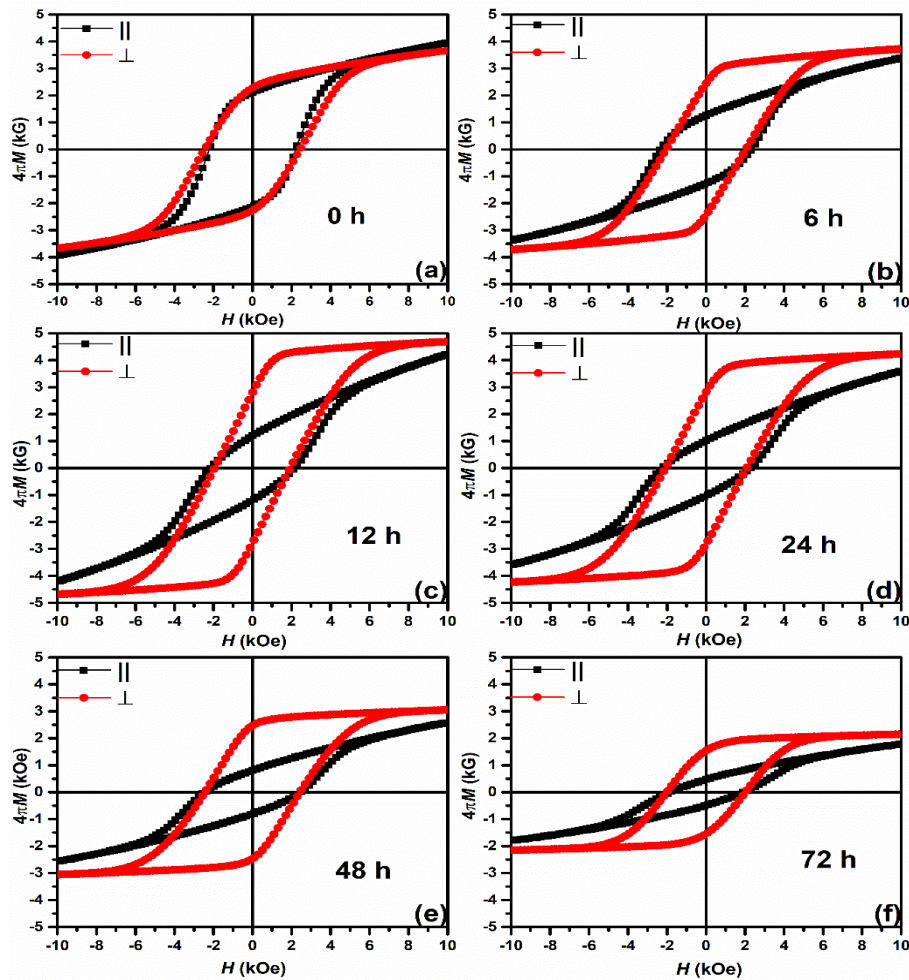
To know the degree of crystallographic orientation of the screen printed films, the lotgering factor is determined from the following relation [225]:

$$f = \frac{P-P_0}{1-P_0} \quad (5.1)$$

where  $P = \sum I_{(001)} / \sum I_{(hkl)}$  of screen printed thick film and  $P_0 = \sum I_{0(001)} / \sum I_{0(hkl)}$  of polycrystalline powders. The maximum lotgering factor of 0.84 is obtained for 12h milled powder films. It has been reported that lotgering factor around 0.80 shows low *FMR* linewidth for textured polycrystalline BaM sphere [226].

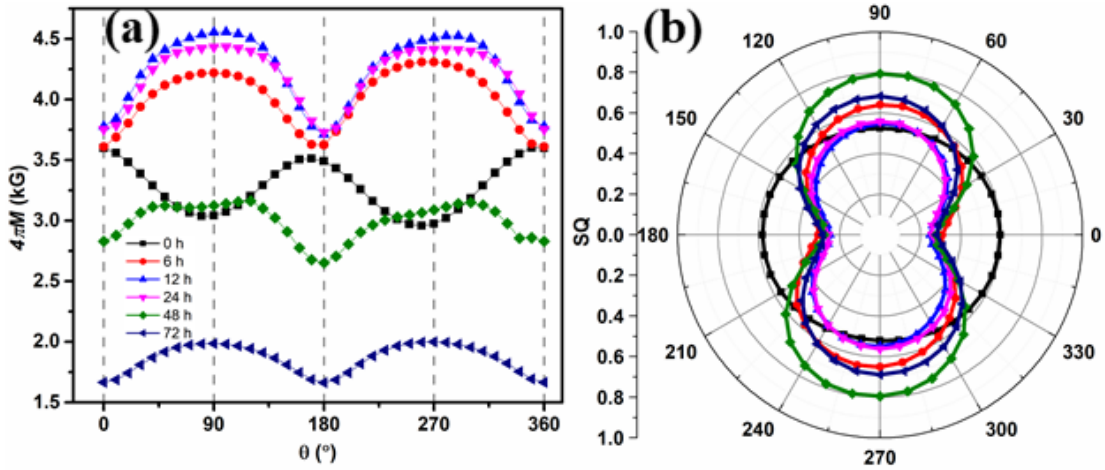
ii. *Magnetic studies*

Fig. 5.6 shows *M-H* plots of BaM thick films fabricated from powder milled for different time. It is clear that films prepared by unmilled (0h) powder (fig. 5.6(a)) shows isotropic nature despite orientating it under the magnetic field.



**Fig. 5.6.** *M-H* plots of BaM thick film fabricated from various milled powder.

However, all films prepared by ball milled powder possess a strong perpendicular anisotropy as evident from fig 5.6 (b-f), which further suggests that the particle orientation under the magnetic field strongly depends upon the particle size and its distribution. Fig. 5.7 (a & b) shows the angular dependence of magnetization and the corresponding polar plot of SQ. The polar plots of SQ depict well-defined formation of ‘8’ like shape which confirms textures growth and perpendicular anisotropy in the films.



**Fig. 5.7.** (a) Angular variation in  $4\pi M$  and (b) Polar SQ plot for screen printed BaM thick films fabricated with different milled powders.

Fig. 5.8 shows the variation in magnetic properties of the films with milling time. Film prepared from 12h milled powder shows the highest  $M$  in both directions. Further increase in milling time,  $M$  decrease gradually and found lowest, i.e. 1.78 ( $\parallel$ ) and 2.15 kG ( $\perp$ ) for 72h milled sample.

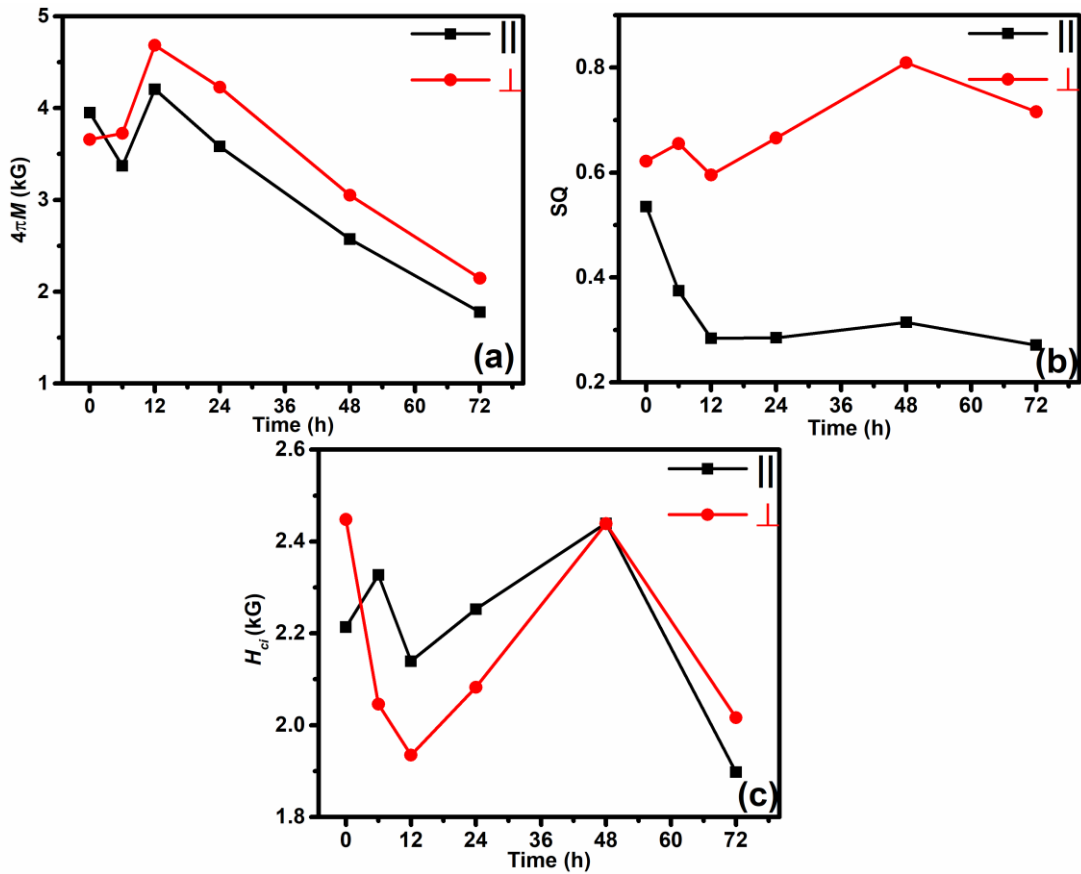


**Fig. 5.8.** Magnetic properties (a)  $4\pi M$ , (b) SQ and (c)  $H_c$  of screen printed BaM thick films with milling time.

The SQ found to increase in  $\perp$  direction with milling time, the maximum of 0.80 is obtained for 48h milled powder film. The corresponding SQ ( $\parallel$ ) decreases with milling time up to 12h (0.28) and then remained constant. The result suggests, near single domain grains have better orientation than multi-domain bigger grains which cancel out the effective orientation. It is interesting to note that  $H_c$  decreases up to 12h milled powder films and then increases. The results are contrary to the  $H_c$  of powder samples (Table 5.1). This suggests that particle size distribution up to 12h milled powder is favourable for better grain growth during sintering. Increase in milling time to 48h, the increase in  $H_c$  might be due to fine grain structure. Further, a drastic decrease (72h) is due to tungsten carbide contamination.

### iii. Microstructural study

Fig. 5.9 (a-c) shows the representative SEM micrographs of textured BaM thick film prepared from 0h, 12h, and 72h milled powders, Film prepared by 0h milled powder shows randomly oriented equiaxed grains with an average grains size of 2.45  $\mu\text{m}$ . It appears that films are not well sintered and possess porous structure. The larger powder size with low surface area may require a higher sintering temperature to effect densification. On other hand, film of 12h milled powder (fig. 5.9 (b)) illustrates a highly textured structure with low porosity. The average size is found to be 2.18  $\mu\text{m}$  with broader grain distribution. Grains up to 10  $\mu\text{m}$  were seen on the film's surface with hexagonal  $c$ - axis of platelets found parallel to the substrate plane. Film from 72h milled powder display polygon-shaped coarse grains with relatively higher porosity than 12h sample. The average grain size found to 1.65  $\mu\text{m}$  with narrow distribution. The cross sectional view (Fig. 5.10 (a - c)) shows that large shrinkage in the film prepared by milled powder. The enlarged view shows platelets are stacked well in 12 h and 72h milled powder films suggest the perpendicular orientation.

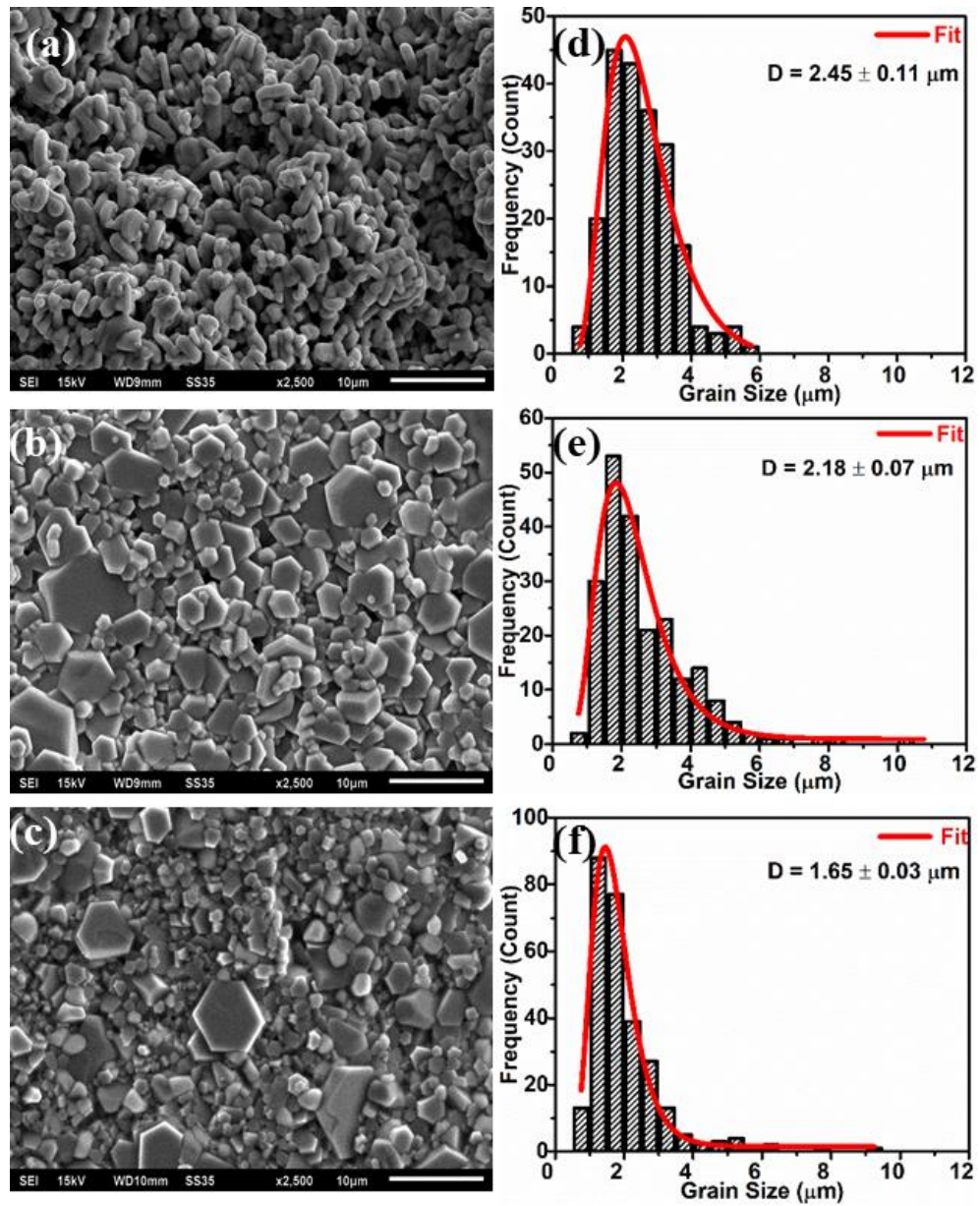


**Fig. 5.9.** SEM micrographs of sintered BaM thick film fabricated from (a) 0h, (b) 12h, (c) 72h milled powders and (d-f) respective grain size distribution.

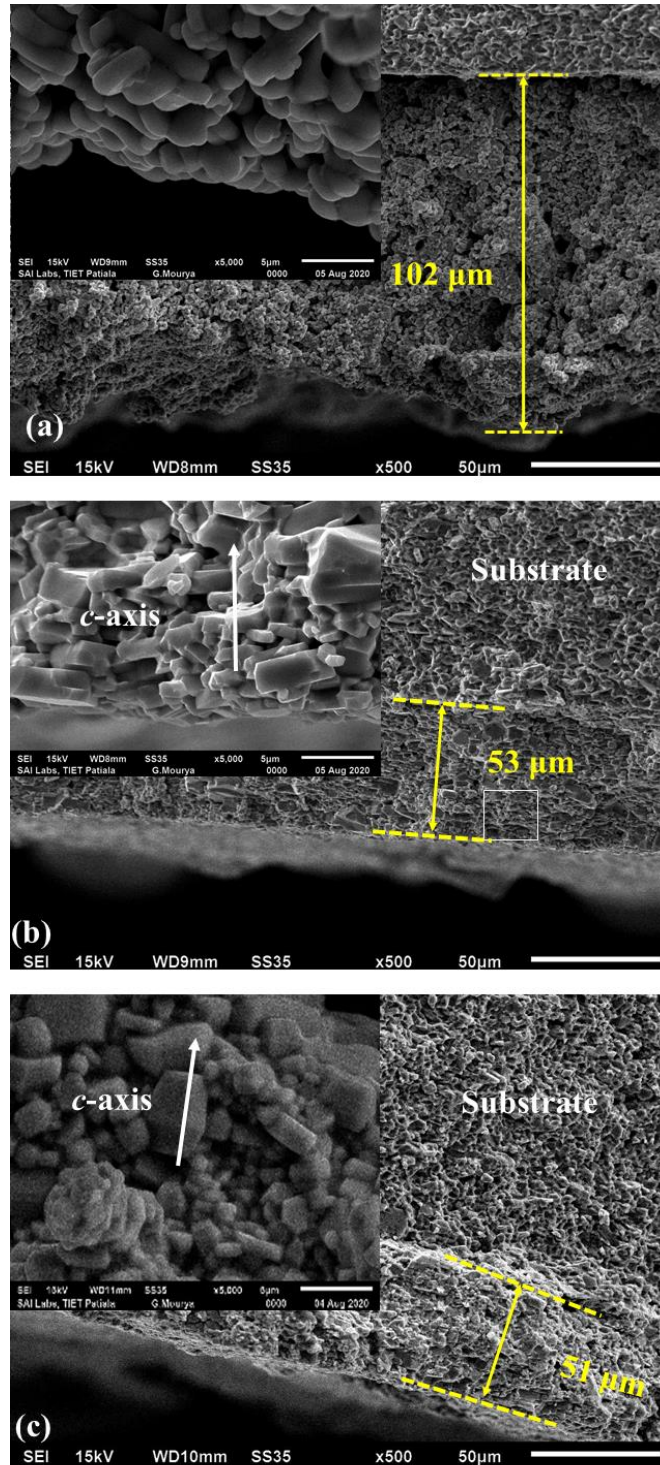


**Fig. 5.10.** Cross sectional micrographs of sintered BaM thick film fabricated from (a) 0h, (b) 12h and (c) 72h milled powders. Inset shows the typical alignment of fabricated films.

## *Chapter 6*

### *Conclusions*

---

---

#### **Overview**

In this chapter, important outcomes from this research are summarized. The impact of various substitution (Al, Ti & La-Co) on magnetic and microwave properties of powders and thick films are concluded. The microwave sintering and novel result obtained from textured BaM thick films are showcased. All the important parameters obtained in the result and discussion are summarized in the table. Finally, the future scope of the work is presented at the end of this chapter.

---

---

In the present dissertation, M-type barium hexaferrite ( $\text{BaFe}_{12}\text{O}_{19}$ ) powders with Al, Ti and La-Co substitutions were prepared by solid state ceramic. Further, isotropic sintered screen printed thick films of as-substituted powder were prepared. Effect of various cationic substitutions on structural, magnetic and microwave properties of powder and thick films were investigated. Also, anisotropic microwave sintered thick films were prepared and effect of particle size distribution on structural and magnetic properties were studied. The important outcomes from the works are summarized:

- Single phase  $\text{BaFe}_{12}\text{O}_{19}$  (BaM) powder has been successfully prepared and hard magnetic behaviour was confirmed by  $M$ - $H$  loop. Screen printed BaM thick film of 100  $\mu\text{m}$  thickness has been fabricated and conventionally sintered at different temperature (1150  $^{\circ}\text{C}$  - 1350  $^{\circ}\text{C}$ ) for 1h. Sample sintered at 1250  $^{\circ}\text{C}$  showed dense morphology with an average grain size of 4.5  $\mu\text{m}$ .  $M$ - $H$  plot showed isotropic magnetic behaviour. The magnetic properties found decreased with sintering temperature.
- Al-substituted BaM powders were prepared by solid state ceramic method. The effective substitution was confirmed by decrease in lattice constant and crystallite size. Reduction in Fe-O bond length at octahedral and tetrahedral coordination was seen by FTIR studies. A linear decrease in magnetization ( $M$ ), remanence ( $M_r$ ), anisotropic field ( $H_a$ ) and first anisotropic constant ( $K_1$ ) were observed, whereas, coercivity ( $H_c$ ) found to increase with Al substitution. Screen printed thick films sintered showed drastic rise in the  $H_c$  up to 7.47 kOe. M-T measurements showed a decrease in Curie temperature ( $T_c$ ) from 497  $^{\circ}\text{C}$  to 437  $^{\circ}\text{C}$  with  $\text{Al}^{3+}$  substitution. Permeability ( $\mu'$ ) in X-band found to be less in Al-substituted samples. Reflection losses ( $R_L$ ) showed a minimum value of -47 dB at 9.3 GHz.
- In Ti-substituted BaM sample, the single phase was obtained after three-step calcination. A slight blue shift in FTIR supported the fraction of  $\text{Ti}^{4+}$  ions substitution increases with subsequent calcination. Bond length calculated from FTIR shows contraction in BaTiM samples. Raman spectroscopy confirmed the presence of  $\text{Ti}^{4+}$  ion in  $12k$ ,  $4f_1$  and  $4f_2$  sites. Drastic decrease in  $M$ ,  $H_c$  and  $H_a$  for was observed in Ti-substituted samples. Micrograph of sintered films showed spherical grains with nearly comparable grain size for pure and substituted samples. Microwave studies in  $K_u$ -band confirmed  $\text{Ti}^{4+}$  substitution reduces dielectric and magnetic losses with overall enhancement in microwave absorbance.

- $\text{Ba}_{1-y}\text{La}_y\text{Fe}_{12-x}\text{Co}_x\text{O}_{19}$  ( $x = 0.0, 0.10, 0.15, 0.2, 0.5$  &  $1, y = 0.0, 0.10, 0.15, 0.20$ ) powder has been prepared. XRD confirmed single phase BaM without any secondary phase up to  $x = 0.5$ . FTIR and Raman spectra confirmed substitution of La and Co ions in BaM crystal lattice. A redshift in Raman for  $2a$ ,  $2b$  and  $4f_2$  sites suggest an effective substitution of La and Co on its respective sites. Mössbauer spectroscopy confirmed that  $\text{Co}^{2+}$  ions preferably occupies  $2a$  and  $2b$  sites, whereas it also occupies  $4f_2$  site with La-Co co-substituted BaM. The average grain size was found to be 2.5 and 2  $\mu\text{m}$  for pure and substituted powder. Room temperature  $M$  and squareness (SQ) found to increase with La and La-Co substitution  $H_a$  found to be lower for substituted samples.  $T_c$  showed a strong dependence on substitution, where the Co ion effect is mostly dominated. Thick films fabricated from substituted BaM were isotropic and showed comparable magnetic properties. Multiple absorbance peaks were obtained for pure and Co-substituted samples  $K_u$ -band. La-substitution found to suppress oscillatory behaviour with absorbance up to 0.9 at 16.64 GHz.
- Anisotropic microwave sintered thick films were prepared from 0h, 6h, 12h, 24h, 48h & 72h milled powder under the presence of an external magnetic field of 0.8 T. Crystallite size found to decrease with milling time as observed by XRD. Equiaxed particles up to 10  $\mu\text{m}$  were seen for unmilled powder, whereas, coagulated microstructure with sub-micron ranged particle was found milled powders. A linear decrease in  $M$ ,  $M_r$ , SQ and  $H_a$  were found with milling time.  $H_c$  found gradually increased up to 12 h milling and then decreases.

Thick films fabricated from as-milled powders were microwave sintered at 1200 °C for 20 min. XRD pattern showed textured growth in the films with milling time. Lotgering factor of 0.84 was found for 12h milled sample.  $M$ - $H$  loop and polar plots of SQ confirmed perpendicular anisotropy in sintered screen printed film. A higher  $M$  and SQ in  $\perp$  direction compared to  $\parallel$  direction were observed. Films prepared by 12 h milled powders showed maximum  $M$  whereas,  $H_{ci}$  in  $\perp$  direction gradually decreases up to 12h and further increased with milling time. Microstructural studies revealed high dense and textured morphology in BaM thick film prepared from 12h milled powder. A very high post sintering shrinkage of 53% was observed in the films.

**Table 6.1.** Summarized magnetic and microwave properties of substituted BaM.

| Sample   |                  | Magnetic Properties |      |                  |      |              |      |              |       | Microwave properties |                      |                  |
|--|------------------|---------------------|------|------------------|------|--------------|------|--------------|-------|----------------------|----------------------|------------------|
|  |                  | $4\pi M$<br>kG      |      | $4\pi M_r$<br>kG |      | $H_c$<br>kOe |      | $H_a$<br>kOe |       | A( $\omega$ )        | R <sub>L</sub><br>dB | Frequency<br>GHz |
|  |                  |                     | ⊥    |                  |      |              | ⊥    |              | ⊥     |                      |                      |                  |
| BaFe <sub>12-x</sub> Al <sub>x</sub> O <sub>19</sub>                                 | 0                | 4.14                | 3.53 | 2.01             | 2.01 | 1.73         | 1.74 | 12.63        | 12.55 | -                    | 14.07                | 9.29             |
|  | 1                | 3.12                | 2.55 | 1.70             | 1.36 | 4.77         | 4.79 | 11.17        | 10.63 | -                    | 18.60                | 8.20             |
|  | 2                | 1.20                | 1.08 | 0.71             | 0.63 | 7.47         | 7.45 | 7.03         | 6.72  | -                    | 15.67                | 9.46             |
| BaFe <sub>12-x</sub> Ti <sub>x</sub> O <sub>19</sub>                                 | 0                | 3.32                | 3.15 | 1.91             | 1.85 | 2.54         | 2.58 | 8.65         | 7.90  | 0.94                 | -                    | 14.53            |
|  | 0.5              | 2.74                | 2.56 | 1.11             | 0.81 | 0.94         | 0.95 | 8.06         | 7.30  | 0.91                 | -                    | 15.98            |
| Ba <sub>1-x</sub> La <sub>x</sub> Fe <sub>12-y</sub> Co <sub>y</sub> O <sub>19</sub> | 0                | 3.17                | 2.95 | 1.85             | 1.62 | 2.30         | 2.25 | 8.99         | 8.65  | 0.57                 | -                    | 13.87            |
|  | x=0.15<br>y=0.15 | 3.23                | 2.85 | 1.87             | 1.66 | 2.52         | 2.49 | 8.54         | 8.41  | 0.85                 | -                    | 14.98            |

**Table 6.2.** Summarized magnetic properties of textured BaM thick film.

| Milling time<br><i>h</i> | $4\pi M$<br>kG |      | $4\pi M_r$<br>kG |      | $H_c$<br>kOe |      | SQ   |      |
|--------------------------|----------------|------|------------------|------|--------------|------|------|------|
|                          |                | ⊥    |                  | ⊥    |              | ⊥    |      | ⊥    |
| 0                        | 3.95           | 3.66 | 2.21             | 2.45 | 2.11         | 2.27 | 0.54 | 0.62 |
| 6                        | 3.37           | 3.73 | 2.33             | 2.05 | 1.26         | 2.44 | 0.37 | 0.66 |
| 12                       | 4.21           | 4.68 | 2.14             | 1.93 | 1.20         | 2.79 | 0.28 | 0.60 |
| 24                       | 3.58           | 4.23 | 2.25             | 2.08 | 1.02         | 2.81 | 0.29 | 0.67 |
| 48                       | 2.57           | 3.05 | 2.44             | 2.44 | 0.81         | 2.47 | 0.31 | 0.81 |
| 72                       | 1.78           | 2.15 | 1.90             | 2.02 | 0.48         | 1.54 | 0.27 | 0.72 |

### **Future Scope**

On the basis of work done a few prospective suggestions for future work are:

- For the realization of fabricated BaM thick films in high frequency applications, FMR measurements need to be investigated.
- The effect of various cationic substitution with the optimized microwave sintering condition studied in this work can be explored.

## References

- [1] J.D. Adam, S. V. Krishnaswamy, S.H. Talisa, K.C. Yoo, Thin-film ferrites for microwave and millimeter-wave applications, *J. Magn. Magn. Mater.* 83 (1990) 419–424. [https://doi.org/10.1016/0304-8853\(90\)90570-G](https://doi.org/10.1016/0304-8853(90)90570-G).
- [2] K.J. Strnat, Modern Permanent Magnets for Applications in Electro-Technology, *Proc. IEEE.* 78 (1990) 923–946. <https://doi.org/10.1109/5.56908>.
- [3] A. Goldman, Ferrites for Microwave Applications, *Mod. Ferrite Technol.* 83 (2006) 375–386. <https://doi.org/10.1007/978-0-387-29413-1>.
- [4] V.G. Harris, Modern Microwave Ferrites, *IEEE Trans. Magn.* 48 (2012) 1075–1104.
- [5] J. Smit, Ferrites : physical properties of ferrimagnetic oxides in relation to their technical applications, N.V. Philips Gloeilampenfabrieken, Eindhoven, 1959.
- [6] K.T. Han, The Origin of FMR Parameter Shift in Polycrystalline  $\text{MgFe}_2\text{O}_4$  Ferrite Spheres, *Phys. Status Solidi.* 155 (1996) 215–222. <https://doi.org/10.1002/pssa.2211550121>.
- [7] X. Zuo, A. Yang, S.D. Yoon, J.A. Christodoulides, V.G. Harris, C. Vittoria, Large induced magnetic anisotropy in manganese spinel ferrite films, *Appl. Phys. Lett.* 87 (2005) 1–3. <https://doi.org/10.1063/1.2084341>.
- [8] J. Chen, C. Sorensen, K. Klabunde, Size-dependent magnetic properties of fine particles synthesized by coprecipitation, *Phys. Rev. B - Condens. Matter Mater. Phys.* 54 (1996) 9288–9296. <https://doi.org/10.1103/PhysRevB.54.9288>.
- [9] K. Maaz, A. Mumtaz, S.K. Hasanain, A. Ceylan, Synthesis and magnetic properties of cobalt ferrite ( $\text{CoFe}_2\text{O}_4$ ) nanoparticles prepared by wet chemical route, *J. Magn. Magn. Mater.* 308 (2007) 289–295. <https://doi.org/10.1016/j.jmmm.2006.06.003>.
- [10] P.C. Dorsey, P. Lubitz, D.B. Chrisey, J.S. Horwitz,  $\text{CoFe}_2\text{O}_4$  thin films grown on (100) MgO substrates using pulsed laser deposition, *J. Appl. Phys.* 79 (1996) 6338. <https://doi.org/10.1063/1.361991>.
- [11] P. Sivakumar, R. Ramesh, A. Ramanand, S. Ponnusamy, C. Muthamizhchelvan, Synthesis and characterization of nickel ferrite magnetic nanoparticles, *Mater. Res. Bull.* 46 (2011) 2208–2211. <https://doi.org/10.1016/j.materresbull.2011.09.009>.
- [12] H. How, P. Shi, C. Vittoria, L.C. Kempel, K.D. Trott, Single-crystal YIG phase shifter using composite stripline structure at X band, *J. Appl. Phys.* 87 (2000) 4966–4968. <https://doi.org/10.1063/1.373217>.
- [13] R.C. Pullar, Hexagonal ferrites: A review of the synthesis, properties and applications of hexaferrite ceramics, *Prog. Mater. Sci.* 57 (2012) 1191–1334. <https://doi.org/10.1016/j.pmatsci.2012.04.001>.
- [14] S.D. Yoon, C. Vittoria, Microwave and magnetic properties of barium hexaferrite films having the c-axis in the film plane by liquid phase epitaxy technique, *J. Appl. Phys.* 93 (2003) 8597–8599. <https://doi.org/10.1063/1.1557791>.
- [15] J. Ding, H. Yang, W.F. Miao, P.G. McCormick, R. Street, High coercivity Ba

- hexaferrite prepared by mechanical alloying, *J. Alloys Compd.* 221 (1995) 70–73.
- [16] F. Licci, G. Turilli, T. Besagni, Phase analysis and single domain detection in hexaferrite powders for magnetic recording, *IEEE Trans. Magn.* 24 (1987) 593–597. <https://doi.org/10.1109/20.43989>.
- [17] J.F. Wang, C.B. Ponton, I.R. Harris, Ultrafine SrM particles with high coercivity by chemical coprecipitation, in: *J. Magn. Magn. Mater.*, North-Holland, 2002: pp. 1464–1467. [https://doi.org/10.1016/S0304-8853\(01\)01104-0](https://doi.org/10.1016/S0304-8853(01)01104-0).
- [18] M. Obol, X. Zuo, C. Vittoria, Oriented Y-type hexaferrites for ferrite device, *J. Appl. Phys.* 91 (2002) 7616–7618. <https://doi.org/10.1063/1.1446113>.
- [19] Z.W. Li, L. Chen, C.K. Ong, High-frequency magnetic properties of W-type barium-ferrite  $\text{BaZn}_{2-x}\text{Co}_x\text{Fe}_{16}\text{O}_{27}$  composites, *J. Appl. Phys.* 94 (2003) 5918–5924. <https://doi.org/10.1063/1.1618945>.
- [20] K.N. Rozanov, Z.W. Li, L.F. Chen, M.Y. Koledintseva, Microwave permeability of  $\text{Co}_2\text{Z}$  composites, *J. Appl. Phys.* 97 (2005) 013905. <https://doi.org/10.1063/1.1827911>.
- [21] G. Xiong, Z.H. Mai, Preparation and magnetic properties of  $\text{Ba}_2\text{Co}_2\text{Fe}_{28}\text{O}_{46}$  nanocrystals, *J. Appl. Phys.* 88 (2000) 519–523. <https://doi.org/10.1063/1.373689>.
- [22] R.C. Pullar, A.K. Bhattacharya, The synthesis and characterisation of  $\text{Co}_2\text{X}$  ( $\text{Ba}_2\text{Co}_2\text{Fe}_{28}\text{O}_{46}$ ) and  $\text{Co}_2\text{U}$  ( $\text{Ba}_4\text{Co}_2\text{Fe}_{36}\text{O}_{60}$ ) ferrite fibres, manufactured from a sol-gel process, 36 (2001) 4805–4812. <https://doi.org/10.1023/A:1017947625940>.
- [23] A.J. Kerecman, T.R. Aucoin, W.P. Dattilo, Ferromagnetic resonance in  $\text{Ba}_4\text{Zn}_2\text{Fe}_{36}\text{O}_{60}$  (ZnU) and Mn-substituted ZnU single crystals, *J. Appl. Phys.* 40 (1969) 1416–1417. <https://doi.org/10.1063/1.1657698>.
- [24] D. Lisjak, M. Drogenik, Synthesis and characterization of Zn<sub>2</sub>U ( $\text{Ba}_4\text{Zn}_2\text{Fe}_{36}\text{O}_{60}$ ) hexaferrite powder, in: *J. Appl. Phys.*, American Institute of Physics AIP, 2003: pp. 8011–8013. <https://doi.org/10.1063/1.1540159>.
- [25] M. Verma, A.P. Singh, P. Sambyal, B.P. Singh, S.K. Dhawan, V. Choudhary, Barium ferrite decorated reduced graphene oxide nanocomposite for effective electromagnetic interference shielding., *Phys. Chem. Chem. Phys.* 17 (2015) 1610–8. <https://doi.org/10.1039/c4cp04284k>.
- [26] G.P. Rodrigue, A Generation of Microwave Ferrite Devices, *Proc. IEEE.* 76 (1988) 121–137. <https://doi.org/10.1109/5.4389>.
- [27] C.N. Chinnasamy, T. Sakai, S. Sivasubramanian, A.F. Yang, C. Vittoria, V.G. Harris, Magnetic and microwave properties of basal-plane oriented  $\text{BaFe}_{11}\text{InO}_{19}$  ferrite thick films processed by screen printing, *J. Appl. Phys.* 103 (2008) 9–12. <https://doi.org/10.1063/1.2829905>.
- [28] S. Verma, S.K. Dhawan, A. Paesano, O.P. Pandey, P. Sharma, Structural, magnetic and microwave properties of barium hexaferrite thick films with different Fe/Ba mole ratio, *J. Magn. Magn. Mater.* 396 (2015) 308–312. <https://doi.org/10.1016/j.jmmm.2015.08.049>.
- [29] Han-Shin Cho, Sung-Soo Kim, H. Cho, S. Kim, M-Hexaferrites with Planar Magnetic Anisotropy and Their Application to High-Frequency Microwave

- Absorbers, *IEEE Trans. Magn.* 35 (1999) 3151–3153.  
<https://doi.org/10.1109/20.801111>.
- [30] M. Karmakar, B. Mondal, M. Pal, K. Mukherjee, Acetone and ethanol sensing of barium hexaferrite particles: A case study considering the possibilities of non-conventional hexaferrite sensor, *Sensors Actuators, B Chem.* 190 (2014) 627–633.  
<https://doi.org/10.1016/j.snb.2013.09.035>.
- [31] T. Kaur, J. Sharma, S. Kumar, A.K. Srivastava, Optical and Multiferroic Properties of Gd-Co Substituted Barium Hexaferrite, *Cryst. Res. Technol.* 52 (2017) 1700098. <https://doi.org/10.1002/crat.201700098>.
- [32] H. Kojima, Fundamental properties of hexagonal ferrites with magnetoplumbite structure, in: K.H.J. Buschow (Ed.), *Handb. Ferromagn. Mater.*, Elsevier, Amsterdam, 1982: pp. 305–391. [https://doi.org/10.1016/S1574-9304\(05\)80057-4](https://doi.org/10.1016/S1574-9304(05)80057-4).
- [33] E.W. Gorter, Saturation Magnetization of Some Ferrimagnetic Oxides With Hexagonal Crystal Structures, *Proc. IEE - Part B Radio Electron. Eng.* 104 (1957) 255–260. <https://doi.org/10.1049/pi-b-1.1957.0042>.
- [34] G. Albanese, A. Deriu, E. Lucchini, G. Slokar, Mossbauer investigation of In and Sc substituted barium hexaferrite, *Appl. Phys. A Solids Surfaces.* 26 (1981) 45–50. <https://doi.org/10.1007/BF01197677>.
- [35] T.M. Perekalina, M.A. Vinnik, R.I. and Zvereva, Shchurova A D, Magnetic Properties of Hexagonal Ferrites with Weak Exchange Coupling between sublattices, *Sov. Phys. J.* 32 (1971) 813–814.
- [36] G. Albanese, A. Deriu, Magnetic properties of Al, Ga, Sc, In substituted barium ferrites: A comparative analysis, *Ceramurg. Int.* 5 (1979) 3–10.  
[https://doi.org/10.1016/0390-5519\(79\)90002-4](https://doi.org/10.1016/0390-5519(79)90002-4).
- [37] L.G. Van Uitert, F.W. Swanekamp, Permanent magnet oxides containing divalent metal ions. II, *J. Appl. Phys.* 28 (1957) 482–485.
- [38] A.H. Mones, E. Banks, Cation substitutions in  $\text{BaFe}_{12}\text{O}_{19}$ , *J. Phys. Chem. Solids.* 4 (1958) 217–222. [https://doi.org/10.1016/0022-3697\(58\)90119-7](https://doi.org/10.1016/0022-3697(58)90119-7).
- [39] S. Capraro, J.P. Chatelon, H. Joisten, M. Le Berre, B. Bayard, D. Barbier, J.J. Rousseau, Magnetic properties of sputtered barium ferrite thick films, *J. Appl. Phys.* 93 (2003) 9898–9901. <https://doi.org/10.1063/1.1576898>.
- [40] Y.Y. Song, S. Kalarickal, C.E. Patton, Optimized pulsed laser deposited barium ferrite thin films with narrow ferromagnetic resonance linewidths, *J. Appl. Phys.* 94 (2003) 5103–5110. <https://doi.org/10.1063/1.1608475>.
- [41] Y.A. Kranov, A. Abuzir, T. Prakash, D.N. McIlroy, W.J. Yeh, Barium hexaferrite thick films made by liquid phase epitaxy reflow method, *IEEE Trans. Magn.* 42 (2006) 3338–3340. <https://doi.org/10.1109/TMAG.2006.879629>.
- [42] I. Wane, A. Bessaudou, F. Cosset, A. Célérier, C. Girault, J.L. Decossas, J.C. Vareille, Thick barium hexaferrite (Ba-M) films prepared by electron-beam evaporation for microwave application, *J. Magn. Magn. Mater.* 211 (2000) 309–313. [https://doi.org/http://dx.doi.org/10.1016/S0304-8853\(99\)00752-0](https://doi.org/http://dx.doi.org/10.1016/S0304-8853(99)00752-0).
- [43] A. Ghasemi, A. Morisako, X. Liu, Magnetic properties of hexagonal strontium

- ferrite thick film synthesized by sol-gel processing using SrM nanoparticles, *J. Magn. Mater.* 320 (2008) 2300–2304.  
<https://doi.org/10.1016/j.jmmm.2008.04.156>.
- [44] S. Verma, O.P. Pandey, A. Paesano, P. Sharma, A. Paesano Jr., P. Sharma, Structural and magnetic properties of CoTi substituted barium hexaferrite thick films, *J. Alloys Compd.* 678 (2016) 284–289.  
<https://doi.org/http://dx.doi.org/10.1016/j.jallcom.2016.03.283>.
- [45] Y. Chen, A.L. Geiler, T. Sakai, S.D. Yoon, C. Vittoria, V.G. Harris, Microwave and magnetic properties of self-biased barium hexaferrite screen printed thick films, *J. Appl. Phys.* 99 (2006) 08M904. <https://doi.org/10.1063/1.2163288>.
- [46] S.A. Oliver, P.M. Zavracky, N.E. Mcgruer, R. Schmidt, A Monolithic Single-Crystal Yttrium Iron Garnet / Silicon X-Band Circulator, 7 (1997) 239–241.
- [47] V.G. Harris, A. Geiler, Y. Chen, S. Dae, M. Wu, A. Yang, Z. Chen, P. He, P. V. Parimi, X. Zuo, C.E. Patton, Recent advances in processing and applications of microwave ferrites, *J. Magn. Mater.* 321 (2009) 2035–2047.  
<https://doi.org/10.1016/j.jmmm.2009.01.004>.
- [48] W.L. Zhang, R. Wang, B. Peng, Z.L. Huang, W.X. Zhang, Barium hexaferrite thick films prepared by screen printing for microwave applications, *Mater. Res. Innov.* 19 (2015) 537.  
<https://doi.org/dx.doi.org/10.1179/1432891715Z.0000000001743>.
- [49] P.M.T. Ikonen, K.N. Rozanov, A.V. Osipov, P. Alitalo, S.A. Tretyakov, Magnetodielectric Substrates in Antenna Miniaturization: Potential and Limitations, *IEEE Trans. Antennas Propag.* 54 (2006) 3391–3399.  
<https://doi.org/10.1109/TAP.2006.884303>.
- [50] J.J. Went, G.W. Rathenau, E.W. Gorter, G.W. Van Oosterhout, Hexagonal iron-oxide compounds as permanent-magnet materials, *Phys. Rev.* 86 (1952) 424–425.  
<https://doi.org/10.1103/PhysRev.86.424.2>.
- [51] G.F. Dionne, A Review of Ferrites for Microwave Applications, in: *Proc. IEEE*, 1975.
- [52] F.F.Y. Wang, K. Ishii, J.B.Y. Tsui, Ferrimagnetic resonance of single-crystal barium ferrite in the millimeter wave region, *J. Appl. Phys.* 32 (1961) 1621–1622.  
<https://doi.org/10.1063/1.1728407>.
- [53] S. Okamoto, Structure of  $\delta$ -FeOOH, *J. Am. Ceram. Soc.* 51 (1968) 594–598.  
<https://doi.org/10.1111/j.1151-2916.1968.tb13329.x>.
- [54] V. Kucski, *Purification of Carboxylic Acids*, 1970.
- [55] T.S. Chin, S.L. Hsu, M.C. Deng, Barium ferrite particulates prepared by a salt-melt method, *J. Magn. Mater.* 120 (1993) 64–68. [https://doi.org/10.1016/0304-8853\(93\)91288-I](https://doi.org/10.1016/0304-8853(93)91288-I).
- [56] G. Litsardakis, A.C. Stergiou, Non-stoichiometric barium ferrite particles for high-density magnetic recording, 120 (1993) 58–60.
- [57] J. Smit, H.G. Beljers, *Philips Res, Rep.* 10 (1955) 113.

- [58] C. Sürig, K.A. Hempel, C. Sauer, Influence of stoichiometry on hexaferrite structure, *J. Magn. Mater.* 157–158 (1996) 268–269. [https://doi.org/10.1016/0304-8853\(95\)01201-X](https://doi.org/10.1016/0304-8853(95)01201-X).
- [59] R.C. Pullar, M.D. Taylor, A.K. Bhattacharya, A halide free route to the manufacture of microstructurally improved M ferrite ( $\text{BaFe}_{12}\text{O}_{19}$  and  $\text{SrFe}_{12}\text{O}_{19}$ ) fibres, *J. Eur. Ceram. Soc.* 22 (2002) 2039–2045. [https://doi.org/10.1016/S0955-2219\(01\)00518-0](https://doi.org/10.1016/S0955-2219(01)00518-0).
- [60] X.H. Wang, L. Li, Z. Gui, S. Shu, J. Zhou, Preparation and characterizations of ultrafine hexagonal ferrite  $\text{Co}_2\text{Z}$  powders, *Mater. Chem. Phys.* 77 (2003) 248–253. [https://doi.org/10.1016/S0254-0584\(01\)00584-3](https://doi.org/10.1016/S0254-0584(01)00584-3).
- [61] V. Sankaranarayanan, Q.A. Pankhurst, D.P.E. Dickson, C.E. Johnson, An investigation of particle size effects in ultrafine barium ferrite, *J. Magn. Mater.* 125 (1993) 199–208.
- [62] M. Jean, V. Nachbaur, J. Bran, J.M. Le Breton, Synthesis and characterization of  $\text{SrFe}_{12}\text{O}_{19}$  powder obtained by hydrothermal process, *J. Alloys Compd.* 496 (2010) 306–312. <https://doi.org/10.1016/j.jallcom.2010.02.002>.
- [63] M. Farhat, J. Joubert, Hydrothermal synthesis and characterisation of the hexagonal ferrite  $\text{Fe}_2\text{-Y}$ , *J. Magn. Mater.* 62 (1986) 353–358.
- [64] B.T. Shirk, W.R. Buessem, Magnetic properties of barium ferrite formed by crystallization of a glass, *J. Am. Ceram. Soc.* 53 (1970) 192–196.
- [65] S. Castro, M. Gayoso, J. Rivas, J.M. Greneche, J. Mira, C. Rodríguez, Structural and magnetic properties of barium hexaferrite nanostructured particles prepared by the combustion method, *J. Magn. Mater.* 152 (1996) 61–69. [https://doi.org/10.1016/0304-8853\(95\)00450-5](https://doi.org/10.1016/0304-8853(95)00450-5).
- [66] G. Elwin, I.P. Parkin, Q.T. Bui, F. Barquin, Q.A. Pankhurst, A. V Komarov, Y.G. Morozov, Self-propagating high-temperature synthesis of  $\text{SrFe}_{12}\text{O}_{19}$  from reactions of strontium superoxide, iron metal and iron oxide powders, *J. Mater. Sci. Lett.* 16 (1997) 1237–1239.
- [67] M. Suarez, J. Corral-huacuz, M. Contreras-Garcia, H. Juarez-Medina, Magnetic properties of  $\text{BaFe}_{11.6-2x}\text{Co}_x\text{Ti}_x\text{O}_{19}$  particles produced by sol-gel and spray-drying, *J. Magn. Mater.* 234 (2001) 73–79.
- [68] I. Bsoul, S.H. Mahmood, A. Lehlooh, S.H. Mahmood, A. Lehlooh, Structural and magnetic properties of  $\text{BaFe}_{12-2x}\text{Ti}_x\text{Ru}_x\text{O}_{19}$ , *J. Alloys Compd.* 498 (2010) 157–161. <https://doi.org/10.1016/j.jallcom.2010.03.142>.
- [69] E.P. Naiden, V.I. Itin, O.G. Terekhova, Mechanochemical Modification of the Phase Diagrams of Hexagonal Oxide Ferrimagnets, *Tech. Phys. Lett.* 29 (2003) 889–891. <https://doi.org/10.1134/1.1631354>.
- [70] H. Hegde, P. Samarasekara, F.J. Cadieu, Nonepitaxial sputter synthesis of aligned strontium hexaferrite,  $\text{SrO}\cdot 6(\text{Fe}_2\text{O}_3)$ , films, *J. Appl. Phys.* 75 (1994) 6640–6642. <https://doi.org/10.1063/1.356880>.
- [71] C.A. Carosella, D.B. Chrisey, P. Lubitz, J.S. Horwitz, P. Dorsey, R. Seed, C. Vittoria, Pulsed laser deposition of epitaxial  $\text{BaFe}_{12}\text{O}_{19}$  thin films, *J. Appl. Phys.* 71 (1992) 5107–5110. <https://doi.org/10.1063/1.350614>.

- [72] S.G. Wang, S.D. Yoon, C. Vittoria, Microwave and magnetic properties of double-sided hexaferrite films on (111) magnesium oxide substrates, *J. Appl. Phys.* 92 (2002) 6728–6732. <https://doi.org/10.1063/1.1517749>.
- [73] M. Vérité, M. Valetas, A. Bessaudou, F. Cosset, J.C.C. Vareille, Properties of barium hexaferrite thick films deposited by electron beam evaporation, *J. Eur. Ceram. Soc.* 25 (2005) 1689–1695. <https://doi.org/10.1016/j.jeurceramsoc.2004.03.019>.
- [74] S. Salemizadeh, S.A. Seyyed Ebrahimi, Magnetic properties of nanocrystalline barium hexaferrite thin films prepared by sol-gel method, in: *IEEE Trans. Magn.*, 2009: pp. 2538–2540. <https://doi.org/10.1109/TMAG.2009.2018781>.
- [75] J. Buršík, Z. Šimša, M. Čerňanský, Magneto-Optical Characteristics of Co, Ti-Substituted Barium Hexaferrite Films Deposited by the Dip-Coating Method, *J. Sol-Gel Sci. Technol.* 8 (1997) 947–951. <https://doi.org/10.1007/BF02436966>.
- [76] C. Vittoria, Ferrite uses at millimeter wavelengths, *J. Magn. Magn. Mater.* 21 (1980) 109–118. [https://doi.org/10.1016/0304-8853\(80\)90495-3](https://doi.org/10.1016/0304-8853(80)90495-3).
- [77] H.P.J. Wijn, A new method of melting ferromagnetic semiconductors. BaFe<sub>18</sub>O<sub>27</sub>, a new kind of ferromagnetic crystal with high crystal anisotropy, *Nature.* 170 (1952) 707–708. <https://doi.org/10.1038/170707a0>.
- [78] L.H. Brixner, Preparation of the Ferrites BaFe<sub>12</sub>O<sub>19</sub> and SrFe<sub>12</sub>O<sub>19</sub> in Transparent Form, *J. Am. Chem. Soc.* 81 (1959) 3841–3843. <https://doi.org/10.1021/ja01524a011>.
- [79] M. Lemke, W. Hoppe, W. Tolksdorf, F. Welz, Magnetically tunable millimetre-wave filter with single-crystal barium ferrite, *IEE J. Microwaves, Opt. Acoust.* 3 (1979) 253–254.
- [80] M. Lemke, A Millimeter-Wave Gunn-Oscillator, Tunable with a Barium-Ferrite Sphere, in: *9th Eur. Microw. Conf. 1979, IEEE, 1979*: pp. 617–620. <https://doi.org/10.1109/EUMA.1979.332645>.
- [81] M. Labeyrie, J.C. Mage, W. Simonet, J.M. Desvignes, H. Le Gall, FMR linewidth of barium hexaferrite at millimeter wavelengths, *IEEE Trans. Magn.* 20 (1984) 1224–1226. <https://doi.org/10.1109/TMAG.1984.1063525>.
- [82] D. Nicholson, A High Performance Hexagonal Ferrite Tunable Bandpass Filter for the 40-60 GHz Region, in: *IEEE MTT-S Int. Microw. Symp. Dig., 1985*: pp. 229–232. <https://doi.org/10.1109/MWSYM.1985.1131948>.
- [83] L.M. Silber, A 54–58 ghz tunable ferrite filter, *IEEE Trans. Magn.* 21 (1985) 1788–1790. <https://doi.org/10.1109/TMAG.1985.1064112>.
- [84] Y.S. Lau, D. Nicholson, Barium Ferrite Tuned-Indium Phosphide Gunn Millimeter Wave Oscillators, in: *IEEE MTT-S Int. Microw. Symp. Dig., 1986*: pp. 183–186. <https://doi.org/10.1109/mwsym.1986.1132144>.
- [85] M. Labeyrie, J.C. Mage, J.P. Ganne, Measurement of the effective linewidth in the millimeter waves range, *J. Appl. Phys.* 64 (1988) 5825–5827. <https://doi.org/10.1063/1.342219>.
- [86] J.R. Truedson, K.D. McKinstry, R. Karim, C.E. Patton, Effective Linewidth due to

- Conductivity Losses in Barium Ferrite at 10 GHz, *IEEE Trans. Magn.* 28 (1992) 3309–3311. <https://doi.org/10.1109/20.179793>.
- [87] M.A. Wittenauer, J.A. Nyenhuis, A.I. Schindler, H. Sato, F.J. Friedlaender, J. Truedson, R. Karim, C.E. Patton, Growth and characterization of high purity single crystals of barium ferrite, *J. Cryst. Growth.* 130 (1993) 533–542. [https://doi.org/10.1016/0022-0248\(93\)90542-5](https://doi.org/10.1016/0022-0248(93)90542-5).
- [88] W.D. Wilber, L.M. Silber, Effective linewidth measurements at 36 GHz in hexagonal and cubic ferrites, *J. Appl. Phys.* 63 (1988) 3353–3355. <https://doi.org/10.1063/1.340779>.
- [89] W.P. Menashi, T.R. AuCoin, J.R. Shappirio, D.W. Eckart, Recrystallization of barium ferrite under high pressure oxygen, *J. Cryst. Growth.* 20 (1973) 68–70. [https://doi.org/10.1016/0022-0248\(73\)90039-0](https://doi.org/10.1016/0022-0248(73)90039-0).
- [90] R. Solé, X.X. Zhang, X. Ruiz, M. Aguiló, F. Díaz, Magnetic properties of  $\text{BaFe}_{12-x-y}\text{Sn}_x\text{Co}_y\text{O}_{19}$  single crystals, *J. Magn. Magn. Mater.* 159 (1996) L39–L44. [https://doi.org/10.1016/0304-8853\(96\)00362-9](https://doi.org/10.1016/0304-8853(96)00362-9).
- [91] S. Dixon, T.R.A. Coin, R.O. Savage, Microwave resonance linewidths in substituted single-crystal barium ferrite, *J. Appl. Phys.* 42 (1971) 1732–1733. <https://doi.org/10.1063/1.1660416>.
- [92] A.B. Ustinov, A.S. Tatarenko, G. Srinivasan, A.M. Balbashov, Al substituted Ba-hexaferrite single-crystal films for millimeter-wave devices, *J. Appl. Phys.* 105 (2009) 10–13. <https://doi.org/10.1063/1.3067759>.
- [93] H.N. Chait, N.G. Sakiotis, R.E. Martin, Reduction of the Loss in Ferrite Materials in the Microwave Region, *J. Appl. Phys.* 24 (1953) 109. <https://doi.org/10.1063/1.1721119>.
- [94] Lindt Willem Jacobus Van De, Electromagnetic device for amplitude-modulation of high-frequency oscillations, US2645758A, 1953.
- [95] J.L. Davis Etal, J.H. Rowen, Broadband nonreciprocal devices, US2909738A, 1959.
- [96] M.T. Weiss, Non reciprocal gyromagnetic device, US2949588A, 1960.
- [97] M.T. Weiss, P.W. Anderson, Ferromagnetic resonance in ferroxidure, *Phys. Rev.* 98 (1955) 925–926. <https://doi.org/10.1103/PhysRev.98.925>.
- [98] G.J. Rensen, J.S. Van Wieringen, Anisotropic Mössbauer fraction and crystal structure of  $\text{BaFe}_{12}\text{O}_{19}$ , *Solid State Commun.* 7 (1969) 1139–1141.
- [99] V.P. Pashchenko, P.P. Kirichok, G.M. Ryabova, N.P. Kapustin, I.F. Klochai, A.M. Nesterov, Effect of the gaseous atmosphere on the phase composition, crystalline structure, and physical properties of barium hexaferrites, *Sov. Powder Metall. Met. Ceram.* 24 (1985) 663–665. <https://doi.org/10.1007/BF00791963>.
- [100] G. Litsardakis, A.C. Stergiou, D. Samaras, Synthesis and Magnetic Properties of Partially Exchanged Nonstoichiometric Hexaferrites, *J. Solid State Chem.* 73 (1996) 68–73.
- [101] E.E. Rams, R.M. Garcia, E. Reguera, Structural transformation with milling on sol

- gel precursor for BaM hexaferrite, *J. Phys. Condens. Matter.* 33 (2000) 2708–2715.
- [102] P. Hernández-Gómez, J.M. Muñoz, C. Torres, C. De Francisco, O. Alejos, Influence of stoichiometry on the magnetic disaccommodation in barium M-type hexaferrites, *J. Phys. D. Appl. Phys.* 36 (2003) 1062–1070. <https://doi.org/10.1088/0022-3727/36/9/303>.
- [103] G. Tan, X. Chen, Structure and multiferroic properties of barium hexaferrite ceramics, *J. Magn. Magn. Mater.* 327 (2013) 87–90. <https://doi.org/10.1016/j.jmmm.2012.09.047>.
- [104] M.L. Ya, I. V Afonin, Magnetic analysis as a means of determining the degree of ferritization of barium ferrite powder, *Sov. Powder Metall. Met. Ceram.* 9 (1970) 221–223.
- [105] I. V Granovskii, D. Stepanova, D. Serebro, A. Lysyak, E. Krisan, Preparation of barium hexaferrite from mixtures of ferric oxide and carbon-containing barium compounds. Part I, *Powder Metall. Met. Ceram.* 621.318.13 (1970). <https://doi.org/10.1016/B978-075067509-3/50026-9>.
- [106] M.H. Hodge, W.R. Bitler, R.C. Bradt, Deformation Texture and Magnetic Properties of BaO.6Fe<sub>2</sub>O<sub>3</sub>, *J. Am. Ceram. Soc.* 56 (1973) 497–501.
- [107] G.I. Yu, Variation of the degree of preferential crystallographic orientation and magnetic properties of texturized barium ferrite permanent magnets during sintering, *Sov. Powder Metall. Met. Ceram.* 10 (1971) 388–392.
- [108] A. Yoshihiko, T. Okazaki, An application of a hexagonal ferrite to a millimeter-wave Y circulator, *IEEE Trans. Magn.* 10 (1974) 374–378.
- [109] W. Harrold, W.R. Reid, Permanent Magnets for Microwave Devices, *IEEE Trans. Magn.* 4 (1968) 229–239. <https://doi.org/10.1109/TMAG.1968.1066274>.
- [110] J.J. Becker, Permanent Magnets Based on Materials with High Crystal Anisotropy, *IEEE Trans. Magn.* 4 (1968) 239–249. <https://doi.org/10.1109/TMAG.1968.1066262>.
- [111] K. Haneda, H. Kojima, Intrinsic Coercivity of substituted BaFe<sub>12</sub>O<sub>19</sub>, *Jpn. J. Appl. Phys.* 12 (1973) 355–360.
- [112] D. Mishra, S. Anand, R.K. Panda, R.P. Das, X-ray diffraction studies on aluminum-substituted barium hexaferrite, *Mater. Lett.* 58 (2004) 1147–1153. <https://doi.org/10.1016/j.matlet.2003.08.027>.
- [113] H. Luo, B.K. Rai, S.R. Mishra, V. V. Nguyen, J.P. Liu, Physical and magnetic properties of highly aluminum doped strontium ferrite nanoparticles prepared by auto-combustion route, *J. Magn. Magn. Mater.* 324 (2012) 2602–2608. <https://doi.org/10.1016/j.jmmm.2012.02.106>.
- [114] D.H. Choi, S.Y. An, S.W. Lee, I.B. Shim, C.S. Kim, Site occupancy and anisotropy distribution of Al substituted Ba-ferrite with high coercivity, *Phys. Status Solidi.* 241 (2004) 1736–1739. <https://doi.org/10.1002/pssb.200304633>.
- [115] J. Qiu, Q. Zhang, M. Gu, Effect of aluminum substitution on microwave absorption properties of barium hexaferrite, *J. Appl. Phys.* 98 (2005) 5–9.

- <https://doi.org/10.1063/1.2135412>.
- [116] J. Qiu, M. Gu, H. Shen, Microwave absorption properties of Al- and Cr-substituted M-type barium hexaferrite, *J. Magn. Magn. Mater.* 295 (2005) 263–268. <https://doi.org/10.1016/j.jmmm.2005.01.018>.
- [117] M.G. Vakhitov, D.S. Klygach, D.A. Vinnik, V.E. Zhivulin, N.S. Knyazev, Microwave properties of aluminum-substituted barium hexaferrite  $\text{BaFe}_{12-x}\text{Al}_x\text{O}_{19}$  ceramics in the frequency range of 32–50 GHz, *J. Alloys Compd.* 816 (2020) 152682. <https://doi.org/10.1016/j.jallcom.2019.152682>.
- [118] S. Kumar, S. Supriya, M. Kar, Multiple electrical phase transitions in Al substituted barium hexaferrite, *J. Appl. Phys.* 122 (2017) 224106. <https://doi.org/10.1063/1.4998719>.
- [119] P. Winotai, S. Thongmee, I.M. Tang, Cation distribution in bismuth-doped M-type barium hexaferrite, *Mater. Res. Bull.* 35 (2000) 1747–1753.
- [120] M. Malassis, H. Zagnazi, P. Poix, C. Chaumont, J.C. Bernier, Structure of cobalt and fluorine doped hexaferrites, *J. Mater. Sci.* 27 (1992) 876–880.
- [121] İ. Araz, F. Genç, Development of broadband microwave absorber and measurement of its magnetic and microwave properties, *J. Supercond. Nov. Magn.* 31 (2018) 279–283. <https://doi.org/10.1007/s10948-017-4216-0>.
- [122] İ. Araz, Microwave Charecterization of Co-Doped Barium Hexaferrite Absorber Metarial, *J. Supercond. Nov. Magn.* 29 (2016) 1545–1550. <https://doi.org/10.1007/s10948-016-3447-9>.
- [123] J. Kreisel, H. Vincent, F. Tasset, P. Wolfers, The magnetic anisotropy change of  $\text{BaFe}_{12-2x}\text{Ir}_x\text{Co}_x\text{O}_{19}$ : single-crystal neutron diffraction study of the accompanying atomic and magnetic structures, *J. Magn. Magn. Mater.* 213 (2000) 262–270.
- [124] A. Gruskova, J. Lipka, M. Papanova, D. Kevicka, A. Gonzalez, G. Mendoza, I. Toth, J. Slama, Mössbauer Study of Microstructure and Magnetic Properties (Co , Ni)– Zr Substituted Ba Ferrite Particles, *Hyperfine Interact.* 156/157 (2004) 187–194.
- [125] J. Slama, A. Gruskova, M. Papanova, D. Kevicka, D. R, V. Jancarik, A. Gonzalez, M. G, Magnetic properties of Me – Zr substituted Ba – hexaferrite, *J. Magn. Magn. Mater.* 276 (2004) 385–387. <https://doi.org/10.1016/j.jmmm.2003.11.156>.
- [126] S.M. Abbas, R. Chatterjee, A.K. Dixit, A.V.R. Kumar, T.C. Goel, Electromagnetic and microwave absorption properties of  $(\text{Co}^{2+}-\text{Si}^{4+})$  substituted barium hexaferrites and its polymer composite, *J. Appl. Phys.* 101 (2007) 074105. <https://doi.org/10.1063/1.2716379>.
- [127] S.M.M. Abbas, A.K.K. Dixit, R. Chatterjee, T.C.C. Goel, Complex permittivity, complex permeability and microwave absorption properties of ferrite-polymer composites, *J. Magn. Magn. Mater.* 309 (2007) 20–24. <https://doi.org/10.1016/j.jmmm.2006.06.006>.
- [128] Y. Guan, Y. Lin, L. Zou, Q. Miao, M. Zeng, Z. Liu, X. Gao, J. Liu, The effects of Co-Ti co-doping on the magnetic, electrical, and magnetodielectric behaviors of M-type barium hexaferrites, *AIP Adv.* 3 (2013) 122115. <https://doi.org/10.1063/1.4860948>.

- [129] J. Lee, Y.-K. Hong, W. Lee, G.S. Abo, J. Park, N. Neveu, W. Seong, S. Park, W.-K. Ahn, Soft M-type hexaferrite for very high frequency miniature antenna applications, *J. Appl. Phys.* 111 (2012) 07A520. <https://doi.org/10.1063/1.3679468>.
- [130] O. Kubo, T. Ido, Y. H, Properties of Ba ferrite particles for perpendicular magnetic recording media, *IEEE Trans. Magn.* 18 (1982) 0–2.
- [131] G.K. Thompson, J. Evans, Order-disorder and magnetic exchange interactions strontium hexaferrite  $\text{SrA}_x\text{Fe}_{12-x}\text{O}_{19}$  (A = Ga, In) in substituted, *J. Appl. Phys.* 75 (1994) 6643–6645.
- [132] Puneet Sharma., R.A. Rocha, S.N. Medeiros, B. Hallouche, A.P. Jr., Structural and magnetic studies on mechanosynthesized  $\text{BaFe}_{12-x}\text{Mn}_x\text{O}_{19}$ , *J. Magn. Magn. Mater.* 316 (2007) 29–33. <https://doi.org/10.1016/j.jmmm.2007.03.207>.
- [133] M. V Bukhtiyarova, A.S. Ivanova, E.M. Slavinskaya, L.M. Plyasova, V.A. Rogov, V. V Kaichev, A.S. Noskov, Catalytic combustion of methane on substituted strontium ferrites, *Fuel.* 90 (2011) 1245–1256. <https://doi.org/10.1016/j.fuel.2010.11.012>.
- [134] V.A.M. Brabers, A.A.E. Stevens, J.H.J. Dalderop, Z. Simga, Magnetization and magnetic anisotropy of  $\text{BaFe}_{12-x}\text{Ti}_x\text{O}_{19}$  hexaferrites, *J. Magn. Magn. Mater.* 196–197 (1999) 312–314.
- [135] P.A.-C. Marino, A.C. Moreno-Borges, G. Orozco-Melgar, J.A. Garcia, E. Govea-Alcaide, Structural and magnetic study of the  $\text{Ti}^{4+}$ -doped barium hexaferrite ceramic samples : Theoretical and experimental results, *Phys. B Phys. Condens. Matter.* 406 (2011) 3130–3136. <https://doi.org/10.1016/j.physb.2011.03.084>.
- [136] P.A. Mariño-Castellanos, J. Anglada-Rivera, A. Cruz-Fuentes, R. Lora-Serrano, Magnetic and microstructural properties of the  $\text{Ti}^{4+}$ -doped Barium hexaferrite, *J. Magn. Magn. Mater.* 280 (2004) 214–220. <https://doi.org/10.1016/j.jmmm.2004.03.015>.
- [137] P. Behera, S. Ravi, Influence of Ti-substitution on structural, magnetic and dielectric properties of M-Type barium hexaferrite, *J. Electron. Mater.* 48 (2019) 5062–5074. <https://doi.org/10.1007/s11664-019-07310-7>.
- [138] Y. Liu, Y. Li, H. Zhang, D. Chen, Q. Wen, Study on magnetic properties of low temperature sintering M-Barium hexaferrites, *J. Appl. Phys.* 107 (2010) 1–3. <https://doi.org/10.1063/1.3338846>.
- [139] W. Jingwu, J. Meiyang, J.L. E, S.H.E. Jiawei, Magnetic properties of La-Zn substituted Sr-hexaferrites by self-propagation high-temperature synthesis, *J. Rare Earths.* 26 (2008) 81–84.
- [140] S. Verma, S. Mahadevan, C. Pahwa, A.P. Singh, S.B. Narang, N. Aggarwal, P. Sharma, Improved Magnetic and Microwave Properties of La-Substituted Barium Hexaferrite Screen-Printed Thick Films, *J. Supercond. Nov. Magn.* 33 (2020) 2507–2512. <https://doi.org/10.1007/s10948-020-05494-2>.
- [141] C.A. Stergiou, I. Manolakis, T. V Yioultsis, G.L. Ā, Dielectric and magnetic properties of new rare-earth substituted Ba- hexaferrites in the 2 – 18 GHz frequency range, *J. Magn. Magn. Mater.* 322 (2010) 1532–1535.

- <https://doi.org/10.1016/j.jmmm.2009.07.082>.
- [142] M.J. Iqbal, S. Farooq, Impact of Pr – Ni substitution on the electrical and magnetic properties of chemically derived nanosized strontium – barium hexaferrites, *J. Alloys Compd.* 505 (2010) 560–567. <https://doi.org/10.1016/j.jallcom.2010.06.073>.
- [143] H. Yanbing, S. Jian, S. Lina, T. Quan, L. Qin, J. Hongxiao, J. Dingfeng, Tailored magnetic properties of Sm ( Zn ) substituted nanocrystalline barium hexaferrites, *J. Alloy. Compd. J.* 486 (2009) 348–351. <https://doi.org/10.1016/j.jallcom.2009.06.143>.
- [144] H. Lou, X. Lu, Y.L. Pan, X. Wang, J. Wang, S. Sun, C. He, Q. Song, Ba<sub>1-x</sub>La<sub>x</sub>Fe<sub>12</sub>O<sub>19</sub> (x = 0.0, 0.2, 0.4, 0.6) hollow microspheres: material parameters, magnetic and microwave absorbing properties, *J. Mater. Sci. Mater. Electron.* 27 (2016) 11231–11240. <https://doi.org/10.1007/s10854-016-5243-5>.
- [145] F.K. Lotgering, P.R. Locher, R.P. van Stapele, Anisotropy of hexagonal ferrites with M, W and Y structures containing Fe<sup>3+</sup> and Fe<sup>2+</sup> as magnetic ions, *J. Phys. Chem. Solids.* 41 (1980) 481–487. [https://doi.org/10.1016/0022-3697\(80\)90178-X](https://doi.org/10.1016/0022-3697(80)90178-X).
- [146] K. Knížek, P. Novák, M. Küpferling, Electronic structure and conductivity of ferroelectric hexaferrite: Ab initio calculations, *Phys. Rev. B - Condens. Matter Mater. Phys.* 73 (2006) 2–5. <https://doi.org/10.1103/PhysRevB.73.153103>.
- [147] F. Kools, A. Morel, R. Grössinger, J.M. Le Breton, P. Tenaud, R. Grossinger, J.M. Le Breton, P. Tenaud, LaCo-substituted ferrite magnets, a new class of high-grade ceramic magnets; intrinsic and microstructural aspects, *J. Magn. Mater.* 245 (2002) 1270–1276. [https://doi.org/10.1016/S0304-8853\(01\)00988-X](https://doi.org/10.1016/S0304-8853(01)00988-X).
- [148] P. Novák, J. Ruzs, Exchange interactions in barium hexaferrite, *Phys. Rev. B - Condens. Matter Mater. Phys.* 71 (2005) 1–6. <https://doi.org/10.1103/PhysRevB.71.184433>.
- [149] C. Wu, Z. Yu, K. Sun, J. Nie, R. Guo, H. Liu, X. Jiang, Z. Lan, Calculation of exchange integrals and Curie temperature for La-substituted barium hexaferrites, *Sci. Rep.* 6 (2016) 1–8. <https://doi.org/10.1038/srep36200>.
- [150] J. Park, Y.K. Hong, W. Lee, B.C. Choi, C.J. Choi, Electronic structure of La-Co substituted strontium hexaferrite (Sr<sub>1-x</sub>La<sub>x</sub>Fe<sub>12-x</sub>Co<sub>x</sub>O<sub>19</sub>) permanent magnet, *IEEE Magn. Lett.* 7 (2016) 2014–2016. <https://doi.org/10.1109/LMAG.2015.2501285>.
- [151] J. Le Breton, J. Teillet, G. Wiesinger, A. Morel, F. Kools, P. Tenaud, Mössbauer Investigation of Sr – Fe – O Hexaferrites With La – Co Addition, *IEEE Trans. Magn.* 38 (2002) 2952–2954.
- [152] X. Liu, W. Zhong, S. Yang, Z. Yu, B. Gu, Y. Du, Influences of La<sup>3+</sup> substitution on the structure and magnetic properties of M-type strontium ferrites, *J. Magn. Mater.* 238 (2002) 207–214. [https://doi.org/10.1016/S0304-8853\(01\)00914-3](https://doi.org/10.1016/S0304-8853(01)00914-3).
- [153] P.C. Dorsey, T.D.B. Chrisey, J.S. Horwitz, P. Lubitz, R.C.Y. Auyeung, Oriented barium hexaferrite thick films grown on c-plane and m-plane sapphire substrates, *IEEE Trans. Magn.* 30 (1994) 4512–4517. <https://doi.org/10.1109/20.334133>.
- [154] F. Huang, J.J. Wolfgang, T.M. Le, D.N. Lambeth, D.D. Stancil, Oxygen Pressure

- Dependence of Laser Deposited Barium Ferrite Films on LLC(111), *IEEE Trans. Magn.* 31 (1995) 3826–3828. <https://doi.org/10.1109/20.489785>.
- [155] S.D. Yoon, C. Vittoria, S.A. Oliver, Magnetic and microwave magnetic properties of barium hexaferrite permanent magnet films having the c-axis in the film plane, *J. Appl. Phys.* 93 (2003) 4023–4026. <https://doi.org/10.1063/1.1544083>.
- [156] Z. Chen, A. Yang, A. Gieler, V.G. Harris, C. Vittoria, P.R. Ohodnicki, K.Y. Goh, M.E. Mchenry, Z. Cai, T.L. Goodrich, K.S. Ziemer, Epitaxial growth of M-type Ba-hexaferrite films on MgO (111)|| SiC(0001) with low ferromagnetic resonance linewidths, *Appl. Phys. Lett.* 91 (2007) 182505. <https://doi.org/10.1063/1.2794011>.
- [157] K. Takahashi, T. Yoshio, K. Oda, F. Kanamaru, Crystallization of amorphous BaOxFe<sub>2</sub>O<sub>3</sub> prepared by the method without melting, *J. Non. Cryst. Solids.* 42 (1980) 157–163. [https://doi.org/10.1016/0022-3093\(80\)90017-4](https://doi.org/10.1016/0022-3093(80)90017-4).
- [158] E. Lacroix, P. Gerard, G. Marest, M. Dupuy, Substrate effects on the crystalline orientation of barium hexaferrite films, *J. Appl. Phys.* 69 (1991) 4770–4772. <https://doi.org/10.1063/1.348274>.
- [159] B. Ramamurthy Acharya, S. Prasad, N. Venkataramani, S.N. Shringi, R. Krishnan, The effect of deposition and annealing conditions on textured growth of sputter-deposited strontium ferrite films on different substrates, *J. Appl. Phys.* 79 (1996) 478. <https://doi.org/10.1063/1.360854>.
- [160] S. Capraro, J.P.P. Chatelon, M. Le Berre, H. Joisten, T. Rouiller, B. Bayard, D. Barbier, J.J.J. Rousseau, Barium ferrite thick films for microwave applications, *J. Magn. Mater.* 272–276 (2004) E1805–E1806. <https://doi.org/10.1016/j.jmmm.2003.12.871>.
- [161] A. Dehlinger, M. Le Berre, E. Bènevent, H. Hassane, Development of millimeter wave integrated circulator based on barium ferrite, *Mater. Sci. Eng. C.* 28 (2008) 755–758. <https://doi.org/10.1016/j.msec.2007.10.063>.
- [162] Y. Li, Y. Liu, J. Li, K. Yang, H. Zhang, Magnetic and self-biased properties of highly oriented M-type barium ferrite films on Pt-coated Si substrate by magnetron sputtering, *J. Appl. Phys.* 113 (2013) 17–306. <https://doi.org/10.1063/1.4798608>.
- [163] N.R. Anderson, R.E. Camley, Multilayer magnetic waveguides: Optimizing nonreciprocal propagation in the 50-70GHz range, *J. Appl. Phys.* 116 (2014) 023903. <https://doi.org/10.1063/1.4887077>.
- [164] B. Peng, J.Y. Jiang, W.L.X. Zhang, H.Z. Xu, W.L.X. Zhang, Thickness effects in barium hexaferrite films deposited by magnetron sputtering, *Mater. Res. Innov.* 19 (2015) S8-654-S8-656. <https://doi.org/10.1179/1432891715Z.0000000001767>.
- [165] R. Bodeux, D. Michau, M. Maglione, M. Josse, Thin films sputtered from Ba<sub>2</sub>NdFeNb<sub>4</sub>O<sub>15</sub> multiferroic targets on BaFe<sub>12</sub>O<sub>19</sub> coated substrates, *Mater. Res. Bull.* 81 (2016) 49–54.
- [166] X. Dong, H. Li, J. Chen, D. Chen, J. Shen, Y. Chen, Ferromagnetic resonance linewidth and magnetic properties of highly c-axis oriented barium ferrite thin films by magnetron sputtering, *Mater. Res. Express.* 6 (2019) 096104. <https://doi.org/10.1088/2053-1591/ab2cee>.
- [167] E.J. Donahue, D.M. Schleich, The deposition of BaFe<sub>12</sub>O<sub>19</sub> by metalorganic

- chemical vapor deposition, *J. Appl. Phys.* 71 (1992) 6013–6017.  
<https://doi.org/10.1063/1.350456>.
- [168] D.F. Ryder, J.H. Fenstermacher, Processing and Characterization of Hexagonal Ferrite Thin Films from Organometallic Compounds, *J. Am. Ceram. Soc.* 73 (1990) 282–285. <https://doi.org/10.1111/j.1151-2916.1990.tb06507.x>.
- [169] S. Saleemizadeh, S.A. Seyyed Ebrahimi, Influence of Fe/Ba ratio, basic agent and calcination temperature on the physical properties of nanocrystalline barium hexaferrite thin films prepared by a sol-gel method, *J. Non. Cryst. Solids.* 355 (2009) 982–985. <https://doi.org/10.1016/j.jnoncrysol.2009.04.014>.
- [170] S.M. Masoudpanah, S. a. Seyyed Ebrahimi, Synthesis and characterization of nanostructured strontium hexaferrite thin films by the sol-gel method, *J. Magn. Magn. Mater.* 324 (2012) 2239–2244.  
<https://doi.org/10.1016/j.jmmm.2012.02.109>.
- [171] I. Harward, Y. Nie, D. Chen, J. Baptist, J.M. Shaw, E. Al, Physical properties of Al doped Ba hexagonal ferrite thin films, *J. Appl. Phys.* 113 (2013).  
<https://doi.org/10.1063/1.4788699>.
- [172] H.L. Glass, J.H.W. Liaw, Growth and characterization of LPE hexagonal ferrites, *J. Appl. Phys.* 49 (1978) 1578–1581. <https://doi.org/10.1063/1.324913>.
- [173] F. Haberey, R. Leckebusch, M. Rosenberg, K. Sahl, Preparation and magnetic properties of LPE-grown hexagonal strontium aluminoferrite films, *Mater. Res. Bull.* 15 (1980) 493–500. [https://doi.org/10.1016/0025-5408\(80\)90056-2](https://doi.org/10.1016/0025-5408(80)90056-2).
- [174] M.S. Yuan, H.L. Glass, L.R. Adkins, Epitaxial barium hexaferrite on sapphire by sputter deposition, *Appl. Phys. Lett.* 53 (1988) 340–341.  
<https://doi.org/10.1063/1.100601>.
- [175] J. Jalli, Y.K. Hong, S. Bae, J.J. Lee, G.S. Abo, A. Lyle, S.H. Gee, H. Lee, T. Mewes, J.C. Sur, S.I. Lee, Growth and characterization of 144  $\mu\text{m}$  thick barium ferrite single crystalline film for microwave device application, *J. Appl. Phys.* 105 (2009) 07A511. <https://doi.org/10.1063/1.3062824>.
- [176] L.D. Živanov, P.M. Nikolić, O.S. Aleksić, Thick film MM-wave isolator, *Le J. Phys. Colloq.* 49 (1988) C8-2021-C8-2022.  
<https://doi.org/10.1051/jphyscol:19888918>.
- [177] L.J.D. Zivanov, P.M. Nikolic, O. Aleksic, Thick film fin-line isolators for the R-band, in: 6th Mediterr. Electrotech. Conf., Publ by IEEE, 1992: pp. 150–153.  
<https://doi.org/10.1109/melcon.1991.161801>.
- [178] Y. Chen, T. Sakai, T. Chen, S.D. Yoon, A.L. Geiler, C. Vittoria, V.G. Harris, Oriented barium hexaferrite thick films with narrow ferromagnetic resonance linewidth, *Appl. Phys. Lett.* 88 (2006) 1–3. <https://doi.org/10.1063/1.2173240>.
- [179] Y. Chen, T. Sakai, T. Chen, S.D. Yoon, C. Vittoria, V.G. Harris, Screen printed thick self-biased, low-loss, barium hexaferrite films by hot-press sintering, *J. Appl. Phys.* 100 (2006) 1–9. <https://doi.org/10.1063/1.2221527>.
- [180] Y. Chen, I. Smith, A.L. Geiler, C. Vittoria, V. Zagorodnii, Z. Celinski, V.G. Harris, Realization of hexagonal barium ferrite thick films on Si substrates using a screen printing technique, *J. Phys. D: Appl. Phys.* 41 (2008) 095006.

- <https://doi.org/10.1088/0022-3727/41/9/095006>.
- [181] D.C.C. Kulkarni, V. Puri, Ku band microwave studies of fritless strontium hexaferrite thick films, *Microelectron. Int.* 27 (2010) 143–147. <https://doi.org/10.1108/13565361011061948>.
- [182] D.C. Kulkarni, V. Puri, Broad band absorbance of barium hexaferrite thick films in the 8-12 GHz frequency spectrum, *Electron. Mater. Lett.* 7 (2011) 51–57. <https://doi.org/10.1007/s13391-011-0308-3>.
- [183] D.M. Chen, Y.L. Liu, Y.X. Li, K. Yang, H.W. Zhang, Texture and self-biased property of an oriented M-type barium ferrite thick film by tape casting, *Chinese Phys. B.* 21 (2012) 2010–2013. <https://doi.org/10.1088/1674-1056/21/6/067502>.
- [184] M. Bellotto, G. Busca, C. Cristiani, G. Groppi, FT-IR Skeletal Powder Spectra of Ba--Aluminas with Compositions  $\text{BaAl}_9\text{O}_{14.5}$ ,  $\text{BaAl}_{12}\text{O}_{19}$ , and  $\text{BaAl}_{14}\text{O}_{22}$  and of Ba-Ferrite,  $\text{BaFe}_{12}\text{O}_{19}$ , *J. Solid State Chem.* 117 (1995) 8–15.
- [185] V.N. Dhage, M.L. Mane, A.P. Keche, C.T. Birajdar, K.M. Jadhav, Structural and magnetic behaviour of aluminium doped barium hexaferrite nanoparticles synthesized by solution combustion technique, *Phys. B Condens. Matter.* 406 (2011) 789–793. <https://doi.org/10.1016/j.physb.2010.11.094>.
- [186] S.M. El-Sayed, T.M. Meaz, M.A. Amer, H.A. El Shersaby, H.A. El Shersaby, Magnetic behavior and dielectric properties of aluminum substituted M-type barium hexaferrite, *Phys. B Condens. Matter.* 426 (2013) 137–143. <https://doi.org/10.1016/j.physb.2013.06.026>.
- [187] B.D. Cullity, *Elements of X-ray Powder Diffraction*, Addison–Wesley Publishing Company, Inc.: USA, 1978.
- [188] G. Caglioti, A. Paoletti, F.P. Ricci, Choice of Collimators for a Crystal Spectrometer for Neutron Diffraction, *Nucl. Instruments.* 3 (1958) 223–228.
- [189] J. Kreisel, G. Lucazeau, H. Vincent, Raman Spectra and Vibrational Analysis of  $\text{BaFe}_{12}\text{O}_{19}$  Hexagonal Ferrite, *J. Solid State Chem.* 137 (1998) 127–137. <https://doi.org/10.1006/jssc.1997.7737>.
- [190] F. Song, X. Shen, J. Xiang, H. Song, Formation and magnetic properties of M-Sr ferrite hollow fibers via organic gel-precursor transformation process, *Mater. Chem. Phys.* 120 (2010) 213–216. <https://doi.org/10.1016/j.matchemphys.2009.10.048>.
- [191] A. Sahai, N. Goswami, Structural and vibrational properties of ZnO nanoparticles synthesized by the chemical precipitation method, *Phys. E Low-Dimensional Syst. Nanostructures.* 58 (2014) 130–137. <https://doi.org/10.1016/j.physe.2013.12.009>.
- [192] S. Thongmee, T. Osotchan, P. Winotai, I.M. Tang, Fluctuations in the local fields due to  $\text{Al}^{3+}$  ions substitution in the M-Type barium hexaferrites,  $\text{BaFe}_{12-x}\text{Al}_x\text{O}_{12}$ , *Int. J. Mod. Phys. B.* 12 (1998) 2847–2855. <https://doi.org/10.1142/S0217979298001666>.
- [193] A. Trukhanov, L. Panina, S. Trukhanov, V. Turchenko, M. Salem, Evolution of structure and physical properties in Al-substituted Ba-hexaferrites, *Chinese Phys. B.* 25 (2016) 016102. <https://doi.org/10.1088/1674-1056/25/1/016102>.

- [194] R. Grossinger, A critical examination of the law of approach to saturation. I. Fit procedure, *Phys. Status Solidi*. 66 (1981) 665–674.
- [195] M.A. Gilleo, Superexchange Interaction Energy for  $\text{Fe}^{3+}\text{-O}-\text{Fe}^{3+}$  Linkages, *Phys. Rev.* 109 (1958) 777–781.
- [196] D. Chen, I. Harward, J. Baptist, S. Goldman, Z. Celinski, Curie temperature and magnetic properties of aluminum doped barium ferrite particles prepared by ball mill method, *J. Magn. Magn. Mater.* 395 (2015) 350–353.
- [197] G. Turilli, A. Paoluzi, M. Lucenti, Surface doping with Al in Ba-hexaferrite powders, *J. Magn. Magn. Mater.* 97 (1991) 338–342.
- [198] S.B. Narang, K. Pubby, C. Singh, Thickness and Composition Tailoring of K- and Ka-Band Microwave Absorption of  $\text{BaCo}_x\text{Ti}_x\text{Fe}_{(12-2x)}\text{O}_{19}$  Ferrites, *J. Electron. Mater.* 46 (2017) 718–728. <https://doi.org/10.1007/s11664-016-5059-3>.
- [199] P.A. Mariño-Castellanos, J. Anglada-Rivera, A. Cruz-Fuentes, R. Lora-Serrano, Magnetic and microstructural properties of the  $\text{Ti}^{4+}$ -doped Barium hexaferrite, *J. Magn. Magn. Mater.* 280 (2004) 214–220. <https://doi.org/10.1016/j.jmmm.2004.03.015>.
- [200] M. V Rane, D. Bahadur, A.K. Nigam, C.M. Srivastava, Mössbauer and FT-IR studies on non-stoichiometric barium hexaferrites, *J. Magn. Magn. Mater.* 192 (1999) 288–296.
- [201] W.Y. Zhao, P. Wei, X.Y. Wu, W. Wang, Q.J. Zhang, Lattice vibration characterization and magnetic properties of M -type barium hexaferrite with excessive iron, *J. Appl. Phys.* 103 (2008) 10–14. <https://doi.org/10.1063/1.2884533>.
- [202] R.A. El-Mallawany, Theoretical and experimental IR spectra of binary rare earth tellurite glasses—1, *Infrared Phys.* 29 (1989) 781–785. [https://doi.org/10.1016/0020-0891\(89\)90125-5](https://doi.org/10.1016/0020-0891(89)90125-5).
- [203] O. Carp, B. Ruxandra, E. Segal, M. Brezeanu, Nonconventional methods for obtaining hexaferrites II. Barium hexaferrite, *Thermochi.* 318 (1998) 57–62. [https://doi.org/10.1016/S0040-6031\(98\)00352-9](https://doi.org/10.1016/S0040-6031(98)00352-9).
- [204] A. Morel, J.M. Le Breton, J. Kreisel, G. Wiesinger, F. Kools, P. Tenaud, Sublattice occupation in  $\text{Sr}_{1-x}\text{La}_x\text{Fe}_{12-x}\text{Co}_x\text{O}_{19}$  hexagonal ferrite analyzed by Mossbauer spectrometry and Raman spectroscopy, *J. Magn. Magn. Mater.* 242–245 (2002) 1405–1407.
- [205] P. Singh, V.K. Babbar, A. Razdan, S.L. Srivastava, V.K. Agrawal, T.C. Goel, Dielectric constant, magnetic permeability and microwave absorption studies of hot-pressed Ba-CoTi hexaferrite composites in X-band, *J. Mater. Sci.* 41 (2006) 7190–7196. <https://doi.org/10.1007/s10853-006-0921-y>.
- [206] S.B. Narang, K. Pubby, S.K. Chawla, P. Kaur, Origin of absorption peaks in reflection loss spectrum in Ku- frequency band of Co-Zr substituted strontium hexaferrites prepared using sucrose precursor, *J. Magn. Magn. Mater.* 426 (2017) 202–205. <https://doi.org/10.1016/j.jmmm.2016.11.054>.
- [207] M.S. Pinho, M.L. Gregori, R.C.R. Nunes, B.G. Soares, Performance of radar absorbing materials by waveguide measurements for X- and Ku-band frequencies,

- Eur. Polym. J. 38 (2002) 2321–2327. [https://doi.org/10.1016/S0014-3057\(02\)00118-0](https://doi.org/10.1016/S0014-3057(02)00118-0).
- [208] S. Verma, P. Sharma, O.P. Pandey, A. Paesano, A. Sun, Structure and Magnetic Properties of  $\text{Ba}_{1-x}\text{La}_x\text{Fe}_{12}\text{O}_{19}$  Prepared by  $\text{Ba}_{1-x}\text{La}_x\text{Fe}_2\text{O}_4$ , IEEE Trans. Magn. 50 (2014) 2101004.
- [209] S. Verma, O.P. Pandey, A. Paesano Jr, P. Sharma, Comparison of structural and magnetic properties of  $\text{La}^{3+}$  substituted  $\text{BaFe}_{12}\text{O}_{19}$  prepared by different substitution methods, Phys. B Condens. Matter. 448 (2014) 57–59. <https://doi.org/http://dx.doi.org/10.1016/j.physb.2014.03.035>.
- [210] B.J. Evans, F. Grandjean, A.P. Lilot, R.H. Vogel, A. Gérard,  $^{57}\text{Fe}$  hyperfine interaction parameters and selected magnetic properties of high purity  $\text{MFe}_{12}\text{O}_{19}$  (M=Sr, Ba), J. Magn. Magn. Mater. 67 (1987) 123–129. [https://doi.org/10.1016/0304-8853\(87\)90728-1](https://doi.org/10.1016/0304-8853(87)90728-1).
- [211] C.H. Sauer, U. Kobler, W. Zinn, High Field Mossbauer effect study of  $\text{LaFe}_{12}\text{O}_{19}$ , J. Phys. Chem. Solids. 39 (1978) 1197–1201.
- [212] H. Nakamura, A. Shimoda, T. Waki, Y. Tabata, C. Mény, Site-dependent cobalt electronic state in La-Co co-substituted magnetoplumbite-type ferrite:  $^{59}\text{Co}$  nuclear magnetic resonance study, J. Phys. Condens. Matter. 28 (2016). <https://doi.org/10.1088/0953-8984/28/34/346002>.
- [213] L. Lechevallier, J.M. Le Breton, J. Teillet, A. Morel, F. Kools, P. Tenaud, Mossbauer investigation of  $\text{Sr}_{1-x}\text{La}_x\text{Fe}_{12-y}\text{Co}_y\text{O}_{19}$  ferrites, Phys. B. 327 (2003) 135–139.
- [214] C. Herme, S.E. Jacobo, P.G. Bercoff, B. Arcondo, Mössbauer analysis of Nd-Co M-type strontium hexaferrite powders with different iron content, Hyperfine Interact. 195 (2009) 205–212. <https://doi.org/10.1007/s10751-009-0121-7>.
- [215] B.D. Cullity, C.D. Graham, Introduction to Magnetic Materials, John Wiley & Sons, Inc., Hoboken, NJ, USA, 2008. <https://doi.org/10.1002/9780470386323>.
- [216] S. Ounnunkad, Improving magnetic properties of barium hexaferrites by La or Pr substitution, Solid State Commun. 138 (2006) 472–475. <https://doi.org/10.1016/j.ssc.2006.03.020>.
- [217] R. Malik, S. Annapoorni, S. Lamba, V. Raghavendra Reddy, A. Gupta, P. Sharma, A. Inoue, Mössbauer and magnetic studies in nickel ferrite nanoparticles: Effect of size distribution, J. Magn. Magn. Mater. 322 (2010) 3742–3747. <https://doi.org/10.1016/j.jmmm.2010.07.019>.
- [218] Z.F. Zi, Q.C. Liu, J.M. Dai, Y.P. Sun, Effects of Ce-Co substitution on the magnetic properties of M-type barium hexaferrites, Solid State Commun. 152 (2012) 894–897. <https://doi.org/10.1016/j.ssc.2012.02.007>.
- [219] S. V. Trukhanov, Peculiarities of the magnetic state in the system  $\text{La}_{0.70}\text{Sr}_{0.30}\text{MnO}_{(3-\gamma)}$  ( $0 \leq \gamma \leq 0.25$ ), J. Exp. Theor. Phys. 100 (2005) 95–105. <https://doi.org/10.1134/1.1866202>.
- [220] S. V. Trukhanov, I.O. Troyanchuk, A. V. Trukhanov, I.M. Fita, A.N. Vasil'ev, A. Maignan, H. Szymczak, Magnetic properties of  $\text{La}_{0.70}\text{Sr}_{0.30}\text{MnO}_{2.85}$  anion-deficient manganite under hydrostatic pressure, JETP Lett. 83 (2006) 33–36.

- <https://doi.org/10.1134/S0021364006010085>.
- [221] V. Šepelák, M. Myndyk, R. Witte, J. Röder, D. Menzel, R.H. Schuster, H. Hahn, P. Heitjans, K.-D. Becker, The mechanically induced structural disorder in barium hexaferrite, BaFe<sub>12</sub>O<sub>19</sub>, and its impact on magnetism, *Faraday Discuss.* 170 (2014) 121–135. <https://doi.org/10.1039/C3FD00137G>.
- [222] M. Manikandan, C. Venkateswaran, Effect of high energy milling on the synthesis temperature, magnetic and electrical properties of barium hexagonal ferrite, *J. Magn. Magn. Mater.* 358–359 (2014) 82–86. <https://doi.org/10.1016/j.jmmm.2014.01.041>.
- [223] P. Sharma, R.A. Rocha, S.N. de Medeiros, A. Paesano, S.N. De Medeiros, A.P. Jr, Structural and magnetic studies on barium hexaferrites prepared by mechanical alloying and conventional route, *J. Alloys Compd.* 443 (2007) 37–42. <https://doi.org/10.1016/j.jallcom.2006.10.022>.
- [224] R. Nowosielski, R. Babilas, G. Dercz, L. Pajak, J. Wrona, Barium ferrite powders prepared by milling and annealing, *J. Achiev. Mater. Manuf. Eng.* 22 (2007) 45–48.
- [225] F.K. Lotgering, Topotactical reactions with ferrimagnetic oxides having hexagonal crystal structures-II, *J. Inorg. Nucl. Chem.* 16 (1960) 100–108. [https://doi.org/10.1016/0022-1902\(60\)80092-9](https://doi.org/10.1016/0022-1902(60)80092-9).
- [226] D.R. Franklin, A.J. Pointon, R.C.L. Jenkins, Franklin D R, Pointon A J, Jenkins R C L, Resonance linewidths and crystallite alignment in oriented samples of polycrystalline barium hexaferrite, *J. Phys. D. Appl. Phys.* 29 (1996) 1268–1273. <https://doi.org/10.1088/0022-3727/29/5/021>.

## Supplementary studies

The other supplementary work carried out on the prepared samples are given in this section.

### 1. Impedance studies of on Co-substituted BaM

The XRD pattern and SEM of BaCoM powder calcined at 1200 °C are shown in [fig. S1](#). The refinement showed the existence of inevitable minor W-type phase with volume percent less than 3.5 %. Fractured surface micrograph showed Co substitution promotes grain growth with well distinguished hexagonal platelets. The increase in average grain size from 2.9 to 9.8  $\mu\text{m}$  is a consequence of oxygen vacancies and defect transportation.

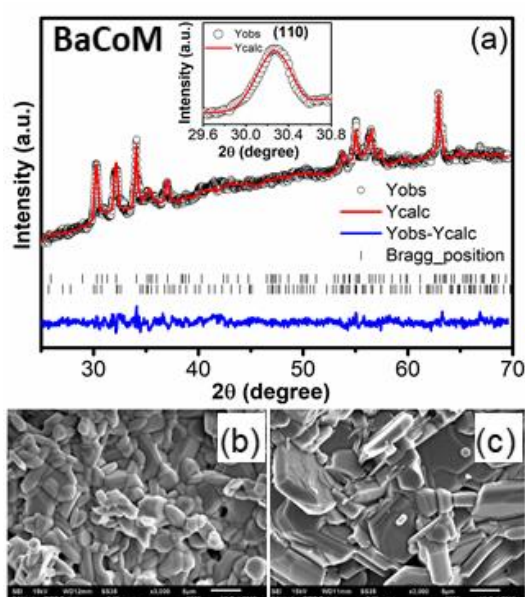


**Fig. S1.** XRD pattern and SEM micrograph BaM and BaCoM sintered pellets.

[Fig.S2](#) shows the room temperature magnetisation plot of BaM and BaCoM. No visible change in magnetisation was observed, however, coercivity ( $H_c$ ) were drastically decreased. The calculated magnetocrystalline anisotropy also found to decrease (10 kOe to 6.9 kOe) with cobalt substitution. It can be concluded that hard magnetic behaviour of BaM transformed to soft magnetic with nearly retained magnetization, hence makes more magnetically permeable.

[Fig. S3](#) illustrates the deconvoluted XPS spectra of BaM and BaCoM. The Fe2p spectra contains seven spectra for  $\text{Fe}^{3+}$  and  $\text{Fe}^{2+}$  ions with an area ratio of 76:24 and 68:32 for BaM and BaCoM, respectively. O1s spectra of BaCoM, fitted with two sub spectra of  $\text{O}^{2-}$  and oxygen defect vacancies ( $\text{O}^{\delta-}$ ). The oxygen defect vacancies were found to be higher in BaCoM (45%) as compare to BaM (25%). Co2p spectrum fitted for  $\text{Co}^{3+}$  and

$\text{Co}^{2+}$  ions and the calculated area ratio of  $\text{Co}^{3+}$  and  $\text{Co}^{2+}$  ions were 69:31. The presence of  $\text{Co}^{2+}$  ions increases  $\text{Fe}^{2+}$  ions and oxygen defects to maintain the charge neutrality.

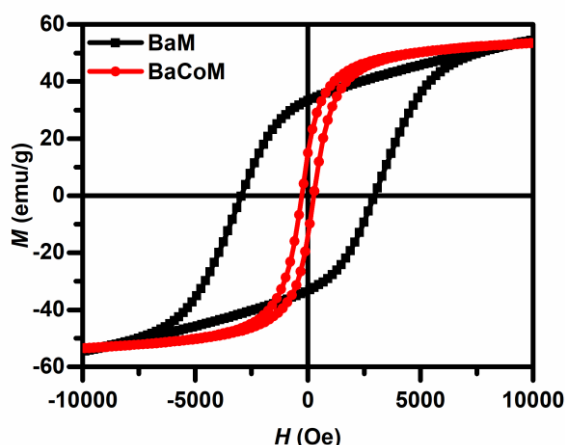


**Fig. S2.**  $M$ - $H$  plots of BaM and BaCoM.

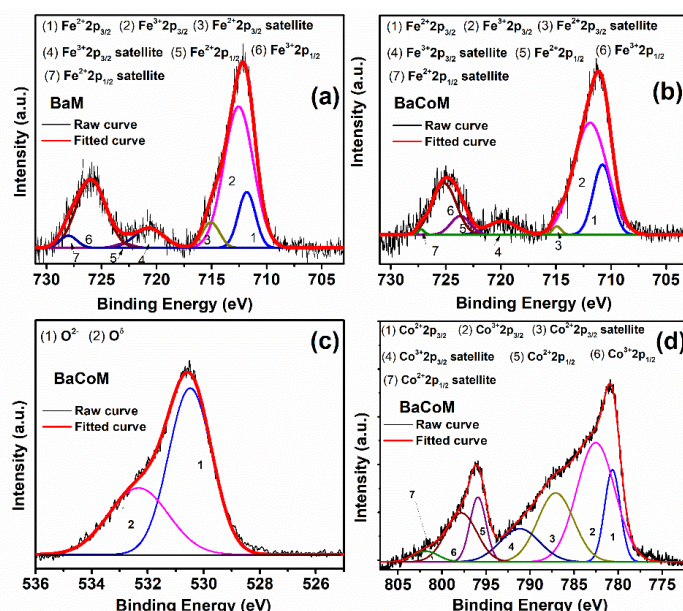


**Fig. S3.** Deconvoluted XPS spectra of sintered pellets, (a) Iron ions in BaM, (b) Iron ions in BaCoM, (c) Oxygen ions in BaCoM and (d) Cobalt ions in BaCoM

The variation in imaginary impedance ( $Z''$ ) with frequency at different temperatures for both BaM and BaCoM are shown in [fig. S4](#).  $Z''$  found to decrease with increase in both frequency and temperature which finally merges to a single frequency that suggests  $Z''$  is frequency independent. The broad relaxation peak(s) shifts toward higher frequency with temperature which confirms electrical responses are thermally activated. The normalised imaginary part of impedance ( $Z''/Z''_{\max}$ ) with frequency at selected temperatures are also shown. The peak position corresponds to relaxation frequency ( $f_{\max}$ ). At 323 K, BaM do not show relaxation peak in the observed frequency

range (10 Hz– 10 MHz). Two resolved asymmetric relaxation peak confirms the multiple relaxations are present in the material at different frequency domains. For BaCoM, single Debye like relaxation peak was found for all temperature. The different  $f_{max}$  for BaM and BaCoM suggested that the relaxations are substitution dependent. The scaling curve, i.e.  $Z''/Z''_{max}$  vs  $\log(\omega/\omega_{max})$  for BaCoM indicated that the dynamic conduction process is temperature independence.

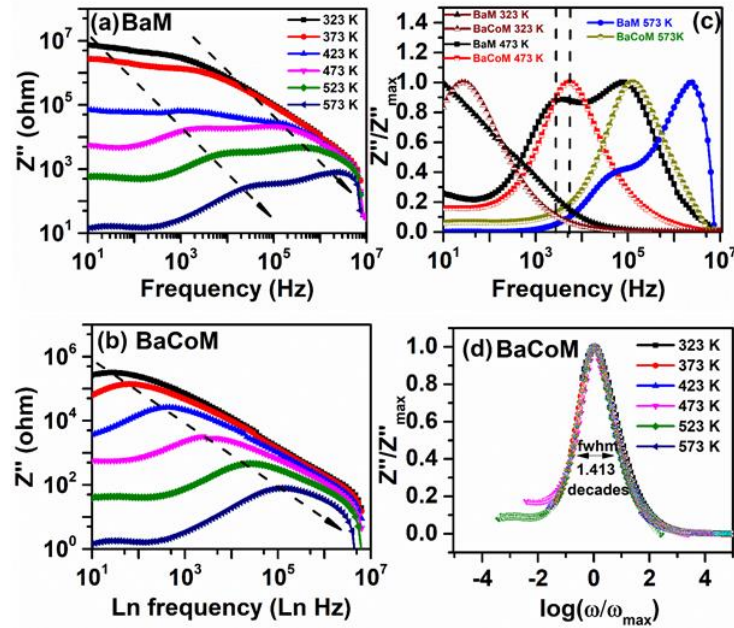


**Fig. S4.** Frequency dependent  $Z''$  at different temperature (a) BaM), (b) BaCoM, (c) Representative frequency dependent normalised  $Z''$  plots and (d) Scaling behaviour of  $Z''$  spectra of BaCoM.

Fig. S5 shows representative complex impedance plane plot for BaM and BaCoM. In BaM, two well resolved arcs corresponds to grain and grain boundary were observed, whereas, single arc was obtained for BaCoM. Significant difference between their impedance behaviour is shown in enlarged view. The representative log-log impedance plots for BaM and BaCoM at different temperatures are also shown. In order to understand the electrical response of microstructural elements, the plots were fitted with equivalent circuits based on the bricklayer model. The model consists of grains, grain boundaries and minor impurity phase (W-type) contribution. However, the possibility of unsubstituted metal oxides as an impurity (not traced in XRD) cannot be ignored, which could also be present along grain boundary. In fitted equivalent circuits  $C_1$  and  $R_1$  are capacitance and resistance for grain;  $R_2$  and  $CPE_1$  denotes resistance and constant phase element ( $Y_{CPE} = A_0(j\omega)^n$ ) assigned for grain boundary contribution, where  $n$  is the dimensionless power

constant varies between zero (ideal resistor) to one (ideal capacitor). Variables  $R_3$  and  $C_2$  are the contributions of impurities at grain boundaries, which were absent in BaM. The fitted value of  $n$  was remained between 0.50-0.80.

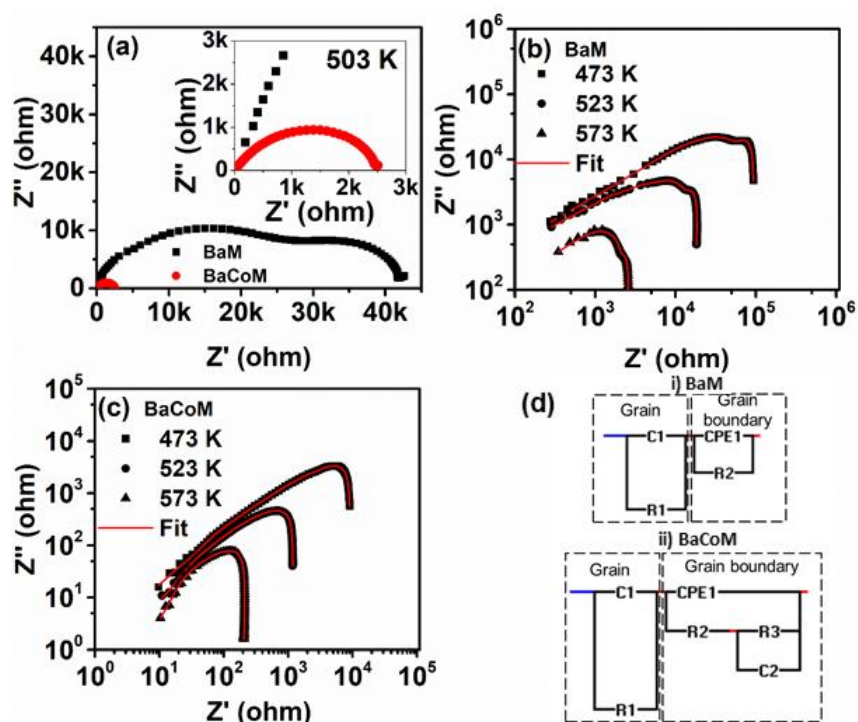


**Fig. S5.** (a) Complex impedance plane plot for BaM and BaCoM. Representative log – log plot of complex impedance ( $Z'$  vs  $Z''$ ) and Equivalent circuit

The grain ( $R_g$ ) and grain boundaries ( $R_{gb}$ ) resistance obtained from the fit are shown in table S1. For BaM,  $R_{gb}$  was not observed upto 170 °C which may show their contribution below 10Hz. However, for BaCoM, grain boundary relaxation was present for all temperatures.

**Table S1.** Resistance obtained from complex impedance plane plot

| T<br>(K) | BaM            |                   | BaCoM          |                   |                |
|----------|----------------|-------------------|----------------|-------------------|----------------|
|          | $R_g$<br>(ohm) | $R_{gb}$<br>(ohm) | $R_g$<br>(ohm) | $R_{gb}$<br>(ohm) | $R_i$<br>(ohm) |
| 323      | 1099187        | -                 | 131667         | 1003456           | 18.3           |
| 373      | 857443         | -                 | 107751         | 319320            | 14.5           |
| 423      | 98517          | -                 | 42854          | 43227             | 8.0            |
| 473      | 15012          | 21752             | 4726           | 2531              | -              |
| 523      | 148.5          | 168.2             | 521.5          | 478.4             | -              |
| 573      | 18.3           | 21.5              | 89.1           | 32.8              | -              |
| 623      | 4.7            | 4.4               | 2.6            | 0.5               | -              |

Fig. S6 shows the  $\ln \sigma$  versus  $1/T$  plots for grain ( $g$ ), grain boundaries ( $g_b$ ) and impurity ( $I$ ) for BaM and BaCoM. Conductivity found to increase with temperature however, higher conductivity of BaCoM is a consequence of more charge carriers as confirmed from XPS. It is also noted, conductivity plot shows three distinct slopes in different temperatures regime named as R I, R II and R III. The activation energy as obtained from Arrhenius plots for different temperature regime is shown in table S2.

The studied temperature range was well below any structural/magnetic phase transition of BaM; therefore, change in the slope may ascribe to parallel conduction mechanisms in the system. The conduction in R I (323 – 393 K) is due to free charge carrier which required low activation energy to participate in conduction. The R II (393 – 473 K) for BaM shows sudden rise in the  $\sigma_g$  with an activation energy of 0.72 eV. In this region, grain boundary contribution was also observed. The rise in conductivity is associated with hopping of charges between  $\text{Fe}^{2+}$ -  $\text{Fe}^{3+}$  from the localised oxygen trap centre to the nearest neighbouring sites as proposed in nearest- neighbouring-hopping model. In BaCoM, the charge conduction through hopping mechanism is dominated over to a wider temperature range (393 – 553 K). This could be due to additional hopping due to  $\text{Co}^{2+}$ -  $\text{Co}^{3+}$  ions. Also the presence of cobalt ions at grain boundaries will provide conduction channels and promote grain to grain conduction as evident by the higher conductivity and low activation energy. The behaviour is also supported by conductivity of impurities which showed metallic like behaviour above 443 K. The important feature is to be noted that for BaM, the transition from R II to R III is occurring at 473 K whereas, transition in BaCoM took place at 553 K. In R III, the same activation energy for BaM and BaCoM suggest the effect of substitution was negligible. In this region the conduction may be due to fragmentation of bigger polaron into smaller polaron which causes a sharp change in conductivity.

To understand the conduction mechanism,  $\sigma_{dc}$  and  $\sigma_{ac}$  contribution were extracted from the real part of complex conductivity ( $\sigma'$ ) using Jonscher's power law.

$$\sigma' = \sigma_{dc} + \left(\frac{\omega}{\omega_H}\right)^S \quad (i)$$

where,  $\left(\frac{\omega}{\omega_H}\right)^S$  is  $\sigma_{ac}$  contribution,  $\omega_H$  is hopping frequency of charge carriers and  $S$  is a dimensionless frequency exponent lies between 0.0 - 1.0. According to law,  $\sigma_{dc}$  is temperature dependent whereas,  $\sigma_{ac}$  is both frequency and temperature dependent. The  $S$

was obtained by fitting frequency dependent conductivity behaviour of BaM and BaCoM at different temperature. The variation in  $S$  with temperature are correlated with various ac conduction mechanisms associated with the system. In general,  $S = 0$  corresponds to free migration of charge carriers and if  $S \sim 1$ , the conduction will be dominated by hopping mechanism. The variation in  $S$  with temperature showed similar behaviour. It is clear that  $S$  value is below one and remains nearly constant upto 533 K. Therefore, the primary conduction mechanism in this region is due to hopping of charges. The higher  $S$  values of BaCoM compared to BaM is due to additional  $\text{Co}^{2+}$  and  $\text{Co}^{3+}$  ions as confirmed from XPS. With increase in temperature,  $S$  decrease to its minimum at 503 K. In this region, high temperature promotes larger lattice vibration which increases the size of polaron. This behaviour was explained in overlapping large polaron tunnelling (OLPT) model. According to model,  $S$  is defined as:

$$S = 1 - \frac{8\alpha R_\omega + 6\beta W_{Ho} r_p / R_\omega}{(2\alpha R_\omega + \beta W_{Ho} r_p / R_\omega)^2} \quad (\text{ii})$$

where,  $R_\omega$  is the hopping distance at frequency  $\omega$ ,  $\beta$  is  $1/k_B T$  (where  $k_B$  is Boltzmann constant and  $T$  is temperature in K),  $\alpha$  is spatial decay parameter for localised wave function,  $r_p$  is the polaron radius and  $W_{Ho}$  is polaron hopping energy. The decrease in  $S$  with temperature occurs for larger  $r_p$ . Further increase in temperature,  $S$  increases rapidly due to fragmentation of larger polaron into smaller one as described in small polaron quantum mechanical tunnelling model (SPQMT). The  $S$  value higher than one is due to site to site motion of mobile charges by quantum mechanical tunnelling between asymmetrical double potential. The behaviour of  $S$  is in accordance with temperature dependent conductivity behaviour.

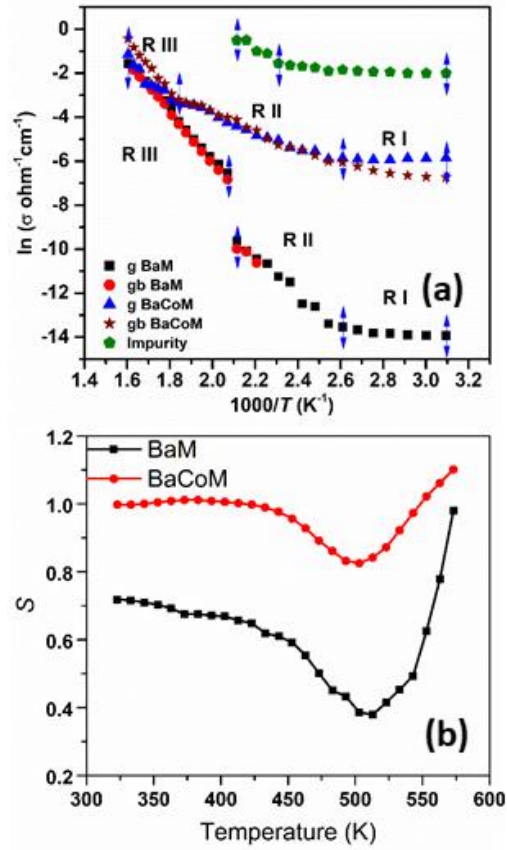


**Fig. S6.** (a) Arrhenius plot of conductivity for BaM and BaCoM and (b) Variation of power law exponent as a function of temperature for BaM and BaCoM

**Table S2.** Activation calculated from Arrhenius plot for BaM and BaCoM

| Microstructural Elements | Activation energy (eV) |      |       |           |           |       |
|--------------------------|------------------------|------|-------|-----------|-----------|-------|
|                          | BaM                    |      |       | BaCoM     |           |       |
|                          | R I                    | R II | R III | R I       | R II      | R III |
| Grain                    | 0.08                   | 0.72 | 0.97  | 0.0069    | 0.33      | 0.82  |
| Grain Boundary           | -                      | 0.59 | 1.00  | 0.09      | 0.35      | 1.00  |
| Impurity                 | -                      | -    | -     | 323-423 K | 423-443 K | -     |
|                          | -                      | -    | -     | 0.041     | 0.56      | -     |

## 2. Dielectric studies on Al-substituted BaM

Fig. S8 shows  $RT$  frequency dependent dielectric constant ( $\epsilon_r$ ) and loss tangent ( $\tan \delta$ ) for pure and Al-substituted BaM.

It is clear that  $\epsilon_r$  is higher in Al-substituted BaM at lower frequencies and gradually decreases with increase in the frequency. This behaviour can be described as existence of interfacial polarization and Maxwell-Wagner two layer model. The dielectric phenomena of ferrites were explained that poorly conducting large grain boundaries act as a barrier between well conducting grains. In the previous studies, the possibility of higher  $\epsilon_r$  was explained on the basis of exchange of electrons between  $\text{Fe}^{3+}$  and  $\text{Fe}^{2+}$  ions, where divalent Ba or trivalent Fe is substituted by trivalent or tetravalent ions respectively. In the present work, the possibility of reduction of  $\text{Fe}^{3+}$  to  $\text{Fe}^{2+}$  can be ignored due to same valency of  $\text{Al}^{3+}$  and  $\text{Fe}^{3+}$  ions. Therefore, the rise in  $\epsilon_r$  at lower frequencies is ascribed to larger grain boundary fraction in substituted BaM with simultaneous increase in space charge polarization. At higher frequencies, hopping of electrons never follow the frequency of applied field and dispersion of charge occurs, which leads to decrease in  $\epsilon_r$ . The  $\tan \delta$  variation is in agreement with  $\epsilon_r$ , where high  $\epsilon_r$  in Al-substituted BaM corresponds to minimum  $\tan \delta$ . On contrary, low  $\epsilon_r$  in pure BaM possess higher  $\tan \delta$ . Inset shows a hump in  $\tan \delta$  in Al-substituted BaM, which corresponds to a sharp decrease in  $\epsilon_r$  with increase in frequency. The dielectric losses can be explained as energy dissipation of the materials caused by conduction of electrons or flow of charges through the materials. The losses in the dielectric materials can be due to two major reasons. Firstly, the intrinsic factors of the materials like substitution, crystal defects and secondly, the extrinsic factors such as particle size and grain size which causes a lag in polarization to the applied field. In the present study the low  $\tan \delta$  in substituted BaM is due to larger grain boundary fraction, which provide hindrance to charge conduction.

The decrease in  $\epsilon_r$  and increase in  $\tan \delta$  with temperature at 1 KHz. The observed variation are due to thermally activated ions which enhances conductivity. As compared to pure, Al-substituted BaM shows lower losses at higher temperature due to high  $\epsilon_r$ . The similar behaviour were also observed for higher frequencies.

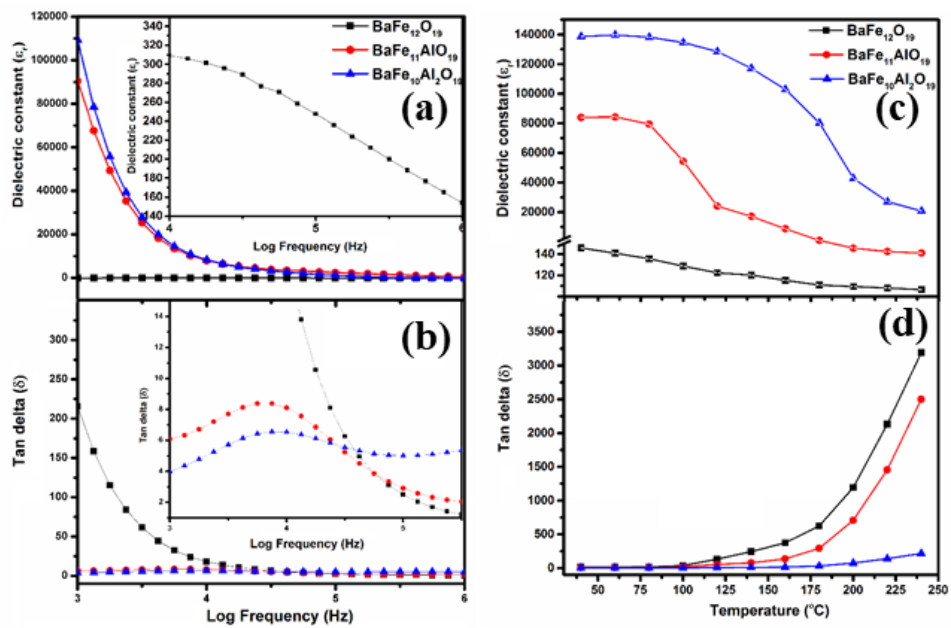
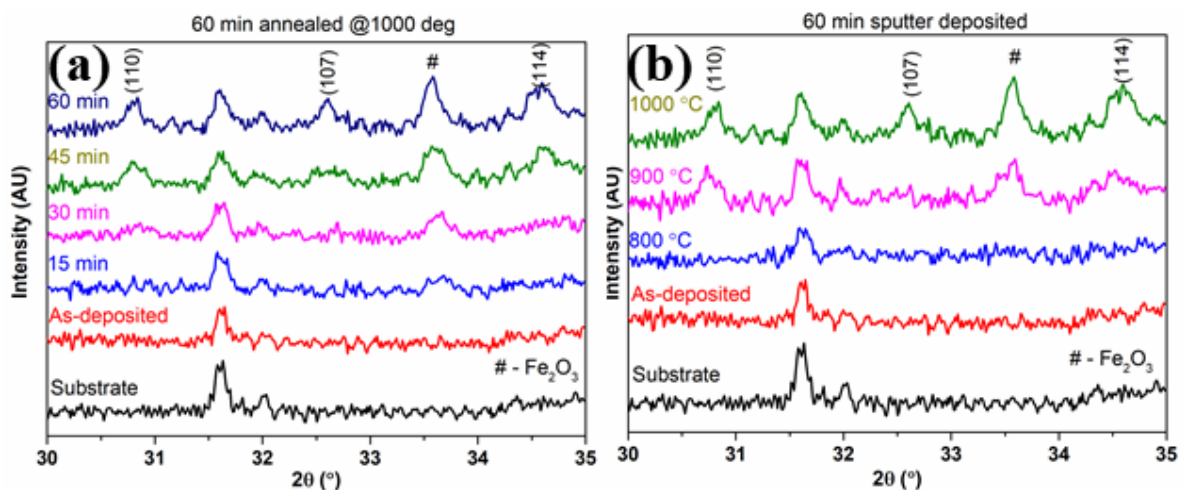


**Fig. S8.** (a) & (b) Frequency dependent  $\epsilon_r$  and  $\tan \delta$ , (c) & (d) Temperature dependent  $\epsilon_r$  and  $\tan \delta$  at 1 KHz of  $\text{BaFe}_{12-x}\text{Al}_x\text{O}_{19}$ .

### 3. Preparation of BaM Thin film

In-house BaM sputtering target of 2 inch diameter were prepared by solid state ceramic method. Thin films were deposited on polycrystalline  $\text{Al}_2\text{O}_3$  substrate using RF-sputtering in argon atmosphere. Target to substrate (T-S) distance was kept constant to 5 cm. The base pressure and argon pressure were kept constant at  $1 \times 10^{-5}$  and  $5 \times 10^{-2}$  mbar, respectively. The deposition time of 60 mins were fixed for an optimum deposition rate at 100 W RF power. Post annealing at  $1000^\circ\text{C}$  for one hour were carried in tubular furnace to check the magnetic properties of the film. However, as-deposited films were utilized as an underlayer for thick film fabrication.

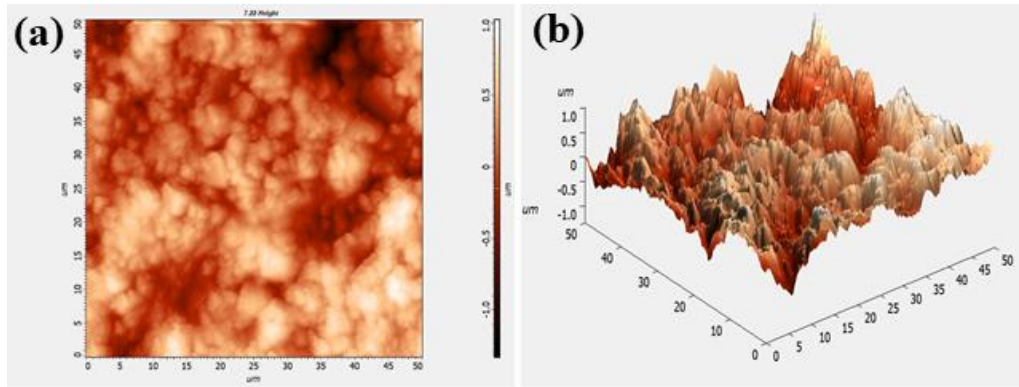
Fig. S9 shows X-ray diffraction pattern for BaM sputtered thin films deposited upto 60 mins and annealed at  $1000^\circ\text{C}$ . A substrate peak is inevitable in all sample. As-deposited film with no ex-situ annealing illustrate no major peak with the observable limit of XRD. A peak at  $33.6^\circ$  confirms the presence of  $\text{Fe}_2\text{O}_3$ . The peak (110), (107) and (114) for BaM were seen in 30 – 60 mins sputter deposited samples along with substrate and  $\text{Fe}_2\text{O}_3$  peaks.



**Fig. S9.** X-ray diffraction pattern for BaM thin film (a & b) ex-situ annealing time and temperature

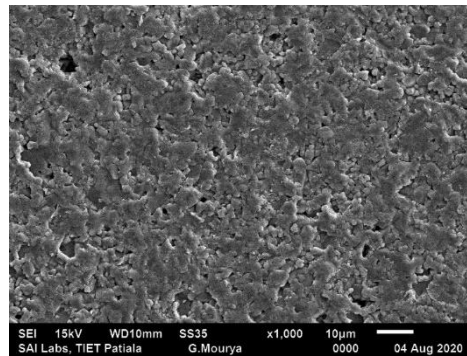
It is clear upto  $800^\circ\text{C}$  no crystalline phase for BaM has been obtained. Peak (110), (107) and (114) originated at  $900^\circ\text{C}$  along with an impurity oxide phase. The peaks intensity were found increase at  $1000^\circ\text{C}$ , whereas, a sharp peak for  $\text{Fe}_2\text{O}_3$  suggest higher crystalline rate of impurity phase. Above  $1100^\circ\text{C}$  fabricated film found volatile and evaporate completely without any trace of structural and magnetic properties.

Fig S10 shows atomic force micrograph of 60 min as-deposited BaM thin film. AFM reveals rough surface of  $\sim 0.3 \mu\text{m}$  particle size.



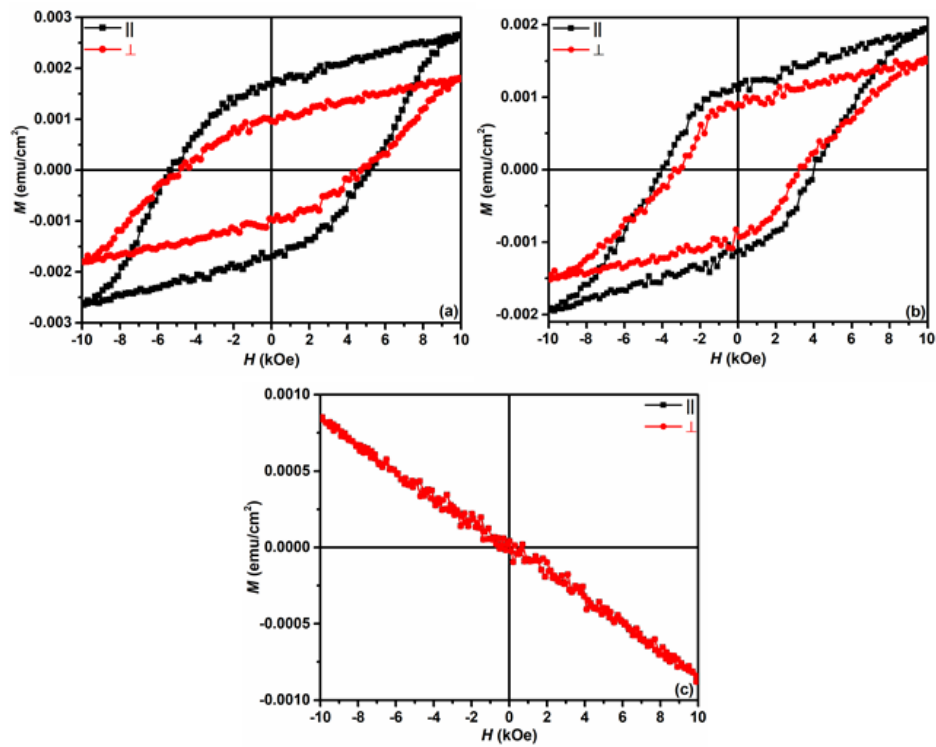
**Fig. S10.** AFM image of fabricated thin film (a) Surface and (b) Roughness plot

Fig. S11 depicts the SEM micrograph of 60 min sputtered deposited and 1000 °C ex-situ annealed BaM thin film. Topographical studies suggest annealed samples shows well defined coagulation of grains



**Fig. S11.** SEM micrograph BaM thin film

Fig. 12 (a & b) shows room temperature magnetic plots of BaM thin film. A well-defined magnetic loop has been observed with squareness of 0.63 and 0.54 for  $\parallel$  and  $\perp$  direction respectively. Fig. 12 (b) shows BaM thick film deposited at higher argon pressure for 60 min and annealed at 1000 °C.  $M$  found to decrease ( $0.0019 \text{ emu/cm}^2$ ) compare to lower argon pressure ( $0.0026 \text{ emu/cm}^2$ ) which may be due to lower sputter yield or higher crystallisation of  $\text{Fe}_2\text{O}_3$ . However, no orientation change has be observed by changing partial argon pressure. Fig. 4 (c) shows the diamagnetic behaviour of polycrystalline alumina substrate used to deposit BaM thin film.



**Fig. 12.**  $R-T$  Hysteresis loop (a & b) BaM thin film with different argon pressure and (c) Alumina substrate

# Site Occupation and Magnetic Studies in La–Co-Substituted Barium Hexaferrite

Santhoshkumar Mahadevan<sup>1</sup>, Vasant Sathe<sup>2</sup>, V. Raghavendra Reddy<sup>2</sup>, and Puneet Sharma<sup>1</sup>

<sup>1</sup>School of Physics and Materials Science, Thapar Institute of Engineering & Technology, Patiala 147004, India

<sup>2</sup>UGC-DAE Consortium for Scientific Research, Indore 452017, India

**In this work, preferential site occupation in La–Co-substituted barium hexaferrites was systematically investigated by micro-Raman and Mössbauer spectroscopy. The effect of substitution on the magnetic properties was studied by vibrating sample magnetometer. Raman studies showed redshift in  $2a$ ,  $2b$ , and  $4f_2$  sites with Co and La substitution. The decrease in isomer shift and the relative sub-spectral area suggest that  $\text{Co}^{2+}$  ions preferably occupy  $2a$  and  $2b$  sites for Co-substituted sample. For La–Co substitution, Co also occupies  $4f_2$  site as evidenced by the reduction in hyperfine field. Anisotropic field calculated by the law of approaching saturation was found to decrease with substitution. Curie temperature showed a strong dependence on La and Co substitution.**

**Index Terms**—Hard magnetic materials, hexaferrite, Raman spectroscopy and Mössbauer spectroscopy.

## I. INTRODUCTION

**B**ARIUM hexaferrite ( $\text{BaFe}_{12}\text{O}_{19}$ ) is primarily used as permanent magnet due to its high remanence, coercivity, uniaxial magnetocrystalline anisotropy, and energy product [1], [2]. The magnetic properties of  $\text{BaFe}_{12}\text{O}_{19}$  (BaM) are strongly associated with close-packed hexagonal crystal structure [3], [4]. A typical unit cell of BaM consists of two formula units with ABAB stacking of S (two layers of  $\text{Fe}_6\text{O}_8$ ) and R ( $\text{BaFe}_6\text{O}_{11}$ ) block, where 24  $\text{Fe}^{3+}$  ions are situated at five different crystallographic sites, that is, octahedral ( $12k$ ,  $4f_2$ , and  $2a$ ), tetrahedral ( $4f_1$ ), and trigonal bipyramid ( $2b$ ) sites. The parallel ( $12k$ ,  $2a$ , and  $2b$ ) and antiparallel ( $4f_1$  and  $4f_2$ )  $\text{Fe}^{3+}$  ion spins contribute a net magnetic moment of  $40 \mu_B$  per unit cell [5].

Over the decades, several processing methods such as sol–gel auto combustion, co-precipitation, and hydrothermal methods were adopted to understand the structure processing property relationship of hexaferrites [6]–[8]. Simultaneously, significant efforts were made to tailor the magnetic properties by partial cationic substitution for Fe and Ba ions. Substitutions such as  $\text{Al}^{3+}$  [9],  $\text{Ga}^{3+}$  [10],  $\text{In}^{3+}$  [11],  $\text{Co}^{2+}$ – $\text{Ti}^{4+}$  [12], and  $\text{Co}^{2+}$ – $\text{Si}^{4+}$  [13] for  $\text{Fe}^{3+}$  and  $\text{La}^{3+}$  [14],  $\text{Sm}^{3+}$  [15],  $\text{Nd}^{3+}$  [16], and so on for  $\text{Ba}^{2+}$  were extensively studied. Besides individual, simultaneous ion substitutions for Fe and Ba were also investigated [17]–[19]. Among these, La–Co-substituted hexaferrite showed enhanced properties well-exploited for the production of commercial permanent magnets. The effect of La/Co substitution on its crystallographic properties and exchange interaction are well-explained in various theoretical studies. The superexchange interaction in the La-substituted BaM was explained by molecular field approximation (MFA) and random phase approximation (RPA). Studies suggested that antiferromagnetic

superexchange interactions between various Fe–Fe ions were more prominent between  $2a$ – $4f_1$ ,  $2a$ – $12k$ ,  $2b$ – $4f_1$ , and  $2b$ – $12k$  [20], [21]. Recently, Park *et al.* [22] derived the electronic structure of the La–Co-substituted strontium hexaferrite by first principle calculation and predicted a reduction in lattice constant and net magnetic moment. The study also suggested its half-metallic behavior with cobalt substituted at  $2a$  sites [22]. Beside theoretical studies, the effect of site occupation on the intrinsic properties and crystal collinearity was also experimentally investigated [23], [24]. To provide more insight, preferential site occupation in simultaneously substituted La–Co hexaferrite was studied and compared with the individually substituted La and Co ions.

In this study,  $\text{BaFe}_{12}\text{O}_{19}$ ,  $\text{BaFe}_{11.85}\text{Co}_{0.15}\text{O}_{19}$ ,  $\text{Ba}_{0.85}\text{La}_{0.15}\text{Fe}_{12}\text{O}_{19}$ , and  $\text{Ba}_{0.85}\text{La}_{0.15}\text{Fe}_{11.85}\text{Co}_{0.15}\text{O}_{19}$  were prepared. Preferential site occupation was studied by Mössbauer and micro-Raman spectroscopy. Its effect on Curie temperature ( $T_c$ ), anisotropic field ( $H_a$ ), and magnetic properties was investigated.

## II. EXPERIMENT

$\text{BaFe}_{12}\text{O}_{19}$  (BaM),  $\text{BaFe}_{11.85}\text{Co}_{0.15}\text{O}_{19}$  (BaCoM),  $\text{Ba}_{0.85}\text{La}_{0.15}\text{Fe}_{12}\text{O}_{19}$  (BaLaM), and  $\text{Ba}_{0.85}\text{La}_{0.15}\text{Fe}_{11.85}\text{Co}_{0.15}\text{O}_{19}$  (BaLaCoM) were prepared by the solid-state ceramic method. Analytical grade  $\text{BaCO}_3$ ,  $\text{Fe}_2\text{O}_3$ ,  $\text{CoO}$ , and  $\text{La}_2\text{O}_3$  with 99.9% purity were used to prepare the samples. The stoichiometric amount of chemicals were weighed and wet mixed for 3 h in a planetary ball mill (Fritsch, Germany). The ball-to-charge ratio and rotations per minute (RPM) were fixed to 5:1 and 250, respectively. Calcination of as-mixed powders was carried out in a conventional muffle furnace at  $1200^\circ\text{C}$  for 3 h. Heating and cooling rates were kept constant at  $5^\circ\text{C}/\text{min}$ . Phase analysis of powders was done by X-ray diffractometer model Shimadzu XRD-6000 using  $\text{Cu K}\alpha_1$  ( $\lambda = 1.54 \text{ \AA}$ ) at a scan rate of  $0.02^\circ/\text{s}$ . Raman spectroscopy was carried out by JOBIN YVON HORIBA HR800 spectra analyzer (instrumental resolution  $\pm 1 \text{ cm}^{-1}$ ) equipped with a 632.8 nm helium–neon laser at 9 mW power. Zero-field room temperature (RT) Mössbauer measurements were performed

Manuscript received January 14, 2020; revised February 26, 2020, May 6, 2020, June 30, 2020, and July 27, 2020; accepted July 28, 2020. Date of publication August 4, 2020; date of current version September 18, 2020. Corresponding author: P. Sharma (e-mail: puneet.sharma@thapar.edu).

Color versions of one or more of the figures in this article are available online at <http://ieeexplore.ieee.org>.

Digital Object Identifier 10.1109/TMAG.2020.3014071

0018-9464 © 2020 IEEE. Personal use is permitted, but republication/redistribution requires IEEE permission.

See <https://www.ieee.org/publications/rights/index.html> for more information.

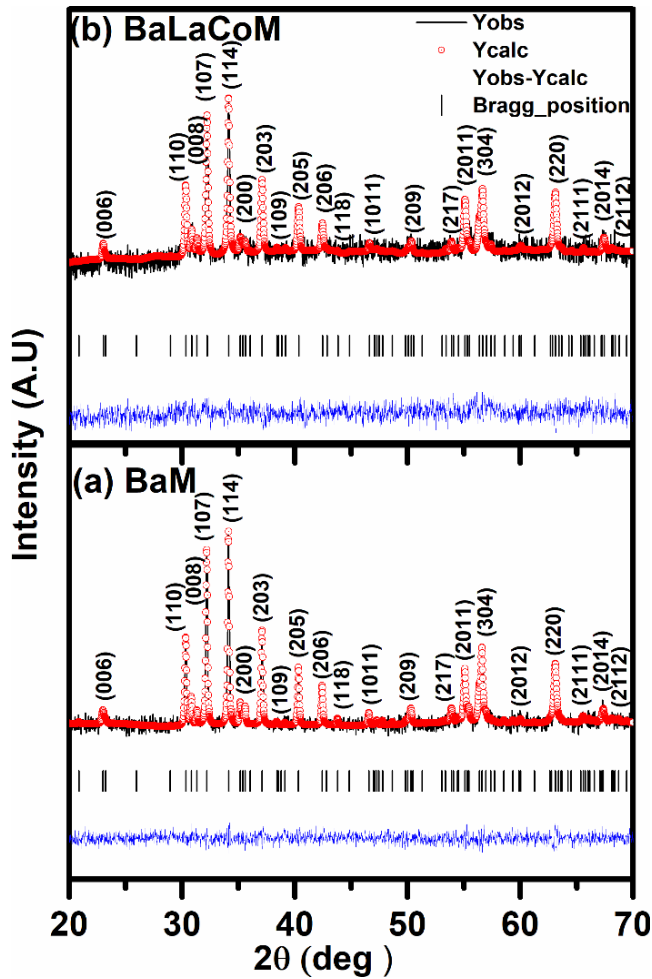


Fig. 1. Refined XRD plot for pure and substituted barium hexaferrite. (a) BaM. (b) BaLaCoM.

using  $^{57}\text{Co}$  (Rh) gamma-ray source in a transmission geometry by WissEl make Mössbauer spectrometer. RT and high-temperature (HT) magnetic measurements were carried out by Lake Shore VSM 7404.

### III. RESULTS AND DISCUSSION

Fig. 1 shows the representative X-ray diffraction (XRD) pattern of pure and substituted BaM. All peaks correspond to  $P6_3/mmc$  space group (#00-007-0276) without any impurity or residual  $\text{Fe}_2\text{O}_3$  phase. A quantitative structural analysis to signify the effect of  $\text{La}^{3+}$  and  $\text{Co}^{2+}$  cations at various atomic positions was carried by Rietveld refinement [25], [26]. The crystallite size and reliability factors obtained from refinement are presented in Table I. Lattice parameter “ $a$ ” remains constant for all the samples except slight shrinkage in BaLaM due to smaller ionic radii of  $\text{La}^{3+}$  (1.16 Å) at dodeca coordination. On the other hand, with  $\text{Co}^{2+}$  ion substitution “ $c$ ”-axis was increased from 22.19 to 23.22 Å due to its bigger ionic radii (0.72 Å) and/or oxygen deficiencies. In BaLaCoM, slight shrinkage in “ $c$ ”-axis was observed, which suggests that shrinkage due to  $\text{La}^{3+}$  ion is dominant over  $\text{Co}^{2+}$  ion substitution. The crystallite size calculated by Scherrer relation was 55 and 39 nm for BaCoM and BaLaM, respectively, whereas BaM and BaLaCoM have the same grain size ( $\sim 50$  nm).

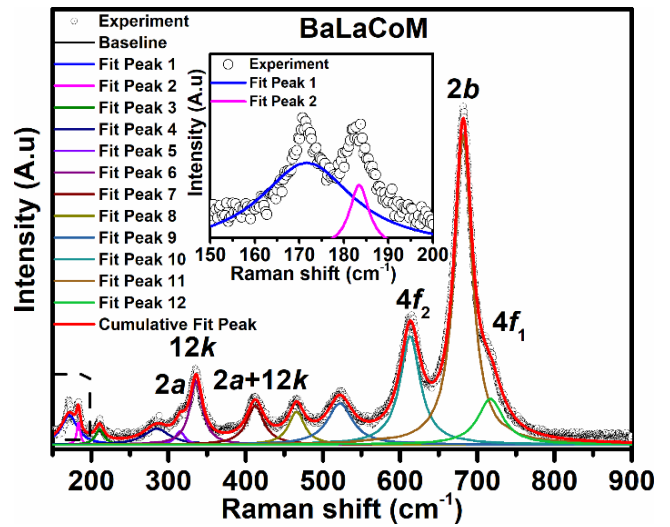


Fig. 2. Representative deconvoluted Raman spectra for substituted barium hexaferrite.

TABLE I  
CRYSTALLITE SIZE AND RELIABILITY FACTORS FROM  
RIETVELD FITTING

| Sample  | C.S<br>Nm | $\chi^2$ | $R_p$<br>% | $R_{wp}$<br>% | $R_{exp}$<br>% |
|---------|-----------|----------|------------|---------------|----------------|
| BaM     | 51.24(3)  | 1.12     | 1.84       | 2.33          | 2.24           |
| BaCoM   | 54.96(4)  | 1.81     | 5.24       | 6.62          | 4.92           |
| BaLaM   | 37.63(7)  | 2.22     | 2.99       | 3.78          | 2.53           |
| BaLaCoM | 49.83(6)  | 1.17     | 2.14       | 2.75          | 2.54           |

Raman spectra is a unique technique to identify any dynamic behavior of substitution at crystallographic sites [27]. Fig. 2 shows the representative micro-Raman spectra of BaLaCoM, where peak represents the various bands suggested in group theory [28], [29]. The peak parameters obtained by 12 Lorentzian fit are given in Table II. A doublet at 171 and 183  $\text{cm}^{-1}$  of the  $E_{1g}$  band was associated with whole spinel block. The peak 171  $\text{cm}^{-1}$  was unaltered with substitution, which shows that the overall effective mass of spinel coordinate was comparable due to nearly similar atomic weight of Fe (55.8 g/mol) and Co (58.9 g/mol) ions in BaCoM and BaLaCoM. In BaLaM,  $\text{La}^{3+}$  ion substitutes  $\text{Ba}^{2+}$  ion in the  $R$  block, and hence its effect in the spinel block was negligible. The peak at 183  $\text{cm}^{-1}$  is more sensitive to localized molecular vibration in the spinel block. The presence of  $\text{Co}^{2+}$  ions at  $2a$  site distorts local vibration and causes a slight red shift in BaCoM [27]. However, no such shift was noticed in BaLaM and BaLaCoM for the whole spinel coordinate. The peaks at 315, 615, 683, and 719  $\text{cm}^{-1}$  represent  $A_{1g}$  bands of  $2a$ ,  $4f_2$ ,  $2b$ , and  $4f_1$  sites, respectively. The peak position at 337  $\text{cm}^{-1}$  denotes the  $E_{2g}$  band of  $12k$  site, whereas peak 411  $\text{cm}^{-1}$  represents the  $A_{1g}$  band of mixed  $12k$  and  $2a$  sites. Furthermore, peaks at 212, 285, 468, and 522  $\text{cm}^{-1}$  represent the spinel coordinate of different crystallographic sites. A slight redshift in bands was apparent in BaCoM due to its higher crystallinity as confirmed from Scherrer relation. It is a well-known fact that the optical and exchange interaction parameters for complex oxides strongly depend on the average crystallite size and crystallite size distribution [30], [31].

TABLE II  
BAND ASSIGNMENT AND RAMAN SHIFT FROM DECONVOLUTED SPECTRA FOR SUBSTITUTED BARIUM HEXAFERRITE

| peak                | band            | BaM | BaCoM | BaLaM | BaLaCoM |
|---------------------|-----------------|-----|-------|-------|---------|
| whole spinel blocks | E1 <sub>g</sub> | 171 | 170   | 171   | 171     |
| whole spinel blocks | E1 <sub>g</sub> | 183 | 181   | 184   | 183     |
| --                  | E1 <sub>g</sub> | 212 | 210   | 212   | 211     |
| --                  | E1 <sub>g</sub> | 285 | 282   | 285   | 284     |
| 2a                  | A1 <sub>g</sub> | 315 | 312   | 313   | 314     |
| 12k                 | E2 <sub>g</sub> | 337 | 334   | 337   | 336     |
| 12k+2a              | A1 <sub>g</sub> | 411 | 410   | 414   | 413     |
| --                  | A1 <sub>g</sub> | 468 | 465   | 467   | 466     |
| --                  | E2 <sub>g</sub> | 522 | 520   | 524   | 522     |
| 4f <sub>2</sub>     | A1 <sub>g</sub> | 615 | 612   | 614   | 613     |
| 2b                  | A1 <sub>g</sub> | 683 | 679   | 683   | 682     |
| 4f <sub>1</sub>     | A1 <sub>g</sub> | 719 | 716   | 719   | 718     |

TABLE III  
HYPERFINE PARAMETERS OF SUBSTITUTED BARIUM HEXAFERRITE POWDERS

| Sites           | Sample  | $\Gamma$<br>(mm/s) | $\delta$<br>(mm/s) | QS<br>(mm/s) | $B_{hf}$<br>(T) | S<br>(%) | $N_{Fe(i)}$ |
|-----------------|---------|--------------------|--------------------|--------------|-----------------|----------|-------------|
| 12k             | BaM     | 0.36               | 0.25               | 0.40         | 41.35           | 50.0     | 6.00        |
|                 | BaCoM   | 0.48               | 0.26               | 0.41         | 41.10           | 52.41    | 6.21        |
|                 | BaLaM   | 0.46               | 0.26               | 0.40         | 41.37           | 50.0     | 6.00        |
|                 | BaLaCoM | 0.51               | 0.25               | 0.41         | 41.10           | 55.56    | 6.58        |
| 4f <sub>1</sub> | BaM     | 0.27               | 0.17               | 0.22         | 49.05           | 16.66    | 2.00        |
|                 | BaCoM   | 0.45               | 0.17               | 0.21         | 48.56           | 21.25    | 2.60        |
|                 | BaLaM   | 0.37               | 0.15               | 0.21         | 48.53           | 16.66    | 2.00        |
|                 | BaLaCoM | 0.35               | 0.13               | 0.20         | 48.47           | 20.28    | 2.40        |
| 2a              | BaM     | 0.20               | 0.26               | 0.08         | 50.42           | 8.33     | 1.00        |
|                 | BaCoM   | 0.11               | 0.26               | 0.06         | 49.70           | 1.20     | 0.14        |
|                 | BaLaM   | 0.48               | 0.24               | 0.05         | 49.46           | 8.33     | 1.00        |
|                 | BaLaCoM | 0.22               | 0.27               | 0.14         | 49.87           | 4.52     | 0.54        |
| 4f <sub>2</sub> | BaM     | 0.23               | 0.27               | 0.15         | 51.68           | 16.66    | 2.00        |
|                 | BaCoM   | 0.37               | 0.28               | 0.17         | 50.96           | 21.96    | 2.60        |
|                 | BaLaM   | 0.33               | 0.28               | 0.23         | 51.01           | 16.66    | 2.00        |
|                 | BaLaCoM | 0.32               | 0.27               | 0.19         | 50.09           | 16.71    | 1.98        |
| 2b              | BaM     | 0.54               | 0.30               | 2.35         | 39.97           | 8.33     | 1.00        |
|                 | BaCoM   | 0.26               | 0.23               | 2.33         | 40.09           | 3.18     | 0.38        |
|                 | BaLaM   | 0.68               | 0.26               | 2.21         | 39.62           | 8.33     | 1.00        |
|                 | BaLaCoM | 0.27               | 0.12               | 2.19         | 39.77           | 2.93     | 0.35        |

However, it is noted that redshift is more prominent for 2a and 2b sites, which suggests preferential occupation of Co<sup>2+</sup> ion at respective sites. On the other hand, BaLaM was expected to show a negligible effect; however, a notable redshift for 2a site is observed, which may be ascribed to the formation of Fe<sup>2+</sup> ions for ionic charge compensation. In BaLaCoM, a prominent shift in 4f<sub>2</sub> site was due to Co<sup>2+</sup> ion substitution, whereas no significant changes were observed in other crystallographic sites due to comparable crystallite size. Furthermore, to verify micro-Raman signatures, the Mössbauer

spectroscopy of powders in transmission geometry was carried out.

RT Mössbauer spectra were obtained for all the samples and fitted with five discrete sextets corresponded to different crystallographic sites. For BaM and BaLaM, the sub-spectral area ratio was constrained to 6:2:2:1:1 and kept free for the remaining samples. The representative fitted Mössbauer spectra for BaM and BaLaCoM are shown in Fig. 3. The fitted parameters, that is, linewidth ( $\Gamma$ ), isomer shift ( $\delta$ ), quadrupolar shift (QS), hyperfine field ( $B_{hf}$ ), and relative sub-spectral area (S),

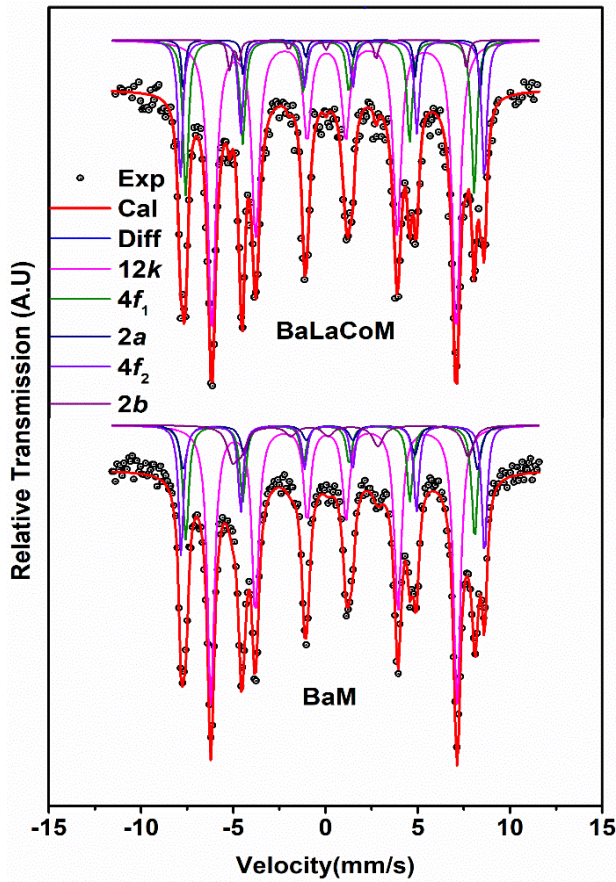


Fig. 3. Representative deconvoluted Mössbauer spectra for pure and substituted barium hexaferrite.

are given in Table III. The  $\delta$  at  $2b$  site was largely affected irrespective of substitution with the lowest value of 0.13 mm/s for BaLaCoM. The change in  $\delta$  with a corresponding decrease in the sub-spectral area suggests that Co ion is occupying the  $2b$  site. In general, this site is highly distorted and has close interaction with  $Ba^{2+}$  ions, and hence, the substitution of  $La^{3+}$  ion will reduce  $\delta$  and QS significantly due to the change in chemical environment [32], [33]. It is noted that in BaCoM and BaLaCoM, the  $2a$  site shows a negligible variation in  $\delta$  irrespective of the presence of cobalt [34].

Fig. 4 shows the calculated occupation number ( $N_{Fe}(i)$ ) and vacancy fraction ( $F(i)$ ) of Fe ions for all five crystallographic sites.  $N_{Fe}(i)$  and  $F(i)$  were determined by the following relation:

$$N_{Fe}(i) = C_{Fe} \left[ \frac{S(i)}{\sum_{i=1}^5 S(i)} \right] \quad (1)$$

$$F(i) = \frac{N(i) - N_{Fe}(i)}{N(i)} \times 100\% \quad (2)$$

where  $C_{Fe}$  denotes the Fe content, and  $S(i)$  and  $N(i)$  are the sub-spectral area and the occupation number, respectively, for the  $i$ th site [12]. For BaCoM,  $F(i)$  at  $2a$  and  $2b$  sites increases to 85% and 60%, respectively, which confirms Co substitution. The La–Co substitution shows a marginal increase in  $F(i)$  at  $4f_2$  site. This change may ascribe the conversion of  $Fe^{3+}$  to  $Fe^{2+}$  or Co occupation [35]. Since La–Co substitution

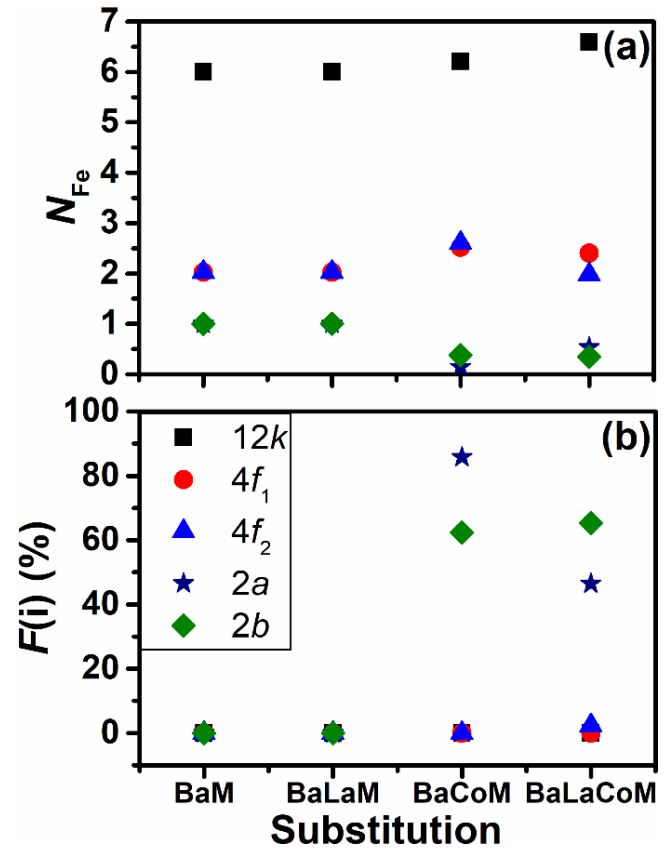


Fig. 4. Variation in (a) site occupation number ( $N_{Fe}$ ) and (b) vacancy fraction for Fe ions at different sites.

itself can compensate the charge variation, an observed  $F(i)$  may be ascribed to  $Co^{2+}$  ion occupation, as supported by a decrease in  $B_{hf}$  (51.68–50.09 T) and previous reported studies [23], [36], [37]. No measurable changes in hyperfine parameters for  $12k$  and  $4f_1$  sites with substitution were observed.

Fig. 5(a) shows the  $M$ – $H$  behavior of substituted BaM powders up to a maximum field of 1 T. The obtained magnetic parameters are given in Table IV. The magnetic properties are an interplay of the Fe ion at different crystallographic sites and their exchange interaction. In complex oxide, superexchange interaction occurs through oxygen ions, and hence, its vacancy significantly affects exchange interactions. As per Goodenough–Kanamori empirical rule, the exchange near the oxygen vacancies is negative, which also leads to weak magnetic state as reported elsewhere [38]–[40]. It is noted that  $Co^{2+}$  substitution decreases magnetization ( $M$ ) from 53 to 51 emu/g, which is due to the presence of lower magnetic moment  $Co^{2+}$  ( $3.6 \mu_B$ ) ions in spin up sites and/or  $O^{2-}$  deficiency. Whereas BaLaM and BaLaCoM showed a considerable increase in  $M$  up to 55 emu/g due to the existence of  $Fe^{2+}/Co^{2+}$  ions in antiparallel  $4f_2$  site as evident by Mössbauer studies. Coercivity ( $H_{ci}$ ) decreases from 1.38 to 1.12 kOe for BaLaM and further 1.02 kOe for BaCoM. It was reported that  $H_{ci}$  primarily depended on magnetocrystalline anisotropy and structural parameter, that is, crystallite size, particle size, and its shape [41]. To understand this change in

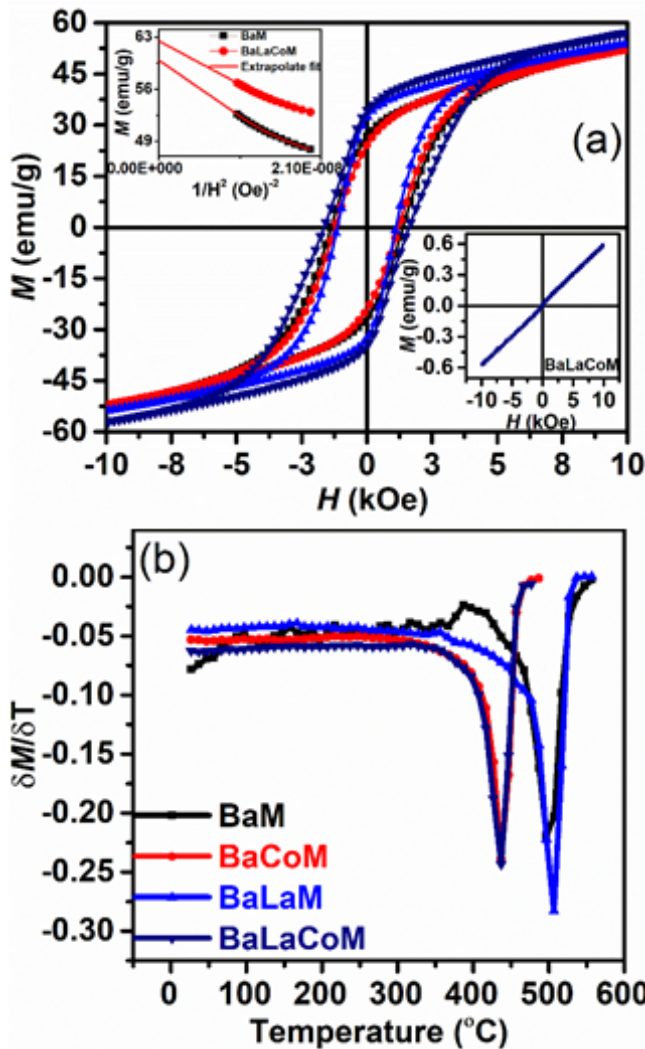


Fig. 5. (a)  $M-H$  plot and (b)  $\delta M/\delta T$  versus temperature plot for substituted barium hexaferrite. Inset: law approaching saturation and a representative  $M-H$  plot at  $T_c = 437^\circ\text{C}$ .

$H_{ci}$ ,  $H_a$  of powders was calculated by the law of approaching saturation (Fig. 5(a), inset) [9], [42]. However,  $H_a$  of polycrystalline powders is significantly less than single crystal due to its orientation. But its variation provides a suggestive to magnetocrystalline anisotropy. It is clear from Table IV that  $H_a$  is lower for all substituted powders. For BaCoM, the reduction in  $H_a$  is due to Co occupation, which reduces the collinearity along  $c$ -axis [43]. It is to be noted that a decrease in  $H_{ci}$  with La substitution is less compared with Co substitution despite a higher reduction in  $H_a$ . This may be ascribed to smaller crystallite size of BaLaM.  $H_a$  for BaLaCoM was decreased due to perturbation in  $2a$  site as evident from the increase in QS, while the QS for  $2b$  site decreased to 2.19 from 2.35 mm/s of BaM (Table III). Fe located at  $2b$  site contributes to quadrupole splitting most, and therefore, to magnetocrystalline anisotropy. However, in this study,  $H_a$  of the polycrystalline powder is found to be low; hence, a marginal increase in  $H_{ci}$  may be dominated by the particle size [5].

Furthermore, to understand the exchange interaction quantitatively, Curie temperature ( $T_c$ ) of all the substituted powders was measured by plotting  $\delta M/\delta T$  graph, as shown in Fig. 5(b).

TABLE IV  
MAGNETIC PARAMETER OF SUBSTITUTED BARIUM HEXAFERRITE

| Sample  | $M_s$<br>emu/g | $H_c$<br>kOe | $M_r$<br>emu/g | $H_a$<br>kOe | SQ   | $T_c$<br>°C |
|---------|----------------|--------------|----------------|--------------|------|-------------|
| BaM     | 52.61          | 1.38         | 26.56          | 9.46         | 0.50 | 497         |
| BaCoM   | 51.94          | 1.02         | 23.91          | 8.96         | 0.46 | 437         |
| BaLaM   | 53.60          | 1.12         | 32.19          | 8.51         | 0.60 | 507         |
| BaLaCoM | 54.28          | 1.49         | 34.22          | 8.59         | 0.63 | 437         |

For BaLaM,  $T_c$  increases from  $497^\circ\text{C}$  to  $507^\circ\text{C}$  due to overall lattice reduction, which enhances the superexchange coupling in a hexagonal crystal. However, the substitution of cobalt in BaM and BaLaM decreases  $T_c$  to  $437^\circ\text{C}$ . This suggests that Co ion plays a significant role in deciding  $T_c$ . The decrease in  $T_c$  may be ascribed to two reasons. First, the valance state of  $\text{Fe}^{3+}$  and  $\text{Co}^{2+}$  weakens the superexchange interaction due to different electronegativity [44]. Second,  $\text{Co}^{2+}$  substitution creates oxygen vacancies, which also change the oxidation degree of 3d-metal cations. The change in charge state as a consequence of oxygen vacancy will significantly affect the magnetic properties such as  $T_c$  [45]. It is reported that exchange integral ( $J_o$ ) which determines  $T_c$  depends on the number of nearest neighboring atom/ion and its distance [46]. The  $M-H$  behavior of BaLaCoM at  $T_c$  (Fig. 5(a), inset) confirms the paramagnetic nature.

In summary, Co-, La-, and La-Co-substituted BaM have been synthesized by the solid-state ceramic method. The XRD refinement confirmed single-phase BaM without any secondary phases. Raman spectra confirmed a redshift at  $2a$ ,  $2b$ , and  $4f_2$  sites with La and Co substitution. Mössbauer spectroscopy confirmed that  $\text{Co}^{2+}$  ions preferably occupy  $2a$  and  $2b$  sites in BaCoM, whereas BaLaCoM also occupies  $4f_2$  site.  $H_a$  is found to be lower for all substitutions compared with pure BaM.  $T_c$  shows a strong dependence on substitution, where the Co ion effect is largely dominated.

#### ACKNOWLEDGMENT

This work was supported by the Department of Science and Technology (DST), India, under Grant SERB—SB/S2/CMP-081/2013. The authors would like to acknowledge Dr. Manoj Kumar and Munish Verma, Department of Physics and Materials Science Engineering, Jaypee Institute of Information Technology, Noida, India, for X-ray diffraction (XRD) characterization. The authors also like to thank the UGC-DAE Consortium for Scientific Research, Indore, India, for micro-Raman and Mössbauer spectroscopy, and the School of Physics and Materials Science, Thapar Institute of Engineering & Technology (TIET), Patiala, India, for providing VSM analysis through the DST-FIST Program.

#### REFERENCES

- [1] A. Cocharadt, "Modified strontium ferrite, a new permanent magnet material," *J. Appl. Phys.*, vol. 34, no. 4, pp. 1273–1274, Apr. 1963.
- [2] Y. Ogata, Y. Kubota, T. Takami, M. Tokunaga, and T. Shinokara, "Improvements of magnetic properties of Sr ferrite magnets by substitutions of La and Co," *IEEE Trans. Magn.*, vol. 35, no. 5, pp. 3334–3336, Sep. 1999.

- [3] R. C. Pullar, "Hexagonal ferrites: A review of the synthesis, properties and applications of hexaferrite ceramics," *Prog. Mater. Sci.*, vol. 57, pp. 1191–1334, Sep. 2012.
- [4] V. G. Harris, "Modern microwave ferrites," *IEEE Trans. Magn.*, vol. 48, no. 3, pp. 1075–1104, Mar. 2012.
- [5] H. Kojima, "Fundamental properties of hexagonal ferrites with magnetoplumbite structure," in *Handbook of Ferromagnetic Materials*, vol. 3, K. Buschow, Ed. Amsterdam, The Netherlands: Elsevier, 1982, pp. 305–391.
- [6] M. Almessiere, Y. Slimani, H. Güngüneş, A. Baykal, S. V. Trukhanov, and A. V. Trukhanov, "Manganese/yttrium codoped strontium nanohexaferrites: Evaluation of magnetic susceptibility and Mössbauer spectra," *Nanomaterials*, vol. 9, no. 1, p. 24, Dec. 2018.
- [7] R. Taherian, A. Soleymani, and S. A. Manafi, "Effects of Co-Mn-Ti and Zn-Mg-Ti substitutions on the structural, magnetic and physical properties of barium hexaferrites synthesized by co-precipitation method," *IEEE Magn. Lett.*, vol. 7, pp. 1–5, 2016.
- [8] D. Guo, P. Zhou, J. Hou, X. Luo, X. Wang, and L. Deng, "Compositional control and millimeter-wave properties of micro-/nano-sized M-type barium hexaferrite synthesized by hydrothermal method," *IEEE Trans. Magn.*, vol. 51, no. 11, pp. 1–4, Nov. 2015.
- [9] S. Mahadevan, C. Pahwa, S. B. Narang, C. Pahwa, S. B. Narang, and P. Sharma, "Structural, dielectric and magnetic properties of BaFe<sub>12-x</sub>Al<sub>x</sub>O<sub>19</sub> hexaferrite thick films," *J. Magn. Magn. Mater.*, vol. 441, pp. 465–474, Nov. 2017.
- [10] G. Albanese and A. Deriu, "Magnetic properties of Al, Ga, Sc, in substituted barium ferrites: A comparative analysis," *Ceramurgia Int.*, vol. 5, no. 1, pp. 3–10, Jan. 1979.
- [11] S. V. Trukhanov *et al.*, "Magnetic and dipole moments in indium doped barium hexaferrites," *J. Magn. Magn. Mater.*, vol. 457, pp. 83–96, Jul. 2018.
- [12] S. Verma, O. P. Pandey, A. Paesano, Jr., and P. Sharma, "Structural and magnetic properties of CoTi substituted barium hexaferrite thick films," *J. Alloys Compounds*, vol. 678, pp. 284–289, Sep. 2016.
- [13] E. D. Solovyova, E. V. Pashkova, V. P. Ivanitski, O. I. V'yunov, and A. G. Belous, "Mössbauer and X-ray diffraction study of Co<sup>2+</sup>-Si<sup>4+</sup> substituted M-type barium hexaferrite BaFe<sub>12-2x</sub>Co<sub>x</sub>Si<sub>x</sub>O<sub>19±γ</sub>," *J. Magn. Magn. Mater.*, vol. 330, pp. 72–75, Mar. 2013.
- [14] S. Verma, P. Sharma, O. P. Pandey, A. Paesano, and A.-C. Sun, "Structure and magnetic properties of Ba<sub>1-x</sub>La<sub>x</sub>Fe<sub>12</sub>O<sub>19</sub> prepared by Ba<sub>1-x</sub>La<sub>x</sub>Fe<sub>2</sub>O<sub>4</sub>," *IEEE Trans. Magn.*, vol. 50, no. 1, Jan. 2014, Art. no. 2101004.
- [15] H. Yanbing *et al.*, "Tailored magnetic properties of Sm(Zn) substituted nanocrystalline barium hexaferrites," *J. Alloys Compounds*, vol. 486, nos. 1–2, pp. 348–351, Nov. 2009.
- [16] T. Kaur, S. Kumar, B. H. Bhat, B. Want, and A. K. Srivastava, "Effect on dielectric, magnetic, optical and structural properties of Nd-Co substituted barium hexaferrite nanoparticles," *Appl. Phys. A, Solids Surf.*, vol. 119, no. 4, pp. 1531–1540, Jun. 2015.
- [17] L. Å. Lechevallier and J. M. Le Breton, "Substitution effects in M-type hexaferrite powders investigated by Mössbauer spectrometry," *J. Magn. Magn. Mater.*, vols. 290–291, pp. 1237–1239, Apr. 2005.
- [18] A. Grusková *et al.*, "La-Zn substituted hexaferrites prepared by chemical method," *Hyperfine Interact.*, vol. 164, pp. 27–33, Jul. 2006.
- [19] C. Herme, S. E. Jacobo, P. G. Bercoff, and B. Arcondo, "Mössbauer analysis of Nd-Co M-type strontium hexaferrite powders with different iron content," *Hyperfine Interact.*, vol. 195, nos. 1–3, pp. 205–212, Jan. 2010.
- [20] P. Novák and J. Ruzs, "Exchange interactions in barium hexaferrite," *Phys. Rev. B, Condens. Matter*, vol. 71, no. 18, pp. 1–6, May 2005.
- [21] C. Wu *et al.*, "Calculation of exchange integrals and curie temperature for La-substituted barium hexaferrites," *Sci. Rep.*, vol. 6, no. 1, pp. 1–8, Dec. 2016.
- [22] J. Park, Y.-K. Hong, W. Lee, B.-C. Choi, and C.-J. Choi, "Electronic structure of La-Co substituted strontium hexaferrite (Sr<sub>1-x</sub>La<sub>x</sub>Fe<sub>12-x</sub>Co<sub>x</sub>O<sub>19</sub>) permanent magnet," *IEEE Magn. Lett.*, vol. 7, pp. 2014–2016, 2016.
- [23] J.-M. Le Breton, J. Teillet, G. Wiesinger, A. Morel, F. Kools, and P. Tenaud, "Mössbauer investigation of Sr-Fe-O hexaferrites with La-Co addition," *IEEE Trans. Magn.*, vol. 38, no. 5, pp. 2952–2954, Sep. 2002.
- [24] X. Liu, W. Zhong, S. Yang, Z. Yu, B. Gu, and Y. Du, "Influences of La<sup>3+</sup> substitution on the structure and magnetic properties of M-type strontium ferrites," *J. Magn. Magn. Mater.*, vol. 238, nos. 2–3, pp. 207–214, Jan. 2002.
- [25] A. V. Trukhanov *et al.*, "Influence of the charge ordering and quantum effects in heterovalent substituted hexaferrites on their microwave characteristics," *J. Alloys Compounds*, vol. 788, pp. 1193–1202, Jun. 2019.
- [26] A. V. Trukhanov *et al.*, "Features of crystal and magnetic structure of the BaFe<sub>12-x</sub>Ga<sub>x</sub>O<sub>19</sub> (x ≤ 2) in the wide temperature range," *J. Alloys Compounds*, vol. 791, pp. 522–529, Jun. 2019.
- [27] A. Morel, J. M. Le Breton, J. Kreisel, G. Wiesinger, F. Kools, and P. Tenaud, "Sublattice occupation in Sr<sub>1-x</sub>La<sub>x</sub>Fe<sub>12-x</sub>Co<sub>x</sub>O<sub>19</sub> hexagonal ferrite analyzed by Mössbauer spectrometry and Raman spectroscopy," *J. Magn. Magn. Mater.*, vols. 242–245, pp. 1405–1407, Apr. 2002.
- [28] M. Bellotto, G. Busca, C. Cristiani, and G. Groppi, "FT-IR skeletal powder spectra of Ba-β-aluminas with compositions BaAl<sub>9</sub>O<sub>14.5</sub>, BaAl<sub>12</sub>O<sub>19</sub>, and BaAl<sub>14</sub>O<sub>22</sub> and of Ba-ferrite, BaFe<sub>12</sub>O<sub>19</sub>," *J. Solid State Chem.*, vol. 117, pp. 8–15, Jun. 1995.
- [29] S. Mahadevan, S. B. Narang, and P. Sharma, "Effect of three-step calcination on structural, magnetic and microwave properties of BaFe<sub>11.5</sub>Ti<sub>0.5</sub>O<sub>19</sub> hexaferrite," *Ceram. Int.*, vol. 45, no. 7, pp. 9000–9006, May 2019.
- [30] S. V. Trukhanov *et al.*, "Study of A-site ordered PrBaMn<sub>2</sub>O<sub>6-δ</sub> manganite properties depending on the treatment conditions," *J. Phys. Condens. Matter*, vol. 17, no. 41, pp. 6495–6506, Oct. 2005.
- [31] S. V. Trukhanov, A. V. Trukhanov, C. E. Botez, A. H. Adair, H. Szymczak, and R. Szymczak, "Phase separation and size effects in Pr<sub>0.70</sub>Ba<sub>0.30</sub>MnO<sub>3+δ</sub> perovskite manganites," *J. Phys. Condens. Matter*, vol. 19, no. 26, Jul. 2007, Art. no. 266214.
- [32] B. J. Evans, F. Grandjean, A. P. Lilot, R. H. Vogel, and A. Gérard, "<sup>57</sup>Fe hyperfine interaction parameters and selected magnetic properties of high purity MFe<sub>12</sub>O<sub>19</sub> (M=Sr, Ba)," *J. Magn. Magn. Mater.*, vol. 67, no. 1, pp. 123–129, May 1987.
- [33] C. Sauer, U. Köbler, W. Zinn, and H. Stäblein, "High field Mössbauer effect study of LaFe<sub>12</sub>O<sub>19</sub>," *J. Phys. Chem. Solids*, vol. 39, no. 11, pp. 1197–1201, 1978.
- [34] H. Nakamura, A. Shimoda, T. Waki, Y. Tabata, and C. Mény, "Site-dependent cobalt electronic state in La-Co co-substituted magnetoplumbite-type ferrite: <sup>59</sup>Co nuclear magnetic resonance study," *J. Phys. Condens. Matter*, vol. 28, no. 34, 2016, Art. no. 346002.
- [35] L. Lechevallier, J. M. Le Breton, J. Teillet, A. Morel, F. Kools, and P. Tenaud, "Mössbauer investigation of Sr<sub>1-x</sub>La<sub>x</sub>Fe<sub>12-y</sub>Co<sub>y</sub>O<sub>19</sub> ferrites," *Phys. B, Condens. Matter*, vol. 327, pp. 135–139, Apr. 2003.
- [36] C. Herme, S. E. Jacobo, P. G. Bercoff, and B. Arcondo, "Mössbauer analysis of Nd-Co M-type strontium hexaferrite powders with different iron content," in *Proc. LACAME*, 2010, pp. 205–212.
- [37] F. Kools, A. Morel, R. Grössinger, J. M. Le Breton, and P. Tenaud, "LaCo-substituted ferrite magnets, a new class of high-grade ceramic magnets; intrinsic and microstructural aspects," *J. Magn. Magn. Mater.*, vols. 242–245, pp. 1270–1276, Apr. 2002.
- [38] J. B. Goodenough, "Electronic and ionic transport properties and other physical aspects of perovskites," *Rep. Prog. Phys.*, vol. 67, no. 11, p. 1915, 2004.
- [39] I. O. Troyanchuk, S. V. Trukhanov, D. D. Khalyavin, and H. Szymczak, "Magnetic properties of anion deficit manganites Ln<sub>0.55</sub>Ba<sub>0.45</sub>MnO<sub>3-γ</sub> (Ln = La, Nd, Sm, Gd, γ ≤ 0.37)," *J. Magn. Magn. Mater.*, vol. 208, no. 3, pp. 217–220, Jan. 2000.
- [40] S. V. Trukhanov, A. V. Trukhanov, A. N. Vasil'ev, A. Maignan, and H. Szymczak, "Critical behavior of La<sub>0.825</sub>Sr<sub>0.175</sub>MnO<sub>2.912</sub> anion-deficient manganite in the magnetic phase transition region," *JETP Lett.*, vol. 85, no. 10, pp. 507–512, Jul. 2007.
- [41] B. D. Cullity and C. D. Graham, *Introduction to Magnetic Materials*. Hoboken, NJ, USA: Wiley, 2008.
- [42] R. Grössinger, "A critical examination of the law of approach to saturation. I. Fit procedure," *Phys. Status Solidi A*, vol. 66, no. 2, pp. 665–674, Aug. 1981.
- [43] S. Ounnunkad, "Improving magnetic properties of barium hexaferrites by La or Pr substitution," *Solid State Commun.*, vol. 138, no. 9, pp. 472–475, Jun. 2006.
- [44] Z. F. Zi, Q. C. Liu, J. M. Dai, and Y. P. Sun, "Effects of Ce-Co substitution on the magnetic properties of M-type barium hexaferrites," *Solid State Commun.*, vol. 152, no. 10, pp. 894–897, 2012.
- [45] N. Raghuram, T. S. Rao, and K. C. B. Naidu, "Investigations on functional properties of hydrothermally synthesized Ba<sub>1-x</sub>Sr<sub>x</sub>Fe<sub>12</sub>O<sub>19</sub> (x = 0.0–0.8) nanoparticles," *Mater. Sci. Semicond. Process.*, vol. 94, pp. 136–150, May 2019.
- [46] J. M. MacLaren, T. C. Schulthess, W. H. Butler, R. Sutton, and M. McHenry, "Electronic structure, exchange interactions, and curie temperature of FeCo," *J. Appl. Phys.*, vol. 85, no. 8, pp. 4833–4835, Apr. 1999.



## Research articles

Charge transport mechanism in BaFe<sub>12</sub>O<sub>19</sub> and BaFe<sub>11</sub>CoO<sub>19</sub>

Santhoshkumar Mahadevan, Puneet Sharma\*

School of Physics &amp; Materials Science, Thapar Institute of Engineering &amp; Technology, Patiala 147004, Punjab, India



## ARTICLE INFO

## Keywords:

Magnetic materials  
Impedance spectroscopy  
Hexaferrite  
Conduction mechanism

## ABSTRACT

The conduction and charge transport mechanism of cobalt substituted barium hexaferrite (BaCoM) were studied by impedance spectroscopy at different temperatures and compared with BaM. Frequency dependent impedance spectra showed two distinct relaxations in BaM whereas a single relaxation peak was present in BaCoM. The relaxation frequencies were found to be temperature dependent. Scaling behaviour confirmed the dynamic conduction process is temperature independent and deviates from Debye type relaxation. Brick layer model has been employed to investigate the charge conduction through grain and grain boundaries. Arrhenius plot of conductivity showed two sharp transitions in three different temperature regime which indicates parallel conduction mechanism in the system. The frequency dependent conductivity was fitted with Jonscher's power law at different temperatures. The variation in frequency exponent with temperature confirmed the evidence of three types of conduction process. Higher conductivity and different transition temperature was observed for BaCoM as compared to BaM. The conduction process was in accordance with overlapping-large polaron tunnelling model.

## 1. Introduction

M-type barium hexaferrite (BaFe<sub>12</sub>O<sub>19</sub>) are widely used as permanent magnets, magnetic recording media and magnetic strip cards [1]. Recent studies suggest that BaFe<sub>12</sub>O<sub>19</sub> (BaM) has an impressive magnetodielectric (MD) characteristic and successfully employed for various applications such as antenna substrates, tunable filters and non-reciprocal microwave devices, etc. [2,3]. The magnetic properties of BaM strongly depends on its complex hexagonal crystal structure, in which 24Fe<sup>3+</sup> ions occupy five different crystallographic sites (octahedral, tetrahedral and trigonal bipyramidal) with a net magnetic moment of 40 μ<sub>B</sub>/unit cell. Moreover, wide substitution flexibility for Ba and Fe can drastically change their magnetic properties. Over the decades, large amount of work was dedicated to understand the role of various cationic substitution on the structural and magnetic properties [4,5]. Apart from magnetic studies, charge transport mechanism and magnetoelectric effect were also investigated in substituted M-type ferrite [6–8]. However, the dielectric properties of BaM were scarcely investigated. Previous reports suggest that the substitution of various divalent and tetravalent cation, i.e. Ni<sup>2+</sup>, Zr<sup>4+</sup>, Ti<sup>4+</sup> and Si<sup>4+</sup> for Fe<sup>3+</sup> ions remarkably affect the permittivity and permeability of BaM [9–12]. Recently, MD properties of Co<sub>2</sub>Z and Mg<sub>2</sub>Y hexaferrites were investigated for their potential use in antenna substrates [13–15]. However, complexity in phase formation is one of the major constraint

associated with these ferrites. Therefore, BaM could be an alternate for MD substrates due to its phase stability over wider compositional and temperature range [16]. However, pure BaM show large difference between complex permittivity (ε<sub>r</sub>) and permeability (μ<sub>r</sub>), which creates impedance mismatching and makes this material not recommendable as MD substrate [17,18]. On the other hand, Co<sup>2+</sup>/Co<sup>3+</sup> substitution showed a drastic decrease in magneto-crystalline anisotropy (H<sub>a</sub>), which eventually enhances its μ<sub>r</sub> with nearly retentive properties, which provide insight for substrate application [19]. Co substituted BaM brought more complex relaxation mechanism than BaM, due to additional hopping between Co<sup>2+</sup> and Co<sup>3+</sup> ions. Hence, investigating the charge transport mechanism for such materials will be of greater interest. Previously, structural, magnetic and dielectric properties of cobalt substituted BaM were widely explored [20–22]. Recently, this ferrite was investigated as a broadband microwave absorber and reported an enhanced polarization and multiple scattering with maximum reflection losses of –45 dB at 13 GHz, which suggests this material is an excellent microwave absorber at Ku band [17,23,24]. However, impedance studies of Co substituted BaM have not been reported. In the present work, frequency and temperature dependent charge transport behaviour of BaCoM was studied and compared with BaM hexaferrite. Further, a comprehensive grain & grain boundary contribution to electrical conductivity has been illustrated with the bricklayer model. The detailed study on temperature dependent conduction mechanism



\* Corresponding author.

E-mail address: [puneet.sharma@thapar.edu](mailto:puneet.sharma@thapar.edu) (P. Sharma).<https://doi.org/10.1016/j.jmmm.2020.167174>

Received 13 March 2020; Received in revised form 19 June 2020; Accepted 19 June 2020

Available online 24 June 2020

0304-8853/ © 2020 Elsevier B.V. All rights reserved.

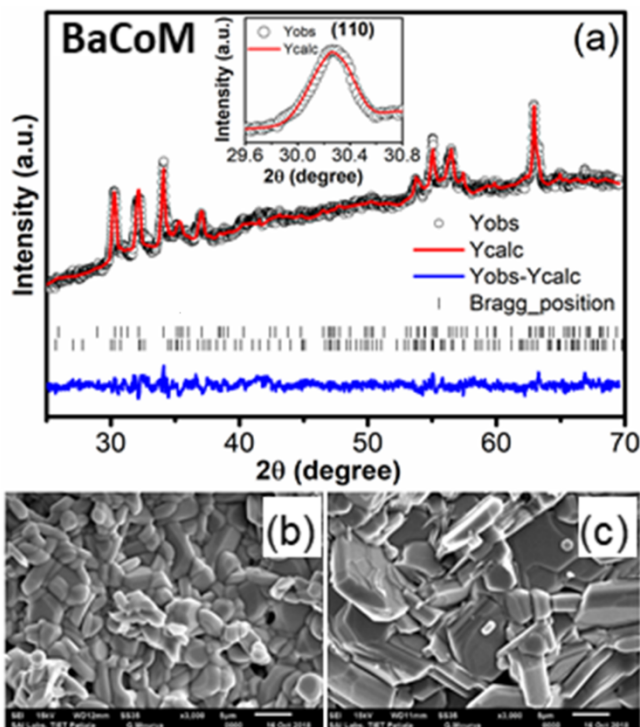


Fig. 1. (a) Refined XRD pattern of BaCoM. SEM micrograph of (b) BaM and (c) BaCoM sintered pellets.

has been illustrated with overlapping large polaron tunnelling model.

## 2. Synthesis and characterization

Analytical grade  $\text{BaCO}_3$ ,  $\text{Fe}_2\text{O}_3$  and  $\text{Co}_2\text{O}_3$  powders were used to prepare BaM and BaCoM by solid-state synthesis method. Stoichiometric composition of precursors were mixed and wet milled for three hours in planetary ball mill. The as-milled powders were calcined at 1473 K for three hours in resistance furnace. The calcined powders were pressed in cylindrical pellets of 10 mm diameter and 1.5 mm thickness. The pellets were sintered at 1523 K for one hour in ambient atmosphere. X-ray diffractometer model Shimadzu XRD – 6000 was used for phase analysis. Microstructure analysis was carried out by scanning electron microscope (SEM) coupled with energy dispersive spectroscopy (EDS) model JEOL (JSM-IT100). Magnetic measurements were performed using VSM model Lake Shore VSM 7400 with a maximum field of 1 Tesla. The valence states of ions in BaM and BaCoM were analysed by X-ray photoelectron spectroscopy model XPS spectrometer-ESCA + using Al-K $\alpha$  (1486.7 eV with line-width of 0.85 eV). The frequency dependent impedance spectroscopy (10 Hz–10 MHz) at different temperature were measured by impedance analyzer solarton- SI 1260.

## 3. Results and discussion

Fig. 1 (a) shows the XRD pattern of BaCoM powder calcined at 1473 K. The Rietveld refinement was carried with M–type and W-type phases of  $\text{P6}_3/\text{mmc}$  space group. The  $\chi^2$  value ( $< 3$ ) suggests that the refinement is best fitted. The refinement showed the existence of inevitable minor W-type phase with volume percent less than 3.5%.

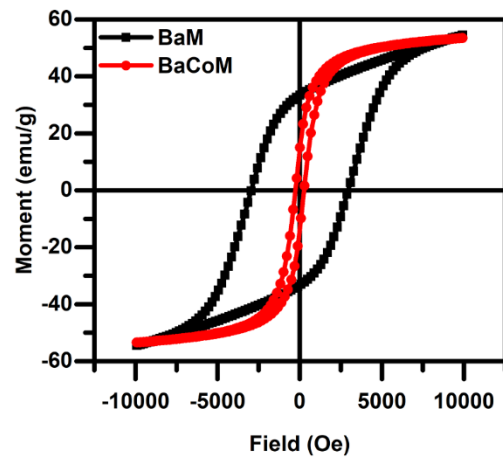


Fig. 2.  $M-H$  plots of BaM and BaCoM.

Previous studies reported the formation of a single M–type phase in Co substituted BaM for a similar composition [17,25]; however, minor W-type phase remains obscure due to the close Bragg position of both the phases in manual identification that misleads to the formation of a single phase. The cobalt substitution induces spinel ( $\text{CoFe}_2\text{O}_4$ ) parasitic phases at much lower temperature which promotes the formation of W-type ferrite ( $\text{M} + 2\text{Spinel}$ ), a similar result has been reported elsewhere [20,26]. Fractured surface micrograph showed (Fig. 1 (b & c)), Co substitution promotes grain growth with well distinguished hexagonal platelets. The increase in average grain size from 2.9 to 9.8  $\mu\text{m}$  is a consequence of oxygen vacancies and defect transportation [27].

Fig. 2 shows the room temperature magnetisation plot of BaM and BaCoM. No visible change in magnetisation was observed, however, coercivity ( $H_c$ ) were drastically decreased. The calculated magneto-crystalline anisotropy also found to decrease (10 kOe to 6.9 kOe) with cobalt substitution [28]. It can be concluded that hard magnetic behaviour of BaM transformed to soft magnetic with nearly retained magnetization, hence makes more magnetically permeable.

Fig. 3 (a–e) illustrates the deconvoluted XPS spectra of BaM and BaCoM. The Fe2p spectra shown in Fig. 3 (a & b) contains seven spectra for  $\text{Fe}^{3+}$  and  $\text{Fe}^{2+}$  ions with an area ratio of 76:24 and BaCoM, respectively. Fig. 3(c) shows O1s spectra with two sub spectra of  $\text{O}^{2-}$  and oxygen defect. The oxygen defect vacancies were found to be higher in BaCoM (45%) as compare to BaM (25%). Fig. 3(d) shows Co2p spectrum fitted for  $\text{Co}^{3+}$  and  $\text{Co}^{2+}$  ions and the calculated area ratio of  $\text{Co}^{3+}$  and  $\text{Co}^{2+}$  ions were 69:31. The presence of  $\text{Co}^{2+}$  ions increases  $\text{Fe}^{2+}$  ions and oxygen defects to maintain the charge neutrality.

In order to understand the electrical heterogeneities at microscopic level; impedance spectroscopy was employed [29]. The variation in imaginary impedance ( $Z''$ ) with frequency at different temperatures for both BaM and BaCoM are shown in Fig. 4 (a & b) respectively.  $Z''$  found to decrease with increase in both frequency and temperature which finally merges to a single frequency that suggests  $Z''$  is frequency independent. The broad relaxation peak(s) shifts toward higher frequency with temperature which confirms electrical responses are thermally activated [30]. Fig. 4 (c) shows the normalised imaginary part of impedance ( $Z''/Z''_{\text{max}}$ ) with frequency at selected temperatures. The peak position corresponds to relaxation frequency ( $f_{\text{max}}$ ). At 323 K, BaM do not show relaxation peak in the observed frequency range (10 Hz–10 MHz), which may appear below 10 Hz. Above 443 K, two resolved

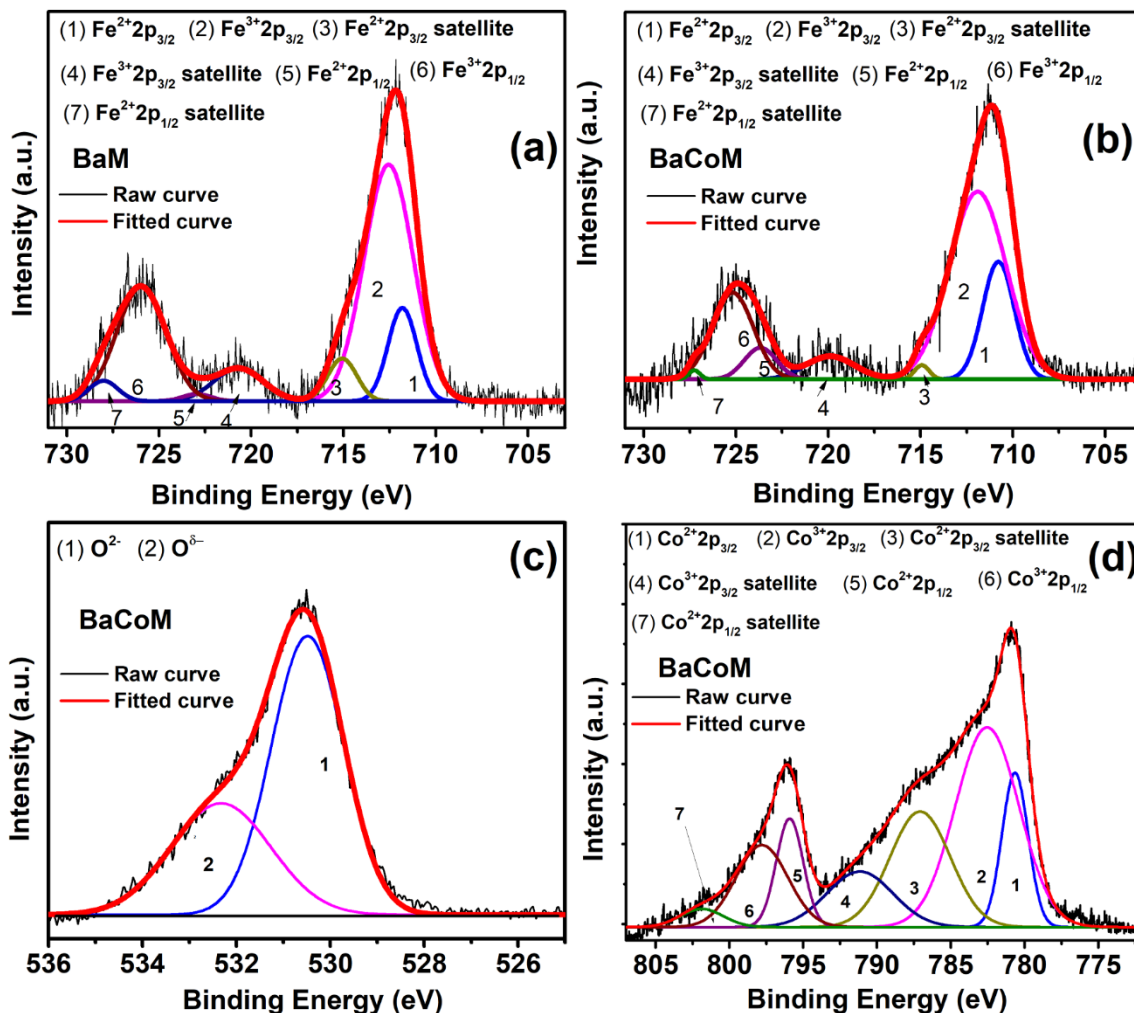


Fig. 3. Deconvoluted XPS spectra of sintered pellets, (a) Iron ions in BaM, (b) Iron ions in BaCoM, (c) Oxygen ions in BaCoM and (d) Cobalt ions in BaCoM.

asymmetric relaxation peak confirms the multiple relaxations are present in the material at different frequency domains [31]. For BaCoM, single Debye like relaxation peak was found for all temperature. The different  $f_{max}$  for BaM and BaCoM suggested that the relaxations are substitution dependent. The scaling curve, i.e.  $Z''/Z''_{max}$  vs  $\log(\omega/\omega_{max})$  for BaCoM (Fig. 4 (d)), indicated that the dynamic conduction process is temperature independent [32]. The calculated FWHM of the curves were higher than ideal Debye type relaxation (1.141 decades), which suggests multiple relaxations at closely distributed frequency domains due to microstructural inhomogeneities such as defects and secondary phases [29,33].

Fig. 5 (a) shows representative complex impedance plane plot for BaM and BaCoM. In BaM, two well resolved arcs corresponds to grain and grain boundary were observed, whereas, single arc was obtained for BaCoM. Significant difference between their impedance behaviour is shown in enlarged view (inset Fig. 5(a)). The representative log-log impedance plots for BaM and BaCoM at different temperatures are shown in Fig. 5. (b & c). In order to understand the electrical response of microstructural elements, the plots were fitted with equivalent circuits based on the bricklayer model. The model consists of grains, grain boundaries and minor impurity phase (W-type) contribution. However,

the possibility of unsubstituted metal oxides as an impurity phase (observed in XRD) cannot be ignored, which could also be a source of grain boundary [34]. The fitted equivalent circuits are shown in Fig. 5 (b & c) where  $C_1$  and  $R_1$  are capacitance and resistance for grain;  $R_2$  and  $CPE_1$  denotes resistance and constant phase element ( $Y_{CPE} = A_0(j\omega)^n$ ) assigned for grain boundary contribution [35], where  $n$  is the dimensionless power constant varies between zero (ideal resistor) to one (ideal capacitor). Variables  $R_3$  and  $C_2$  are the contributions of impurities at grain boundaries, which were absent in BaM. The fitted value of  $n$  was remained between 0.50 and 0.80.

The grain ( $R_g$ ) and grain boundaries ( $R_{gb}$ ) resistance obtained from the fit are shown in Table 1. For BaM,  $R_{gb}$  was not observed upto 170 °C which may show their contribution below 10 Hz. However, for BaCoM, grain boundary relaxation was present for all temperatures.

The conductivity ( $\sigma$ ) was calculated using resistances obtained from fitted complex impedance plane plot (Table 1).

Fig. 6 (a) shows the  $\ln \sigma$  versus  $1/T$  plots for grain (g), grain boundaries ( $g_b$ ) and impurity (I) for BaM and BaCoM. Conductivity found to increase with temperature however, higher conductivity of BaCoM is a consequence of more charge carriers as confirmed from XPS. It is also noted, conductivity plot shows three distinct slopes in

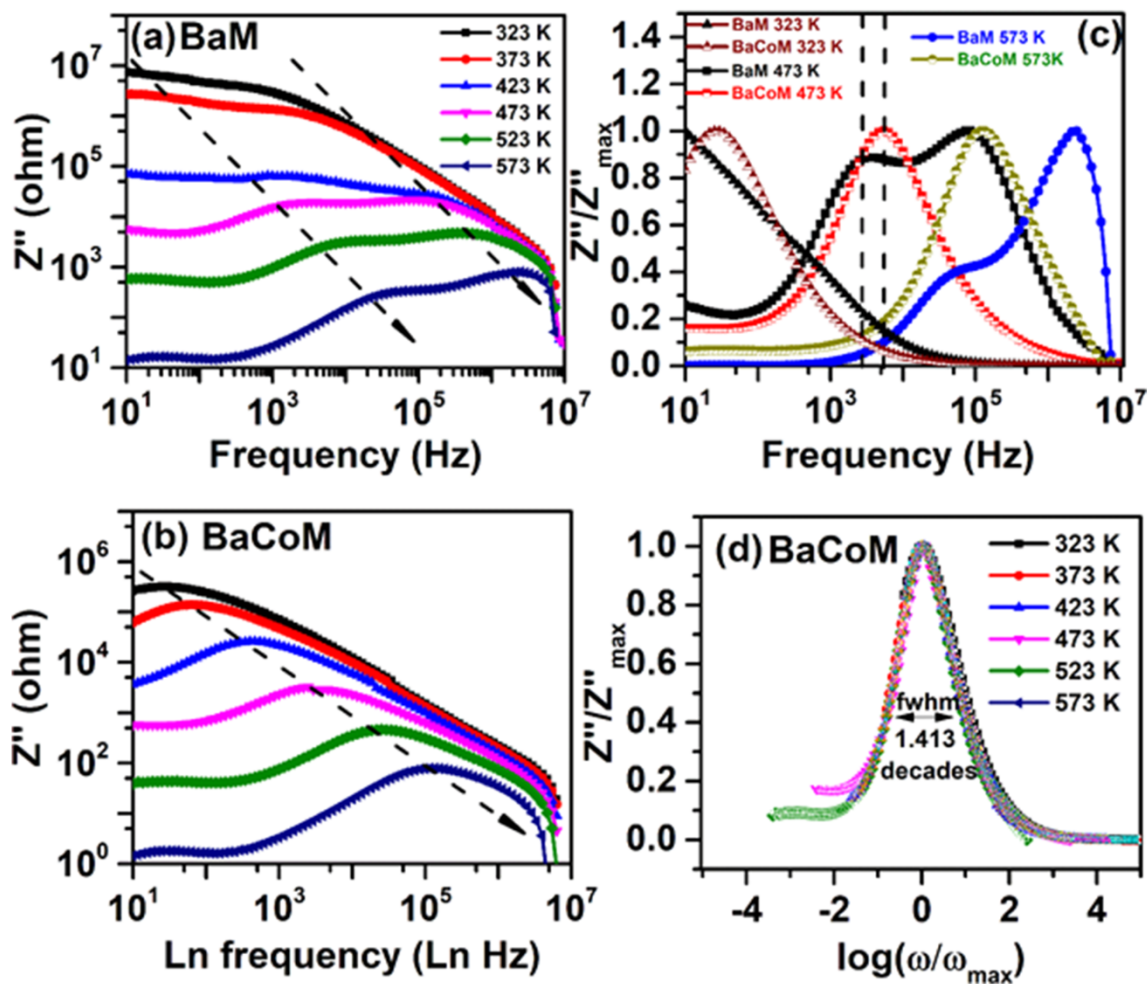


Fig. 4. Frequency dependent  $Z''$  at different temperature (a) BaM, (b) BaCoM, (c) Representative frequency dependent normalised  $Z''$  plots and (d) Scaling behaviour of  $Z''$  spectra of BaCoM.

different temperatures regime named as R I, R II and R III. The activation energy as obtained from Arrhenius plots for different temperature regime is shown in Table 2.

The studied temperature range was well below any structural/magnetic phase transition of BaM; therefore, change in the slope may ascribe to parallel conduction mechanisms in the system. The conduction in R I (323–393 K) is due to free charge carrier which required low activation energy to participate in conduction. The R II (393–473 K) for BaM shows sudden rise in the  $\sigma_g$  with an activation energy of 0.72 eV. In this region, grain boundary contribution was also observed. The rise in conductivity is associated with hopping of charges between  $\text{Fe}^{2+}$ - $\text{Fe}^{3+}$  from the localised oxygen trap centre to the nearest neighbouring sites as proposed in nearest-neighbouring-hopping model [36,37]. In BaCoM, the charge conduction through hopping mechanism is dominated over to a wider temperature range (393–553 K). This could be due to additional hopping due to  $\text{Co}^{2+}$ - $\text{Co}^{3+}$  ions. Also the presence of cobalt ions at grain boundaries will provide conduction channels and promote grain to grain conduction as evident by the higher conductivity and low activation energy. The behaviour is also supported by conductivity of impurities which showed metallic like behaviour above

443 K. The important feature is to be noted that for BaM, the transition from R II to R III is occurring at 473 K whereas, for BaCoM, it took place at 553 K. In R III, the same activation energy for BaCoM suggest the effect of substitution was negligible. In this region the conduction may be due to fragmentation of bigger polaron into smaller polaron which causes a sharp change in conductivity.

Further, to understand the conduction mechanism,  $\sigma_{dc}$  and  $\sigma_{ac}$  contribution were extracted from the real part of complex conductivity ( $\sigma'$ ) using Jonscher's power law [38].

$$\sigma' = \sigma_{dc} + \left( \frac{\omega}{\omega_H} \right)^S \quad (1)$$

where,  $\left( \frac{\omega}{\omega_H} \right)^S$  is  $\sigma_{ac}$  contribution,  $\omega_H$  is hopping frequency of charge carriers and  $S$  is a dimensionless frequency exponent lies between 0.0 and 1.0. According to law,  $\sigma_{dc}$  is temperature dependent whereas,  $\sigma_{ac}$  is both frequency and temperature dependent. The  $S$  was obtained by fitting frequency dependent conductivity behaviour of BaM and BaCoM at different temperature. The variation in  $S$  with temperature are correlated with various ac conduction mechanisms associated with the

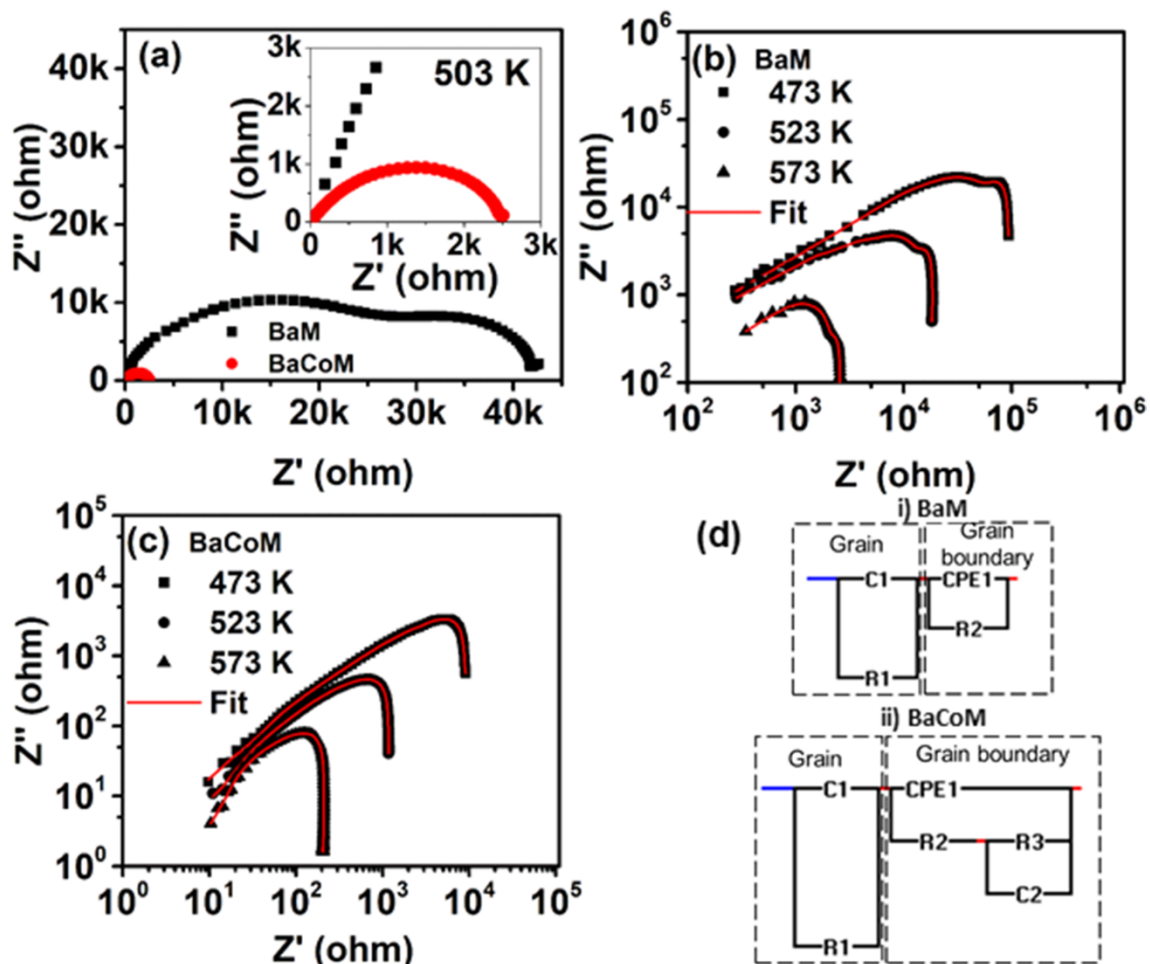


Fig. 5. (a) Complex impedance plane plot for BaM and BaCoM at 503 K, (b & c) Representative log – log plot of complex impedance ( $Z'$  vs  $Z''$ ) at different temperature and (d) Equivalent circuit based on the brick – layer model for the impedance spectra.

**Table 1**  
Resistance obtained from complex impedance plane plot.

| T (K) | BaM         |                | BaCoM       |                | $R_i$ (ohm) |
|-------|-------------|----------------|-------------|----------------|-------------|
|       | $R_g$ (ohm) | $R_{gb}$ (ohm) | $R_g$ (ohm) | $R_{gb}$ (ohm) |             |
| 323   | 1,099,187   | –              | 131,667     | 1,003,456      | 18.3        |
| 373   | 857,443     | –              | 107,751     | 319,320        | 14.5        |
| 423   | 98,517      | –              | 42,854      | 43,227         | 8.0         |
| 473   | 15,012      | 21,752         | 4726        | 2531           | –           |
| 523   | 148.5       | 168.2          | 521.5       | 478.4          | –           |
| 573   | 18.3        | 21.5           | 89.1        | 32.8           | –           |
| 623   | 4.7         | 4.4            | 2.6         | 0.5            | –           |

system. In general,  $S = 0$  corresponds to free migration of charge carriers and if  $S \sim 1$ , the conduction will be dominated by hopping mechanism. Fig. 6(b) shows the variation in  $S$  with temperature; both BaM and BaCoM showed similar behaviour. It is clear that  $S$  value is below one and remains nearly constant upto 533 K. Therefore, the primary conduction mechanism in this region is due to hopping of charges. The higher  $S$  values of BaCoM compared to BaM is due to

additional  $\text{Co}^{2+}$  and  $\text{Co}^{3+}$  ions as confirmed from XPS. With increase in temperature,  $S$  decrease to its minimum at 503 K. Further increase in temperature promotes larger lattice vibration which leads to the formation of polaron.

This behaviour was explained in overlapping large polaron tunneling (OLPT) model [39]. According to model,  $S$  is defined as:

$$S = 1 - \frac{8\alpha R_\omega + 6\beta W_{Ho} r_p / R_\omega}{(2\alpha R_\omega + \beta W_{Ho} r_p / R_\omega)^2} \quad (2)$$

where,  $R_\omega$  is the hopping distance at frequency  $\omega$ ,  $\beta$  is  $1/k_B T$  (where  $k_B$  is Boltzmann constant and  $T$  is temperature in K),  $\alpha$  is spatial decay parameter for localised wave function,  $r_p$  is the polaron radius and  $W_{Ho}$  is polaron hopping energy. The decrease in  $S$  with temperature occurs for larger  $r_p$ . Further increase in temperature,  $S$  increases rapidly due to fragmentation of larger polaron into smaller one as described in small polaron quantum mechanical tunnelling model (SPQMT) [39]. The  $S$  value higher than one is due to site to site motion of mobile charges by quantum mechanical tunnelling between asymmetrical double potential [40]. The behaviour of  $S$  is in accordance with temperature dependent conductivity behaviour.

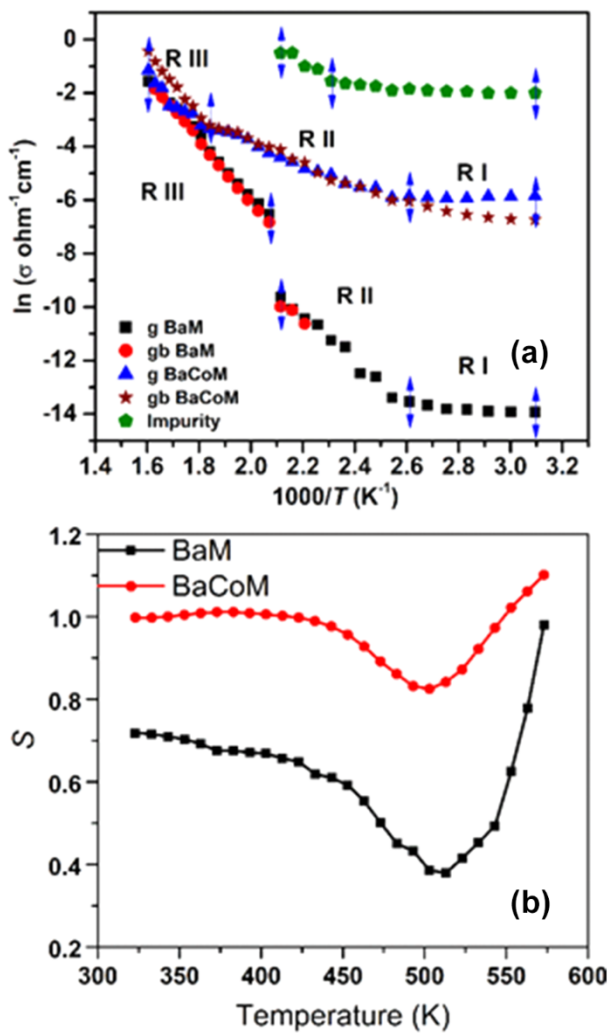


Fig. 6. (a) Arrhenius plot of conductivity for BaM and BaCoM (b) Variation of power law exponent as a function of temperature for BaM and BaCoM.

Table 2

Activation energy calculated from Arrhenius plot for BaM and BaCoM.

| Microstructural Elements | Activation energy (eV) |      |       |           |           |       |
|--------------------------|------------------------|------|-------|-----------|-----------|-------|
|                          | BaM                    |      |       | BaCoM     |           |       |
|                          | R I                    | R II | R III | R I       | R II      | R III |
| Grain                    | 0.08                   | 0.72 | 0.97  | 0.0069    | 0.33      | 0.82  |
| Grain Boundary           | -                      | 0.59 | 1.00  | 0.09      | 0.35      | 1.00  |
| Impurity                 | -                      | -    | -     | 323–423 K | 423–443 K | -     |
|                          | -                      | -    | -     | 0.041     | 0.56      | -     |

#### 4. Conclusion

In summary, charge transport mechanism for cobalt substituted barium hexaferrites has been investigated by impedance spectroscopy and compared with BaM. VSM confirms the soft magnetic nature BaCoM. XPS revealed that the cobalt substitution increases the fraction of  $\text{Fe}^{2+}$  ions and oxygen defect vacancies. Two individual relaxation peaks as observed in BaM were converge to a single relaxation peak with Co-substitution. The scaling behaviour confirms a deviated Debye type relaxation. The brick layer model were fitted by considering grain

and grain boundary contribution for BaM with an additional impurity contribution for BaCoM. The  $\ln \sigma$  versus  $1/T$  plots concludes three different conduction mechanisms. At low temperatures (323 – 393 K) the conduction is by free ions, followed by hopping of individual charges in intermediate temperature range (393 – 553 K). At higher temperatures ( $> 553$  K), the larger polarons fragmented into smaller ones and dominated the conduction process. Above this temperature, the conductivity of BaM and BaCoM converges that indicates the conduction process is substitution independent. The frequency dependent conductivity follows the Jonscher's power law. The variation in frequency exponent with temperature also confirmed three types of conduction process in different temperature regime. The studied conduction mechanism are in accordance to overlapping large polaron tunnelling (OLPT) model.

#### CRedit authorship contribution statement

**Santhoshkumar Mahadevan:** Conceptualization, Methodology, Data curation, Writing - original draft. **Puneet Sharma:** Supervision, Writing - review & editing.

#### Declaration of Competing Interest

The authors declare that they have no known competing financial interests or personal relationships that could have appeared to influence the work reported in this paper.

#### Acknowledgments

This work has been carried out under the financial support provided by DST (SERB No. SB/S2/CMP-081/2013). The authors would like to acknowledge Prof. K Singh and Mrs. Nethu Bansal, School of Physics and Materials Science, Thapar Institute of Engineering & Technology for Impedance Measurements.

#### References

- [1] R.C. Pullar, Hexagonal ferrites : A review of the synthesis, properties and applications of hexaferrite ceramics, *Prog. Mater. Sci.* 57 (2012) 1191–1334.
- [2] G. Lawes, T. Kimura, C.M. Varma, M.A. Subramanian, N. Rogado, R.J. Cava, A.P. Ramirez, Magnetodielectric effects at magnetic ordering transitions, *Prog. Solid State Chem.* 37 (2009) 40–54, <https://doi.org/10.1016/j.progsolidstchem.2009.08.001>.
- [3] V.G. Harris, Modern microwave ferrites, *IEEE Trans. Magn.* 16 (1980) 1038–1047.
- [4] H. Izadkhan, S. Zare, S. Somu, C. Vittoria, Effects of cobalt substitutions on the magnetoelectric coupling of M-type hexaferrite films, *Appl. Phys. Lett.* 106 (2015) 1–5, <https://doi.org/10.1063/1.4916102>.
- [5] J.E. Beevers, C.J. Love, V.K. Lazarov, S.A. Cavill, H. Izadkhan, C. Vittoria, R. Fan, G. van der Laan, S.S. Dhesi, Enhanced magnetoelectric effect in M-type hexaferrites by Co substitution into trigonal bi-pyramidal sites, *Appl. Phys. Lett.* 112 (2018) 082401, <https://doi.org/10.1063/1.5017683>.
- [6] L. Wang, D. Wang, Q. Cao, Y. Zheng, H. Xuan, J. Gao, Y. Du, Electric control of magnetism at room temperature, *Sci. Rep.* 2 (2012) 1–5, <https://doi.org/10.1038/srep00223>.
- [7] Q. Zhu, R. Tang, H. Zhou, Y. Wang, S. Xu, J. Zhang, C. Jiang, X. Su, H. Yang, Impedance spectroscopy and conduction mechanism of magnetoelectric hexaferrite BaFe<sub>10</sub>2Sc1.8O19, *J. Am. Ceram. Soc.* 102 (2019) 4038–4047, <https://doi.org/10.1111/jace.16275>.
- [8] S. Kumar, S. Guha, S. Supriya, L.K. Pradhan, M. Kar, Correlation between crystal structure parameters with magnetic and dielectric parameters of Cu-doped barium hexaferrite, *J. Magn. Mater.* 499 (2020) 166213, <https://doi.org/10.1016/j.jmmm.2019.166213>.
- [9] Han-Shin Cho, Sung-Soo Kim, M-hexaferrites with planar magnetic anisotropy and their application to high-frequency microwave absorbers, *IEEE Trans. Magn.* 35 (1999) 3151–3153, <https://doi.org/10.1109/20.801111>.
- [10] S.M. Abbas, R. Chatterjee, A.K. Dixit, A.V.R. Kumar, T.C. Goel, Electromagnetic and microwave absorption properties of (Co<sup>2+</sup>+Si<sup>4+</sup>) substituted barium hexaferrites and its polymer composite, *J. Appl. Phys.* 101 (2007) 074105, <https://doi.org/10.1063/1.2716379>.
- [11] J. Lee, Y.-K. Hong, W. Lee, G.S. Abo, J. Park, N. Neveu, W.-M. Seong, S.-H. Park, W.-K. Ahn, Soft M-type hexaferrite for very high frequency miniature antenna applications, *J. Appl. Phys.* 111 (2012) 07A520, <https://doi.org/10.1063/1.3679468>.
- [12] C. Liu, Q. Xu, Y. Tang, Z. Wang, R. Ma, N. Ma, P. Du, Zr<sup>4+</sup> doping-controlled permittivity and permeability of BaFe<sub>12</sub>xZrxO<sub>19</sub> and the extraordinary EM

- absorption power in the millimeter wavelength frequency range, *J. Mater. Chem. C* 4 (2013) 9532, <https://doi.org/10.1039/c6tc03430f>.
- [13] X. Zhang, Y.G. Zhao, Y.F. Cui, L.D. Ye, J.W. Wang, S. Zhang, H.Y. Zhang, M.H. Zhu, Magnetodielectric effect in Z-type hexaferrite, *Appl. Phys. Lett.* 100 (2012) 032901, <https://doi.org/10.1063/1.3677672>.
- [14] K. Zhai, N. Su, J. Sun, J. Cheng, Z. Liu, Y. Sun, Pressure effect on spin-driven multiferroicity in a Y-type hexaferrite, *J. Mater. Chem. C* 7 (2019) 4173–4177, <https://doi.org/10.1039/C9TC00477G>.
- [15] Y. Wang, S. Zhang, W.K. Zhu, L. Ling, L. Zhang, Z. Qu, L. Pi, W. Tong, M. Tian, Reversal and non-reversal ferroelectric polarizations in a Y-type hexaferrite, *J. Mater. Chem. C* 7 (2019) 340–345, <https://doi.org/10.1039/C8TC05247F>.
- [16] P. Sharma, A. Verma, R.K. Sidhu, O.P. Pandey, Effect of processing parameters on the magnetic properties of strontium ferrite sintered magnets using Taguchi orthogonal array design, *J. Magn. Mater.* 307 (2006) 157–164, <https://doi.org/10.1016/j.jmmm.2006.03.063>.
- [17] K. Rana, P. Thakur, M. Tomar, V. Gupta, A. Thakur, Investigation of cobalt substituted M-type barium ferrite synthesized via co-precipitation method for radar absorbing material in Ku-band (12–18 GHz), *Ceram. Int.* 44 (2018) 6370–6375, <https://doi.org/10.1016/J.CERAMINT.2018.01.028>.
- [18] P.M.T. Ikonen, K.N. Rozanov, A.V. Osipov, P. Alitalo, S.A. Tretyakov, Magnetodielectric substrates in antenna miniaturization: potential and limitations, *IEEE Trans. Antennas Propag.* 54 (2006) 3391–3399, <https://doi.org/10.1109/TAP.2006.884303>.
- [19] J. Lee, Y.-K. Hong, W. Lee, G.S. Abo, Soft M-type hexaferrite for very high frequency miniature antenna applications, *J. Appl. Phys.* 111 (2012) 7–520, <https://doi.org/10.1063/1.3679468>.
- [20] K.K. Mallick, P. Shepherd, R.J. Green, Magnetic properties of cobalt substituted M-type barium hexaferrite prepared by co-precipitation, *J. Magn. Mater.* 312 (2007) 418–429, <https://doi.org/10.1016/j.jmmm.2006.11.130>.
- [21] P. Shepherd, K.K. Mallick, R.J. Green, Dielectric properties of cobalt substituted M-type barium hexaferrite prepared by co-precipitation, *J. Mater. Sci. Mater. Electron.* 18 (2007) 527–534, <https://doi.org/10.1016/j.jmmm.2006.11.130>.
- [22] A.I. Drokin, S. Ni, S.S. Gendeleev, N.I. Vershinina, Losses from rotational hysteresis and magnetic anisotropy in single crystals of barium and barium-cobalt hexaferrites, *Sov. Phys. J.* 11 (1968) 7–12.
- [23] İ. Araz, F. Genç, Development of broadband microwave absorber and measurement of its magnetic and microwave properties, *J. Supercond. Nov. Magn.* 31 (2018) 279–283, <https://doi.org/10.1007/s10948-017-4216-0>.
- [24] İ. Araz, Microwave characterization of co-doped barium hexaferrite absorber material, *J. Supercond. Nov. Magn.* 29 (2016) 1545–1550, <https://doi.org/10.1007/s10948-016-3447-9>.
- [25] G.B. Teh, D.A. Jefferson, High-resolution transmission electron microscopy studies of sol-gel-derived cobalt-substituted barium ferrite, *J. Solid State Chem.* 167 (2002) 254–257.
- [26] M. Malassis, H. Zagnazi, P. Poix, C. Chaumont, J.C. Bernier, Structure of cobalt and fluorine doped hexaferrites, *J. Mater. Sci.* 27 (1992) 876–880.
- [27] G.Z. Zang, J.F. Wang, H.C. Chen, W. Bin Su, C.M. Wang, P. Qi, Effect of Co<sub>2</sub>O<sub>3</sub> on the microstructure and electrical properties of Ta-doped SnO<sub>2</sub> varistors, *J. Phys. D, Appl. Phys.* 38 (2005) 1072–1075, <https://doi.org/10.1088/0022-3727/38/7/017>.
- [28] R. Grossinger, A critical examination of the law of approach to saturation. I. Fit procedure, *Phys. Status Solidi.* 66 (1981) 665–674.
- [29] E. Barsoukov, J.R. Macdonald, *Impedance Spectroscopy*, Wiley, Third, 2018.
- [30] J. Liu, C.-G. Duan, W.-G. Yin, W.N. Mei, R.W. Smith, J.R. Hardy, Large dielectric constant and Maxwell-Wagner relaxation in Bi<sub>2/3</sub>Cu<sub>3</sub>Ti<sub>4</sub>O<sub>12</sub> (n.d.), doi:10.1103/PhysRevB.70.144106.
- [31] C.K. Suman, K. Prasad, R.N.P. Choudhary, Complex impedance studies on tungsten-bronze electroceramic: Pb<sub>2</sub>Bi<sub>3</sub>LaTi<sub>5</sub>O<sub>18</sub>, *J. Mater. Sci.* 41 (2006) 369–375, <https://doi.org/10.1007/s10853-005-2620-5>.
- [32] S. Saha, T.P. Sinha, Low-temperature scaling behavior of BaFe<sub>0.5</sub>Nb<sub>0.5</sub>O<sub>3</sub>, *Phys. Rev. B* 65 (2002) 1–7, <https://doi.org/10.1103/PhysRevB.65.134103>.
- [33] E. Barsoukov, J.R. Macdonald, *Impedance Spectroscopy Theory, Experiment, and Applications*, second, Wiley, 2005.
- [34] M. Drofenik, A. Znidaršič, I. Zajc, Highly resistive grain boundaries in doped MnZn ferrites for high frequency power supplies, *J. Appl. Phys.* 82 (1997) 333–340, <https://doi.org/10.1063/1.365817>.
- [35] R. Tang, C. Jiang, J. Jian, Y. Liang, X. Zhang, H. Wang, H. Yang, Impedance spectroscopy and scaling behaviors of Sr<sub>3</sub>Co<sub>2</sub>Fe<sub>24</sub>O<sub>41</sub> hexaferrite, *Appl. Phys. Lett.* 106 (2015) 022902.
- [36] Nevill F. Mott, Edward A. Davis, *Electronic Processes In Non-Crystalline Materials*, Oxford University Press, 2012 [https://books.google.co.in/books?hl=en&lr=&id=P11b\\_yhKH-YC&oi=fnd&pg=PP1&dq=Mott,+N.+F.%3B+Davis,+E.+A.+Electronic+Processes+in+Non-crystalline+Materials%3B+Clarendon:+Oxford,+1979&ots=d6x-aCD2\\_d&sig=mI9V9oULQ0TSQjwgC8xyTIZxh0#v=onepage&q&f=false](https://books.google.co.in/books?hl=en&lr=&id=P11b_yhKH-YC&oi=fnd&pg=PP1&dq=Mott,+N.+F.%3B+Davis,+E.+A.+Electronic+Processes+in+Non-crystalline+Materials%3B+Clarendon:+Oxford,+1979&ots=d6x-aCD2_d&sig=mI9V9oULQ0TSQjwgC8xyTIZxh0#v=onepage&q&f=false) (accessed September 22, 2019).
- [37] H. Zheng, W. Weng, G. Han, P. Du, Colossal permittivity and variable-range-hopping conduction of polarons in Ni<sub>0.5</sub>Zn<sub>0.5</sub>Fe<sub>2</sub>O<sub>4</sub> ceramic, *J. Phys. Chem. C* 117 (2013) 12966–12972, <https://doi.org/10.1021/jp402320b>.
- [38] A.K. Jonscher, The ‘universal’ dielectric response, *Nature* 267 (1977) 673–679, <https://doi.org/10.1038/267673a0>.
- [39] Aswini Ghosh, Frequency-dependent conductivity in bismuth-vanadate glassy semiconductors, *Phys. Rev. B* 41 (1990) 1479–1488, <https://doi.org/10.1017/CBO9781107415324.004>.
- [40] K.S. Gilkoy, W.A. Phillips, An asymmetric double-well potential model for structural relaxation processes in amorphous materials, *Philos. Mag. B Phys. Condens. Matter; Stat. Mech. Electron. Opt. Magn. Prop.* 43 (1981) 735–746, <https://doi.org/10.1080/01418638108222343>.



ELSEVIER

Contents lists available at ScienceDirect

Ceramics International

journal homepage: [www.elsevier.com/locate/ceramint](http://www.elsevier.com/locate/ceramint)

# Effect of three-step calcination on structural, magnetic and microwave properties of BaFe<sub>11.5</sub>Ti<sub>0.5</sub>O<sub>19</sub> hexaferrite

Santhoshkumar Mahadevan<sup>a</sup>, Sukhleen Bindra Narang<sup>b</sup>, Puneet Sharma<sup>a,\*</sup>

<sup>a</sup> School of Physics & Materials Science, Thapar Institute of Engineering & Technology, Patiala, 147004, Punjab, India

<sup>b</sup> Department of Electronics Technology, Guru Nanak Dev University, Amritsar, India

## ARTICLE INFO

### Keywords:

Hexaferrite  
Magnetic properties  
Microwave absorption

## ABSTRACT

BaFe<sub>12</sub>O<sub>19</sub> and BaFe<sub>11.5</sub>Ti<sub>0.5</sub>O<sub>19</sub> were prepared by three-step calcination method. Phase analysis and microstructural study were carried out by X-ray diffraction (XRD) and scanning electron microscopy (SEM). Site occupancy of Ti<sup>4+</sup> ions with calcination step were investigated by Fourier-transform infrared (FTIR) and Raman spectroscopy. The magnetic and microwave properties (Ku-band) were measured by vibration sample magnetometer and vector network analyzer. XRD patterns confirmed the hexaferrite phase formation in all samples. FTIR showed the presence of Ti<sup>4+</sup> ions at spin down octahedral and tetrahedral sites. The peak shift in FTIR and Raman spectra suggested that ion occupancy increases with calcination step. A drastic decrease in the coercivity was observed with substitution. Low dielectric and magnetic losses were observed in Ti-substituted samples. SEM revealed that Ti-substitution promotes hexagonal grain with decreased size. Overall microwave absorbance was greatly improved by three step calcination method.

## 1. Introduction

Owing to high natural ferromagnetic resonance (FMR) frequency 43–50 GHz, M-type barium hexaferrite (BaFe<sub>12</sub>O<sub>19</sub>) has gained considerable attention for high-frequency device application [1,2]. Its high magnetocrystalline anisotropy field ( $H_a$ ) overcomes the requirement of external bias magnetic field and facilitates miniaturization [3]. The FMR frequency ( $\omega_r$ ) is determined by the relation [4]:

$$\omega_r = \gamma(H_o + H_a \pm 4\pi M_s) \quad (1)$$

where,  $H_o$ ,  $\gamma$  and  $M_s$  are external bias magnetic field, gyromagnetic ratio and saturation magnetization respectively. It is evident that  $\omega_r$  can be tuned by intrinsic parameters ( $H_a$  and  $M_s$ ) and external bias field. The high  $H_a$  of BaFe<sub>12</sub>O<sub>19</sub> (BaM) lies in its crystal structure; consisted of two formula units, where 24 Fe<sup>3+</sup> ions occupies five different crystallographic sites i.e., three octahedral sites (12k, 4f<sub>2</sub> and 2a), one tetrahedral (4f<sub>1</sub>) and one trigonal bipyramidal (2b) site respectively. Presence of Fe<sup>3+</sup> ions at spin up 12k, 2a, 2b sites and spin down 4f<sub>1</sub>, 4f<sub>2</sub> sites contributes to a net magnetic moment of 40 $\mu_B$  per unit cell [5]. Suitable partial cationic substitution for Fe<sup>3+</sup> ions is widely adopted method to tune  $H_a$  and hence operable frequency. It is reported that substitution of Sc, or In ions reduces  $H_a$ , and frequency can be tuned to X- and Ku-band [6]. Further, suitable substitution of Co–Ti ions for Fe can change FMR to 1 GHz [7]. On contrary, Al and Ga leads to increase

$H_a$  for application upto U-, E- and W- bands [8]. Several other work by researchers well demonstrated the role of cationic substitution on magnetic and microwave properties of BaM [9–12]. The effective cation substitution also depends on adopted processing method and parameters. Therefore, effect of processing methods were also investigated for the same cationic substitution [13–15]. It is worth to mention that in all processing method, calcination is an important parameter. An inadequate calcination may lead to secondary phase formation and un-substituted cations [16]. The single step calcination method is widely adopted method to prepare substituted BaM [17]. However, it does not confirms effective site occupancy of chosen cation even upto 1400 °C reported earlier [18]. It is reported that un-substituted cations affect structure-sensitive coercivity ( $H_c$ ) due to pinning effect [14]. In order to understand the role of calcination on cation occupancy, Ti-substituted BaM (BaFe<sub>11.5</sub>Ti<sub>0.5</sub>O<sub>19</sub>) were prepared by three-step calcination method. Previously, multiple calcination with intermediate grinding were suggested to reduce impurities in hexagonal ferrite [19]. The present work focuses to investigate the effect of calcination step on the occupancy of Ti<sup>4+</sup> ions by XRD, FTIR, and Raman spectroscopy. The effect of calcination on the microwave and magnetic properties were studied by vibrating sample magnetometer (VSM) and vector network analyzer (VNA). It was observed that three-step calcination significantly improves the substitution fraction and affects magnetic and microwave properties of BaM.

\* Corresponding author.

E-mail address: [puneet.sharma@thapar.edu](mailto:puneet.sharma@thapar.edu) (P. Sharma).

<https://doi.org/10.1016/j.ceramint.2019.01.233>

Received 7 November 2018; Received in revised form 28 January 2019; Accepted 28 January 2019

0272-8842/ © 2019 Published by Elsevier Ltd.

## 2. Experimental

### 2.1. Preparation

In the present work, analytical grade  $\text{BaCO}_3$ ,  $\text{Fe}_2\text{O}_3$  and  $\text{TiO}_2$  of 99.9% purity from Sigma-Aldrich were used to prepare  $\text{BaFe}_{12-x}\text{Ti}_x\text{O}_{19}$ , ( $x = 0.0, 0.5$ ) by three-step calcination method. Precursors were weighed in stoichiometric composition and wet-mixed for 3 h using planetary ball mill. As mixed powders were subsequently pelletized at a pressure of 150 MPa using hydraulic press. In the first step, as-prepared pellets were calcined at 1200 °C for 3 h using muffle furnace. Heating and cooling rate were kept constant at 5 °C/min. The calcined pellets were pulverized to powder using vibratory mill. In the second step, pulverized powder was pelletized and re-calcined at 1200 °C for 3 h. Similar step was repeated for third step calcination. The pure BaM powder obtained from first, second and third step calcination process were labelled as BaM 1, BaM 2 and BaM 3, whereas Ti-substituted powders as BaTiM 1, BaTiM 2 and BaTiM 3 respectively. As-calcined powders from each step were mixed with binder (5% PVA) and pressed in rectangular die ( $16 \times 8$  mm) at a pressure of 250 MPa. Thickness of pellets were kept constant to 4 mm. The as-pressed pellets were sintered at 1250 °C for 1 h. For VNA measurements; the sintered rectangular pellets were ground to the size of wave guide cavity ( $15.74 \times 7.96$  mm).

### 2.2. Characterisation

Phase analysis was carried by X-ray diffractometer model Shimadzu XRD-6000 using  $\text{Cu } K_{\alpha 1}$  ( $1.54 \text{ \AA}$ ) radiation with a scan rate of  $0.02^\circ/\text{sec}$ . Nujol mull plots for Fourier Transform Infrared (FTIR) was carried out by Perkin Elmer spectrum 400. The measurements were done between wavenumber  $100 \text{ cm}^{-1}$  to  $2500 \text{ cm}^{-1}$  on KBr setting (ratio between KBr and ferrites were fixed to 25:1). Raman spectroscopy was carried by Renishaw RA 802 series equipped with a  $514.5 \text{ nm}$   $\text{Ar}^+$  laser at 20 mW. Microstructure analysis of sintered pellets were carried out by scanning electron microscope (SEM) coupled with energy dispersive spectroscopy (EDS) model JEOL (JSM-IT100). Prior to SEM, surface was made conducting by Au sputtering to avoid any charging during SEM. Average grain size was calculated statistically with the help of AxioVision SE64 and originPro 9 software. Magnetic measurements were performed using VSM model Lake Shore VSM 7400 with a maximum field of 1 T. Microwave absorption studies in  $K_u$ -band ( $12.4\text{--}18 \text{ GHz}$ ), were carried out by VNA model Agilent 5225A PNA series.

## 3. Results and discussion

### 3.1. XRD study

Fig. 1 shows representative XRD patterns of first and third step calcined BaM and BaTiM powders. In BaM, single phase was formed in first step calcination. No further changes were observed after subsequent calcinations. Whereas, BaTiM shows residual  $\text{Fe}_2\text{O}_3$  (~2%) upto second step calcination and diminished in third step calcination. After third step calcination, a marginal peak shift from  $34.08^\circ$  to  $34.14^\circ$  suggested the effective substitution. Due to comparable ionic radii of  $\text{Ti}^{4+}$  and  $\text{Fe}^{3+}$  ions, no noticeable change in lattice parameters were observed [20]. A marginal increase in calculated crystallite size [21] from 30 nm to 37 nm was observed with the calcination step.

### 3.2. Morphological study

Fig. 2(a and b) shows pulverized BaM particles of calcined samples. BaM 1 possess uniform particles with an average size of  $\sim 1.2 \mu\text{m}$ . However, repeated calcination coarsen the particle in BaM 3. The similar trends were obtained for BaTiM powders. Fig. 3(a–d) shows the

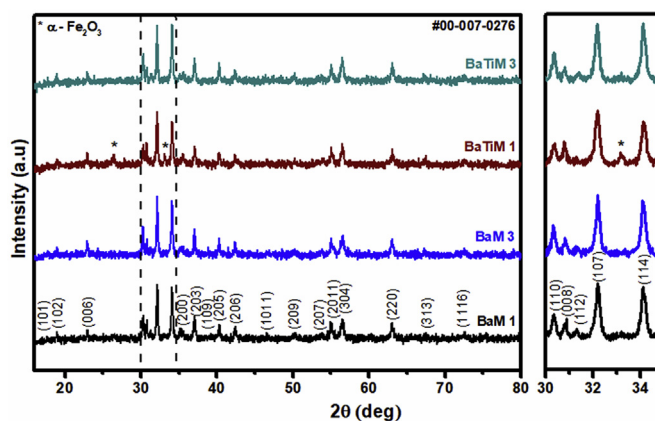


Fig. 1. Representative XRD plot for BaM and BaTiM. Magnified plot depicts peak shift in Ti-substituted powder.

microstructure of fractured surface of sintered BaM pellets. BaM1 shows elongated grains with an average grain size of  $3.6 \mu\text{m}$ . The larger grains size ( $4.9 \mu\text{m}$ ) were observed for BaM3 sample, which suggest that calcination step has significant effect on grain size. In BaTiM1 (Fig. 3 (c)) confirms that Ti-substitution promotes hexagonal morphology; it has been reported hexagonal grains around single domain size or greater tend to give improved microwave properties [22]. The grains for  $\text{Ti}^{4+}$  substituted ferrites in Fig. 3(c and d) appear smaller than BaM. The average grain size of BaTiM1 was  $2.6 \mu\text{m}$ . Morphology of BaTiM3 (Fig. 3 (d)) shows comparatively bigger grains with an average grain size of  $3.62 \mu\text{m}$ , however, the hexagonal morphology remains unaffected.

### 3.3. Fourier Transform Infrared Spectroscopy (FTIR)

Fig. 4 shows the FTIR spectrum ( $2500\text{--}100 \text{ cm}^{-1}$ ) of pure and substituted BaM. As the result of group theory, BaM compounds may give rise to 30 IR active modes ( $13A_{2u} + 17E_{1u}$ ), however, in the present spectra, only 6 active modes were observed due to partial superimposition of “spinel block” region [23]. FTIR spectrum for BaM shows the negligible effect of calcination steps, whereas, BaTiM shows a slight variation in the spectra over successive calcination. The observed frequency modes and the calculated bond length are tabulated in Table 1. The band at  $100\text{--}150 \text{ cm}^{-1}$  ( $A_{2u}$ ) primarily associated with dodecaordinated alkali heavy metals, the red shift ( $152\text{--}140 \text{ cm}^{-1}$ ) obtained in this region shows a stronger correlation between  $2b$  bipyramidal site and  $\text{Ba}^{2+}$  ions [24]. The split IR band around 220 and  $240 \text{ cm}^{-1}$  depicts iron-oxygen bond for  $2b$  ( $\text{FeO}_5$ ) and  $12k_1$  ( $\text{FeO}_6$ ) sites respectively. This  $2b$  band was not observed in BaTiM 1, however, in BaTiM 2 and BaTiM 3 band at  $223$  and  $226 \text{ cm}^{-1}$  respectively were observed. The  $12k_1$  band shows increment in wavenumber over calcination process due to increase site occupation by  $\text{Ti}^{4+}$  ions. The band at  $309 \text{ cm}^{-1}$  is due to residual  $\text{Fe}_2\text{O}_3$  as supported by XRD. The band at  $360 \text{ cm}^{-1}$  belongs to  $A_{2u}$  &  $E_{1u}$  modes of  $2a$  ( $\text{FeO}_6$ ) site. The  $A_{2u}$  mode of  $4f_1$  and  $4f_2$  site are visible at  $620 \text{ cm}^{-1}$  and  $450 \text{ cm}^{-1}$  respectively [25]. The gradual shift of  $4f_1$  and  $4f_2$  band towards higher wavenumber suggested the substitution of smaller  $\text{Ti}^{4+}$  ions. An overall blue shift in BaTiM 3 as compared to BaM 3 was due to  $\text{Ti}^{4+}$  occupation. The bond length for  $4f_1$  and  $4f_2$  band were calculated by force constant method as suggested previously [26]. The continuous reduction in bond length from  $2.27 \text{ \AA}$  to  $2.25 \text{ \AA}$  and  $1.86 \text{ \AA}$  to  $1.83 \text{ \AA}$  were observed with calcination steps. Additionally, this result supports that  $\text{Ti}^{4+}$  ion prefers to occupy the spin down  $4f_2$  and  $4f_1$  sites. A broad frequency band at  $830 \text{ cm}^{-1}$  depicts the existence of heavier  $\text{Ba}^{2+}$  ions [27]. To verify the substitution of  $\text{Ti}^{4+}$  ions with calcination step; Raman studies were carried out.

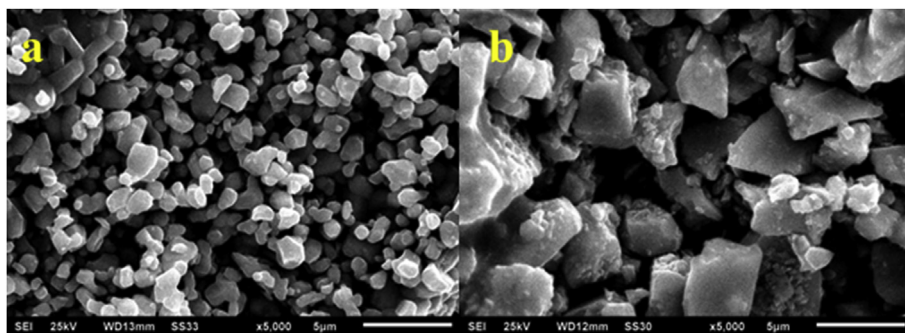


Fig. 2. Scanning electron micrographs of pulverized powder (a) BaM 1 and (b) BaM 3.

### 3.4. Raman spectroscopy

Fig. 5 shows the fitted Raman spectra recorded in the range of 200–800  $\text{cm}^{-1}$ . Among 42 Raman active modes ( $11A_{1g} + 14E_{1g} + 17E_{2g}$ ) as reported elsewhere [28] only five distinct peaks were observed at 271, 438, 522, 621 and 694  $\text{cm}^{-1}$  for BaM. No changes were observed in repeated calcination. However, BaTiM shows a blue shift towards higher wavenumber due to gradual substitution. The Raman modes of calcined powders are given in Table 2. The peak at 271  $\text{cm}^{-1}$  signifies vibration mode of  $E_{1g}$  for O – Fe – O bridge. The broad frequency band at 438  $\text{cm}^{-1}$  corresponds to  $A_{1g}$  metal oxide mode of 12k ( $\uparrow$ ) site [29]. The minor peak at 522  $\text{cm}^{-1}$  denotes  $E_{1g}$  mode of metal oxide bonds for the mixed site 12k ( $\uparrow$ ) and 2a ( $\uparrow$ ). The gradual shift were observed due to continuous substitution with calcination steps. The modes at 694  $\text{cm}^{-1}$  seems to be superimposed band of weak 2b (690  $\text{cm}^{-1}$ ) and strong  $4f_1$  (710  $\text{cm}^{-1}$ ) sites. This band shows the characteristic behaviour of  $A_{1g}$  tetrahedral oxygen coordinates. The variation in the mode after calcination signifies the effective substitution of  $\text{Ti}^{4+}$  ions.

### 3.5. Magnetic study

Fig. 6(a and b) shows the  $M$ - $H$  behaviour of BaM and BaTiM powders with maximum field of 1 T. The measured magnetic properties were tabulated in Table 3. The gradual rise in the saturation

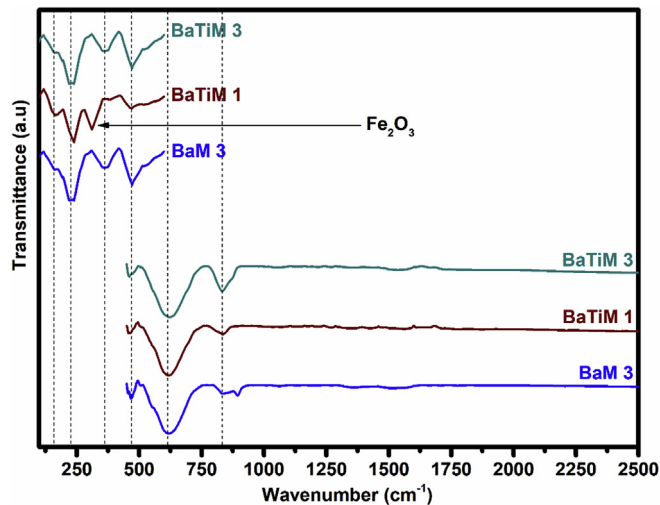


Fig. 4. FTIR spectrum of BaM and BaTiM powders.

magnetization ( $M$ ) with the calcination step for BaM (Fig. 6(a)) may attributed to decrease in residual  $\text{Fe}_2\text{O}_3$ , which was below the detectable limit of XRD. However,  $H_c$  and remanence ( $M_r$ ) merely affected by repeated calcination. The anisotropy field ( $H_a$ ) calculated by law of

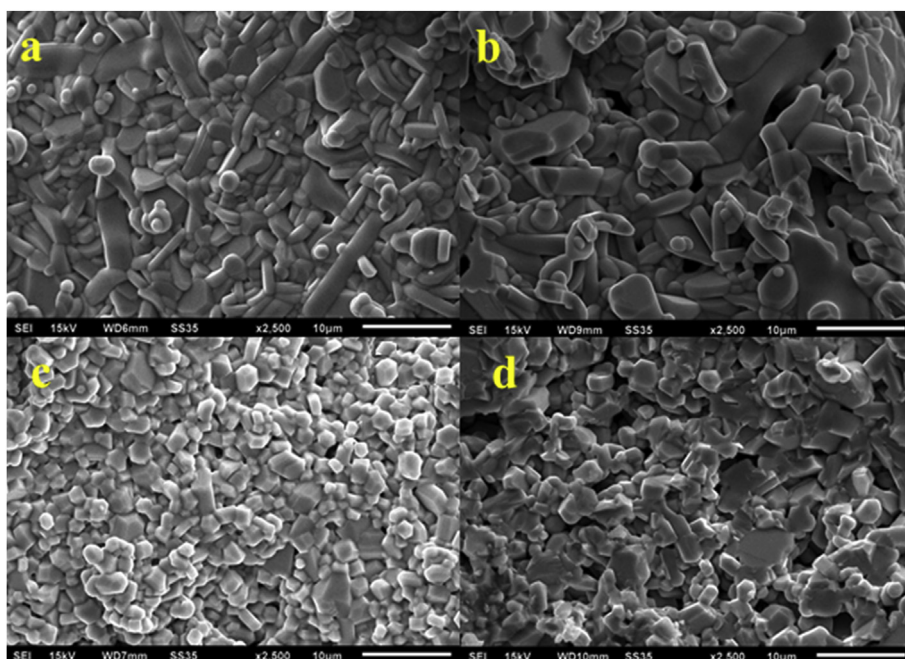


Fig. 3. Fractured surface of pure and Ti-substituted sintered pellets (a) BaM 1, (b) BaM 3, (c) BaTiM 1, (d) BaTiM 3.

**Table 1**  
FTIR modes of BaM and BaTiM.

| Bond                             | Mode              | Site             | BaM 3<br>( $\text{cm}^{-1}$ ) | BaTiM 1<br>( $\text{cm}^{-1}$ ) | BaTiM 2<br>( $\text{cm}^{-1}$ ) | BaTiM 3<br>( $\text{cm}^{-1}$ ) |
|----------------------------------|-------------------|------------------|-------------------------------|---------------------------------|---------------------------------|---------------------------------|
| Ba -O                            | $A_{2u}$          |                  | 135                           | 152                             | 144                             | 140                             |
| Fe -O                            | $A_{2u}$          | 2b               | 222                           | -                               | 223                             | 226                             |
|                                  | $A_{2u}$          | 12k <sub>1</sub> | 238                           | 239                             | 236                             | 242                             |
| Fe -O                            | $A_{2u} + E_{1u}$ | 2a               | 362                           | 361                             | 363                             | 366                             |
| Fe - O                           | $A_{2u}$          | $4f_2$           | 458                           | 469                             | 462                             | 464                             |
| Fe - O                           | $A_{2u}$          | $4f_1$           | 620                           | 616                             | 622                             | 625                             |
| Mass of $\text{Ba}^{2+}$         | -                 | -                | 837                           | 835                             | 833                             | 833                             |
| $\alpha - \text{Fe}_2\text{O}_3$ | -                 | -                | -                             | 309                             | -                               | -                               |

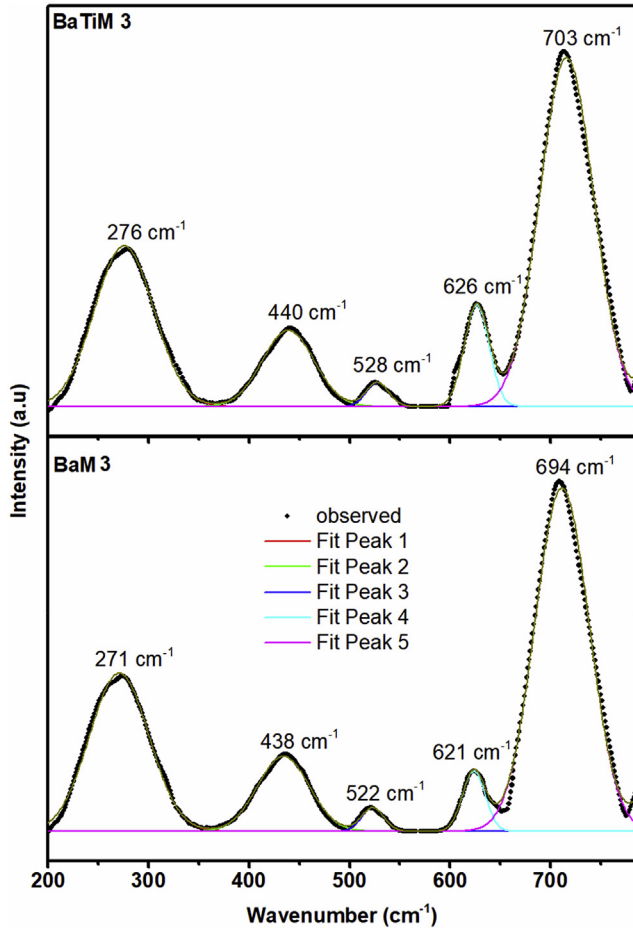


Fig. 5. Micro-Raman spectrum of BaM 3 and BaTiM 3 powders.

**Table 2**  
Raman modes of BaM and BaTiM.

| Bond         | Mode     | Site              | BaM<br>3 $\text{cm}^{-1}$ | BaTiM<br>1 $\text{cm}^{-1}$ | BaTiM<br>2 $\text{cm}^{-1}$ | BaTiM<br>3 $\text{cm}^{-1}$ |
|--------------|----------|-------------------|---------------------------|-----------------------------|-----------------------------|-----------------------------|
| Fe -O bridge | $E_{1g}$ | -                 | 271                       | 270                         | 275                         | 276                         |
| Fe -O        | $E_{2g}$ | 12k               | 438                       | 438                         | 439                         | 440                         |
| Fe -O        | $E_{1g}$ | 12k +<br>2a mixed | 522                       | 524                         | 525                         | 528                         |
| Fe -O        | $A_{1g}$ | $4f_2$            | 621                       | 622                         | 626                         | 626                         |
| Fe -O        | $A_{1g}$ | $4f_1$            | 694                       | 695                         | 699                         | 703                         |

approaching to saturation [30]; was significantly improved from 691.53 to 700.28 kA/m with calcination step due to reduction of oxygen vacancy. Whereas, a drastic decrease in  $H_c$  was observed in Ti-substituted (Fig. 6 b) samples. Further,  $H_c$  also found to decrease with calcination step, which suggests the gradual occupation of  $\text{Ti}^{4+}$  ion at

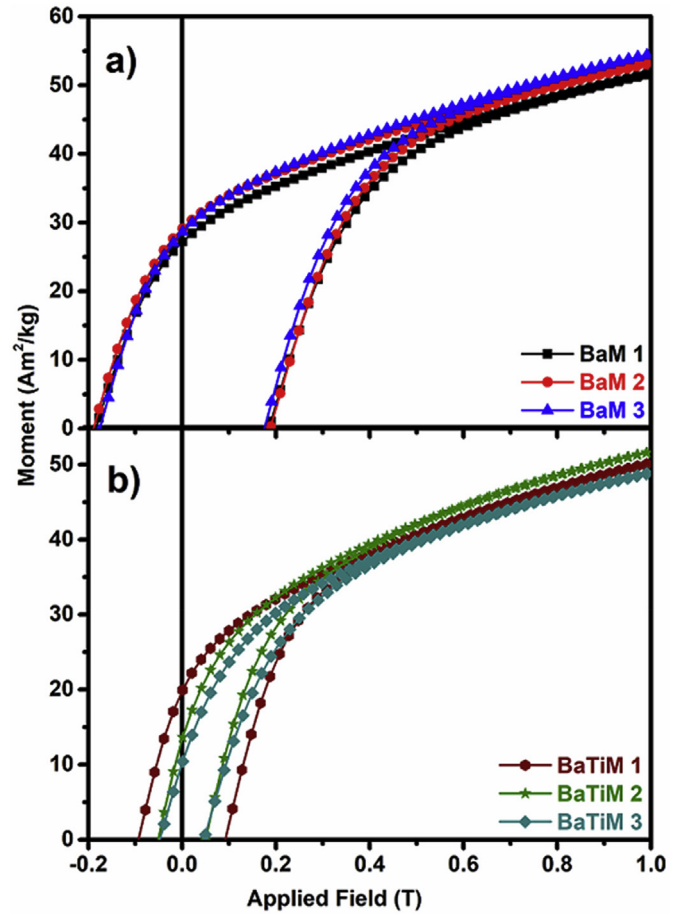


Fig. 6. M-H plot of BaM and BaTiM powders.

**Table 3**  
Magnetic properties of the BaM and BaTiM.

| Properties                             | Samples |        |        |         |         |         |
|--|---------|--------|--------|---------|---------|---------|
|  | BaM 1   | BaM 2  | BaM 3  | BaTiM 1 | BaTiM 2 | BaTiM 3 |
| $M_s$ (at 1 T) $\text{Am}^2/\text{kg}$ | 51.64   | 53.17  | 54.45  | 50.12   | 51.62   | 48.82   |
| $H_{ci}$ kA/m                          | 146.42  | 149.61 | 139.26 | 74.08   | 40.58   | 37.40   |
| $H_a$ kA/m                             | 691.53  | 683.57 | 700.28 | 696.30  | 689.14  | 672.43  |

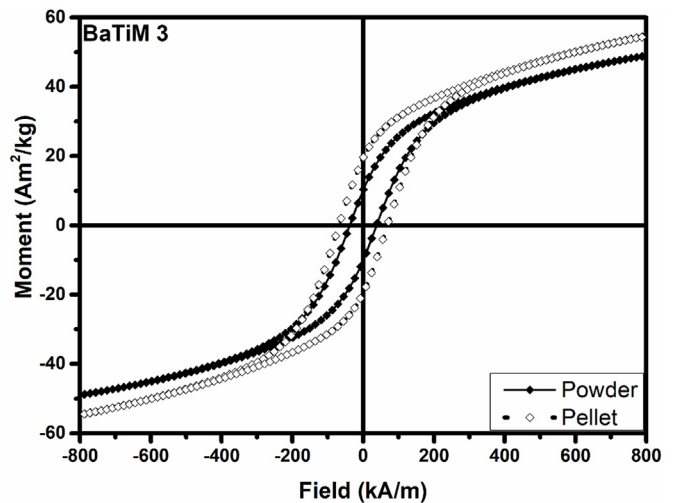


Fig. 7. Comparative M-H plot of BaTiM 3 powder and pellet.

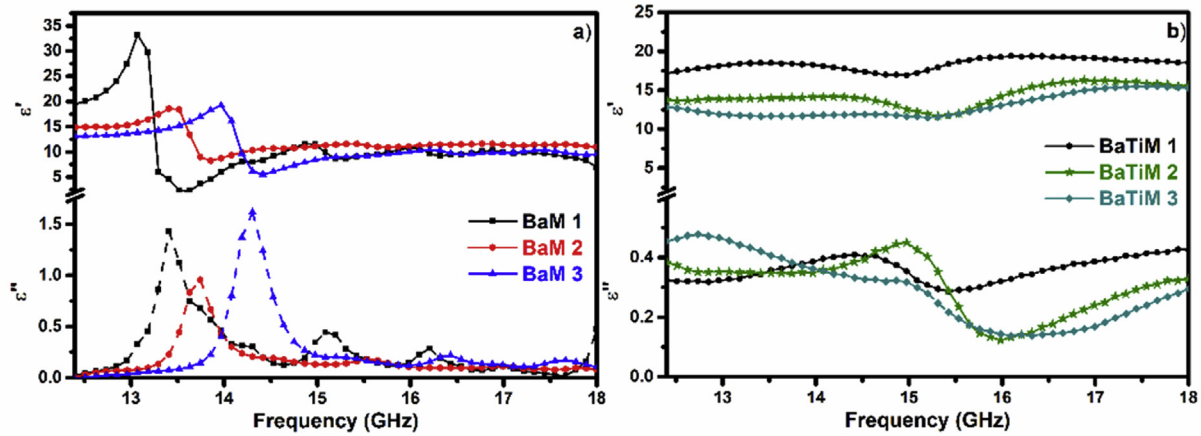


Fig. 8. Real and imaginary part of complex permittivity of (a) BaM and (b) BaTiM in Ku-band.

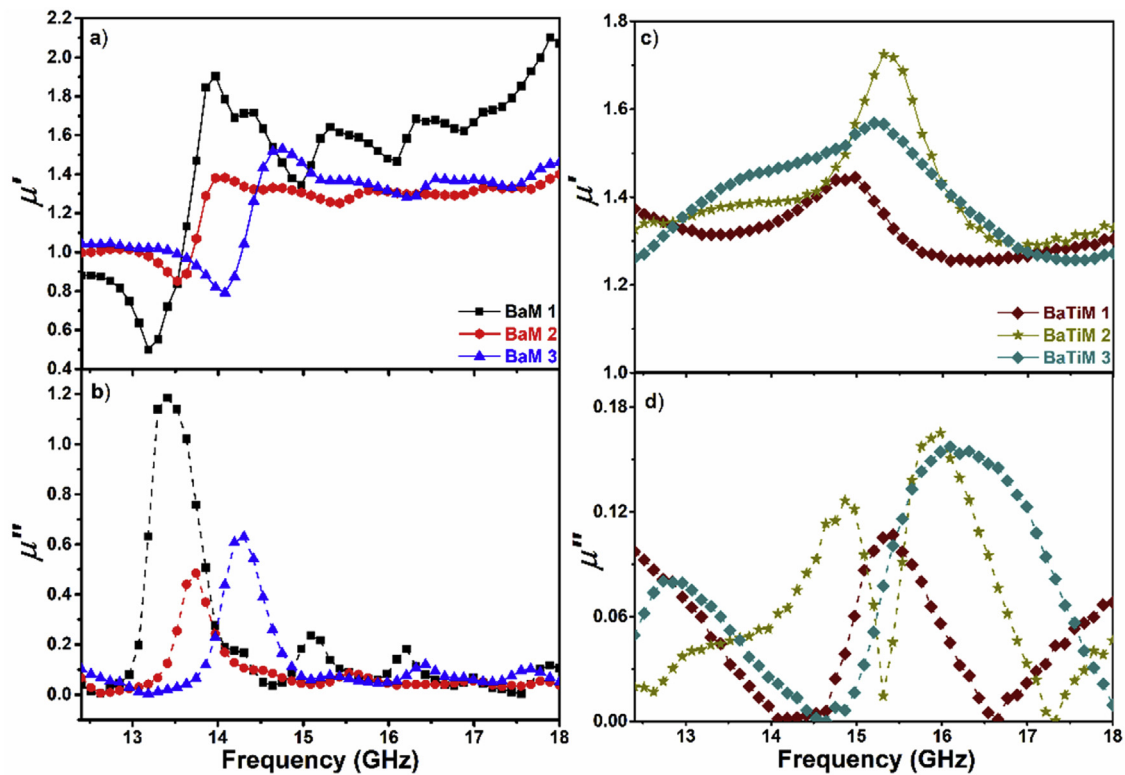


Fig. 9. Real and imaginary complex permeability (a & b) BaM and (c & d) BaTiM in Ku-band.

respective site. In addition to this,  $M$  found to be low in Ti substituted samples. Among substituted samples,  $M$  found to be higher in BaTiM2 despite  $\text{Ti}^{4+}$  occupation. This suggested that increase in  $M$  was attributed to substitution of  $\text{Ti}^{4+}$  ions at spin down  $4f_1$  &  $4f_2$  site. Further decrease in  $M$  verifies the substitution in spin up sites as suggested by FTIR and Raman studies. An overall reduction in magnetic parameters were ascribed to substitution of nonmagnetic  $\text{Ti}^{4+}$  ions, the results are comparable to earlier reported studies [31]. Fig. 7 illustrate the comparative plot of powder and sintered BaTiM3; similar magnetic behaviour was observed.

### 3.6. Electromagnetic studies

#### 3.6.1. Permittivity

The variations in the dielectric constant ( $\epsilon'$ ) and loss ( $\epsilon''$ ) in Ku-band are shown in Fig. 8 (a, b). In BaM, the decrease in  $\epsilon'$  is due to

suppression of interfacial and dipole polarization at higher frequency [32]. However, decrease in  $\epsilon'$  with calcination steps is attributed to reduction of bulk density. The presence of  $\text{Ba}^{2+}$ ,  $\text{Fe}^{3+}$  and  $\text{O}^{2-}$  ions in BaM contributes oscillatory behaviour of  $\epsilon'$  and  $\epsilon''$  as an effect of dipole polarization and relaxation [33]. The intensity of  $\epsilon'$  was found to be reduce from 33 to 19 and shifted to higher frequency (13.07–13.97 GHz) due to the variation in the dipole strength. The obtained  $\epsilon'$  values in Ku-band are comparable to previous studies, the marginal variation is ascribed to adopted processing methodology [34]. Similar oscillatory behaviour in  $\epsilon''$  for unsubstituted BaM were observed. The minimum in  $\epsilon'$  at maximum  $\epsilon''$  gives good agreement for damping of dipole polarization [35]. On the other hand, substituted BaM Fig. 8(b) shows a suppressed oscillatory behaviour in  $\epsilon'$  and throughout the frequency range. This suppressed behaviour is associated with multiple dipoles and relaxation persuaded by  $\text{Ti}^{4+}$  ions [33]. Minimal  $\epsilon''$  was observed (0.4–0.5) for substituted BaM, which,

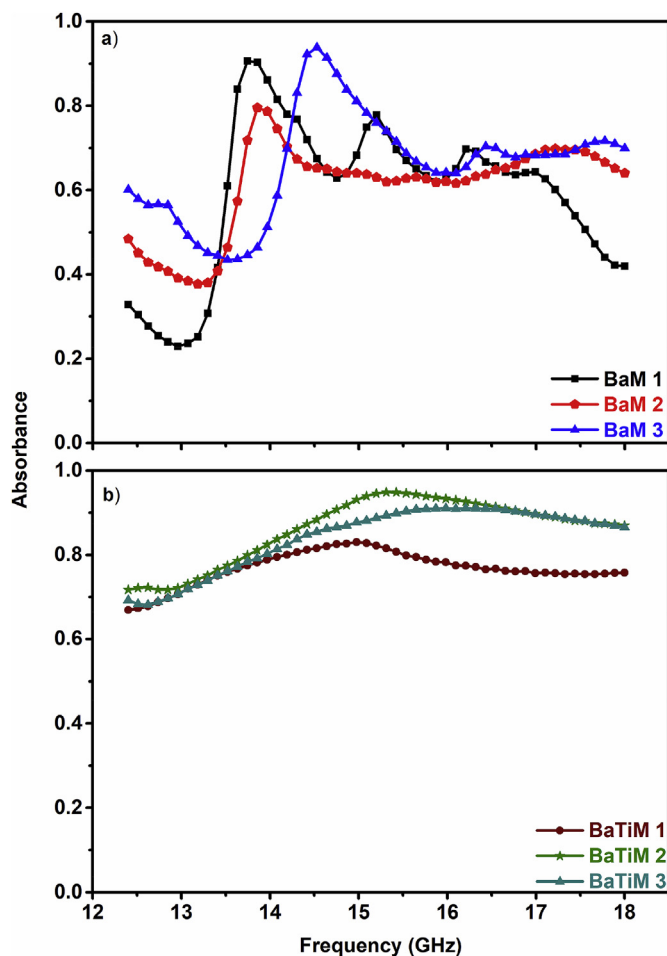


Fig. 10. Microwave absorbance vs frequency plot of BaM and BaTiM.

suggest  $Ti^{4+}$  substitution lower the lossy behaviour in the  $K_u$ -band which is prerequisite for microwave absorbing materials [36].

### 3.6.2. Permeability

Fig. 9(a and b) shows real ( $\mu'$ ) and imaginary ( $\mu''$ ) parts of complex permeability spectra in  $K_u$ -band.  $\mu'$  for Pure BaM (Fig. 9 a) shows an overall oscillatory increase with frequency. Fig. 9 b shows oscillatory behaviour of  $\mu''$  and peaks found to be shifted towards higher frequency with calcination steps. The variation in  $\mu'$  and  $\mu''$  were attributed to domain wall resonance with relaxation type dispersion [35]. The peak maxima of  $\mu'$  with 2.10 at 17.88 GHz for BaM 1 was reduced and shifted to 1.53 at 14.98 GHz for BaM 3. This confirms the variation in domain wall motion and relaxation dispersion varies with heat treatment. The observed oscillatory behaviour and  $\mu'$  values are in comparison with previously reported studies [34]. However suppression in such oscillations were observed for substituted BaM (Fig. 9 b). Highest  $\mu'$  for substituted samples were founded to be  $\sim 1.73$  at 15.31 GHz for BaTiM 2. The peaks in  $\mu''$  and  $\epsilon''$  at frequency may contribute to reduces the impedance mismatch [34].

### 3.6.3. Microwave absorbance

Fig. 10(a and b) shows the absorbance ( $A(\omega)$ ) plots for BaM and BaTiM respectively, obtained after each calcination step. Absorbance in a microwave region is related to reflection coefficient and transmission coefficient by the relation:

$$A(\omega) = 1 - \text{Reflectance } (R(\omega)) - \text{Transmittance } (T(\omega)) = 1 - |S_{11}|^2 - |S_{12}|^2 \quad (2)$$

where  $S_{11}$  is a reflection coefficient and  $S_{12}$  is transmission coefficient.

BaM 1 showed multiple  $A(\omega)$  peaks at 13.74 GHz, 15.20 GHz and 16.21 GHz with the absorbance of 0.91, 0.78 and 0.70 respectively. The peaks at 15.20 GHz and 16.21 GHz were completely diminished for BaM 2. The peak exhibited at 13.74 GHz showed absorbance of 0.80. The BaM 3 showed  $A(\omega)$  peaks at 14.53 GHz and 16.43 GHz with the coefficients of 0.93 and 0.70 respectively. Since the full FMR values cannot be obtained from these data as natural FMR of BaM occurs at much higher frequencies (above 40 GHz), therefore, the observed absorbance peaks in  $K_u$ -band were primarily due to domain wall motion as evident from our permittivity and permeability studies [32]. The oscillatory behaviour for the sample obtained from the different calcination step might be due to relocation and migration of  $Fe^{3+}$  ions in the crystal structure. The absorbance of BaTiM was observed to be higher than BaM with suppressed oscillatory behaviour. The absorbance peaks of Ti-substituted samples might have shifted other frequency bands. The highest absorbance of 0.95 was obtained for BaTiM 2. It is to mention that the absorption in the X and Ku bands is still of great interest for radar absorbing RAM applications [2,37].

## 4. Conclusion

In the present work, the effect of three-step calcination process was investigated for BaM and BaTiM. XRD confirmed the gradual reduction of residual  $Fe_2O_3$  in BaTiM with consecutive calcination steps. A slight blue shift in FTIR and Raman spectroscopy supported the fraction of  $Ti^{4+}$  ions substitution increases with successive calcination. Bond length calculated from FTIR shows contraction with calcination steps in BaTiM samples. Microstructural analysis confirmed the formation of highly dense hexagonal grains with smaller size in Ti-substituted BaM. Magnetic studies showed  $Ti^{4+}$  substitution drastically decreases  $H_c$ . Further, calcination in BaTiM showed remarkable changes in magnetic parameters. Microwave studies in  $K_u$ -band confirmed  $Ti^{4+}$  substitution reduces dielectric and magnetic losses with enhancement in microwave absorbance. These results justifies, that the multiple calcination improves occupancy fraction of  $Ti^{4+}$  ions which greatly affects the structural, magnetic and microwave properties of BaM.

## Acknowledgment

This work has been carried out under the financial support provided by DST (SERB/F/2947/2014–2015), India. The authors would like to acknowledge Dr. Manoj Kumar and Mr. Munish Verma, Department of Physics and Materials Science Engineering at Jaypee Institute of Information Technology (Noida) for XRD characterisation.

## References

- [1] L.M. Silber, E. Tsantes, P. Angelo, Ferromagnetic resonance in a uniaxial anisotropic ferrite:  $BaFe_{12}O_{19}$ , *J. Appl. Phys.* 38 (1967) 5315–5318, <https://doi.org/10.1063/1.1709321>.
- [2] R.C. Pullar, Hexagonal ferrites: a review of the synthesis, properties and applications of hexaferrite ceramics, *Prog. Mater. Sci.* 57 (2012) 1191–1334.
- [3] V.G. Harris, Modern microwave ferrites, *IEEE Trans. Magn.* 48 (2012) 1075–1104.
- [4] Ü. Özgür, Y. Alivov, H. Morkoç, Microwave ferrites, part 1: fundamental properties, *J. Mater. Sci. Mater. Electron.* 20 (2009) 789–834, <https://doi.org/10.1007/s10854-009-9923-2>.
- [5] H. Kojima, Chapter 5 Fundamental Properties of Hexagonal Ferrites with Magnetoplumbite Structure, (1982), [https://doi.org/10.1016/S1574-9304\(05\)80091-4](https://doi.org/10.1016/S1574-9304(05)80091-4).
- [6] G. Albanese, A. Deriu, Magnetic properties of Al, Ga, Sc, in substituted barium ferrites: a comparative analysis, *Ceramurg. Int.* 5 (1979) 3–10, [https://doi.org/10.1016/0390-5519\(79\)90002-4](https://doi.org/10.1016/0390-5519(79)90002-4).
- [7] E. Neckenburger, H. Severin, J.K. Vogel, G. Winkler, Ferrite hexagonaler Kristallstruktur mit hoher Grenzfrequenz, *Z. Angew. Phys.* 18 (1965) 65.
- [8] G. Albanese, Mössbauer investigation of aluminium substituted barium hexaferrite in the paramagnetic state, *J. Magn. Magn Mater.* 147 (1995) 421–426, [https://doi.org/10.1016/0304-8853\(95\)00063-1](https://doi.org/10.1016/0304-8853(95)00063-1).
- [9] X. Batlle, X. Obradors, J. Rodríguez-Carvajal, M. Pernet, M. V. Cabanas, M. Vallet, Cation distribution and intrinsic magnetic properties of Co-Ti-doped M-type barium ferrite, *J. Appl. Phys.* 70 (1991) 1614–1623.
- [10] T.M. Clark, B.J. Evans, G.K. Thompson, S. Freeman,  $57Fe$  Mossbauer spectroscopic

- investigation of complex magnetic structures in Ga, Sc, and In substituted M -type hexagonal ferrites, *J. Appl. Phys.* 85 (1999) 5229–5230.
- [11] V. V Soman, V.M. Nanoti, D.K. Kulkarni, Dielectric and magnetic properties of Mg – Ti substituted barium hexaferrite, *Ceram. Int.* 39 (2013) 5713–5723, <https://doi.org/10.1016/j.ceramint.2012.12.089>.
- [12] H. Sözeri, H. Deligöz, H. Kavas, A. Baykal, Magnetic, dielectric and microwave properties of M–Ti substituted barium hexaferrites (M=Mn<sup>2+</sup>, Co<sup>2+</sup>, Cu<sup>2+</sup>, Ni<sup>2+</sup>, Zn<sup>2+</sup>), *Ceram. Int.* 40 (2014) 8645–8657, <https://doi.org/10.1016/j.ceramint.2014.01.082>.
- [13] J. Qiu, M. Gu, H. Shen, Microwave absorption properties of Al- and Cr-substituted M-type barium hexaferrite, *J. Magn. Magn Mater.* 295 (2005) 263–268, <https://doi.org/10.1016/j.jmmm.2005.01.018>.
- [14] S. Mahadevan, C. Pahwa, S.B. Narang, C. Pahwa, S.B. Narang, P. Sharma, Structural, dielectric and magnetic properties of BaFe<sub>12-x</sub>Al<sub>x</sub>O<sub>19</sub> hexaferrite thick films, *J. Magn. Magn Mater.* 441 C (2017) 465–474 doi:S0304-8853(17)30633-9 <https://doi.org/10.1016/j.jmmm.2017.05.087>.
- [15] S. Kumar, S. Supriya, M. Kar, Multiple electrical phase transitions in Al substituted barium hexaferrite, *J. Appl. Phys.* 122 (2017), <https://doi.org/10.1063/1.4998719>.
- [16] P. Sharma, A. Verma, R.K. Sidhu, O.P. Pandey, Effect of processing parameters on the magnetic properties of strontium ferrite sintered magnets using Taguchi orthogonal array design, *J. Magn. Magn Mater.* 307 (2006) 157–164, <https://doi.org/10.1016/j.jmmm.2006.03.063>.
- [17] I. V Granovskii, D. Stepanova, A. Lysyak, Preparation of barium hexaferrite from mixtures of ferric oxide and barium nitrate or barium oxides and from mixtures produced by nonceramic methods. Communication II, *Powder Metall. Met. Ceram.* 11 (1971) 895–901.
- [18] D.A. Vinnik, D.S. Klygach, V.E. Zhivulin, A.I. Malkin, M.G. Vakhitov, S.A. Gudkova, D.M. Galimov, D.A. Zherebtsov, E.A. Trofimov, N.S. Knyazev, V. V Atuchin, A. V Trukhanov, D.S. Klygach, V.E. Zhivulin, A.I. Malkin, M.G. Vakhitov, D.M. Galimov, D.A. Zherebtsov, E.A. Trofimov, N.S. Knyazev, V. V Atuchin, S. V Trukhanov, A. V Trukhanov, Electromagnetic properties of BaFe<sub>12</sub>O<sub>19</sub>:Tiat centimeter wavelengths, *J. Alloy. Comp.* 755 (2018) 177–183, <https://doi.org/10.1016/j.jallcom.2018.04.315>.This.
- [19] J. Le Breton, J. Teillet, G. Wiesinger, A. Morel, F. Kools, P. Tenaud, Mössbauer investigation of Sr – Fe – O hexaferrites with La – Co addition, *IEEE Trans. Magn.* 38 (2002) 2952–2954.
- [20] P.A. Marino-Castellanos, J. Anglada-Rivera, A. Cruz-Fuentes, R. Lora-Serrano, Magnetic and microstructural properties of the Ti 4+ -doped Barium hexaferrite, *J. Magn. Magn Mater.* 280 (2004) 214–220, <https://doi.org/10.1016/j.jmmm.2004.03.015>.
- [21] B.D. Cullity, *Elements of X-Ray Diffraction*, (1956).
- [22] S. Tyagi, P. Verma, H.B. Baskey, R.C. Agarwala, V. Agarwala, T.C. Shami, Microwave absorption study of carbon nano tubes dispersed hard/soft ferrite nanocomposite, *Ceram. Int.* 38 (2012) 4561–4571, <https://doi.org/10.1016/j.ceramint.2012.02.034>.
- [23] M. Bellotto, G. Busca, C. Cristiani, G. Groppi, FT-IR skeletal powder spectra of Ba-β-Aluminas with compositions BaAl 9 O 14.5, BaAl 12 O 19, and BaAl 14 O 22 and of Ba-ferrite, BaFe 12 O 19, *J. Solid State Chem.* 117 (1995) 8–15.
- [24] M. V Rane, D. Bahadur, A.K. Nigam, C.M. Srivastava, Mössbauer and FT-IR studies on non-stoichiometric barium hexaferrites, *J. Magn. Magn Mater.* 192 (1999) 288–296.
- [25] W.Y. Zhao, P. Wei, X.Y. Wu, W. Wang, Q.J. Zhang, Lattice vibration characterization and magnetic properties of M -type barium hexaferrite with excessive iron, *J. Appl. Phys.* 103 (2008) 10–14, <https://doi.org/10.1063/1.2884533>.
- [26] R.A. El-Mallawany, Theoretical and experimental IR spectra of binary rare earth tellurite glasses—1, *Infrared Phys.* 29 (1989) 781–785, [https://doi.org/10.1016/0020-0891\(89\)90125-5](https://doi.org/10.1016/0020-0891(89)90125-5).
- [27] O. Carp, B. Ruxandra, E. Segal, M. Brezeanu, Nonconventional methods for obtaining hexaferrites II. Barium hexaferrite, *Thermochim. Acta* 318 (1998) 57–62, [https://doi.org/10.1016/S0040-6031\(98\)00352-9](https://doi.org/10.1016/S0040-6031(98)00352-9).
- [28] J. Kreisel, G. Lucazeau, H. Vincent, Raman spectra and vibrational analysis of BaFe<sub>12</sub>O<sub>19</sub>Hexagonal ferrite, *J. Solid State Chem.* 137 (1998) 127–137, <https://doi.org/10.1006/jssc.1997.7737>.
- [29] A. Morel, J.M. Le Breton, J. Kreisel, G. Wiesinger, F. Kools, P. Tenaud, Sublattice occupation in Sr1 – xLaxFe12 – xCoxO19 hexagonal ferrite analyzed by Mossbauer spectrometry and Raman spectroscopy, *J. Magn. Magn Mater.* 242–245 (2002) 1405–1407.
- [30] R. Grossinger, A critical examination of the law of approach to saturation. I. Fit procedure, *Phys. Status Solidi* 66 (1981) 665–674.
- [31] P.A.-C. Marino, A.C. Moreno-Borges, G. Orozco-Melgar, J.A. Garcia, E. Govea-Alcaide, Structural and magnetic study of the Ti 4+ -doped barium hexaferrite ceramic samples : theoretical and experimental results, *Phys. B Phys. Condens. Matter.* 406 (2011) 3130–3136, <https://doi.org/10.1016/j.physb.2011.03.084>.
- [32] P. Singh, V.K. Babbar, A. Razdan, S.L. Srivastava, V.K. Agrawal, T.C. Goel, Dielectric constant, magnetic permeability and microwave absorption studies of hot-pressed Ba-CoTi hexaferrite composites in X-band, *J. Mater. Sci.* 41 (2006) 7190–7196, <https://doi.org/10.1007/s10853-006-0921-y>.
- [33] S.M. Abbas, A.K. Dixit, R. Chatterjee, T.C. Goel, Complex permittivity, complex permeability and microwave absorption properties of ferrite–polymer composites, *J. Magn. Magn Mater.* 309 (2007) 20–24, <https://doi.org/10.1016/J.JMMM.2006.06.006>.
- [34] S.B. Narang, K. Pubby, S.K. Chawla, P. Kaur, Origin of absorption peaks in reflection loss spectrum in Ku- frequency band of Co-Zr substituted strontium hexaferrites prepared using sucrose precursor, *J. Magn. Magn Mater.* 426 (2017) 202–205, <https://doi.org/10.1016/j.jmmm.2016.11.054>.
- [35] S.B. Narang, K. Pubby, C. Singh, Thickness and composition tailoring of K- and Ka-band microwave absorption of BaCoxTixFe(12-2x)O19 ferrites, *J. Electron. Mater.* 46 (2017) 718–728, <https://doi.org/10.1007/s11664-016-5059-3>.
- [36] Han-Shin Cho, Sung-Soo Kim, M-hexaferrites with planar magnetic anisotropy and their application to high-frequency microwave absorbers, *IEEE Trans. Magn.* 35 (1999) 3151–3153, <https://doi.org/10.1109/20.801111>.
- [37] M.S. Pinho, M.L. Gregori, R.C.R. Nunes, B.G. Soares, Performance of radar absorbing materials by waveguide measurements for X- and Ku-band frequencies, *Eur. Polym. J.* 38 (2002) 2321–2327, [https://doi.org/10.1016/S0014-3057\(02\)00118-0](https://doi.org/10.1016/S0014-3057(02)00118-0).



## Research articles

Structural, dielectric and magnetic properties of BaFe<sub>12-x</sub>Al<sub>x</sub>O<sub>19</sub> hexaferrite thick filmsSanthoshkumar Mahadevan<sup>a</sup>, Chhavi Pahwa<sup>a</sup>, Sukhleen Bindra Narang<sup>b</sup>, Puneet Sharma<sup>a,\*</sup><sup>a</sup> School of Physics and Materials Science, Thapar University, Patiala 147004, Punjab, India<sup>b</sup> Department of Electronics Technology, Guru Nanak Dev University, Amritsar, India

## ARTICLE INFO

## Article history:

Received 17 February 2017

Received in revised form 30 May 2017

Accepted 30 May 2017

Available online 6 June 2017

## ABSTRACT

BaFe<sub>12-x</sub>Al<sub>x</sub>O<sub>19</sub> (0 ≤ x ≤ 2.5) powders and thick films were prepared by solid state synthesis method and screen printing technique respectively. X-ray diffraction confirmed the single phase without any impurity phase. Bond length calculation from FTIR spectra suggested the occupation of Al<sup>3+</sup> ions at octahedral and tetrahedral sites. Magnetic measurements showed that coercivity ( $H_c$ ), saturation magnetization ( $M_s$ ) and anisotropic field ( $H_a$ ) strongly depends on the substitution amount. As compared to the powder, substituted thick films possess higher  $H_c$  despite its larger grain size.  $M$ - $T$  measurement showed a decrease in Curie temperature from ~497 °C ( $x = 0.0$ ) to ~437 °C ( $x = 2.0$ ). High dielectric constant ( $\epsilon_r$ ) and low losses ( $\tan \delta$ ) were observed in Al<sup>3+</sup> substituted samples. However,  $\epsilon_r$  decrease and  $\tan \delta$  increase with temperature. Scanning electron micrographs showed that Al<sup>3+</sup> substitution promotes hexagonal shaped grains in sintered thick films. Complex permeability behavior in X-band frequency is also investigated and found to be less in Al-substituted samples. Reflection losses are increased with Al<sup>3+</sup> substitution and found maximum (-47 dB at 9.3 GHz) for  $x = 1.5$ .

© 2017 Elsevier B.V. All rights reserved.

## 1. Introduction

M-type Strontium/Barium hexaferrite (Sr/BaM) continuing its dominance in permanent magnet market due to its high saturation magnetization ( $M_s$ ), moderate coercivity ( $H_c$ ) and high magnetocrystalline anisotropic field ( $H_a \sim 17$  KOe) [1]. The characteristic magnetic properties of M-type ferrite lies in its hexagonal crystal structure, where 24 Fe<sup>3+</sup> ions are distributed among five different crystallographic sites i.e. three octahedral (12k, 4f<sub>2</sub>, 2a), one tetrahedral (4f<sub>1</sub>) and one trigonal bipyramid sites (2b). The spin up (12k, 2a, 2b) and spin down (4f<sub>1</sub>, 4f<sub>2</sub>) configuration of Fe<sup>3+</sup> ions gives a net magnetic moment of 40  $\mu_B$  per unit cell [2]. Apart from its wide application as permanent magnets, its high permittivity, self biasing nature, high  $H_a$ , and high natural ferromagnetic resonance (FMR) frequency (~35 GHz) makes them suitable for microwave and millimeter wave applications [3]. The FMR frequency ( $\omega_r$ ) depends on applied magnetic field ( $H_o$ ),  $M_s$  and  $H_a$  by the relation [4]:

$$\omega_r = \gamma(H_o + H_a \pm 4\pi M_s) \quad (1)$$

where  $\gamma$  is gyromagnetic ratio

From the Eq. (1), the FMR frequency can be tuned by  $H_o$ ,  $M_s$  and  $H_a$ . Any variation in these magnetic parameters will widen the operable frequency (1–100 GHz) [3]. Efforts have been made to understand the effect of various cationic substitution for Fe<sup>3+</sup> ions on magnetic properties of M-type ferrites. Cations such as Sc<sup>3+</sup> and In<sup>3+</sup> reportedly decreases  $H_a$  [5], whereas increases with Ga<sup>3+</sup> and Al<sup>3+</sup> substitution [6]. Recently, a considerable attention laid to develop hexaferrite thick films by screen printing method for self biased microwave devices such as circulators, phase shifters and isolators etc., where film thickness (>100  $\mu m$ ) is primary criterion [7,8]. The screen printing technique overcomes the limitation to grow thick film by Rf sputtering and pulse laser deposition [9,10]. Previously, various studies on pure hexaferrite thick films were reported [11–13], however, limited studies were carried out on substituted thick films [14,15]. Ustinov et al. showed that Al-substituted single crystal film of BaM possess high  $H_a$  [16]. Other studies on Al-substituted BaM showed wide variation in the magnetic properties [17–21]. Therefore, in the present work, Al-substituted BaM has been prepared and their structural, magnetic dielectric properties and microwave properties were investigated. Further, screen printed thick films has been made and characterized for realization in future micro/mm wave devices. It is found that Al<sup>3+</sup> substitution remarkably changes its magnetic properties and  $H_a$ .

\* Corresponding author.

E-mail address: [puneet.sharma@thapar.edu](mailto:puneet.sharma@thapar.edu) (P. Sharma).

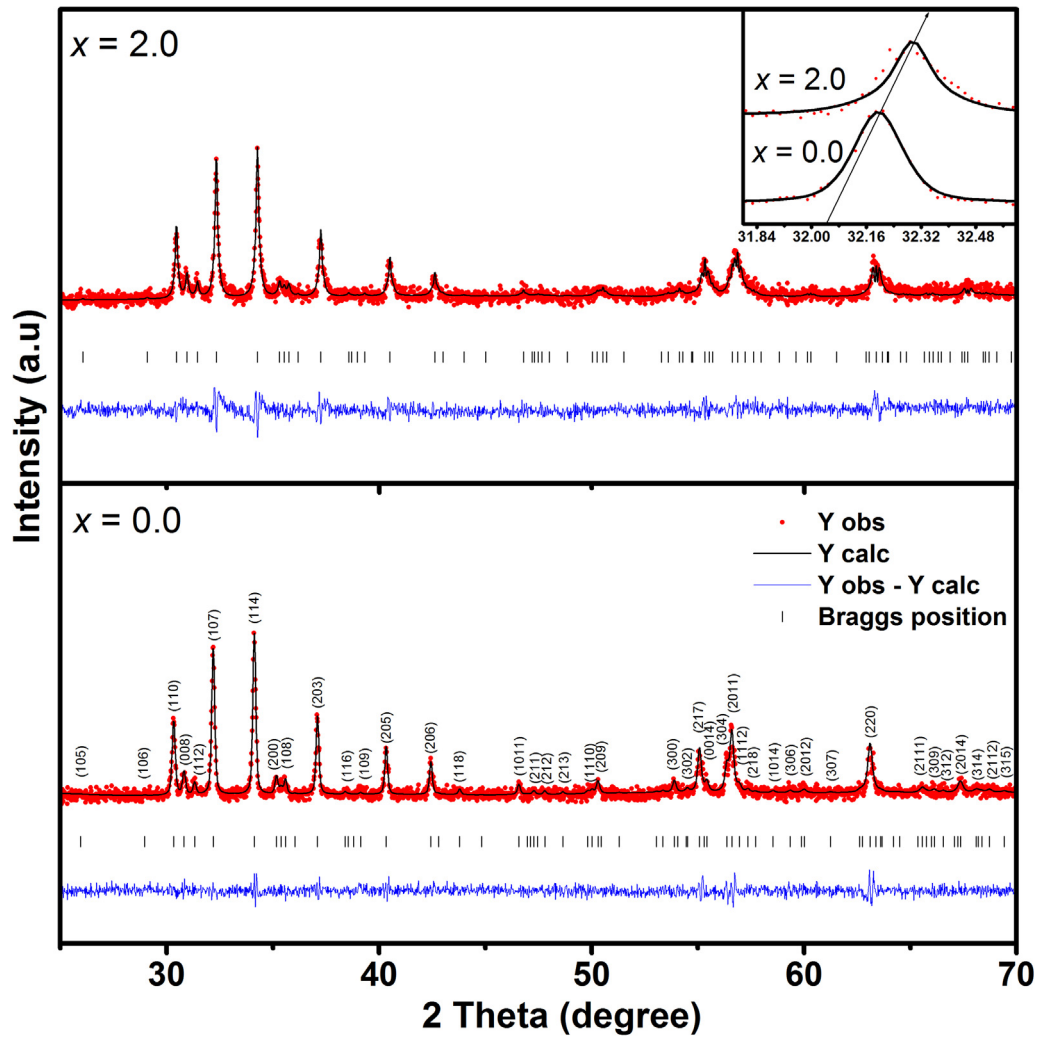


Fig. 1. Refined  $\text{BaFe}_{12-x}\text{Al}_x\text{O}_{19}$  powder ( $x = 0.0$  and  $2.0$ ). Inset depicts peak shift towards higher  $2\theta$ .

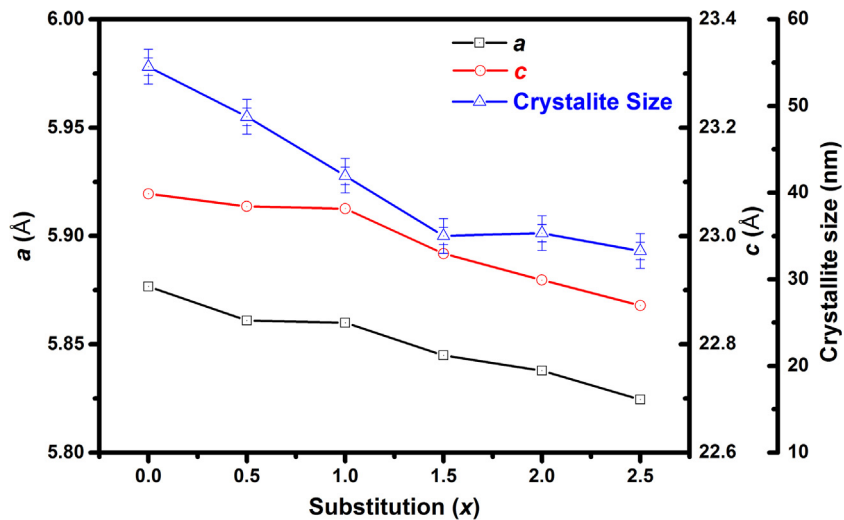


Fig. 2. Variation in lattice parameters and crystallite size with substitution amount.

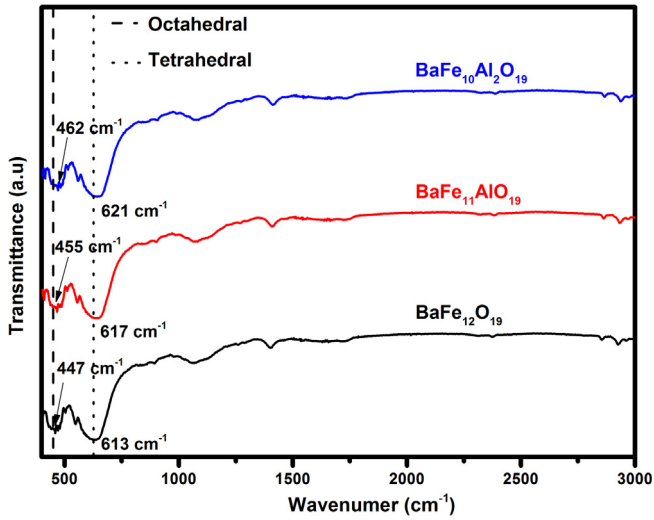


Fig. 3. FTIR spectrum data of  $\text{BaFe}_{12-x}\text{Al}_x\text{O}_{19}$ .

## 2. Synthesis and characterization

In the present work, analytical grade  $\text{BaCO}_3$ ,  $\text{Fe}_2\text{O}_3$  and  $\text{Al}_2\text{O}_3$  were used to prepare  $\text{BaFe}_{12-x}\text{Al}_x\text{O}_{19}$ , ( $x = 0.0-2.5$ ) by solid state synthesis method. Precursors were weighed in stoichiometric composition and wet mixed for 3 h using planetary ball mill. RPM and ball-to-charge ratio were fixed to 200 and 2:1 respectively. As-

Table 1

Wavenumber, force constant ( $K$ ) and atomic radius ( $r$ ) for octahedral and tetrahedral sites with substitution amount.

| Site        | Dopant (Al) % | Wavenumber $\text{cm}^{-1}$ | $K$ N/m | $R$ Å |
|-------------|---------------|-----------------------------|---------|-------|
| Octahedral  | 0             | 447                         | 138.27  | 2.30  |
|             | 1             | 455                         | 143.26  | 2.28  |
|             | 2             | 462                         | 147.70  | 2.26  |
| Tetrahedral | 0             | 613                         | 260.03  | 1.87  |
|             | 1             | 617                         | 263.44  | 1.86  |
|             | 2             | 621                         | 266.86  | 1.85  |

mixed powders were calcined at  $1150^\circ\text{C}$  for 3 h in a resistance furnace. Heating and cooling rate were fixed to  $2^\circ\text{C}/\text{min}$ . Phase analysis was carried by X-ray diffractometer model Shimadzu XRD-6000 using  $\text{Cu K}\alpha_1$  ( $1.54 \text{ \AA}$ ) radiation. The scan rate was fixed to  $0.02^\circ/\text{s}$ . To prepare thick films, as synthesized powder were mixed with PVB (Polyvinyl butyral) binder and screen printed on  $\text{Al}_2\text{O}_3$  substrate using a screen of  $175 \mu\text{m}$  thickness. As-printed films were sintered at  $1250^\circ\text{C}$  for 1 h in ambient atmosphere. Microstructure analysis of powder and thick films were carried out by scanning electron microscope (SEM) coupled with energy dispersive spectroscopy (EDS) model JEOL (JSM-IT100).  $M-H$  loops were measured by vibrating sample magnetometer (VSM) model Lake Shore (VSM) 7404. Fourier Transformer Infrared (FTIR) spectroscopy were carried out by IRAffinity-1S. The dielectric measurements were performed in the frequency range of  $1 \text{ kHz}-1 \text{ MHz}$  using impedance analyzer Solartron – SI 1260. Microwave proper-

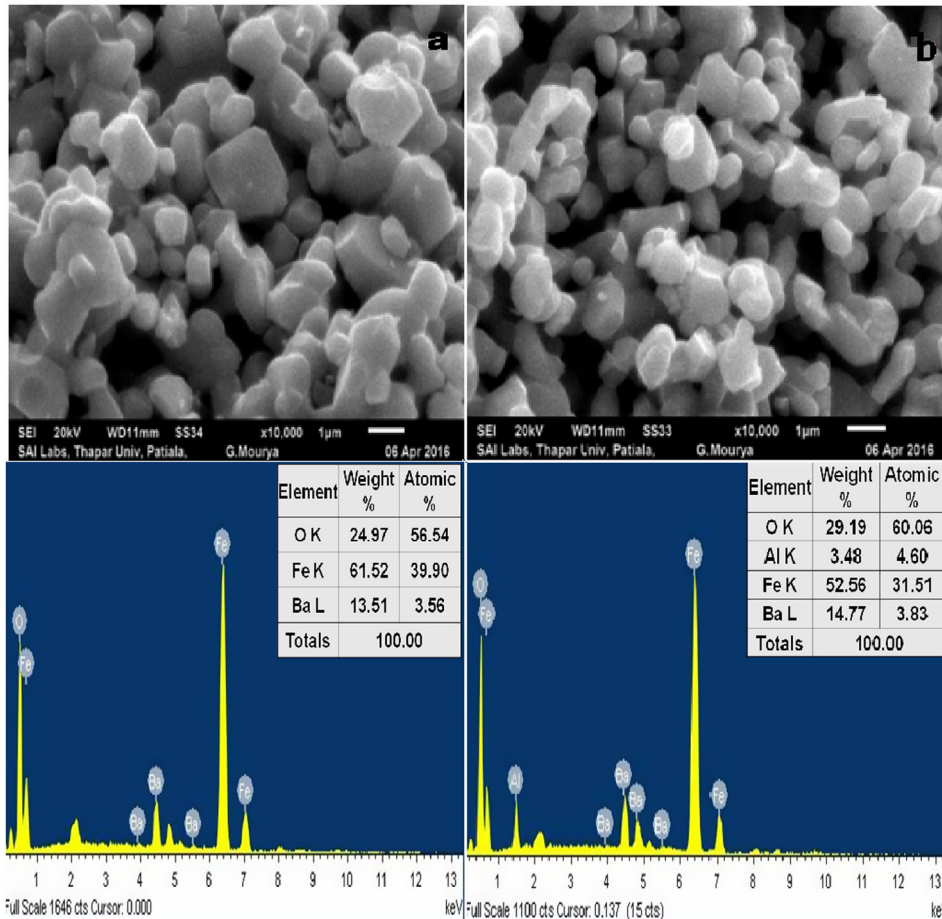


Fig. 4. SEM micrograph and EDS analysis images of  $\text{BaFe}_{12-x}\text{Al}_x\text{O}_{19}$  (a)  $x = 0.0$  (b)  $x = 2.0$ .

ties in X-band (8.2–12.4 GHz) were measured using Agilent 5225A PNA series network analyzer. For the study fine powder where compacted in a rectangular shape with dimension  $22.86 \times 10.16 \times 2.1 \text{ mm}^3$  under a pressure of 50 MPa. As prepared pellets were sintered at 1250 °C for 1 h. Reflection and transmission method were used to calculate permeability, suggested Weir [22] and Nicolson-Ross [23].

### 3. Results and discussion

#### 3.1. X-ray diffraction analysis

Fig. 1 shows the representative X-ray diffraction patterns of  $\text{BaFe}_{12-x}\text{Al}_x\text{O}_{19}$  ( $x = 0.0$  and  $2.0$ ). Reitveld refinement of all patterns were carried out by fullprof software. The  $\chi^2$  values and  $R$  parameters were below 1.5 and 5.0 respectively, which shows that all XRD patterns are best fitted. All the diffraction peaks corresponds to single phase BaM without any impurity. It is clear from inset Fig. 1 that the peak at  $32.2^\circ$  for pure BaM has been shifted to  $32.4^\circ$  with  $\text{Al}^{3+}$  substitution. The shift towards higher angle suggests tensile stress within the system due to smaller ionic radii of  $\text{Al}^{3+}$  (0.52 Å) compare to  $\text{Fe}^{3+}$  (0.67 Å) ion [21,24]. Fig. 2 shows the variation in lattice parameters  $a$ ,  $c$  and crystallite size with  $\text{Al}^{3+}$  substitution. The crystallite size was calculated by Debye Scherrer equation [25].

$$C.S = \frac{k\lambda}{\beta \cos \theta} \quad (2)$$

where  $k$  is dimensionless shape factor taken as 0.92 for hexagonal system,  $\lambda$  is the wavelength,  $\theta$  is Bragg's angle in degree and  $\beta$  is the full width at half maxima calculated by Caglioti equation [26].

$$H = [u \tan^2 \theta + v \tan \theta + w]^{1/2} \quad (3)$$

where,  $u$ ,  $v$  and  $w$  are the shape parameters as obtained by Reitveld refinement.

It is clear from the plot that  $a$ ,  $c$  and crystallite size is decreasing with  $\text{Al}^{3+}$  substitution due to lower ionic radii of the  $\text{Al}^{3+}$  ion, which causes lattice shrinkage and reduces crystallite size.

#### 3.2. Fourier Transformer Infrared (FTIR) spectroscopy

Fig. 3 depicts FTIR plot of  $\text{BaFe}_{12-x}\text{Al}_x\text{O}_{19}$  ( $x = 0.0, 1.0$  &  $2.0$ ) from  $3000 \text{ cm}^{-1}$ – $400 \text{ cm}^{-1}$ . As the result of group theory, BaM compound may give rise to 189 optical modes [27], where only 31 modes ( $13 A_{2u} + 18 E_{1u}$ ) are IR active. In the present case, only two active modes at  $447$  and  $613 \text{ cm}^{-1}$  of Fe–O bond in octahedral ( $4f_2$ ) and tetrahedral ( $4f_1$ ) sites are visible due to vibrational modes of  $E_{1u}$  [28]. With the  $\text{Al}^{3+}$  substitution, slight blue shift from  $447$  to  $462 \text{ cm}^{-1}$  and  $613$  to  $621 \text{ cm}^{-1}$  is observed, which is due to lesser atomic weight of  $\text{Al}^{3+}$  ions compared to  $\text{Fe}^{3+}$  ions as wavenumber is inversely proportional to atomic weight [24]. The bond length of Fe–O is determined by using frequency of vibrational modes and force constant  $K$ . The  $K$  is correlated to the average bond length ( $r$ ) by following relation [29]:

$$K = \frac{17}{r^3} \quad (4)$$

where  $K$  is calculated by using Eq. [5]

$$v = \frac{1}{2\pi c} \sqrt{\frac{K}{\mu}} \quad (5)$$

where  $v$  is the frequency of vibration,  $c$  is the velocity of light, and  $\mu$  is effective mass. Effective mass is defined as following:

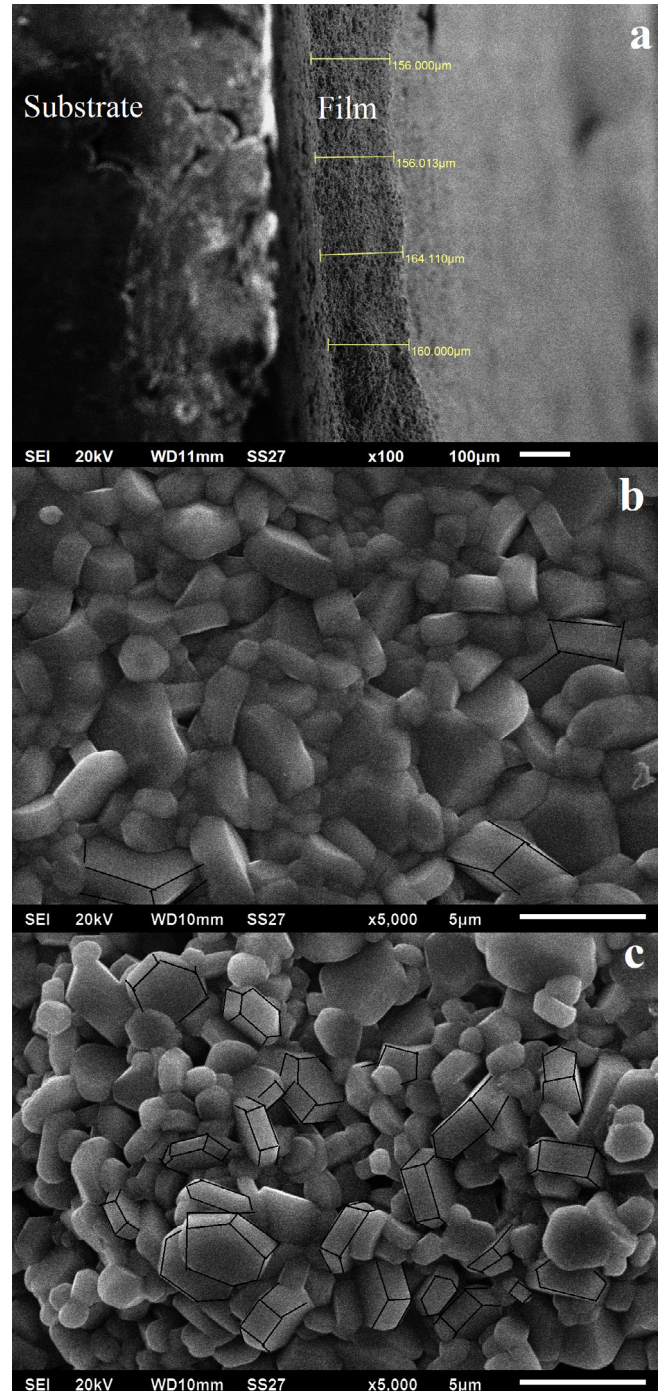


Fig. 5. SEM micrograph of  $\text{BaFe}_{12-x}\text{Al}_x\text{O}_{19}$  thick films (a) cross section (b)  $x = 0.0$  (c)  $x = 2.0$ .

$$\mu = \frac{M_O X M_{Fe}}{M_O + M_{Fe}} \quad (6)$$

where  $M_O$  &  $M_{Fe}$  are the atomic weight of O and Fe.

The calculated bond length values are tabulated in the Table 1, which suggests that the bond length is reducing with  $\text{Al}^{3+}$  substitution and supports the unit cell shrinkage as observed from XRD results. The increase in  $K$  and decrease in  $r$  is due smaller ionic radii of  $\text{Al}^{3+}$  ion. Further, the reduction in bond length confirms the  $\text{Al}^{3+}$  has preferential occupation in the spin down sites ( $4f_1$  and  $4f_2$ ) as reported [30]. Previous studies on site occupation also confirmed that  $\text{Al}^{3+}$  preferably occupies  $4f_1$  and  $12k$  sites [31,32].

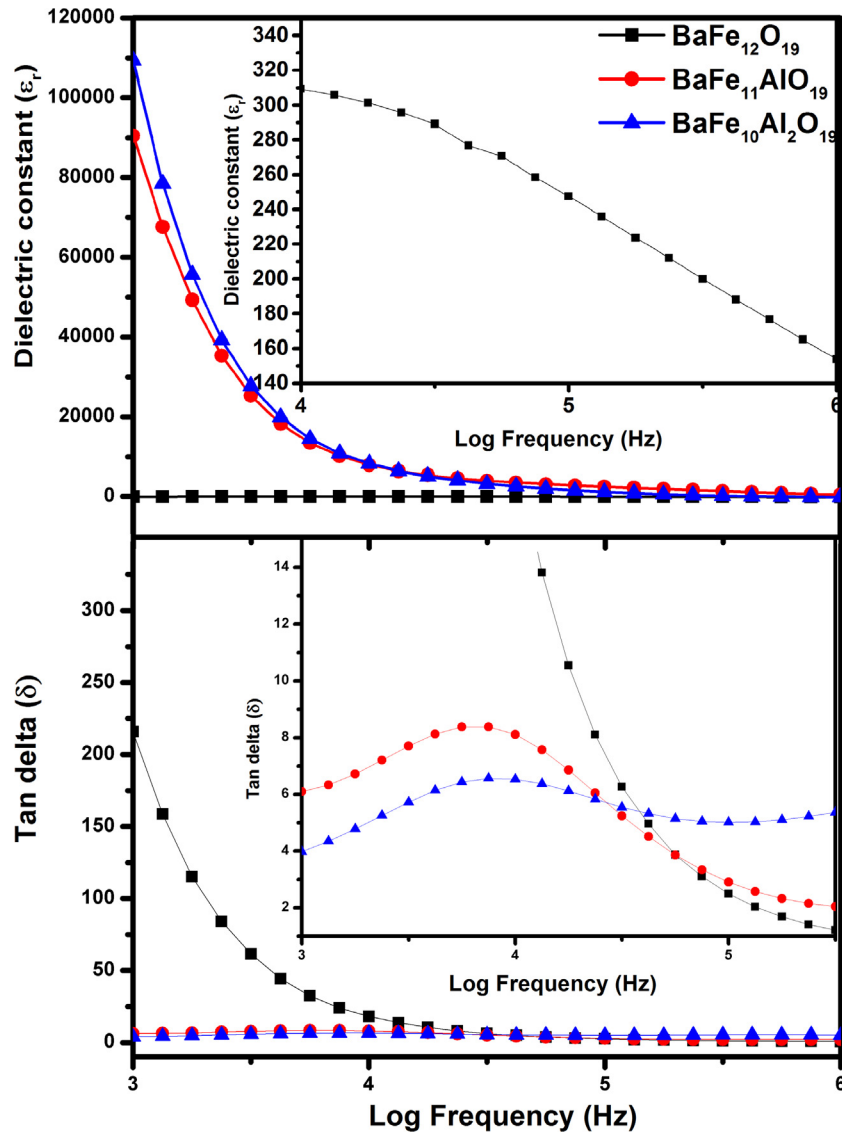


Fig. 6. Frequency dependent (a)  $\epsilon_r$  (b)  $\tan \delta$  of  $\text{BaFe}_{12-x}\text{Al}_x\text{O}_{19}$ .

### 3.3. Microstructural study

Fig. 4 shows the SEM micrographs of pure and Al-substituted BaM powders. The powders show similar morphology, however, particle size slightly decreased (1.5–1  $\mu\text{m}$ ) with  $\text{Al}^{3+}$  substitution. The decrease in particle size could be ascribed to two reasons, firstly, due to pinning effect by residual  $\text{Al}_2\text{O}_3$  particles, which may remain unsubstituted and secondly, due to decrease in crystallite size (Fig. 4). However, the residual  $\text{Al}_2\text{O}_3$  is not evidenced in XRD patterns due to its small fraction. The XRD peak shift towards higher angle side confirms that  $\text{Al}^{3+}$  ions are also occupying the vacant  $\text{Fe}^{3+}$  sites. Further, particle size reduction is confirmed by measuring the crystallinity index ( $I_{\text{CRY}}$ ) [29].

$$I_{\text{CRY}} = \frac{D_p(\text{SEM, TEM})}{\tau(\text{XRD})} \quad (7)$$

where  $D_p$  is average particle size obtained from micrograph and  $\tau$  is average crystallite size as obtained from Scherrer equation. The calculated values of  $I_{\text{CRY}}$  for pure and Al-substituted BaM are found to be same, i.e.  $\sim 25$ , which suggest the lattice shrinkage due to  $\text{Al}^{3+}$  substitution. The corresponding EDS spectrum shows the elemental composition of as-synthesized powders which confirms the pres-

ence of Ba, O and Fe. In the substituted sample, a peak of Al is also present.

Fig. 5(a–c) shows the cross sectional and surface micrographs of the pure and Al-substituted screen printed films, sintered at 1250  $^\circ\text{C}$ . A uniform thickness of  $\sim 160 \mu\text{m}$  is evident from Fig. 5 (a). Surface micrograph (b and c) shows that films are well sintered, however, film surface is rough with limited porosity. Previously, screen printed films were hot pressed and sintered to improve surface roughness and densification [33]. In another work, a mild pressure was applied to the films prior to sintering for better surface roughness [34]. In the present work, films were prepared without applying pressure, due to thin  $\text{Al}_2\text{O}_3$  substrate. The average grain size of pure BaM films is  $\sim 2.5 \mu\text{m}$ , which found to be smaller ( $\sim 2 \mu\text{m}$ ) for substituted film ( $x = 2.0$ ). It is also clear from micrographs that  $\text{Al}^{3+}$  substitution is promoting hexagonal shaped grains. The average diameter to thickness ratio of hexagonal plates is decreasing from 0.65 ( $x = 0.0$ ) to 0.36 ( $x = 2.0$ ).

### 3.4. Dielectric studies

To understand the charge transfer mechanism in BaM, frequency and temperature dependent dielectric measurements were

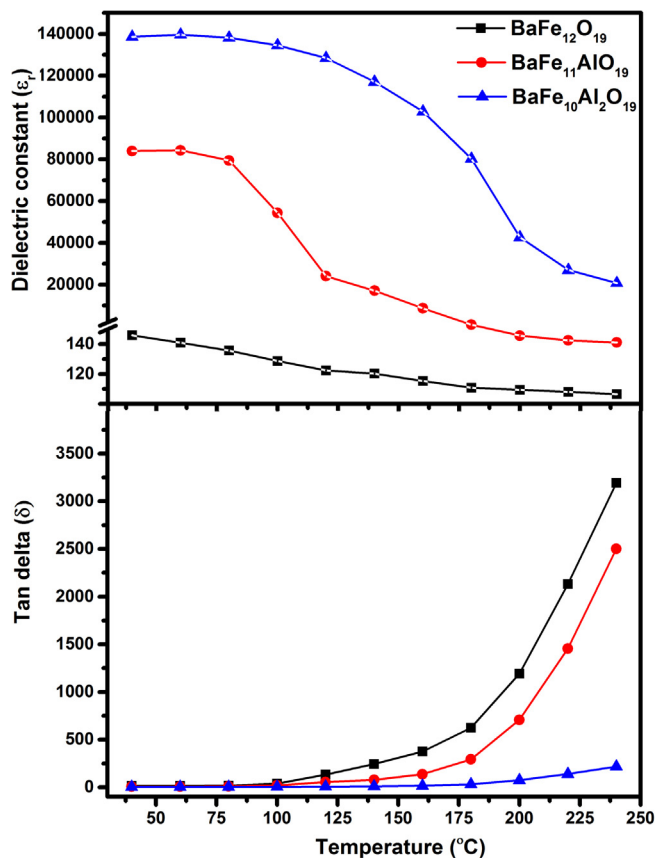


Fig. 7. Temperature dependent (a)  $\epsilon_r$  (b)  $\tan \delta$  of  $\text{BaFe}_{12-x}\text{Al}_x\text{O}_{19}$  at 1 kHz.

carried out. Fig. 6 shows RT frequency dependent dielectric constant ( $\epsilon_r$ ) and loss tangent ( $\tan \delta$ ) for pure and Al-substituted BaM.

It is clear from Fig. 6 (a) that  $\epsilon_r$  is higher in Al-substituted BaM at lower frequencies and gradually decreases with increase in the frequency. This behavior can be described as existence of interfacial polarization [35] and Maxwell-Wagner two layer model [36]. The dielectric phenomena of ferrites were explained that poorly conducting large grain boundaries act as a barrier between well

conducting grains. In the previous studies, the possibility of higher  $\epsilon_r$  was explained on the basis of exchange of electrons between  $\text{Fe}^{3+}$  and  $\text{Fe}^{2+}$  ions, where divalent Ba or trivalent Fe is substituted by trivalent or tetravalent ions respectively [37,38]. In the present work, the possibility of reduction of  $\text{Fe}^{3+}$  to  $\text{Fe}^{2+}$  can be ignored due to same valency of  $\text{Al}^{3+}$  and  $\text{Fe}^{3+}$  ions. Therefore, the rise in  $\epsilon_r$  at lower frequencies is ascribed to larger grain boundary fraction in substituted BaM with simultaneous increase in space charge polarization. At higher frequencies, hopping of electrons never follow the frequency of applied field and dispersion of charge occurs, which leads to decrease in  $\epsilon_r$  [39]. The  $\tan \delta$  variation is in agreement with  $\epsilon_r$ , where high  $\epsilon_r$  in Al-substituted BaM corresponds to minimum  $\tan \delta$ . On contrary, low  $\epsilon_r$  in pure BaM possess higher  $\tan \delta$ . Inset Fig. 6(b) shows a hump in  $\tan \delta$  in Al-substituted BaM, which corresponds to a sharp decrease in  $\epsilon_r$  with increase in frequency. The dielectric losses can be explained as energy dissipation of the materials caused by conduction of electrons or flow of charges through the materials. The losses in the dielectric materials can be due to two major reasons. Firstly, the intrinsic factors of the materials like substitution, crystal defects and secondly, the extrinsic factors such as particle size and grain size which causes a lag in polarization to the applied field [40,41]. In the present study the low  $\tan \delta$  in substituted BaM is due to larger grain boundary fraction, which provide hindrance to charge conduction.

Fig. 7(a, b) shows the decrease in  $\epsilon_r$  and increase in  $\tan \delta$  with temperature at 1 kHz. The observed variation are due to thermally activated ions which enhances conductivity [39]. As compared to pure, Al-substituted BaM shows lower losses at higher temperature due to high  $\epsilon_r$ . The similar behavior were also observed for higher frequencies.

### 3.5. Magnetic studies

Fig. 8 shows the  $M$ - $H$  behavior of the pure and Al-substituted BaM powders. It is clear that magnetization ( $M$ ) at 1T is decreasing and coercivity ( $H_c$ ) is increasing with  $\text{Al}^{3+}$  substitution. The decrease in  $M$  is attributed to the substitution of nonmagnetic  $\text{Al}^{3+}$  ions at magnetic  $\text{Fe}^{3+}$  sites. [21]. The decrease in  $M$  is attributed to preferential occupation of  $\text{Al}^{3+}$  ions at spin up sites ( $12k$ ,  $2a$ ,  $2b$ ). Previous Mössbauer studies reported that spin down  $4f_1$  and  $4f_2$  sites are also occupied by  $\text{Al}^{3+}$  ions at lower substitution amount ( $x = 0.15$ ) [30]. However, the larger fraction of  $\text{Al}^{3+}$  substi-

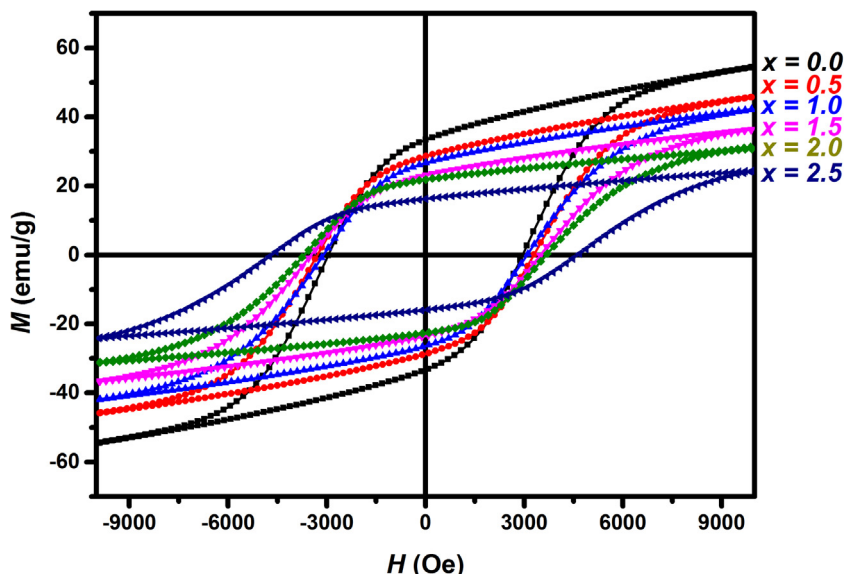


Fig. 8.  $M$ - $H$  loop of  $\text{BaFe}_{12-x}\text{Al}_x\text{O}_{19}$  powders.

**Table 2**  
Magnetic properties of BaFe<sub>12-x</sub>Al<sub>x</sub>O<sub>19</sub> powders and thick films.

|        | <i>x</i> | <i>M</i><br>emu/g | <i>M<sub>r</sub></i><br>emu/g | <i>H<sub>c</sub></i><br>kOe | <i>H<sub>a</sub></i> | <i>k</i> <sub>1</sub> × 10 <sup>6</sup><br>erg/cm <sup>3</sup> |      |
|--------|----------|-------------------|-------------------------------|-----------------------------|----------------------|--|------|
| Powder | 0.0      | 54.4              | 33.3                          | 2.95                        | 8.54                 | 1.57   |      |
|        | 0.5      | 45.8              | 28.6                          | 3.29                        | 7.82                 | 1.19   |      |
|        | 1.0      | 42.2              | 26.6                          | 3.09                        | 7.45                 | 1.04   |      |
|        | 1.5      | 36.4              | 23.3                          | 3.48                        | 6.89                 | 0.81   |      |
|        | 2.0      | 31.3              | 22.3                          | 3.68                        | 5.75                 | 0.56   |      |
|        | 2.5      | 24.4              | 16.1                          | 4.65                        | 5.67                 | 0.45   |      |
|        | 0.0      | 0°                | 62.2                          | 30.2                        | 1.73                 | 12.63  | 2.10 |
|        | 90°      | 53.0              | 20.3                          | 1.74                        | 12.55                | 1.77   |      |
| Film   | 1.0      | 0°                | 47.5                          | 25.9                        | 4.77                 | 11.17  | 1.39 |
|        |          | 90°               | 38.8                          | 20.6                        | 4.79                 | 10.63  | 1.06 |
|        | 2.0      | 0°                | 18.7                          | 11.0                        | 7.47                 | 7.03   | 0.34 |
|        |          | 90°               | 16.8                          | 9.8                         | 7.45                 | 6.72   | 0.29 |

tution predominantly occupies spin up sites which suppresses the contribution to net magnetization [31]. The *H<sub>c</sub>* is increasing with the increase in Al<sup>3+</sup> substitution. The *H<sub>c</sub>* is primarily governed by intrinsic (magnetocrystalline anisotropy) and extrinsic (particle size and shape) factors. In the present study, *H<sub>c</sub>* is increasing despite the decrease in anisotropic constant (*k*<sub>1</sub>) (table 2), hence, the increase in *H<sub>c</sub>* is dominated by decrease in crystallite size with Al<sup>3+</sup> substitution and the pinning by residual Al<sub>2</sub>O<sub>3</sub>. The in-plane (0°) and out of plane (90°) *M-H* plots of pure and Al-substituted BaM thick films are shown in Fig. 9. *M* and remanence (*M<sub>r</sub>*) are found to be higher for in-plane direction; however, *H<sub>c</sub>* is nearly same for both the orientations. At *x* = 0.0, *H<sub>c</sub>* of BaM film (1.7 kOe) is found to be less than the powder (3.0 kOe) due to obvious increase in grain size after sintering. However, on contrary, the *H<sub>c</sub>* of the substituted films is very high despite its larger grain size. The highest *H<sub>c</sub>* of 7.47 KOe is observed at *x* = 2.0, which is due to dominant Al<sub>2</sub>O<sub>3</sub> pinning effect in sintered films [42,43]. The magnetic properties of Al-substituted BaM powder and films are shown in Table 2.

The law of approach to saturation is used to obtain *H<sub>a</sub>* and first anisotropy constant (*k*<sub>1</sub>) for the powder and films [44].

The calculated values of *H<sub>a</sub>* and *k*<sub>1</sub> (table 2) found to decrease with Al<sup>3+</sup> substitution. Fig. 10 (a) shows the magnetization vs temperature (*M-T*) behavior at 1000 Oe for pure and substituted (*x* = 2.0) BaM. The decrease in *M* with temperature is due to thermal effect. Curie temperature (*T<sub>c</sub>*) is measured by plotting derivative of *M* (*dM/dT*) with respect to *T* (Fig. 10(b)). The *T<sub>c</sub>* found to decrease from 497 °C (*x* = 0.0) to 437 °C (*x* = 2.0). The *T<sub>c</sub>* can be expressed in term of number of exchange interactions between Fe<sup>3+</sup>-O<sup>2-</sup>-Fe<sup>3+</sup> ions [45]. The reduction in *T<sub>c</sub>* is due to weakening of super exchange coupling [20]. The inset Fig. 10(b) shows the *M-H* behavior at *T<sub>c</sub>*, which clearly shows the paramagnetic nature of the samples.

### 3.6. High frequency complex permeability

Fig. 11(a and b) shows the variation of real (*μ'*) and imaginary (*μ''*) part of complex permeability (*μ<sub>r</sub>* = *μ'* - *jμ''*) for pure and Al-substituted BaM as a function of frequency.

Parameters *μ'* and *μ''* represents the storage and losses of magnetic energy respectively. It is observed that *μ'* of the Al-substituted BaM is lesser than the pure BaM. However, within the substitution, *μ'* increases with increase in Al content. The variation may be attributed to the non-magnetic nature of Al<sup>3+</sup> ions. It is clear from the Fig. 11(b) that *μ''* for Al-substituted BaM is larger and maximum were observed for *x* = 1. These losses may due to change in grain size, sintered density, or lag between magnetization and applied field [46].

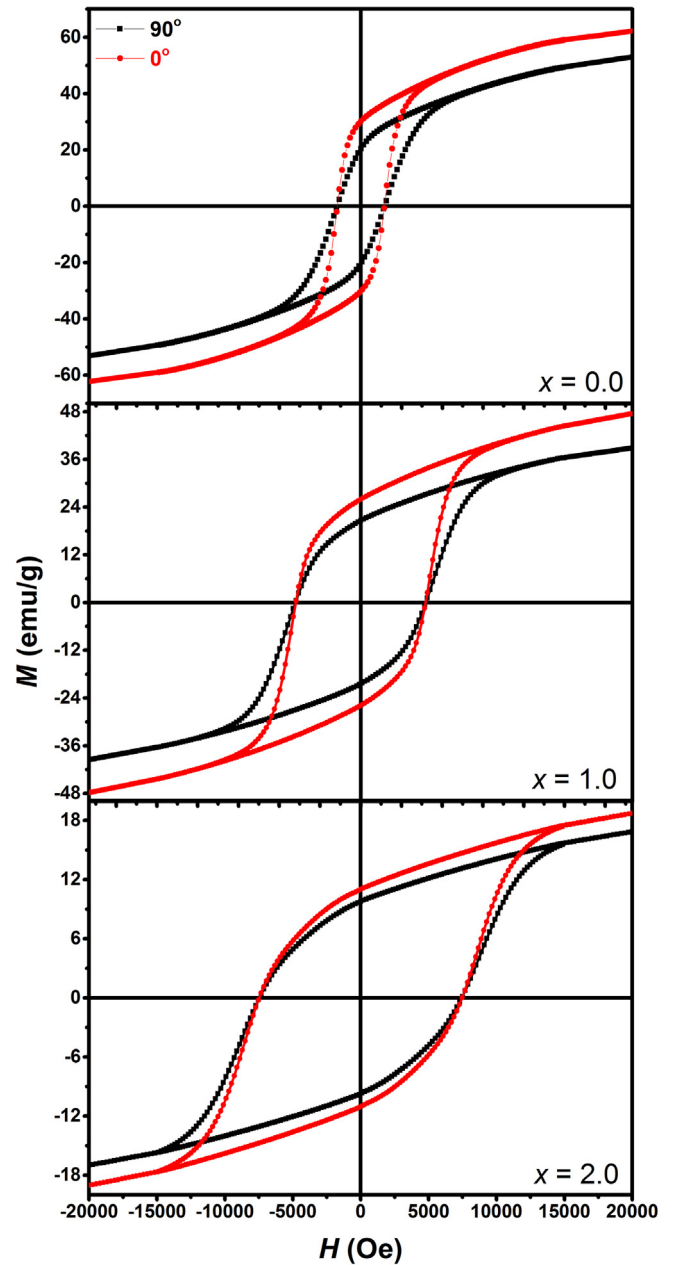


Fig. 9. In-plane and out of plane *M-H* loop of BaFe<sub>12-x</sub>Al<sub>x</sub>O<sub>19</sub> films.

### 3.7. Microwave reflection losses

Fig. 12 depicts the reflection loss of Al-substituted BaM in X-band. Reflection loss were calculated by the following relation;

$$R_L = 20 \log \left| \frac{Z_{in} - Z_0}{Z_{in} + Z_0} \right| \quad (8)$$

where, *Z<sub>in</sub>* is given by:

$$Z_{in} = Z_0 \sqrt{\frac{\mu_r}{\epsilon_r}} \tanh \left\{ j \left( \frac{2\pi f t}{c} \right) \sqrt{\mu_r \epsilon_r} \right\} \quad (9)$$

where *f* is the frequency, *t* is the thickness of sample, *μ<sub>r</sub>* and *ε<sub>r</sub>* are the complex relative permeability and permittivity of the sample, *c* is the velocity of the light, *Z<sub>0</sub>* is the impedance of air and *Z<sub>in</sub>* is the input impedance at the absorber surface. The reflection loss dips are observed at the frequency where absorption is maximum. It can

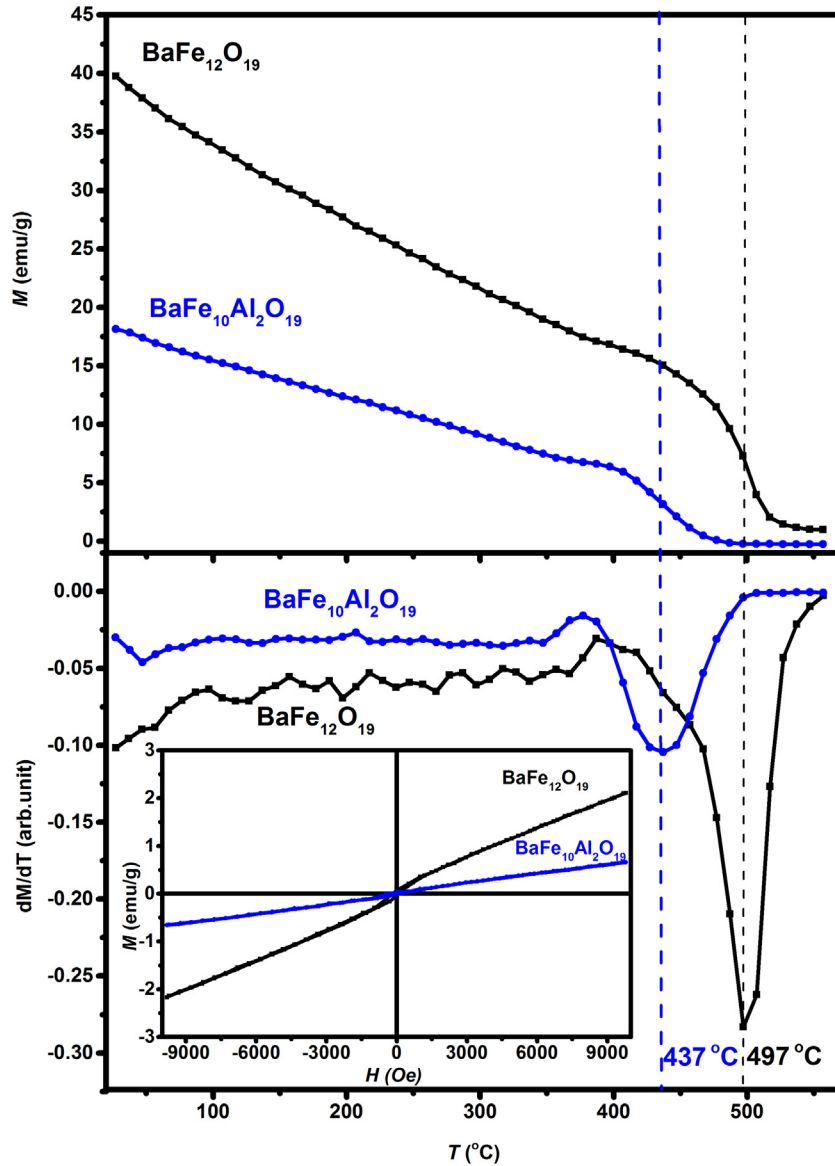


**Fig. 10.** High temperature (a)  $M$ - $T$  plot (b)  $dM/dT$  vs  $T$  for  $\text{BaFe}_{12-x}\text{Al}_x\text{O}_{19}$ . Inset (b) shows  $M$ - $H$  behavior at Curie temperature.

be seen that all compositions have reflection dip in the studied frequency range except for the composition  $x = 1$ . The observed reflection loss  $R_i$  is varying from  $-14.05$  dB ( $x = 0.0$ ) to  $-47.06$  dB ( $x = 1.5$ ) at 9.3 GHz frequency. Thus, these reflection losses dip shows that Al-substitution improves the absorption property of BaM.

#### 4. Conclusion

Al-substituted BaM powders were prepared by solid state synthesis method and their structural, dielectric and magnetic properties have been investigated. XRD patterns confirmed the formation of single phase for all the substituted samples. Phase refinement confirmed shrinkage in the lattice parameters and decrease in crystallite size with  $\text{Al}^{3+}$  substitution. Further, FTIR

confirmed the reduction in Fe-O bond length at octahedral and tetrahedral co-ordination. Very high  $\epsilon_r$  and relatively less  $\tan \delta$  were observed in the Al-substituted BaM. As-prepared powders were further screen printed on  $\text{Al}_2\text{O}_3$  substrate to prepare thick films. Drastic rise in the  $H_c$  was observed in substituted sintered films, irrespective to its larger grain size. The rise in  $H_c$  were ascribed to the dominant pinning by residual  $\text{Al}_2\text{O}_3$  in sintered films.  $M$  found to decrease with  $\text{Al}^{3+}$  substitution.  $T_c$  was found to decrease with  $\text{Al}^{3+}$  substitution. Frequency dependent permeability study ensures rise in the  $\text{Al}^{3+}$  substitution increase the complex permeability ( $\mu'$ ). Reflection losses found to be maximum at  $x = 1.5$ . The study demonstrated that Al-substituted BaM thick films with tunable  $H_a$  can be used for microwave application.

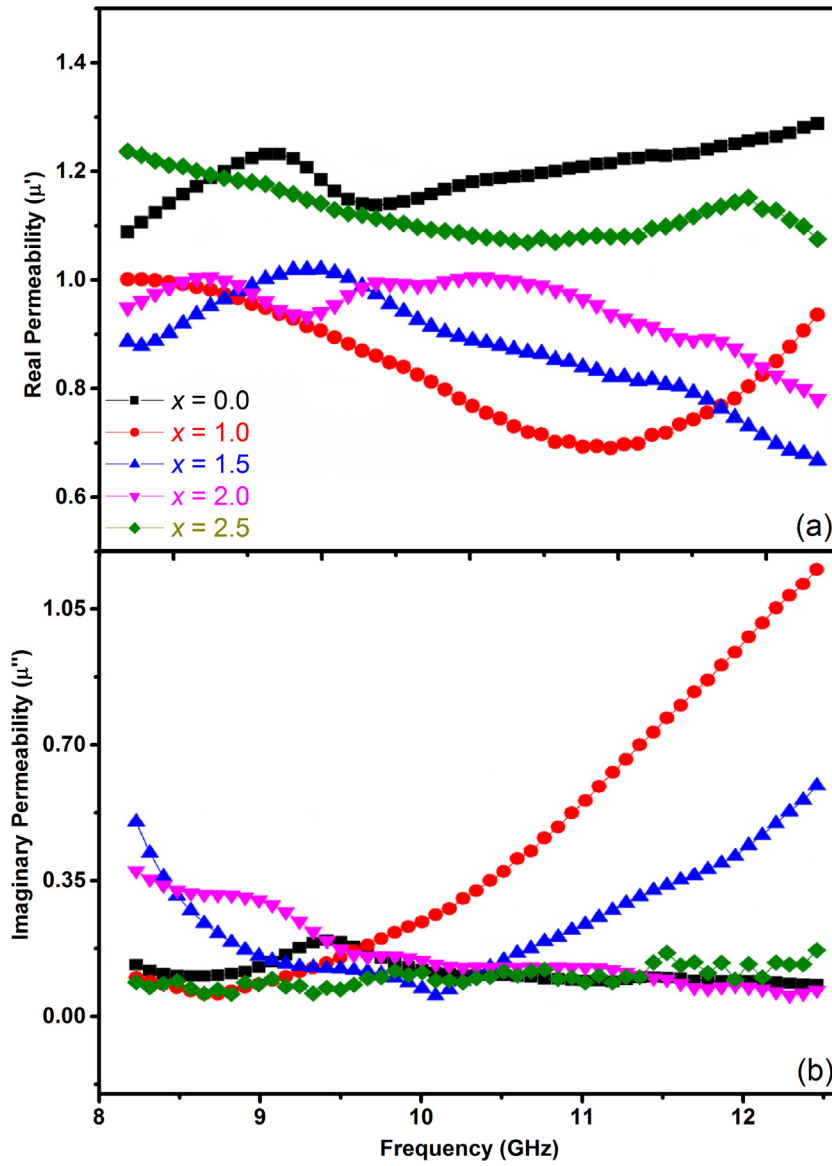


Fig. 11. Frequency dependent real (a) and imaginary (b) permeability of  $BaFe_{12-x}Al_xO_{19}$  in X-band.

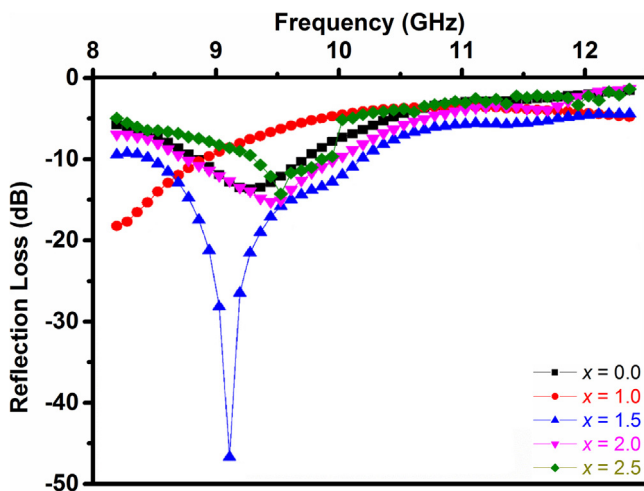


Fig. 12. Frequency dependent reflection loss of  $BaFe_{12-x}Al_xO_{19}$  in X-band.

### Acknowledgment

This work has been carried out under the financial support provided by DST (SERB/F/2947/2014-2015). The authors would like to acknowledge Dr. Manoj Kumar and Mr. Munish Verma, Department of Physics and Materials Science Engineering at Jaypee Institute of Information Technology (Noida) for characterization.

### References

- [1] R.C. Pullar, Hexagonal ferrites: a review of the synthesis, properties and applications of hexaferrite ceramics, *Prog. Mater. Sci.* 57 (2012) 1191–1334.
- [2] H. Kojima, Chapter 5 Fundamental Properties of Hexagonal Ferrites with Magnetoplumbite Structure, 1982. [http://dx.doi.org/10.1016/S1574-9304\(05\)80091-4](http://dx.doi.org/10.1016/S1574-9304(05)80091-4).
- [3] V.G. Harris, Modern microwave ferrites, *IEEE Trans. Magn.* 48 (2012) 1075–1104.
- [4] U. Ozgur, Y. Alivov, H. Morkoc, Microwave Ferrites, Part 1: Fundamental Properties, 2009. <http://dx.doi.org/10.1007/s10854-009-9923-2>.
- [5] G. Albanese, A. Deriu, E. Lucchini, G. Slokar, Mossbauer investigation of In and Sc substituted barium hexaferrite, *Appl. Phys. A: Solids Surfaces* 26 (1981) 45–50, <http://dx.doi.org/10.1007/BF01197677>.

- [6] G. Albanese, A. Deriu, Magnetic properties of Al, Ga, Sc, In substituted barium ferrites: a comparative analysis, *Ceramurg. Int.* 5 (1979) 3–10, [http://dx.doi.org/10.1016/0390-5519\(79\)90002-4](http://dx.doi.org/10.1016/0390-5519(79)90002-4).
- [7] P.C. Dorsey, T.D.B. Chrisey, J.S. Horwitz, P. Lubitz, R.C.Y. Auyeung, Oriented barium hexaferrite thick films grown on c-plane and m-plane sapphire substrates, *IEEE Trans. Magn.* 30 (1994) 4512–4517, <http://dx.doi.org/10.1109/20.334133>.
- [8] S.A. Oliver, S.D. Yoon, I. Kozulin, M.L. Chen, C. Vittoria, Growth and characterization of thick oriented barium hexaferrite films on MgO (111) substrates, *Appl. Phys. Lett.* 76 (2000) 3612, <http://dx.doi.org/10.1063/1.126723>.
- [9] Z. Xu, Z. Lan, K. Sun, R. Guo, Z. Yu, X. Jiang, G. Zhu, Properties of Ba-hexaferrite thin films with different thicknesses, *Appl. Surf. Sci.* 271 (2013) 362–368, <http://dx.doi.org/10.1016/j.apsusc.2013.01.203>.
- [10] Z. Chen, A. Yang, A. Gieler, V.G. Harris, C. Vittoria, P.R. Ohodnicki, K.Y. Goh, M.E. Mchenry, Z. Cai, T.L. Goodrich, K.S. Ziemer, Epitaxial growth of M-type Ba-hexaferrite films on MgO (111), SiC(0001) with low ferromagnetic resonance linewidths, *Appl. Phys. Lett.* 91 (2007) 182505, <http://dx.doi.org/10.1063/1.2794011>.
- [11] Y. Chen, T. Sakai, T. Chen, S.D. Yoon, A.L. Geiler, C. Vittoria, V.G. Harris, Oriented barium hexaferrite thick films with narrow ferromagnetic resonance linewidth, *Appl. Phys. Lett.* 88 (2006) 1–3, <http://dx.doi.org/10.1063/1.2173240>.
- [12] Y. Chen, I.C. Smith, A.L. Geiler, C. Vittoria, V. Zagorodnii, Z. Celinski, V.G. Harris, Microstructural, magnetic and microwave properties of large area BaFe<sub>12</sub>O<sub>19</sub> thick films (100 m) deposited on /a-SiO<sub>2</sub>/Si and /a-Al<sub>2</sub>O<sub>3</sub>/Si substrates, *IEEE Trans. Magn.* 44 (2008), <http://dx.doi.org/10.1109/TMAG.2008.2002573>.
- [13] Y. Chen, I. Smith, A.L. Geiler, C. Vittoria, V. Zagorodnii, Z. Celinski, V.G. Harris, Realization of hexagonal barium ferrite thick films on Si substrates using a screen printing technique, *J. Phys. D: Appl. Phys.* 41 (2008) 95006, <http://dx.doi.org/10.1088/0022-3727/41/9/095006>.
- [14] C.N. Chinnaamy, T. Sakai, S. Sivasubramanian, A.F. Yang, C. Vittoria, V.G. Harris, Magnetic and microwave properties of basal-plane oriented BaFe<sub>11</sub>N<sub>1</sub>O<sub>19</sub> ferrite thick films processed by screen printing, *J. Appl. Phys.* 103 (2008) 10–12, <http://dx.doi.org/10.1063/1.2829905>.
- [15] S. Verma, O.P. Pandey, A. Paesano Jr., P. Sharma, Structural and magnetic properties of CoTi substituted barium hexaferrite thick films, *J. Alloys Compd.* 678 (2016) 284–289, <http://dx.doi.org/10.1016/j.jallcom.2016.03.283>.
- [16] A.B. Ustinov, A.S. Tatarenko, G. Srinivasan, A.M. Balbashov, Al substituted Ba-hexaferrite single-crystal films for millimeter-wave device, *J. Appl. Phys.* 105 (2009) 23908, <http://dx.doi.org/10.1063/1.3067759>.
- [17] S. Singhal, A.N. Garg, K. Chandra, Evolution of the magnetic properties during the thermal treatment of nanosize BaMFe<sub>11</sub>O<sub>19</sub> (M = Fe, Co, Ni and Al) obtained through aerosol route, *J. Magn. Magn. Mater.* 285 (2005) 193–198, <http://dx.doi.org/10.1016/j.jmmm.2004.07.039>.
- [18] Y. Liu, M.G.B. Drew, J. Wang, M. Zhang, Y. Liu, Efficiency and purity control in the preparation of pure and/or aluminum-doped barium ferrites by hydrothermal methods using ferrous ions as reactants, *J. Magn. Magn. Mater.* 322 (2010) 366–374, <http://dx.doi.org/10.1016/j.jmmm.2009.09.062>.
- [19] D.A. Vinnik, D.A. Zhrebtsov, L.S. Mashkovtseva, S. Nemrava, A.S. Semisalova, D.M. Galimov, S.A. Gudkova, I.V. Chumanov, L.I. Isaenko, R. Niewa, Growth, structural and magnetic characterization of Al-substituted barium hexaferrite single crystals, *J. Alloys Compd.* 628 (2015) 1043–1046, <http://dx.doi.org/10.1016/j.jallcom.2014.12.124>.
- [20] D. Chen, I. Harward, J. Baptist, S. Goldman, Z. Celinski, Curie temperature and magnetic properties of aluminum doped barium ferrite particles prepared by ball mill method, *J. Magn. Magn. Mater.* 395 (2015) 350–353.
- [21] V.N. Dhage, M.L. Mane, A.P. Keche, C.T. Birajdar, K.M. Jadhav, Structural and magnetic behaviour of aluminium doped barium hexaferrite nanoparticles synthesized by solution combustion technique, *Phys. B: Condens. Matter.* 406 (2011) 789–793, <http://dx.doi.org/10.1016/j.physb.2010.11.094>.
- [22] W.B. Weir, Automatic measurement of complex dielectric constant and permeability at microwave frequencies, *Proc. IEEE* 62 (1974) 33–36, <http://dx.doi.org/10.1109/PROC.1974.9382>.
- [23] A.M. Nicolson, G.F. Ross, Measurement of the intrinsic properties of materials by time-domain techniques, *IEEE Trans. Instrum. Meas.* 19 (1970) 377–382, <http://dx.doi.org/10.1109/TIM.1970.4313932>.
- [24] S.M. El-Sayed, T.M. Meaz, M.A. Amer, H.A. El Shersaby, H.A. El Shersaby, Magnetic behavior and dielectric properties of aluminum substituted M-type barium hexaferrite, *Phys. B: Condens. Matter.* 426 (2013) 137–143, <http://dx.doi.org/10.1016/j.physb.2013.06.026>.
- [25] B.D. Cullity, *Elements of X-ray Powder Diffraction*, Addison-Wesley Publishing Company Inc, USA, 1978.
- [26] G. Caglioti, A. Paoletti, F.P. Ricci, Choice of Collimators for a crystal spectrometer for neutron diffraction, *Nucl. Instruments* 3 (1958) 223–228.
- [27] J. Kreisel, G. Lucazeau, H. Vincent, Raman spectra and vibrational analysis of BaFe<sub>12</sub>O<sub>19</sub> hexagonal ferrite, *J. Solid State Chem.* 137 (1998) 127–137, <http://dx.doi.org/10.1006/jssc.1997.7737>.
- [28] F. Song, X. Shen, J. Xiang, H. Song, Formation and magnetic properties of M-Sr ferrite hollow fibers via organic gel-precursor transformation process, *Mater. Chem. Phys.* 120 (2010) 213–216, <http://dx.doi.org/10.1016/j.matchemphys.2009.10.048>.
- [29] Anshuman Sahai, N. Goswami, Structural and vibrational properties of ZnO nanoparticles synthesized by the chemical precipitation method, *Phys. E* 58 (2014) 130–137, <http://dx.doi.org/10.1016/j.physe.2013.12.009>.
- [30] S. Thongmee, T. Osotchan, P. Winotai, I.M. Tang, Fluctuations in the local fields due to Al 3+ ions substitution in the M-type barium hexaferrites, BaFe<sub>12-x</sub>Al<sub>x</sub>O<sub>12</sub>, *Int. J. Mod. Phys. B* 12 (1998) 2847–2855.
- [31] D.H. Choi, S.Y. An, S.W. Lee, I.B. Shim, C.S. Kim, Site occupancy and anisotropy distribution of Al substituted Ba-ferrite with high coercivity, *Phys. Status Solidi* 241 (2004) 1736–1739, <http://dx.doi.org/10.1002/pssb.200304633>.
- [32] A. Trukhanov, L. Panina, S. Trukhanov, V. Turchenko, M. Salem, Evolution of structure and physical properties in Al-substituted Ba-hexaferrites, *Chin. Phys. B* 25 (2016) 16102, <http://dx.doi.org/10.1088/1674-1056/25/1/016102>.
- [33] Y. Chen, T. Sakai, T. Chen, S.D. Yoon, C. Vittoria, V.G. Harris, Screen printed thick self-biased, low-loss, barium hexaferrite films by hot-press sintering, *J. Appl. Phys.* 100 (2006) 1–9, <http://dx.doi.org/10.1063/1.2221527>.
- [34] S. Verma, S.K. Dhawan, A. Paesano, O.P. Pandey, P. Sharma, Structural, magnetic and microwave properties of barium hexaferrite thick films with different Fe/Ba mole ratio, *J. Magn. Magn. Mater.* 396 (2015) 308–312, <http://dx.doi.org/10.1016/j.jmmm.2015.08.049>.
- [35] C. Koops, On the dispersion of resistivity and dielectric constant of some semiconductors at audiofrequencies, *Phys. Rev.* 83 (1951) 121–124.
- [36] H. Fricke, The Maxwell-Wagner dispersion in a suspension of ellipsoids, *J. Phys. Chem.* 57 (1953) 934–937, <http://dx.doi.org/10.1021/ji150510a018>.
- [37] C.A. Stergiou, I. Manolakis, T.V. Yioultsis, G. Litsardakis, Dielectric and magnetic properties of new rare-earth substituted Ba-hexaferrites in the 2–18 GHz frequency range, *J. Magn. Magn. Mater.* 322 (2010) 1532–1535, <http://dx.doi.org/10.1016/j.jmmm.2009.07.082>.
- [38] H. Sözeri H. Deligöz H. Kavas A. Baykal Magnetic, dielectric and microwave properties of M-Ti substituted barium hexaferrites (M = Mn<sup>2+</sup>, Co<sup>2+</sup>, Cu<sup>2+</sup>, Ni<sup>2+</sup>, Zn<sup>2+</sup>) *Ceram. Int.* 40 2014 8645 8657 10.1016/j.ceramint.2014.01.082
- [39] V.V. Soman, V.M. Nanoti, D.K. Kulkarni, Dielectric and magnetic properties of Mg-Ti substituted barium hexaferrite, *Ceram. Int.* 39 (2013) 5713–5723, <http://dx.doi.org/10.1016/j.ceramint.2012.12.089>.
- [40] K. Iwauchi, C.G. Koops, J.C. Maxwell, K.W. Wagner, R.B. Hirborn, M. Kiyama, N. K.G. Gotoh, T. Hanai, A. Smakula, O. Jantzen, R.G. Breckenridge, J.H. De Boer, Dielectric properties of fine particles of Fe<sub>3</sub>O<sub>4</sub> and some ferrites, *Jpn. J. Appl. Phys.* 10 (1971) 1520–1528, <http://dx.doi.org/10.1143/JJAP.10.1520>.
- [41] A. Ghasemi, A. Hossienpour, A. Morisako, A. Saatchi, M. Salehi, Electromagnetic properties and microwave absorbing characteristics of doped barium hexaferrite, *J. Magn. Magn. Mater.* 302 (2006) 429–435, <http://dx.doi.org/10.1016/j.jmmm.2005.10.006>.
- [42] K. Haneda, H. Kojima, Intrinsic coercivity of substituted BaFe<sub>12</sub>O<sub>19</sub>, *Jpn. J. Appl. Phys.* 12 (1973) 355–360.
- [43] G. Turilli, A. Paoluzi, M. Lucenti, Surface doping with Al in Ba-hexaferrite powders, *J. Magn. Magn. Mater.* 97 (1991) 338–342.
- [44] R. Grossinger, A critical examination of the law of approach to saturation. I. Fit procedure, *Phys. Status Solidi* 66 (1981) 665–674.
- [45] M.A. Gilleo, Superexchange interaction energy for Fe<sup>3+</sup>-O-Fe<sup>3+</sup> linkages, *Phys. Rev.* 109 (1958) 777–781.
- [46] S.B. Narang, K. Pubby, C. Singh, Thickness and composition tailoring of K- and Ka-band microwave absorption of BaCo<sub>x</sub>Ti<sub>x</sub>Fe<sub>(12-2x)</sub>O<sub>19</sub> ferrites, *J. Electron. Mater.* 46 (2017) 718–728, <http://dx.doi.org/10.1007/s11664-016-5059-3>.

# Turnitin Originality Report

Processed on: 14-Sep-2020 19:24 +0530  
 ID: 1386760798  
 Word Count: 16248  
 Submitted: 1

Similarity Index

15%

## Similarity by Source

Internet Sources: 3%  
 Publications: 6%  
 Student Papers: 9%

Santhosh Thesis By Santhosh Mahadevan

5% match (student papers from 25-May-2018)

[Submitted to Thapar University, Patiala on 2018-05-25](#)

3% match (student papers from 13-Jan-2020)

[Submitted to Thapar University, Patiala on 2020-01-13](#)

1% match (publications)

[Samiksha Verma, S.K. Dhawan, Andrea Paesano, O.P. Pandey, Puneet Sharma. "Structural, magnetic and microwave properties of barium hexaferrite thick films with different Fe/Ba mole ratio", Journal of Magnetism and Magnetic Materials, 2015](#)

1% match (publications)

[Chhavi Pahwa, Santhoshkumar Mahadevan, Sukhleen Bindra Narang, Puneet Sharma. "Structural, magnetic and microwave properties of exchange coupled and non-exchange coupled BaFe<sub>12</sub>O<sub>19</sub>/NiFe<sub>2</sub>O<sub>4</sub> nanocomposites", Journal of Alloys and Compounds, 2017](#)

< 1% match (publications)

[Verma, Samiksha, O.P. Pandey, Andrea Paesano, and Puneet Sharma. "Structural and magnetic properties of CoTi substituted barium hexaferrite thick films", Journal of Alloys and Compounds, 2016.](#)

< 1% match (publications)

[Shivani Punj, K. Singh. "Blue-green light emitting inherent luminescent glasses synthesized from agro-food wastes", Journal of Materials Science: Materials in Electronics, 2019](#)

< 1% match (publications)

[Samiksha Verma, Santhoshkumar Mahadevan, Chhavi Pahwa, Anoop Pratap Singh, Sukhleen Bindra Narang, Neha Aggarwal, Puneet Sharma. "Improved Magnetic and Microwave Properties of La-Substituted Barium Hexaferrite Screen-Printed Thick Films", Journal of Superconductivity and Novel Magnetism, 2020](#)

< 1% match (Internet from 09-Sep-2020)

<https://aip.scitation.org/doi/10.1063/1.4998719>

< 1% match (publications)

[Vincent G. Harris. "Microwave Ferrites and Applications", Wiley, 2017](#)

< 1% match (student papers from 20-Mar-2019)

[Submitted to Universiti Teknologi Malaysia on 2019-03-20](#)

## Santhoshkumar M

Research Associate,  
School of Physics & Materials Science (SPMS),  
Thapar Institute of Engineering & Technology,  
P.O. Box 32, Bhadson Road, Patiala,  
Pin -147004,  
India.



Mobile : +919176792144,

Email ID : santhosh.phd21@gmail.com, santhoshbero1991@gmail.com

---

### Objective

To engage a challenging career and be part of progressive research that gives scope to enhance my knowledge, skills and to reach the pinnacle in the research field with sheer determination, dedication and hard work.

### Research Interest

Materials science has been a part of my curriculum throughout my education. I build up my interest in static and dynamic magnetic properties of ferrite and its underlying physics. To be specific my recent interest are to develop M-barium hexaferrite ( $BaFe_{12}O_{19}$ ) and exchange coupled nanocomposites for next generation microwave device applications. The primary focus of my research is to develop ready to support industrial needs of ferrite devices in a convenient, reliable and cost effective methods.

### Work Experience

- Research Associate** : **October 09, 2018 – July 31, 2021**  
Development of exchange coupled hard/soft ferrite nanocomposites for tunable microwave application.
- Teaching Associate** : **August 01, 2017 – October 08, 2018**  
Course – Materials Science and Engineering (Graduate level – B.Tech second year)
- Junior Research Fellow** : **September 04, 2015 – July 27, 2017**  
Development of M-type hexaferrite film for microwave device application.

### Educational Qualification

- PhD** : **Materials Science (CGPA (Course work) – 8.7/10), 2015-2021**  
Thapar Institute of Engineering & Technology, Patiala, Punjab.
- M.Tech** : **Materials Science and Engineering (CGPA – 8.7/10), 2013-2015**  
Jaypee Institute of Information Technology, Noida, Uttar Pradesh.
- B.Tech** : **Aeronautical Engineering (CGPA – 8.6/10), 2009-2013**  
Vel Tech Dr. RR & Dr.SR Technical University, Avadi, Chennai.
- H. Secondary** : **State Board (Major – Biology, Physics, Chemistry and Mathematics) (Percentage 74%), 2009**  
St.Mary's Matriculation Higher Secondary School, Sriperumbudur, Kancheepuram.

**SSLC** : **Matric (Percentage 68%), 2007**  
Holy Crescent Matriculation School Higher Secondary, Sriperumbudur,  
Kancheepuram.

## Thesis

**PhD** : Development of M-type hexaferrite films for microwave device application.

M-type hexaferrite has been extensively used in microwave devices due to its large magnetocrystalline anisotropy, high magnetization and ferromagnetic resonance frequency over 50 GHz. Its high versatility in magnetic and dielectric properties with low losses in off-resonance frequency provides a significant important in non-reciprocal devices such as circulator, isolators, phase shifter and band filters. Substantial effort has been drawn to miniaturize these devices with self- biased ferrite materials. In the present dissertation, barium hexaferrite (BaM) powders with various substitution (Al, Ti, La & Co) were prepared. To understand the insight of the substitution, the powder were characterized by Raman spectroscopy, FTIR, and Mössbauer spectroscopy. As substituted powder were used to fabricate the screen printed thick films. The microstructural and magnetic properties of the films were measured in perpendicular and in plane direction. Microwave properties of substituted sample were compared with pure BaM in X-band and Ku band. Apart from isotropic thick films, anisotropic microwave sintered thick films were also prepared under the presence of external magnetic field of 0.8 T. The effect of milling time on structural and magnetic properties of thick films were investigated.

**M.Tech Minor:** Investigation of Nanomaterials Prepared by Exploding Wire Technique.

**M.Tech Major:** Investigation of Copper Particles in Carbon Environment.

**B.Tech** : Study of Sandwich Composite Floor Panel for Aircraft - Designing, Testing & characterization.

## Laboratory skills

**As operator** : Vibrating sample magnetometer, Fourier-transform infrared spectroscopy, Sputtering and Inductively coupled plasma mass spectrometry.

**As user** : X-ray Diffractometer, Electron microscopy, Impedance analyzer, Vector network analyzer, Raman, Mössbauer and, X-ray photoelectron spectroscopies.

**Expertise** : Reitveld refinement, XPS fit, Moss fit, Origin and Electrochemical impedance spectroscopy spectrum analyser.

**Certified** : Non destructive testing (NDT) level – 2 (Dye penetrant, Magnetic particle, ultrasonic and Radiographic testing), Diploma in professional CADD and computational fluid dynamics.

**Course** : Materials science and engineering, Nanoscience and engineering, Thin film technology, Semiconductor device and IC technology, Optoelectronics materials and devices, Photovoltaic techniques and process, Engineering ceramics and composite, Structure and characterization of materials, Thermodynamics and kinetics, Properties and processing of engineering materials, Rocket and missiles, Avionics, Aircraft stability and control, Space mechanics, Aircraft performance, Aerodynamics, Aircraft production and technology, and Strength of materials.

**Publications: *h-index - 04, i10-index - 02***

1. **Santhoshkumar Mahadevan**, Vasant Sathe, V Raghavendra Reddy, Puneet Sharma, Site occupation and magnetic studies in La-Co substituted barium hexaferrite, IEEE Trans. Magn. 56 (2020) 1-6. DOI: 10.1109/tmag.2020.3014071
2. **Santhoshkumar Mahadevan**, Puneet Sharma, Charge transport mechanism in  $\text{BaFe}_{12}\text{O}_{19}$  and  $\text{BaFe}_{11}\text{CoO}_{19}$ , J. Magn. Magn. Mater. 514 (2020) 167174.
3. **Santhoshkumar Mahadevan**, Sukhleen Bindra Narang, Puneet Sharma, Effect of three-step calcination on structural, magnetic and microwave properties of  $\text{BaFe}_{11.5}\text{Ti}_{0.5}\text{O}_{19}$  hexaferrite, Ceram. Int. 45 (2019) 9000–9006.
4. **Santhoshkumar Mahadevan**, Chhavi Pahwa, Sukhleen Bindra Narang, Puneet Sharma, Structural, dielectric and magnetic properties of  $\text{BaFe}_{12-x}\text{Al}_x\text{O}_{19}$  hexaferrite thick films, J. Magn. Magn. Mater. 441 (2017).
5. **Santhoshkumar Mahadevan**, Alok Prathap Singh Chauhan, Investigation of synthesized nanosized copper by polyol technique with graphite powder, Adv. Powder Technol. 27 (2016) 1852–1856.
6. Neha Rani, Surjeet Chahal, **Santhoshkumar Mahadevan**, Parmod Kumar, Rajni Shukla, SK Singh, Development of hierarchical magnesium oxide anchored cerium oxide nanocomposites with improved magnetic properties and photocatalytic performance, Nanotechnology. 31 (2020) 374004.
7. Samiksha Verma, **Santhoshkumar Mahadevan**, Chhavi Pahwa, Anoop Pratap Singh, Sukhleen Bindra Narang, Neha Aggarwal, Puneet Sharma, Improved Magnetic and Microwave Properties of La-Substituted Barium Hexaferrite Screen-Printed Thick Films, J. Supercond. Nov. Magn. 33 (2020) 2507–2512.
8. Chhavi Pahwa, **Santhoshkumar Mahadevan**, Sukhleen Bindra Narang, Puneet Sharma Structural, magnetic and microwave properties of exchange coupled and non-exchange coupled  $\text{BaFe}_{12}\text{O}_{19}/\text{NiFe}_2\text{O}_4$  nanocomposites, J. Alloys Compd. 725 (2017) 1175–1181.
9. Chhavi Pahwa, **Santhoshkumar Mahadevan**, Sukhleen Bindra Narang, Puneet Sharma, Studies on exchange-coupled magnetodielectric ceramics for microwave application in K<sub>u</sub>-band, IEEE Trans. Magn. 57 (2020) 1-7.
10. Denis Vinnik, **Santhoshkumar Mahadevan** and Puneet Sharma, Magnetic study on divalent ion substituted barium hexaferrites, Defect Diffus. Forum. 410 (2021) 714-719.
11. **Santhoshkumar Mahadevan**, Alok PS Chauhan “Preparation and Characterization of Fine Copper Nanoparticles” *NCRACMS-15*, pp-48, ISBN - 978-93-84224-25-7. (Non-SCI)

## Professional Activities:

### 1. Conferences & Symposium

- **Santhoshkumar Mahadevan**, Vasant Sathe, V Raghavendra Reddy, Sukhleen Bindra Narang, Puneet Sharma, “Role of anisotropy variation on magnetic and microwave performance of La-Co substituted barium hexaferrite”, 12<sup>th</sup> International Conference on Ferrites (ICF-12, 2019), October 29- November 01, 2019, Boston ,MA, USA. (**Oral presentation**).
- **Santhoshkumar Mahadevan**, Puneet Sharma “High coercive Al-substituted M-type hexaferrite thick films for microwave device application.” International Conference on Magnetism and Magnetic Materials (ICMAGMA- 2018) December 09-13, 2018, NISER, Bhubaneswar (**Poster presentation**).
- **Santhoshkumar Mahadevan**, Puneet Sharma “Effect of structural and magnetic properties of BaFe<sub>12-x</sub>Al<sub>x</sub>O<sub>19</sub> hexaferrite thick films processed via two different methodology”. Young Materials Researchers’ Meet 2017 (YMRM-2017) December 10-11, 2017, Baba Atomic Research Centre (BARC), Mumbai (**Poster presentation – Best poster award**).
- **Santhoshkumar Mahadevan**, Chhavi Pahwa, Anoop Pratap Singh and Puneet Sharma “Structural and magnetic properties of BaFe<sub>12-x</sub>Al<sub>x</sub>O<sub>19</sub> hexaferrite thick films” National symposium on materials for advanced technology (MAT-2017), February 20-21, 2017, DIT university, Dehradun (**Poster presentation – Best poster award**).
- **Santhoshkumar Mahadevan**, Puneet Sharma, “Structural, magnetic and vibrational properties of BaFe<sub>11.5</sub>Ti<sub>0.5</sub>O<sub>19</sub> prepared by three step calcination method” International Conference on Magnetism and Magnetic Materials (ICMAGMA- 2017) February 01-03, 2017, DMRL, Hyderabad (**Oral presentation**).
- **Santhoshkumar Mahadevan**, Alok PS Chauhan “Investigating effect of crystalline carbon with polyol synthesized pure copper at elevated temperature” National Conference on Microscopy & Advances in Material Science (NCMAMS-2015), March 02- 04, 2015, Jammu University, Jammu, (**Poster presentation**).
- **Santhoshkumar Mahadevan**, Alok PS Chauhan “Preparation and characterization of fine copper nanoparticles” Nation Conference on Recent Advances in Chemical and Materials Science (NCRACMS-15), February 23-24 2015, Madan Mohan Malaviya University of Technology, Gorakhpur, (**Oral presentation**).

### 2. Workshop and Seminar

- “The European School on Magnetism - Magnetism and Societal Challenges” Saarbrücken, Germany, September 28 – October 02, 2020 (online)
- “Two days webinar on MIMO antennas for 5G communications using CST studio suite” Department of electronic science, University of Delhi (South campus), New Delhi, June 5 - 6, 2020. (Online)

- “Summer School on Magnetism (SSM-2016)” organized by School of Physics & Materials Science, Thapar Institute of Engineering & Technology, Patiala July 11-15, 2016.
- “National Workshop on Advanced Techniques for surface characterization” organized by School of Physics & Materials Science, Thapar Institute of Engineering & Technology, Patiala, October 28-30, 2015.
- “Bringing the Nanoworld Together by Oxford Instrument”, Indian Institute of Technology, Delhi, 2014.
- “Synthesis and Characterization of Smart Material”, Sri Ram Engineering College, Chennai, 2011.

## Reference

1. **Dr. Puneet Sharma**, Professor (Doctrate supervisor),  
Incharge – Magentic materials Lab,  
G252, School of Physics & Materials Science,  
Thapar Institute of Engg. & Tech., Patiala (Pb).  
puneet.sharma@thapar.edu
2. **Dr. Kulvir Singh**, Professor & Head,  
School of Physics & Materials Science,  
Thapar Institute of Engg. & Tech., Patiala (Pb).  
kusingh@thapar.edu
3. **Dr. Bhupendrakumar Chudasama**, Professor,  
Incharge – Nano magnetic lab,  
School of Physics & Materials Science,  
Thapar Institute of Engg. & Tech., Patiala (Pb).  
bnchudasama@thapar.edu

## Activities and Societies:

1. Life Member of Material Research Society of India (MRSI).
2. Life Member of Magnetic Society of India (MSI).

## Linguistic Ability:

1. Tamil : Native or bilingual proficiency.
2. English : Full professional proficiency.
3. German : Limited working proficiency.

## Personal Interest:

1. Reading books.
2. Astrophotography.

**Personal Details:**

Name : Santhoshkumar M  
Date of Birth : September 27, 1991  
Gender : Male  
Marital Status : Married  
Nationality : Indian  
Spouse Name : Ratchakambal Santhoshkumar  
Permanent Address : S/o R. Mahadevan, 1/17a, Vellaler Street,  
Vallam village, Mathur post, Kancheepuram (Dt), 602105.

---

**Declaration:**

I hereby declare that all the details furnished above are true to the best of my knowledge and belief.



**(Santhoshkumar M)**

Date : September 8, 2021

Place : Patiala